

I. Introduction

1.1 Overview

Accurate Quantitative Precipitation Forecasting (QPF) has been a long-standing goal of the operational forecasting community. However, this goal has proved elusive since mesoscale precipitation features largely affect precipitation accumulation. Mesoscale band formation in extratropical cyclones has been a popular focus for study in improving QPF, since these features can dramatically affect the basic intensity, timing, and subsequent accumulation of precipitation. The effects of mesoscale bands are especially evident during the cold season, when snowfall associated with the bands can produce “white out” conditions and significant snowfall accumulations. Despite these dramatic effects, the mesoscale nature of precipitation bands has made their diagnosis and prediction challenging.

Numerous theoretical and observational studies (e.g., Emanuel 1985; Sanders and Bosart 1985; Moore and Lambert 1993; Nicosia and Grumm 1999) have established that mesoscale bands are primarily forced by frontogenesis in the presence of small moist symmetric stability. Although Conditional Symmetric Instability (CSI) (Bennetts and Hoskins 1979) has often been cited as a condition for banded precipitation, considerable debate surrounds its correct operational diagnosis (Schultz and Schumacher 1999). As Schultz and Schumacher (1999) point out, the theoretical constraints of CSI make operational diagnosis difficult. Furthermore, the co-existence of frontogenetical forcing, banded elevated upright convection, and CSI (e.g., Reuter and Yau 1990; Martin 1998a,b) often complicates real-time dynamical assessment. Whether or not pure CSI is

found within cases becomes secondary to the fact that frontogenesis is coincident with weak symmetric stability, which results in a narrow sloping updraft as shown by Emanuel (1985).

Several case studies in the northeast United States (US) (e.g., Sanders and Bosart 1985; Sanders 1986; Nicosia and Grumm 1999) have established the occurrence of significant mesoscale banding events associated with strong frontal zones, but a comprehensive investigation establishing the frequency, variety, dynamical forcing, and environmental stability of banded events has not been conducted. In the past, a lack of observational data on the scale of banded features prohibited such a comprehensive investigation. However, the operational deployment of the National Weather Service (NWS) Weather Surveillance Radar-1988 Doppler (WSR-88D) national radar network (Klazura and Imy 1993) in the 1990s and the recent availability of gridded daily precipitation datasets allows for the examination of precipitation systems in their entirety as they evolve through time and space, and provides a standardized base to objectively identify mesoscale bands. These tools are employed to conduct a comprehensive study of mesoscale band formation in the northeast US.

1.2 Literature Review

1.2.1 Cyclone Conceptual Models

The Norwegian Cyclone Model (NCM) (Fig. 1.1) (Bjerknes 1919; Bjerknes and Solberg 1922) has served as a conceptual foundation for describing the evolution of extratropical cyclones. Although the NCM successfully documents the primary features

of mid-latitude cyclone evolution, observational and numerical research during the past 80 years has revealed the existence of cyclone evolutions that do not conform to the traditional model (e.g., Mass 1991).

Specifically, the reliance of the operational meteorological community on the NCM for the analysis of fronts is a source of contention (Mass 1991; Uccellini 1992). The NCM identifies the cold front, warm front, and occluded fronts as well-defined airmass boundaries; however cyclones often display diffuse air mass boundaries. In an analysis of an oceanic warm front, Wakimoto and Bosart (2001) showed that the surface front did not exhibit a strong discontinuity in wind, temperature or moisture, and could only be identified aloft along a short horizontal distance, resulting in a “short and stubby” warm front. Wallace and Hobbs (1977) contend that the development of the occluded front as depicted by the NCM is rarely observed. In addition to these criticisms, the NCM does not account for lee troughs, dry lines, or inverted troughs - features which separate air masses not accounted for in the NCM (Hobbs et al. 1996). However, these features often serve as a focus for precipitation (e.g., Uccellini 1992; Keshishian et al. 1994). To further explain these observations several subsequent cyclone paradigms have been proposed.

The conveyor-belt model of cyclones (Fig. 1.2), developed by Browning and Harold (1969), and more recently by Carlson (1980), depicts airflow through cyclones on multiple isentropic surfaces. This conceptual model builds on the pioneering work of Danielsen (1968), who utilized isentropic analysis and potential vorticity (PV) conservation techniques to document how chemical constituents residing in the stratosphere can be transported to the surface in developing cyclones. In contrast to the

NCM, which stresses large-scale air mass boundaries, the conveyor belt model stresses coherent flows originating within such airmasses, which interact during the cyclone evolution.

The conveyor-belt conceptual model suggests that the cloud and precipitation structures of cyclones can be described in terms of the Warm Conveyor Belt (WCB), Cold Conveyor Belt (CCB), and dry airstream (Browning 1990). The WCB is an airstream originating in the warm sector of cyclones, flowing poleward and sloping upward ahead of the cyclone. The WCB is responsible for the majority of clouds and precipitation along and ahead of the traditional cold and warm fronts. The CCB originates in the anticyclonic low-level flow ahead of the warm front, and undercuts the WCB. As air within the CCB travels towards the cyclone center it slowly ascends, producing low-level clouds and light precipitation. Carlson (1980) contends the westward extension of the CCB is responsible for the comma head portion of cyclones. The dry airstream, as shown by Danielsen (1968), originates in the upper troposphere and lower stratosphere and descends into the cyclone center. The marked dryness of this airstream results in the development of the dry slot.

The most prominent modification to the NCM frontal analysis scheme is the Shapiro-Keyser (1990) conceptual model (Fig. 1.3). This model was spurred by early numerical studies of developing baroclinic waves (e.g., Hoskins 1976; Hoskins and West 1979) in which nontraditional frontal characteristics, most notably the westward migration of warm frontal structure behind the surface cyclone, were produced. This evolution resulted in the largest baroclinicity during the life-cycle being found behind the surface cyclone. Subsequent maritime field studies such as the Genesis of Atlantic

Lows Experiment (GALE) (Dirks et al. 1988) in 1986 and the Experiment on Rapidly Intensifying Cyclones over the Atlantic (ERICA) (Hadlock and Kreitzberg 1988) in 1988-1989 provided observational evidence for the existence of such frontal structures.

Based on these field studies Shapiro and Keyser (1990) developed the Shapiro-Keyser conceptual model of cyclones. In this model, during cyclogenesis the cold front becomes diffuse near the cyclone center (called a frontal fracture) allowing the cold and warm front to maintain a perpendicular orientation throughout the cyclone evolution (referred to as a T-bone frontal structure). Consequently the primary baroclinic zone is zonally oriented, found on the poleward flank of the cyclone and extending behind the surface cyclone center. The westward extension of the primary baroclinic zone behind the surface cyclone center was termed the “bent-back” warm front (Shapiro and Keyser 1990) in recognition of its warm frontal characteristics.

1.2.2 Models of Cyclone Substructure

The advent of radar and satellite technology has revealed the mesoscale nature of precipitation in extratropical cyclones. For example, Austin and Houze (1972) documented this fact in a quantitative description of precipitation patterns in nine New England storms by utilizing radar observations and detailed rain gauge records. Contemporary models addressing such structure are now discussed.

Browning (1985) and Browning (1990) summarized contemporary conceptual models of precipitation systems in the context of warm and cold conveyor belts, concentrating on cold front bands which frequently affect western Europe. The WCB is

found to be the principal airstream contributing to precipitation ahead of the cold front, with a small component of flow across the front contributing to post-frontal precipitation. Browning (1999) concentrates on the role the dry airstream plays in initiating banded convection. Specifically, the dry intrusion may be considered an upper-cold front (Fig. 1.4) (Hobbs et al. 1990), thus initiating convection along its leading interface. Browning (1999) notes that midlevel convection frequently occurs where the dry intrusion overruns the bent-back warm front. Additionally the juxtaposition of the dry airstream over the WCB can lead to layers of potential instability within the dry slot, which may be released as intense convection.

Most of the conceptual models discussed thus far were developed from observations in maritime climates. Keshishian et al. (1994) demonstrate that the unique geography of continental regions can lead to a number of features not accounted for in the preceding models (Fig. 1.5), including lee troughs, drylines, low-level jets, and arctic fronts among others. In recognition of the complex continental cyclone evolution in the central US, Hobbs et al. (1996) present the Structurally Transformed by Orography Model (STORM) conceptual model. This model describes the evolution of mesoscale features associated with continental cyclones in the lee of the Rocky Mountains, placing their development in the context of continental cyclones. Focus is placed on the development of synoptic-scale rainbands associated with drytroughs (a lee trough that also has characteristics of a dryline) (Fig. 1.6) and upper-cold fronts (Fig. 1.7). In many ways these rainbands are similar to the rainbands identified by Browning (1985) and Browning (1999) since they are forced along an upper-level transition zone in which dry mid-level air is superimposed over moist air, resulting in potential instability and

subsequent convection. Although intended for the Great Plains, the STORM conceptual model has been noted to apply to rainbands well into the eastern US (Locatelli et al. 1989; Koch 2001).

One noted deficiency of the STORM model is that it does not explicitly account for mesoscale precipitation bands on the poleward side of cyclones, or address the formation of the comma head. Martin (1998a,b, 1999) addresses mesoscale substructure in the comma head portion of cyclones in an investigation of a continental cyclone. Drawing on the “three front model” developed by scientists at the Canadian Meteorological Service during the 1950s (Godson 1951; Penner 1955; Galloway 1960), Martin (1998) explains the comma head formation in terms of the Trough of Warm Air Aloft (trowal). The trowal is a line connecting the crests of a thermal wave at successive heights (Crocker et al. 1947; Galloway 1958), or as summarized by Martin (1998), “the axis of warm air ahead of the upper cold front in a warm occluded cyclone.” Thus the trowal can be considered as the upper-level representation of the classical occluded front [although an occluded front need not be present (Godson 1951)].

The continental cyclone studied by Martin (1998a,b) exhibited a well-defined trowal. This feature played an integral role in the distribution of precipitation in the comma head portion of the cyclone. Isentropic analysis dramatically revealed the development of the trowal, and further revealed a striking similarity to the Shapiro-Keyser cyclone model, with the trowal being represented as the westward extension of the warm front (Fig. 1.8). Parcel trajectories confirmed that air within the trowal originated from within the warm sector, and ascended rapidly within the trowal, creating clouds and precipitation. Such air motion led to the suggestion of the addition of the

trowal airstream to the conveyor-belt model of cyclones, defined as the cyclonically turning portion of the WCB that is responsible for precipitation in the occluded quadrant of cyclones.

The trowal airstream has recently been acknowledged by Browning (1999) and Schultz (2001). Based on a case study by Browning and Roberts (1994), Browning (1999) incorporates the trowal airstream into the original conveyor-belt model by adding a cyclonically turning portion of the CCB (Fig. 1.9). In a reexamination of Carlson (1980), Schultz (2001) found that the CCB identified in the original case study was split into ascending anticyclonically and cyclonically turning airstreams, with the sense of turning dependent on the chosen isentropic surface. Additionally, it was shown that the cyclonically turning airstream ascended as it wrapped around the cyclone. Thus the cyclonically turning airstream in the original Carlson (1980) case could be considered the trowal airstream.

1.2.3 Mesoscale Band Studies

Precipitation associated with the features discussed above has often been observed to be organized into bands with widths less than 100 km. Numerous studies have investigated the characteristics of these bands through descriptive, case study and composite analysis, of which the most pertinent to this study will be reviewed. For a comprehensive, modern review of cold-season banded precipitation studies see Schultz and Schumacher (1999). This review summarizes theoretical and observational knowledge at the end of the 20th Century.

1.2.3a Band Descriptions

Numerous observational studies have established that frontal precipitation is frequently organized into bands. Some of the first include Knettner (1959), Harper and Beimers (1958), and Boucher and Wexler (1961). In a study of Pacific cyclones along the southern California coast during three winter seasons, Elliott and Hovind (1964) demonstrated numerous examples of convective bands. In a detailed case study of a cyclone in the British Isles, Browning and Harrold (1969) showed that a cyclone can exhibit several types of banded structure during its lifetime, and proposed warm frontal rainbands and warm sector rainbands as a general classification. Kreitzberg and Brown (1970) echoed these results in a study of an occluded cyclone in New England. Out of the eight banded features they identified on radar, three were parallel to the warm frontal zone, while four others were parallel to the cold frontal zone. Browning and Harrold (1970) additionally document a very narrow band (~10 km) along the surface cold front.

The Cyclonic Extratropical Storms Project (CYCLES) afforded the Cloud Physics Group at the University of Washington the opportunity to survey the mesoscale structure of rainfall in occluded cyclones. The goal of the project was to confirm the existence of warm and cold frontal bands in western Washington state, and provide descriptive definitions.

In a radar survey of 11 maritime cyclones affecting western Washington state, Houze et al. (1976) identified and defined six types of rainbands, providing a contemporary band classification scheme. The six types were: warm frontal, warm

sector, cold frontal-wide, cold frontal-narrow, wave, and post frontal. The bands were defined as the following, quoted directly from Houze et al. (1976):

“Warm frontal. Bands approximately 50 km in width oriented parallel to the warm front and found toward the leading edge of a frontal cloud shield.

Warm sector. Bands typically 50 km in width, found south of the intersection of the surface warm and cold fronts and tending to be parallel to cold fronts.

Cold frontal: wide. Bands approximately 50 km in width oriented parallel to the cold front and found toward the trailing edge of a frontal cloud shield.

Cold frontal: narrow. Extremely narrow band (~5 km in width) coinciding with surface cold front.

Wave. Bands occurring in a very regular pattern similar to waves, typically 10-20 km wide.

Post frontal. Rainbands located in the convective cloud field behind a frontal cloud shield.”

This band classification scheme influenced research efforts for the next 20 years, and remains today. Hobbs (1978) subsequently developed a schematic which placed these bands relative to surface fronts and surface cyclone positions (Fig.1.10).

Elaborating on the band classification scheme of Hobbs et al. (1976), Hobbs (1978) summarized the dynamical and microphysical structures associated with the different types of rainbands. Narrow cold frontal bands were found along the immediate cold frontal zone, associated with boundary layer convergence along the leading edge of the front. Wide cold frontal bands were found behind the surface cold front in a convectively stable environment. In contrast, warm sector rainbands were found to be

convective, generally propagating away from the surface cold front. Hobbs (1978) additionally identified prefrontal cold-surge bands as being associated with pulses of cold air ahead of the primary cold front in an occlusion. This feature would later be termed a Cold Front Aloft (CFA) by Hobbs (1990).

Wang and Hobbs (1983) in a case study of an occluded cyclone further investigated the wave rainbands, finding that they were ~5 km wide, ~80 km long, periodically spaced 5-10 km apart, and arranged nearly parallel to the winds at their upper levels. Further they showed through observations with the National Oceanic Atmospheric Administration (NOAA) P-3 aircraft that temperatures and vertical velocities fluctuated ~1-2 °C and 1-2 m s⁻¹ respectively, in a wavelike manner while flying through the bands.

K. A. Browning conducted complementary studies of rainbands in Great Britain during the 1980s and 1990s, many of which have been reviewed above. Most recently Browning and Roberts (1999) document a case of fast-moving, arc-shaped narrow rainbands in a dry slot, which they term arc rainbands. Browning and Roberts (1999) concluded that the bands could be analyzed as upper cold fronts, embedded within a broad cold-frontal zone associated with the advancing dry intrusion. Defined as such, these bands may be similar to the prefrontal, cold-surge bands proposed by Hobbs (1978).

1.2.3b CSI

Bands occurring ahead of the cold front, or in the warm sector of a cyclone can readily be understood in terms of the release of conditional or potential instability along linear forcing, resulting in banded convection. However, bands occurring behind the cold front, ahead of the warm front, or in the occluded quadrant of cyclones often occur in an environment stable to upright convection. Proposed mechanisms to explain the existence of these bands include: frontogenesis, boundary-layer instabilities, gravity waves, Kelvin-Helmholtz instability, topographical effects, and CSI (Schultz and Shumacher 1999). Among these, CSI has gained considerable attention.

CSI may be manifest as elongated precipitation structures oriented nearly parallel to the tropospheric thermal wind (Emanuel 1985). Typical band widths range from 50 to 100 km with lengths ranging from 75 to 400 km, while lifetimes are generally limited to a few hours (1-3 h) (Wiesmueller and Zubrick 1998).

Bennetts and Hoskins (1979) proposed CSI as a possible explanation for mesoscale bands. CSI occurs in an unsaturated moist environment stable to upright and horizontal motions, but unstable to slantwise ascent. According to parcel theory, an environment is conditionally unstable to slantwise displacements if a parcel achieves positive buoyancy when lifted along a surface of constant geostrophic pseudo-angular momentum surface (M-surface) (Emanuel 1985). Therefore, CSI can be diagnosed when the saturated equivalent potential temperature (θ_{es}) decreases along a constant M-surface in an unsaturated moist environment. An alternative diagnosis as proposed by Sanders and Bosart (1985) and Moore and Lambert (1993) identifies regions which are statically

stable, but exhibit negative saturation equivalent potential vorticity (EPV) in an unsaturated moist environment, as susceptible to CSI. For a concise summary of the theoretical background and application of CSI see Houze (1993, 53-56)

Geostrophic frontogenetical forcing is the principal mechanism found to release CSI. Emanuel (1985) proposed a coupled relationship between frontogenesis and moist symmetric stability through manipulation of the Sawyer–Eliassen equation (Sawyer 1956; Eliassen 1962). Specifically, when the symmetric stability is small on the warm side of a frontal boundary (as it often is in baroclinic systems) and larger on the cold side, the direct circulation induced by frontogenesis is dramatically enhanced on the warm side of the circulation. By mass conservation arguments, the response takes the form of a concentrated sloping updraft on the warm side of the frontogenesis maximum (resulting in a band), with weak downward motion elsewhere (Fig. 1.11). It is important to note that the symmetric stability need not be negative for a narrow updraft to occur.

Xu (1992) points out that the single band produced by a frontal circulation in the presence of small moist symmetric stability can last longer than pure CSI bands since the band is stable and supported by large-scale forcing and moisture supply. However, this combination cannot account for multiple banding. Through a viscous semigeostrophic model, Xu (1992) shows that in an environment exhibiting large negative EPV, CSI bands can exhibit finescale multibanded structures that stretch and merge into the dominant single band of moist ascent.

1.3.3c Observational Case and Composite Studies

Case study and composite analysis has largely confirmed the theoretical work of Emanuel (1985) and Xu (1992), often finding frontogenesis in the presence of small moist symmetric stability coincident with mesoscale banding. Sanders and Bosart (1985) in a case study of an intense snowband along the northeast U.S. coast, found that the region of banding underwent frontogenetical forcing in the presence of small moist symmetric stability, resulting in a narrow, intense updraft located on the equatorward flank of the frontogenesis maximum. Sanders (1986) in a case study of another major New England snowstorm found that banding observed in the comma head portion of the storm coincided with strong frontogenetical forcing and weak symmetric stability. However this case exhibited several different bands instead of a single, dominant band as observed by Sanders and Bosart (1985).

Intensive field experiments of maritime cyclones provided an observational wealth of data. During GALE Emanuel (1988) utilized the NCAR King Air research aircraft to construct M-surface soundings in four developing warm frontal zones. In three of the four cases the atmosphere was almost exactly neutral to slantwise ascent, while statically and inertially stable. These findings implied that CSI had been released, returning the atmosphere back to a state of slantwise neutrality.

The Canadian Atlantic Storms Project (CASP) (Stewart 1991) sampled 16 maritime cyclones affecting Atlantic Canada. Many of the same banded structures identified by Hobbs (1976) were observed; however, in contrast to Hobbs (1976), most of the banded structures were found ahead of the warm front and in the comma head

portion of cyclones, while the surface cold front was seldom associated with substantial precipitation, let alone banded structure. Reuter and Yau (1990) investigated the environments of seven precipitation bands observed during CASP during a three month period over Nova Scotia. The existence of seven significant precipitation bands in a small geographical area, during the limited study period highlighted the relative frequency of mesoscale banding in Atlantic Canada. Cross-sectional analysis of the band environments exhibited shallow layers susceptible to CSI in each case, but it was hypothesized the CSI was only released in the lower atmosphere where saturation is maintained. A complication was the existence of layers neutral to upright convection, and layers of slantwise neutrality. These results corroborated the hypothesis of Emanuel (1988) that once CSI is released, the atmosphere readily tends toward a state of slantwise neutrality.

Mesoscale observational data gathered during the FRONTS 87 experiment over northwest France were used by Lemaitre et al. (2002) to demonstrate the combined role of frontogenetical forcing and CSI in mesoscale band formation along a cold front. Using space-time conversion, the ascending branch of the frontogenetical circulation is shown to exhibit embedded convective rolls. These rolls were found 3–4 km above the surface, with a spacing of ~160 km. Comparison of these convective rolls with CSI theory showed close agreement, leading the authors to conclude that the rolls were evidence of CSI, generated by frontogenetical forcing in the presence of a symmetrically neutral to slightly unstable atmosphere.

Byrd (1989) conducted a composite study of precipitation bands utilizing eight Weather Service radar – 1957 (WSR-57) (non Doppler) sites in the southern Plains and

complementary sounding sites in an investigation of the relevance of CSI theory to overrunning precipitation events. Cases for study were limited to overrunning situations in which more than 0.5 cm of precipitation (liquid equivalent) was measured in the radar vicinity. Radar signatures were subjectively identified as nonbanded, weakly banded, and strongly banded, and the nearest sounding to the event was included in each composite. The nonbanded sounding composite exhibited a colder and more stable boundary layer, with less midlevel shear than strongly banded cases. Unfortunately, the composites showed little difference in Richardson number (used as a measure of dynamic stability) for banded and nonbanded cases, highlighting the difficulty in assessing banded situations from sounding data.

Although moist slantwise convection seems an attractive mechanism for band formation, several studies have documented intense bands without its presence. In these cases elevated upright convection manifest by the release of potential instability has been documented. In a study of a continental cyclone, Martin (1998a,b) showed through parcel trajectories that elevated convection within the trough was forced by intense mid-level frontogenesis. This forcing in the presence of potential instability resulted in the formation of an intense snowband. Recently Trapp et al. (2000) examined a winter storm over the southern plains, finding that upright convection associated with Convective Available Potential Energy (CAPE) in part accounted for an observed snowband. They also documented an intense cell with an updraft originating from the boundary layer well into the cold air.

1.3.3d *Operational Approaches*

The implementation of the WSR-88D radar network, and the advent of mesoscale models and advanced forecast processing workstations during the 1990s has led to innovative operational applications concerning mesoscale band formation (Nicosia and Grumm 1999). Traditionally, assessment of the dynamic stability and subsequent anticipation of band formation required cross-sectional analysis of M_g and θ_e surfaces (Snook 1992). However, this analysis can be rather cumbersome and, more importantly, time consuming (Wiesmueller and Zubrick 1998). As an alternative to the traditional M_g and θ_e analysis, Wiesmueller and Zubrick (1998) favor the use of EPV as discussed by Moore and Lambert (1993), and provide two case studies of its use. They are clear to note, however, that the static stability should be examined within regions of low EPV since the atmosphere may exhibit CSI and Conditional Instability (CI) simultaneously, in which case CI will dominate.

Although cross section analysis will reveal the possibility of enhanced vertical motion (whether via CSI or CI), forecasters are still left with the prospect of placing the cross section in both time and space. In acknowledgment of this fact, Grumm and Forbes (1994) have suggested that research should first focus on identifying the synoptic patterns conducive to banding, thus providing a context for the cross section analysis.

Spurred by this suggestion and utilizing the EPV framework, Nicosia and Grumm (1999) provided a dynamical review of three mesoscale banded cases in the northeast US. In contrast to the Hobbs and Browning studies, they found that each storm exhibited banded structure *north and west* of the cyclone center rather than ahead of the

classic warm front or along the cold front. These bands were coincident with frontogenesis in the deformation zone, north and west of the developing cyclone. They further found that the juxtaposition of these parameters most frequently occurs to the north of the developing midlevel (near 700 hPa) low during cyclogenesis. Cross-sectional analysis through this region in each cyclone revealed that intense mid-level frontogenesis was coincident with a deep layer of negative EPV, characterized by regions of both CSI and CI. Therefore, a key conclusion was that band development could be anticipated during cyclogenesis, just north of the 700 hPa low, when a vertically deep layer of negative EPV is found in conjunction with intense frontogenesis.

Based on the similarities observed in each case, Nicosia and Grumm (1999) provided a conceptual model of band formation in the comma head portion of cyclones (Fig. 1.12). This model summarizes the dynamical banding environment in terms of the conveyor-belt model, frontogenesis, and the reduction of EPV. Namely, they suggest that the EPV is reduced in a zone where the midlevel dry airstream overlaid a low-level easterly jet (CCB), usually south of the midlevel frontogenesis maximum. This zone is characterized by differential moisture advection, which readily steepens the θ_{es} surfaces, and frontogenetical forcing, which also steepens the θ_{es} surfaces, and additionally decreases the slope of M-surfaces. The coexistence of frontogenesis and low EPV then leads to mesoscale band formation in the comma head portion of cyclones in the manner demonstrated by Emanuel 1985.

Additionally, the relationship between frontogenesis and symmetric stability is placed in the context of a positive feedback system. By thermal wind arguments the increasing temperature gradient forced by frontogenesis results in increased vertical

shear. The increased shear decreases the slope of M-surfaces, which reduces the EPV since the M-surfaces may now slope less than the isentropes (a condition for negative EPV). This reduction of EPV leads to enhanced ascent, and subsequent enhanced low-level convergence. The enhanced convergence contributes to even stronger frontogenesis. Thus the existence of frontogenesis provides an environment favoring low EPV. This synergism between frontogenesis and symmetric stability provides a complementary interpretation of Xu (1992), explaining the observed long-lasting (>10 h) bands that are theoretically unlikely in pure CSI theory.

Recently Wetzel and Martin (2001) have developed winter season “ingredients maps” intended to identify regions of heavy precipitation. They assert that the forecast process of winter season precipitation is analogous to its counterpart for summer season precipitation – namely identifying the coincidence of lift, instability, and moisture. They additionally note that precipitation microphysics become an important constituent when assessing snowfall. To diagnose the coincidence of these parameters they develop “ingredients maps.” These maps highlight the PVQ parameter, defined as the product of the Q vector divergence and EPV. Thus when PVQ is greater than zero there is potential for heavy precipitation. Ingredients cross sections are then recommended through the positive PVQ region to assess the vertical structure of PVQ, moisture, and temperature.

Although this method facilitates the placement of cross sections by dynamical reasoning and provides a diagnostic method, it is not intended to identify mesoscale banding such as the model proposed by Nicosia and Grumm, nor does it provide synoptic context. Additionally, Schultz and Doswell (2001) suggest caution in the use of the PVQ diagnostic since heavy precipitation can occur on a variety of scales (not just

synoptic scale as implied by the use of the Q vector), and can be observed without the collocation of the parameters (the instability is found equatorward of the forcing or above the forcing). They also note that the magnitude of the PVQ diagnostic is dependent on the data resolution. Wetzel and Martin (2002) address these criticisms by stressing that the PVQ parameter is only intended to identify regions susceptible to convection (slantwise and upright), not all areas susceptible to heavy precipitation.

Dixion et al. (2002) utilize the ingredients based methodology to develop the Vertically Integrated extent of Realizable Symmetric instability (VRS) diagnostic. This diagnostic measures the number of model layers at a point at which the following environmental conditions are met:

EPV < 0

Conditionally stable

Relative Humidity > 95% (with respect to ice)

Upward vertical motion

Intertially stable

A spatial map of the number of layers where these conditions are met explicitly shows the vertical depth of symmetric instability, and thus outlines the area most susceptible to symmetric instability. In a conceptual summary of the cyclones studied, Dixion et al. (2002, Fig. 12) note that the VRS diagnostic frequently exhibited maxima in the comma head portion the cyclone, reinforcing the conceptual model developed by Nicosia and Grumm (1999).

1.3 Study Goals

The primary goal of this research is to improve diagnosis and subsequent prediction of mesoscale banded features in the northeast US. Although numerous studies have extensively addressed this problem through numerical, case study and composite analysis, emphasis has been placed on bands occurring along the cold front, in the warm sector, or ahead of the warm front. The current study focuses on band development in the comma head portion of cyclones. Additionally this study utilizes the WSR-88D composite radar data during five cold seasons. The resultant dataset of 89 significant precipitation cases, including over 150 significant individual banded events, provides an unprecedented wealth of observational data. Perhaps more importantly, this dataset includes nonbanded cases – a component of the problem rarely studied.

The first part of this study develops a band climatology that documents the frequency and variety of banded features observed in the northeast US. The NWS WSR-88D national radar network is utilized to develop a band classification scheme documenting the various types of mesoscale bands observed in the northeast US. Although classification schemes exist and are well established (e.g., Hobbs et al.1976), none has been developed with the current WSR-88D radar network, which provides standardized observations, nor do current schemes explicitly account for the existence of mesoscale bands in the comma head portion of cyclones as observed in numerous case studies in the northeast US and adjacent Atlantic Canada (e.g., Sanders and Bosart 1985; Sanders 1986; Reuter and Yau 1991). Application of the new band classification scheme

to five recent cold seasons provides a limited climatology of mesoscale banding in the northeast U.S.

The resultant dataset of banded cases is then used for composite investigations to identify the synoptic-scale patterns conducive to mesoscale band formation. Although these composites do not explicitly resolve the circulations responsible for the bands, they highlight the key dynamical features involved in mesoscale band formation, and illustrate how the synoptic flow evolution influences cyclone substructure. This component of the study fully addresses the suggestion of Grumm and Forbes (1994) and builds on Nicosia and Grumm (1999) by placing mesoscale banding in the context of the synoptic flow evolution. Subsequent composite cross-section analysis reveals the characteristic environmental forcing, stability, and first-order microphysics of the different types of banded events. Case study comparisons are presented to illustrate how the composite results can be used in an operational setting to diagnose mesoscale band formation.

It is our hope that these study results will be used by forecasters to physically understand how the multiscale dynamics of a cyclone affect band formation and evolution; namely, that the anticipated synoptic flow evolution can be used to determine first whether a banding environment will be supported, and second, where within the cyclone this environment will exist. Therefore, instead of catching up to a banded event, forecasters can anticipate the future evolution.

THE EVOLUTION OF CYCLONES

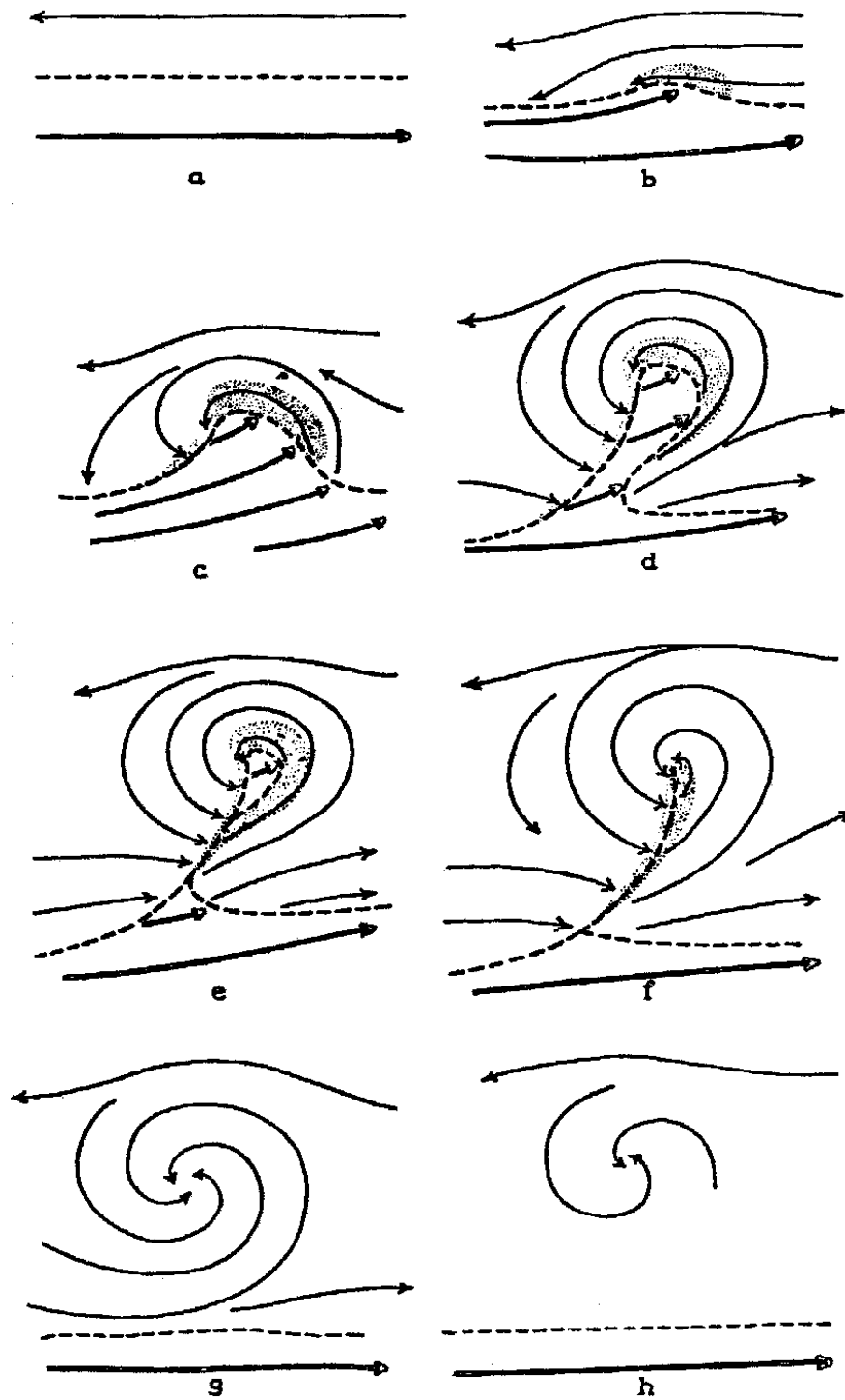


Fig. 1.1. Schematic of cyclone development in the Norwegian Cyclone Model. As shown by Bjerknes and Solberg (1922).

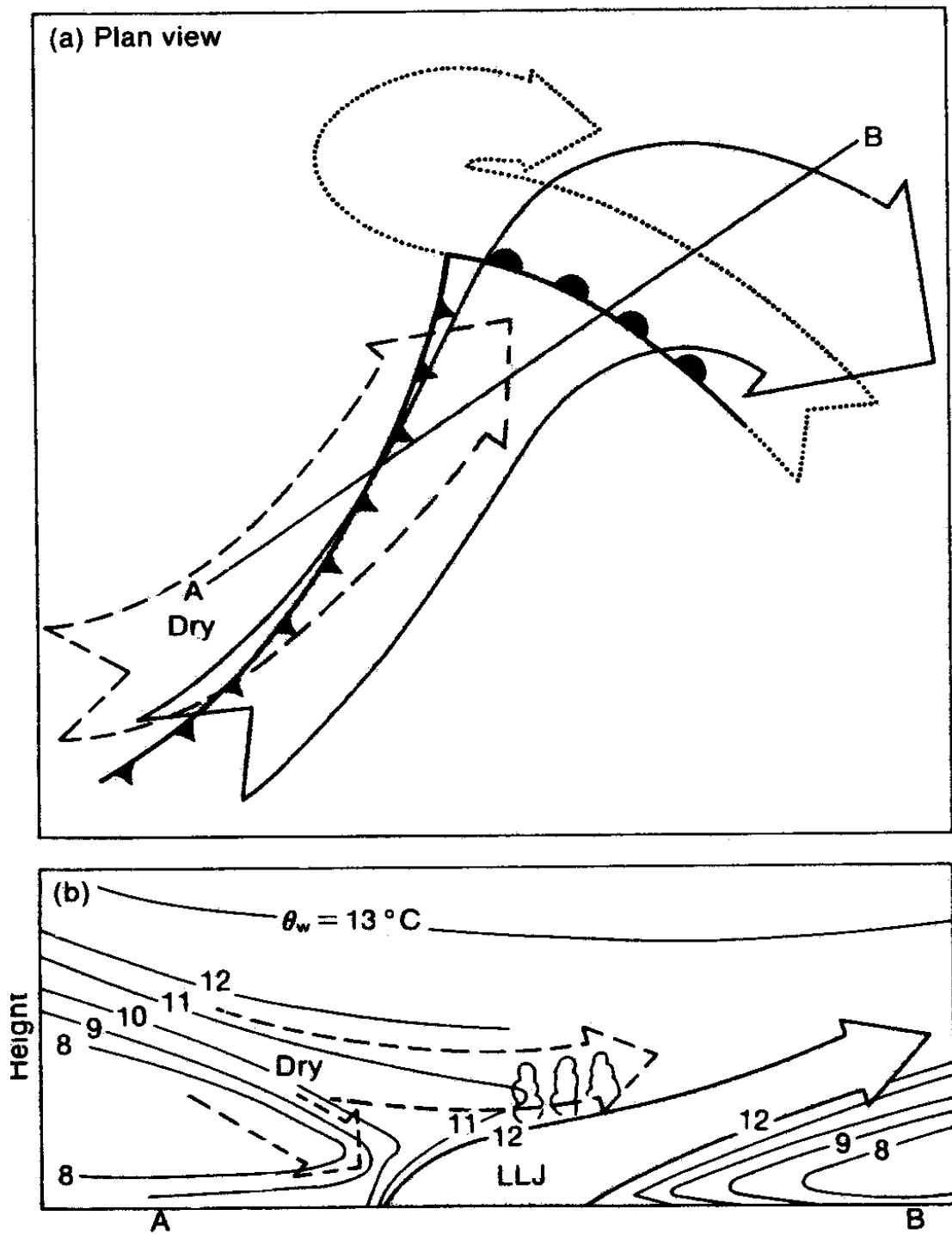


Fig. 1.2. (a) Schematic showing the three principal airstreams in the conveyor belt model. (b) Cross-section (A-B) showing the web-bulb potential temperature (thin black lines), and the vertical interaction between the principal airstreams (arrows). Adopted from Browning (1990).

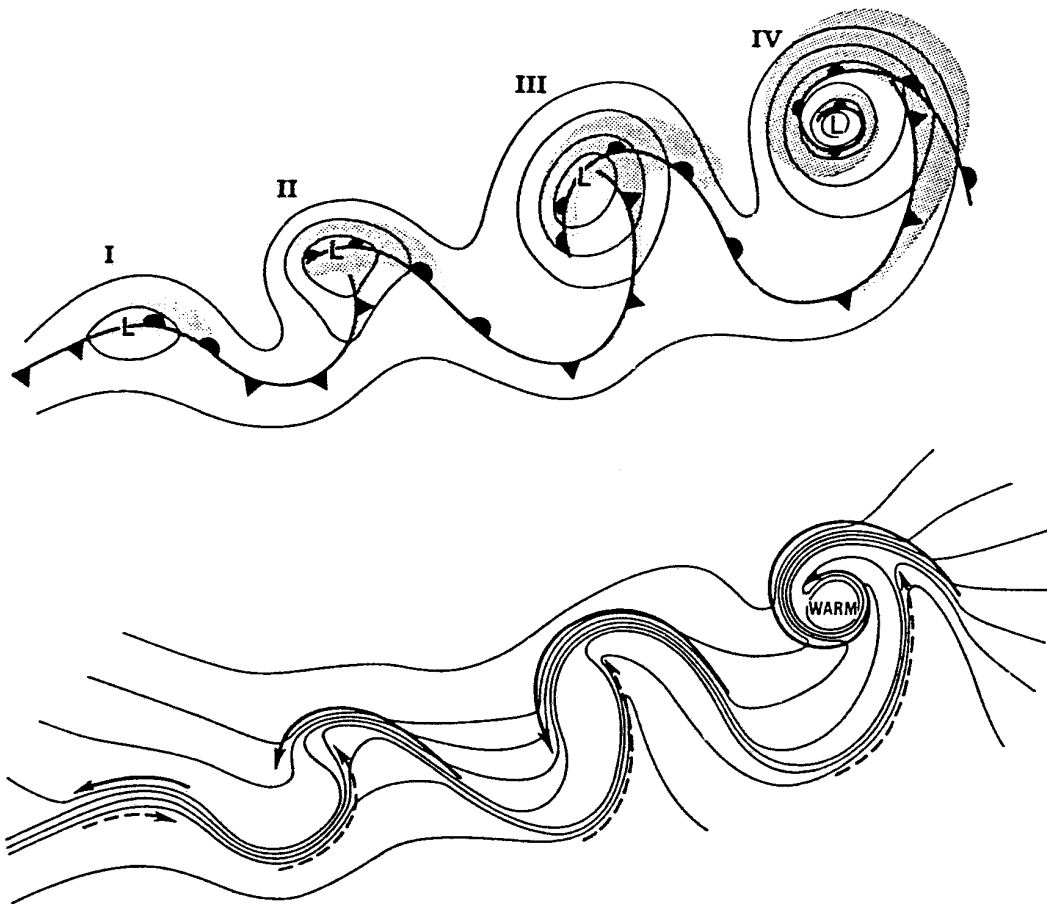


Fig. 1.3. Schematic of the Shapiro and Keyser (1990) model of a maritime extratropical cyclone showing the frontal fracture (II) and bent-back warm front (III). (top) Sea level pressure (solid), fronts (bold), and cloud field (shaded). (bottom) Temperature (solid) and cold and warm air currents (solid and dashed arrows, respectively).

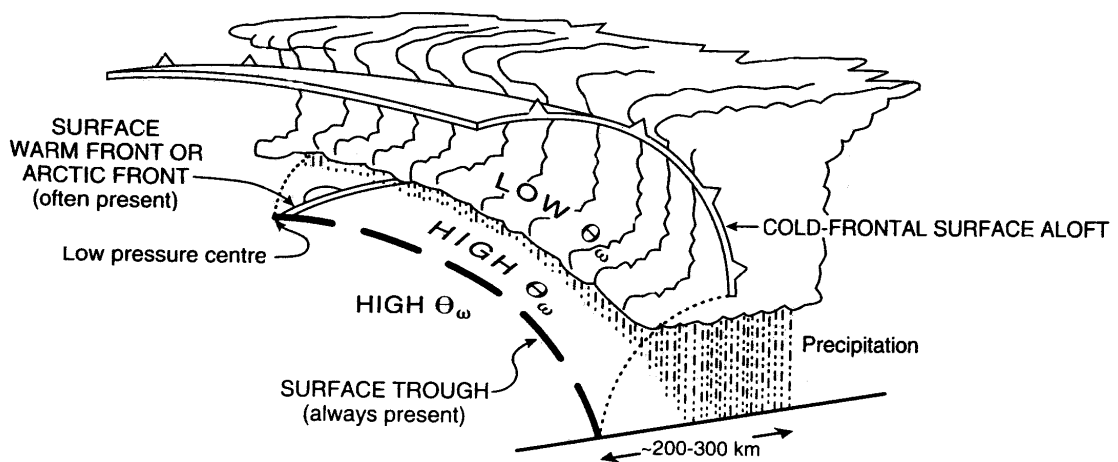
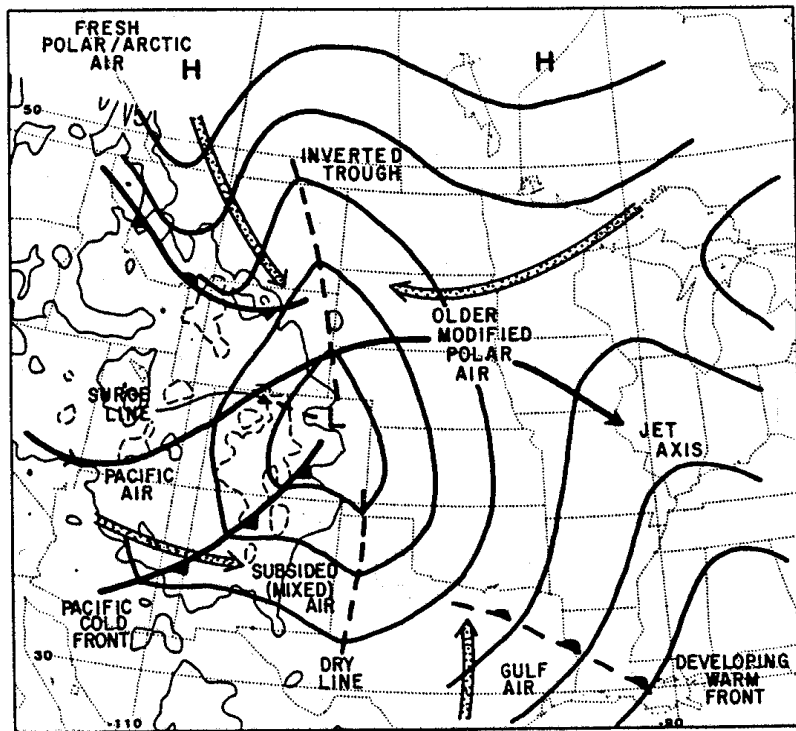
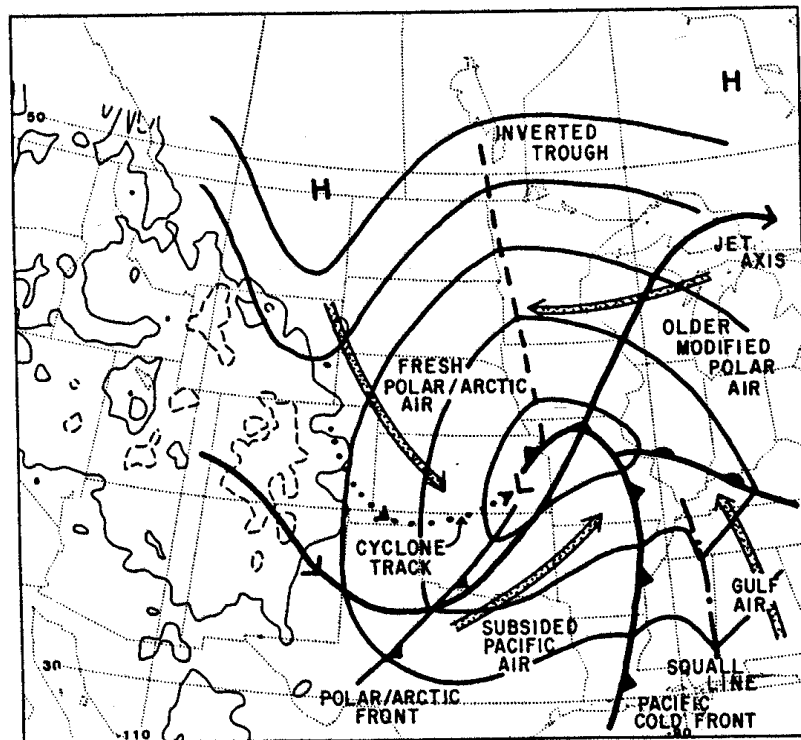


Fig. 1.4. Schematic of a cold front aloft. Adopted from Browning (1990).



(a)



(b)

Fig. 1.5. Schematic of cyclogenesis east of the Rocky Mountains (adopted from Keshishian (1994)) when an inverted trough is present for (a) initial time and (b) some later (~24 h) time.

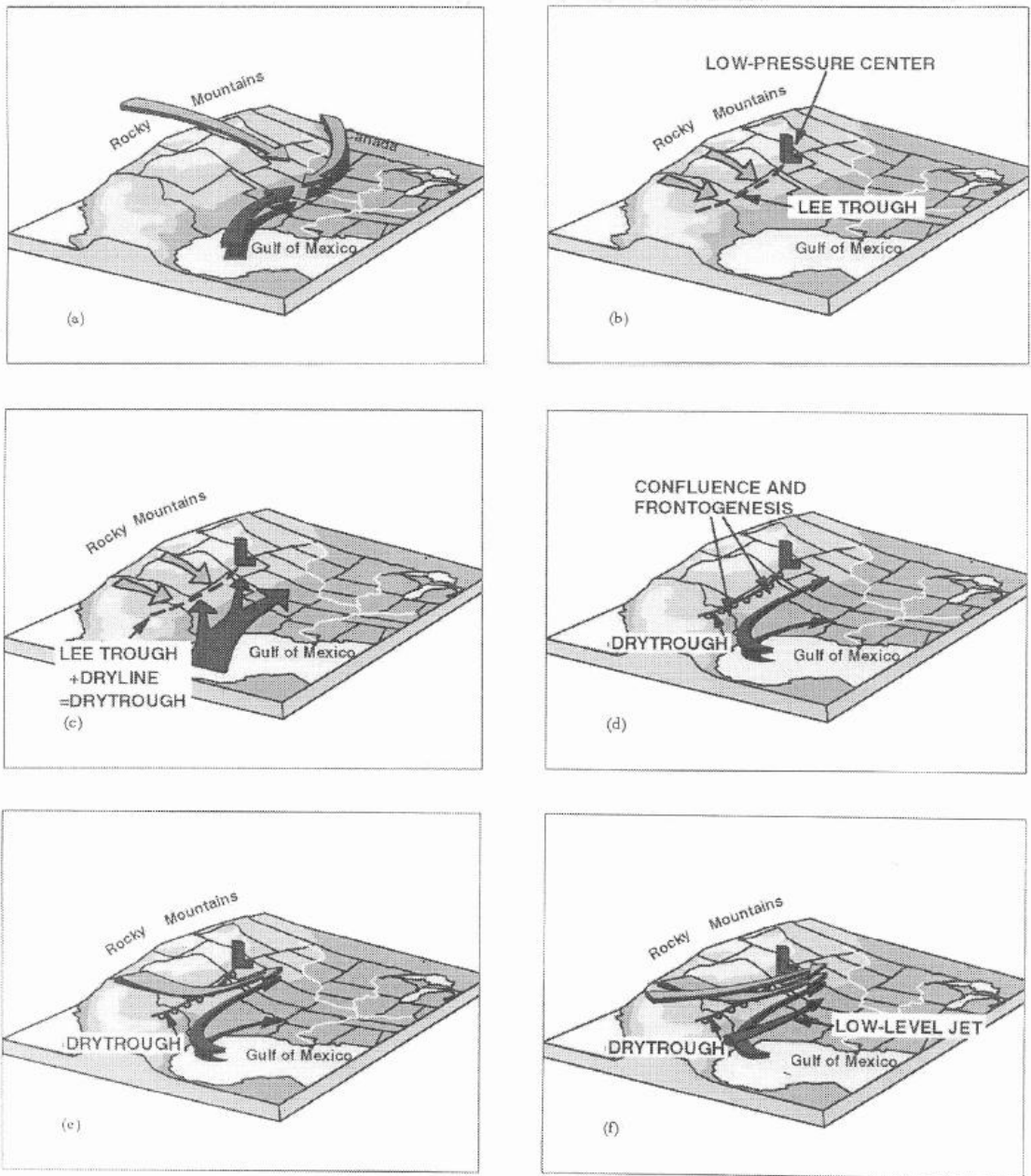


Fig. 1.6. Schematics illustrating airflows and the formation of a drytrough as an eastward moving shortwave trough passes over the Rocky Mountains. Adopted from Hobbs et al. (1996).

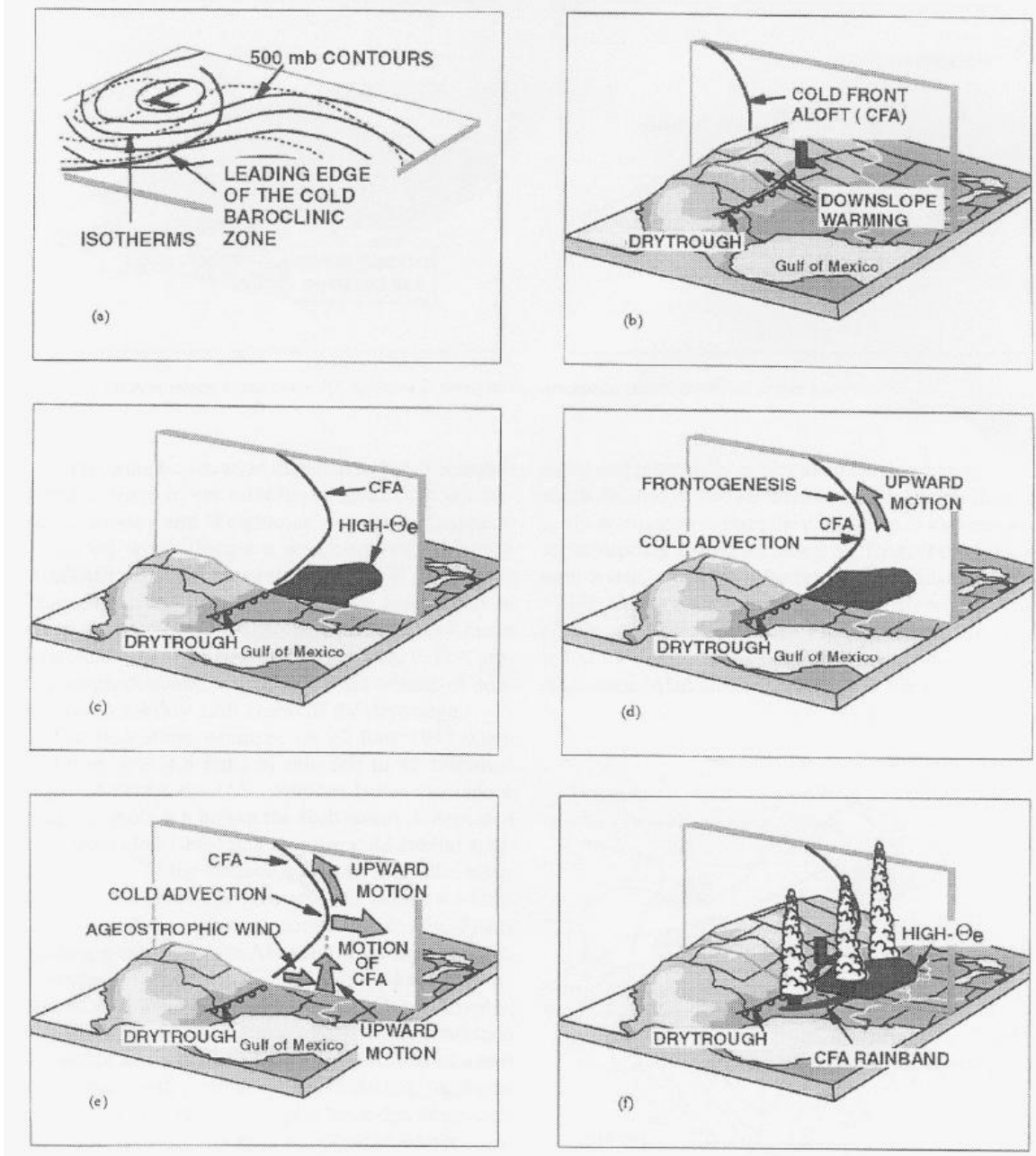


Fig. 1.7. Schematics illustrating the approach of the CFA and the formation of the CFA rainband. Adopted from Hobbs et al. (1996).

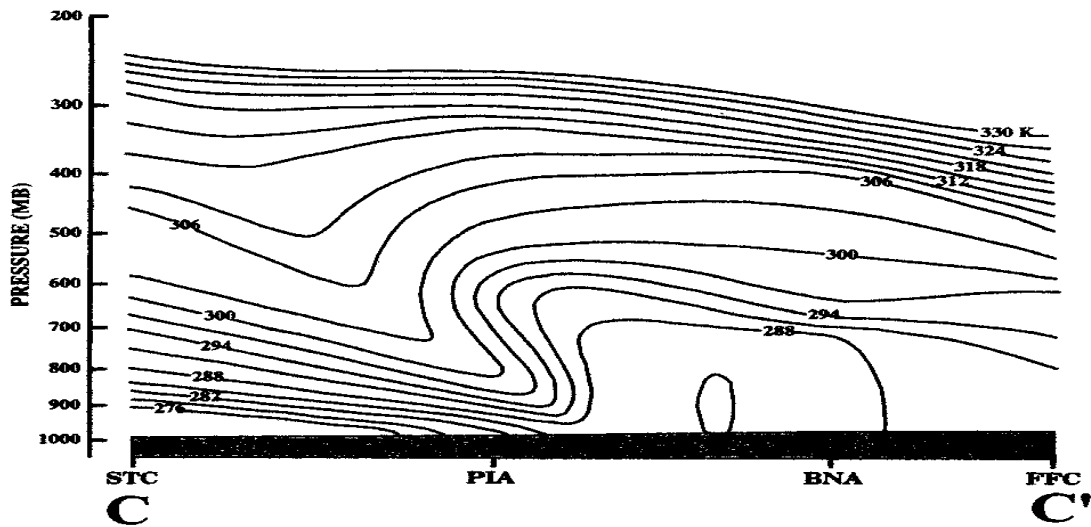
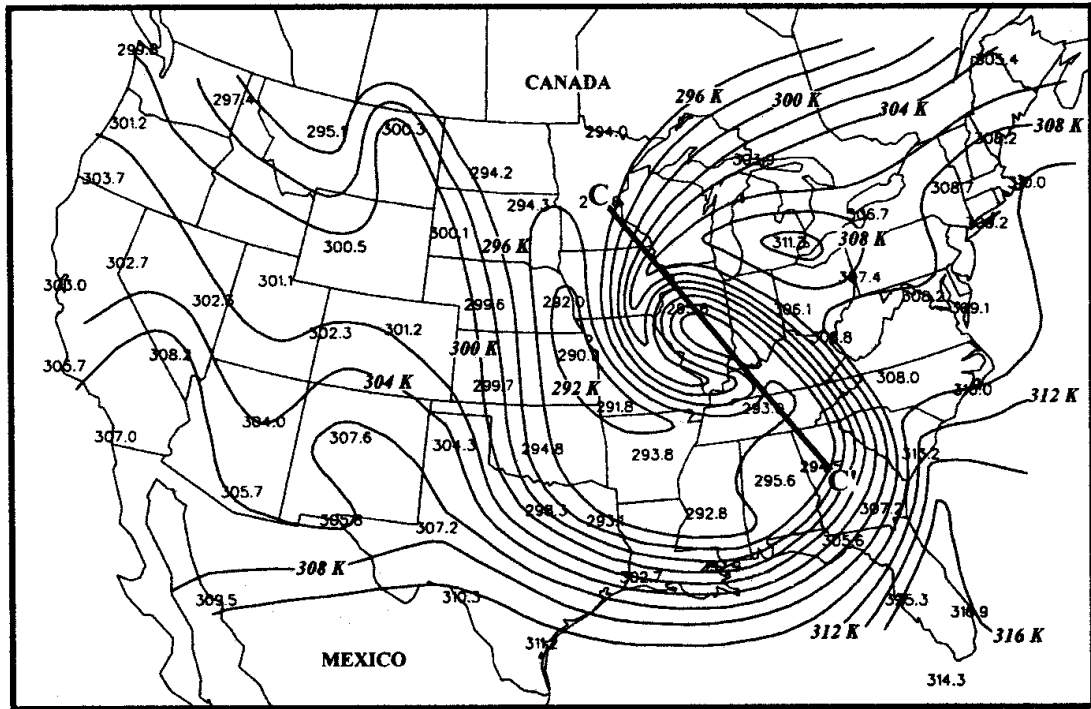


Fig. 1.8. (top) Analysis of 700 hPa θ_e (thin solid lines), valid at 0000 UTC 20 January 1995, and cross section orientation (C-C'). (bottom) Vertical cross section (C-C') through the trowal with θ_e (thin solid lines) contoured every 3 K. Adopted from Martin (1998a).

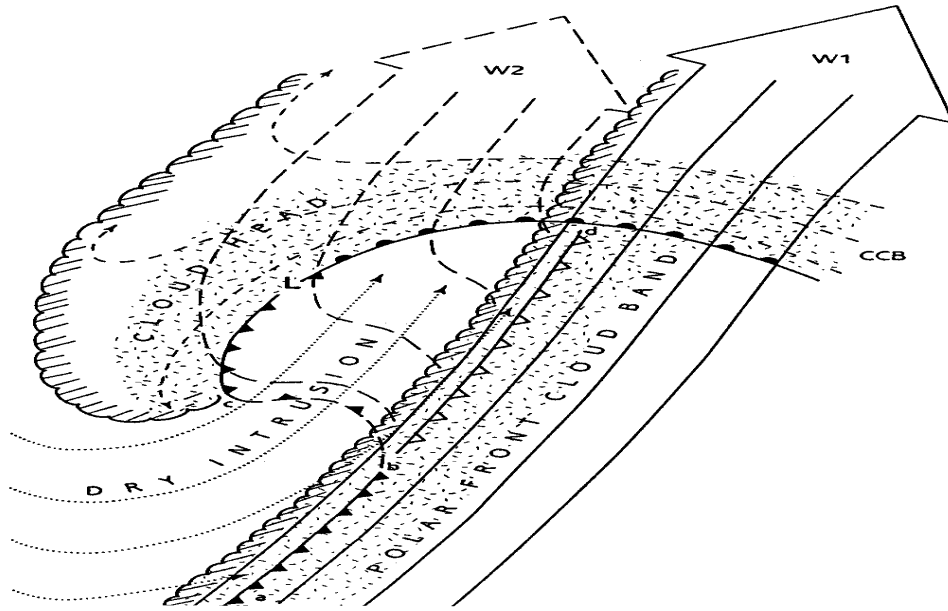


Fig. 1.9. Structure of a developing extratropical cyclone based on Browning and Roberts (1994) showing the principal airstreams with the addition of the W2 airstream. Adopted from Browning (1999).

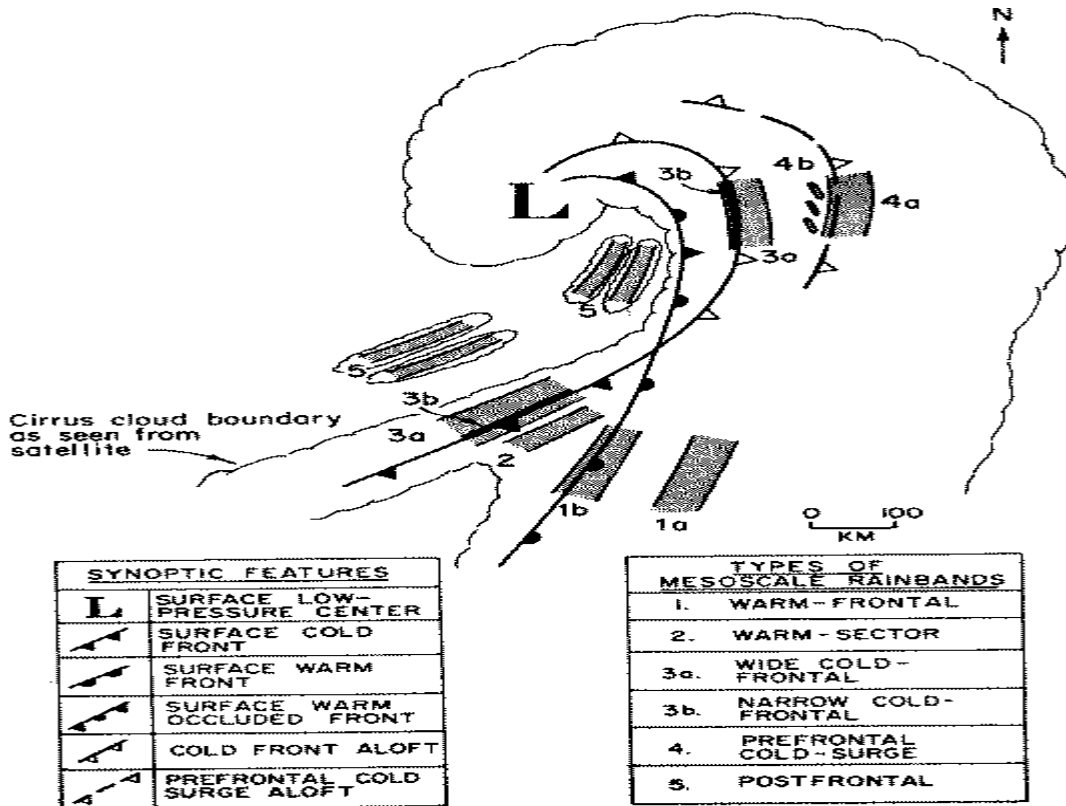


Fig. 1.10. Schematic adopted from Hobbs (1978) illustrating the types of bands and their locations observed during a study of 11 Pacific Northwest cyclones. Note that the 4b represents wave bands.

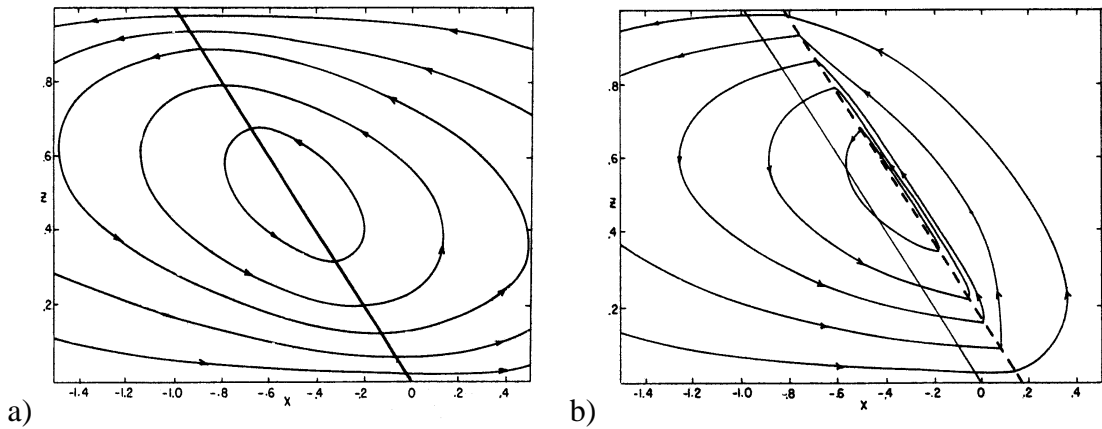


Fig. 1.11. Application of the Sawyer-Eliassen equation to an environment of large symmetric stability (a) and an environment of weak symmetric stability (b) in terms of streamfunction (thin black). Adopted from Emanuel (1985).

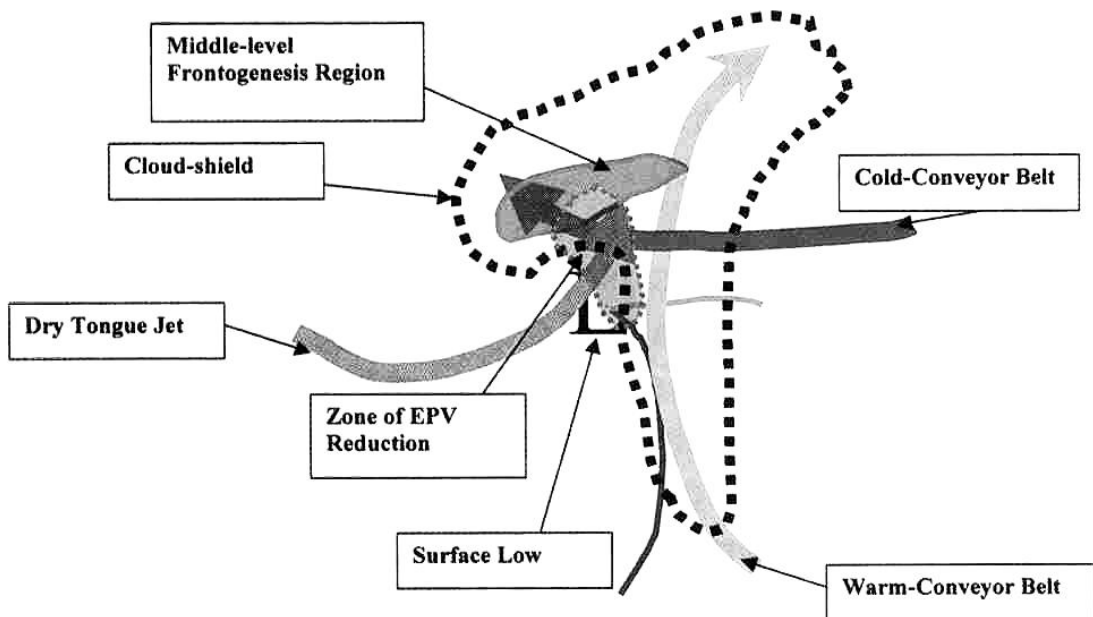


Fig. 1.12. Conceptual model depicting the frontogenesis region and zone of equivalent potential vorticity reduction within the context of the major components of a developing extratropical cyclone. Adopted from Nicosia and Grumm (1999).

2. Data and Methodology

2.1 Data Sources

2.1.1 Selection of Cases

The Unified Precipitation Dataset (UPD) (<http://www.cdc.noaa.gov/cdc/data.unified.html>) was utilized to identify cases exhibiting significant precipitation in the northeast US. This national dataset incorporates the National Oceanic Atmospheric Administration (NOAA) first order station precipitation measurements, daily cooperative observation measurements, and River Forecast Centers data, representing over 13,000 stations in the US (after 1992). After 1996, WSR – 88D precipitation estimates were used in regions where surface measurements were absent (e.g., near coastal waters, large lakes). Precipitation amounts represent 24 h accumulation ending at 1200 UTC, interpolated to a 0.25° latitude-longitude grid. Although the UPD provides a high-resolution gridded precipitation dataset, it has been noted to underestimate precipitation maxima due to data smoothing. However, for the precipitation criteria involved in this study (2.5 cm), the underestimation is minimal. The UPD is available from 1948 through 1998.

The NOAA Daily Weather Maps weekly series (DWM) (NOAA 1996-2001) was used to corroborate the UPD measurements and determine the predominant precipitation type (rain/snow). This publication provides daily North American surface, surface snowcover, and 500 hPa maps valid at 1200 UTC each day. In addition, recorded temperature maxima and minima's, and precipitation for the 24 h period prior to 1200 UTC are plotted for over 120 stations in the US.

As previously stated, the advent of the WSR-88D radar network was a major motive for the current study. National composite radar data were acquired from the Cooperative Program for Operational Meteorology, Education and Training (COMET) program. The composite data are composed of reflectivity returns from the 0.5° elevation slice from each radar site, combined into a seamless composite image with 2 km spatial and 5 min temporal resolution. Archived data were available in April 1995 and then from October 1996 (when the radar network was fully established) through April 2001, although a large portion of the 1996 – 1997 winter season was missing.

These three datasets were used to identify significant precipitation systems affecting the northeast US, determine the predominant precipitation type, and identify individual banded precipitation events.

2.1.2 Composite Analyses

The National Centers for Environmental Prediction (NCEP)/ National Centers for Atmospheric Research (NCAR) reanalysis was utilized for the initial composite investigation (Kalnay et al. 1996; Kistler et al. 2002). This global dataset has a 2.5° latitude-longitude spatial resolution and a 6 h time resolution.

In order to ascertain the environmental stability in the region of banding, a higher resolution dataset was required. Locally archived NCEP Eta model (<http://www.emc.ncep.noaa.gov/modelinfo/>) analysis and 6 h forecast fields were utilized for this purpose. Although the Eta model resolution and physics changed through the course of the study period (see

<http://www.emc.ncep.noaa.gov/mmb/research/eta.log.html> for a list of changes), the Eta model was chosen since it had mesoscale resolution, was available for the entire study period, and is the current operational model. Regardless of the model resolution at any time, the data used had been interpolated to an 80 km grid in the interest of conserving storage space, facilitating smooth analysis, and providing data uniformity.

2.1.3 Case Study Analyses

Locally archived NCEP Eta model short-range forecasts, interpolated to 80 km resolution, were used for case study synoptic summaries and cross-section analyses. The UPD, DWM series, hourly surface, ship and buoy, and synop data were also used to describe the surface conditions. The most representative cases with respect to the composite evolutions of banded, nonbanded, and null case evolutions were selected for case study analysis.

2.2 Methodology

The study method is summarized in a flow chart (Fig. 2.1). Study terms to be defined in the text are provided, along with the number of each respective element included in the term. The reader is encouraged to refer to Fig. 1 when following the text.

2.2.1 Climatology

The first task was to compile a database of significant precipitation systems during the cold season in April 1995 and from October 1996 through April 2001. From this database a band classification scheme was developed to document the types of banded structures observed in the northeast US, their relative frequency, and geographical location.

2.2.1a. Selection of Cases

The area of study for this project was defined as the latitude-longitude box covering 36.5°N to 50°N and 65°W to 85°W as outlined in Fig. 2.2. Although a portion of southeast Canada is included in the domain, the study was restricted to data from the US radar network. Precipitation systems affecting the northeast US during the cold season (October through April) were studied in April 1995 and from October 1996 (when the radar network was fully established) through April 2001. A precipitation system was defined as a coherent precipitation pattern that could be linked to the evolution of an identifiable atmospheric disturbance. Only precipitation systems exhibiting precipitation greater than 25 mm, or 12.5 mm liquid equivalent in the case of frozen precipitation, during a 24 h period at a point in the study domain were identified for further study. These precipitation systems will be referred to as “cases”. In the rare occurrence of more than one case observed within the domain at one time, both cases were independently assessed.

The UPD was used to identify cases in April 1995 and then from October 1996 through December 1998 (when the dataset ended). A comparison between the UPD and the DWM precipitation reports showed all cases identified by using the DWM were captured in the UPD, while only a few cases identified in the UPD were not captured in the DWM. This result supported use of the DWM for identifying cases for the remaining study period (January 1999 through April 2001), although it is likely that a few marginal cases may not have been identified. A total of 111 cases met the precipitation criteria during the study period (see Appendix). Out of the 111 cases identified for study, 88 had available composite radar data. Cases for which radar data was available were termed “study cases”.

2.2.1b. Development of Band Classification Scheme

The radar data from the 88 study cases were reviewed to develop a subjective band classification scheme. Although the composite radar time resolution was on the order of 5 min, 15 min time steps were used to create radar loops in order to reduce the number of images viewed, while providing a smooth animation that retained temporal changes. Study cases during the first two cold seasons of the study (October 1996 through April 1998) were reviewed to sample the variety of banded structures observed in the northeast US. Although some meso-alpha scale (200 km wide, 500 km long) precipitation areas may be considered bands, this study focuses on the mesoscale bands found within these precipitation areas. Based on previous classification schemes in the literature (e.g., Browning and Harold 1969; Houze et al. 1976; Byrd 1989), and after

consultation with operational forecasters, a preliminary classification scheme was developed. This scheme was further refined to capture the most significant banded structures with the idea that these structures would require a special weather statement under operational circumstances.

The resulting classification scheme (Table 2.1) defines single, multi, narrow cold-frontal, and transitory banded structures. A single banded structure is defined as a linear reflectivity feature greater than 250 km in length and approximately 20 – 100 km in width. Furthermore, the banded structure must maintain an intensity of 30 dBZ along its length for a minimum of 2 h. These criteria are consistent with the three to one aspect ratios used by the CYCLES studies and the 0.5 h to 3 h lifetime criterion used by Byrd (1989).

The multibanded structure is defined as a region exhibiting more than three finescale bands with similar spatial orientation and periodic spacing. The finescale bands are defined as having widths between 5 and 20 km, spaced no greater than 40 km apart, and having intensities greater than 10 dBZ over the background reflectivity. This structure must be maintained for at least 2 h.

The most frequently studied mesoscale banded structure is the narrow cold-frontal band, first defined by Houze et al. (1976). For this study this structure is defined as a narrow (10 – 50 km wide), long (at least 300 km in length) band found along the surface cold front or in the warm sector of a cyclone, which maintains an intensity of at least 40 dBZ along its length for at least 2 h. The definition used here is deliberately more general than that used in Houze et al. (1976) in order to incorporate warm sector bands (Houze et al. 1976) into the category. The narrow cold-frontal structure is

differentiated from the single banded structure based on the band location relative to the cyclone (equatorward vs. poleward), intensity (40 dBZ vs. 30 dBZ), and width (10 km vs. 20 km minimum), which is characteristic of its upright convective nature.

Transitory bands are defined as a structure that meets all respective criteria in a given category, except one. In most cases either the lifetime or intensity threshold is not met. Transitory bands are analogous to the weakly banded class defined by Byrd (1989), allowing for a continuum of banding, from no banding, to transitory structures, to full-blown single, multi, or narrow cold-frontal banding.

A few banded structures were ambiguous due to bright banding or incomplete radar data. These features were classified as undefined. Study cases which exhibited no banding as defined above were classified as nonbanded cases. The occurrence of a banded structure as defined above was termed an “event”.

2.2.2 Composites

2.2.2a Composite Analysis Stratifications

Composite analyses were created for single and multiband events, and nonbanded cases. Focus on the single and multiband events was motivated by their occurrence in regions of a cyclone where intense convective precipitation is not expected (poleward side of the cyclone).

In order to develop composite analysis stratifications, a surface cyclone relative composite of the single band distribution was developed. Surface cyclone positions at the analysis time most representative of the banded structure were determined by

utilizing the NCEP/NCAR Reanalysis dataset 1000 hPa height fields (henceforth used as a surrogate for the sea level pressure field), and the band location at this time was determined from radar. Because the time resolution of the NCEP/NCAR reanalysis is 6 h, and by definition the single banded structure must persist for at least 2 h, the longest a representative analysis time could be from the band event onset is just 2 h. Note that all events exhibited an identifiable surface low at their respective analysis time. In the occurrence of secondary cyclogenesis, the surface low closest to the banded structure was used as the cyclone position.

The resulting surface cyclone relative distribution is shown in Figure 2.3. Note that bands to the northeast of the surface cyclone exhibited a northwest-southeast mean orientation, while bands to the northwest exhibited a southwest-northeast mean orientation. These orientations are consistent with the idealized orientation of the thermal wind in a developing cyclone (an “S” thermal structure).

Table 2.2 summarizes the composite stratifications. The single band events were stratified into four composite classes according to the surface cyclone relative distribution. Events in which the single band exhibited a majority of its length in the northwest quadrant relative to the surface cyclone were classified as the northwest class. This class was subdivided into events where the bands exhibited a majority of their length within 500 km of the surface cyclone (northwest-near class), and beyond 500 km (northwest-far class). Events in which the single band exhibited a majority of its length in the northeast or southeast quadrant relative to the surface cyclone were classified as the east class. A few study cases exhibited bands in more than one region of the cyclone, and therefore were included in more than one composite class.

The multiband events were stratified in the same manner as the single bands. The multiband event distribution relative to the surface cyclone position is shown in Figure 2.4. Note that since multibanding occurs over a region, each multiband event was represented by a shaded area instead of a dominant band axis. Multibanded events were divided into events occurring in any portion of the northeast or northwest quadrant within 700 km of the cyclone center, and events occurring wholly in the southeast quadrant (incorporating the remaining events). Only one multiband composite class (events in northeast or northwest quadrant) was calculated due to the unique concentration of multiband events found just ahead of the surface cyclone.

Study cases that did *not* exhibit any type of banding (including transitory and undefined banded events) remained defined as nonbanded cases, and were included in the nonbanded composite class.

2.2.2b Synoptic Composite Method

The initial analysis time for each event was defined as the closest NCEP/NCAR reanalysis time to the onset of the event. The initial analysis time for the nonbanded cases was defined as the analysis time closest to the middle of the study case. FORTRAN code was developed to composite each composite class. This code takes the reanalysis data within a 60° by 120° latitude-longitude box centered on the surface cyclone position, and averages basic diagnostic parameters at all event times included in the composite class. If more than one event in the same composite class occurred, only one analysis time was included in the composite. These composite fields were

calculated at ten levels (1000, 925, 850, 700, 600, 500, 400, 300, 250, and 200 hPa) at 6 hour intervals from 12 h before to 12 h after band initiation for each composite class. The centroid position of each composite class was used as geographical reference for the resulting composite fields.

2.2.2c Model Composite Method

The composite program was modified to incorporate the interpolated Eta 80 km grids, including 17 vertical levels. Because the Eta model is a regional model with boundaries, the cyclone centered data box was reduced in size. Based on the cyclone locations and model boundaries a ~2500 km by ~2500 km data box centered on the cyclone position at the initial analysis time was devised. If any portion of a particular event data box went off the Eta model domain, the specific grid points included in that portion were not included in the composite calculation. This contingency was only an issue on the eastern edge of the composite. The Eta analysis or 6-h forecast fields corresponding to the initial analysis time from each event (or case for nonbanded cases) were used in the composites. If more than one event in the same composite class occurred near the same initial analysis time, only one initial analysis time was included in the composite. As with the synoptic composites, the centroid position of each composite class was used as geographical reference for the resulting composite fields.

The model composite was only run at the initial analysis time for all composite classes since the model data archive was not complete. Thus different analyses would be included in the composite at different times. Related to this limitation, the nonbanded,

northwest and northwest-near model composite classes were calculated with a few less analyses than their respective synoptic composite counterparts due to missing data. In order to investigate the demise of events in the northwest class, an additional composite was run with analyses nearest the end of each event included in the northwest class.

2.3 Calculations

The General Meteorology Package (GEMPAK) (desJardins et al. 1991) version 5.6 was used extensively to calculate various kinematic parameters and visualize the various gridded datasets. The simplified 2-D form of the Miller (1948) frontogenesis equation was used to examine the frontogenetical effect of the horizontal confluence. This simplification was made since the frontal zones included in this study were nearly saturated, so that the tilting and diabatic terms oppose one another in the updraft region of a thermally direct frontogenetical circulation. Displays of the tangential wind took no account of the frontal motion when assessing the transverse frontal circulation.

Calculations of EPV were made with θ_{es} and the geostrophic wind. It should be noted that in highly curved flows the geostrophic wind may be a poor approximation of the flow, in which case the EPV may be erroneous.

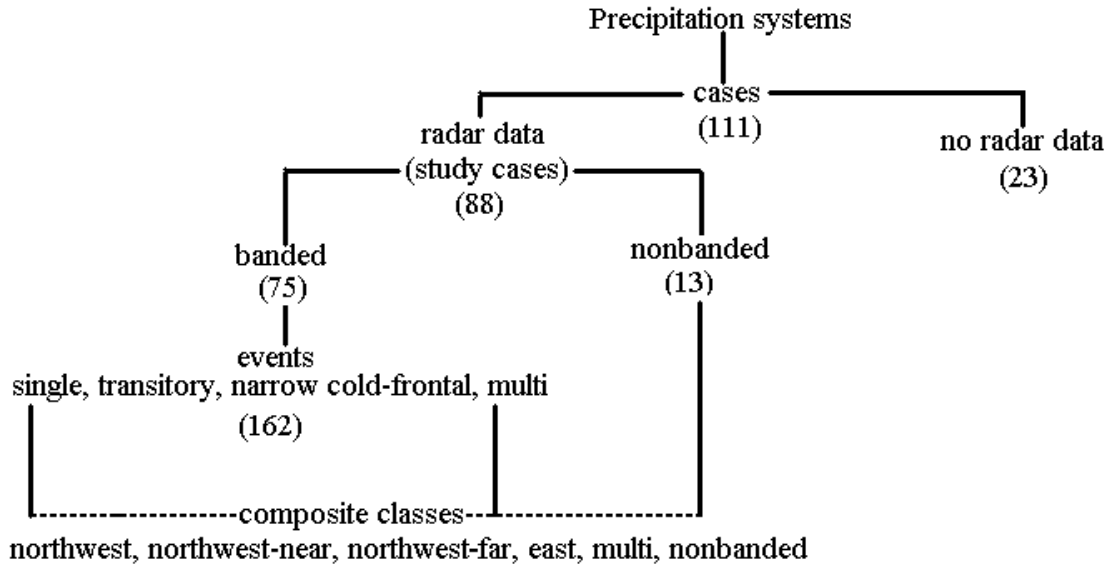


Fig. 2.1. Summary flow chart of the study method and terminology. The number of each element is denoted in the parenthesis.

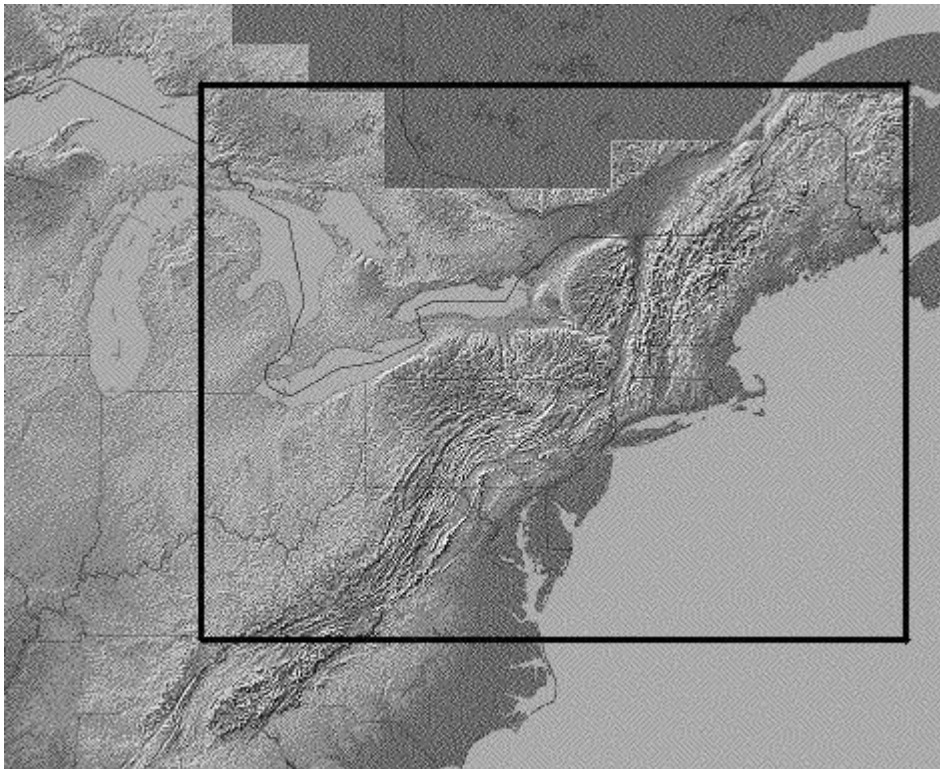


Fig. 2.2. Topographic map of the northeast US, with the study domain enclosed within black box (Adopted from <http://fermi.jhuapl.edu/states> ©1995)

Table 2.1: Band Classification Scheme

Band Type	Band Description
Single	Linear structure > 250 km in length, ~ 20 – 100 km in width, with an intensity > 30 dBZ maintained for at least 2 h
Multi	> 3 finescale (5–20 km width) bands with periodic spacing and of the same spatial orientation, with intensities > 10 dBZ over the background reflectivity, maintained for at least 2 h
Narrow cold-frontal	Narrow (10–50 km), long (> 300 km) band found along surface cold front or in the warm sector with an intensity > 40 dBZ maintained for at least 2 h
Transitory	Structure that meets all respective criteria in a given category, except one (usually the lifetime)
Undefined	Ambiguous due to bright banding or incomplete radar data
Nonbanded	None of the above criteria are met

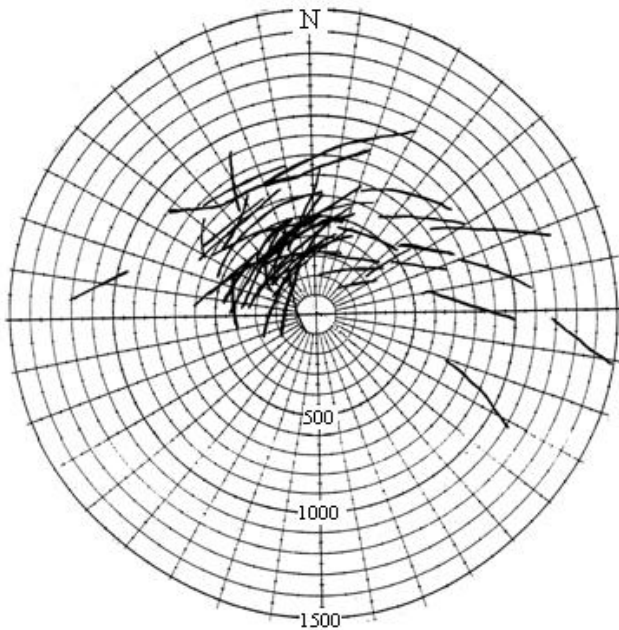


Fig. 2.3. Distribution of single bands relative to surface cyclone position (origin). Each black line represents the axis of a single band at the most representative analysis time. Radial distance scale is in kilometers.

Table 2.2: Composite stratifications

Class	Subdivision	Incorporated events
Northwest		Majority of band length in NW quadrant
	Northwest-near	Majority of “ “ within 500 km of surface low center
	Northwest-far	Majority of “ “ beyond 500 km of surface low center
East		Majority of band length in NE or SE quadrant
Multi		Multiband events with a portion in the NE or NW quadrant
Nonbanded		Case exhibited no type of banding

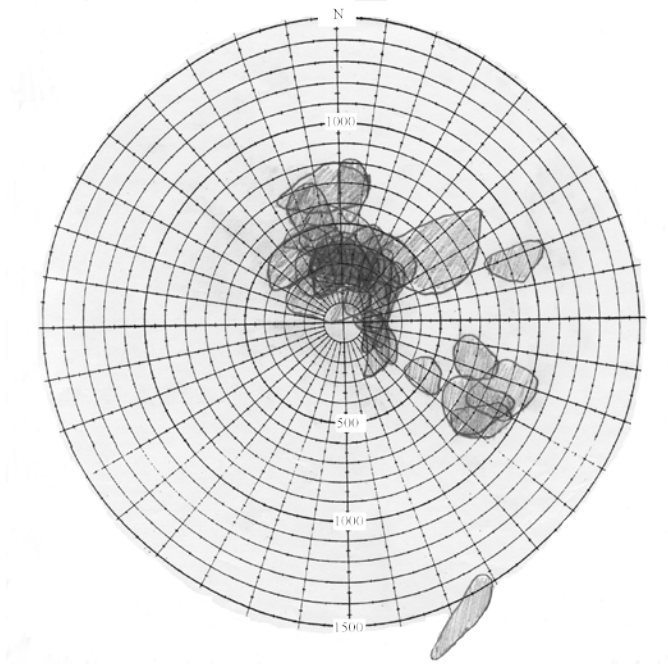


Fig. 2.4 Distribution of multibands relative to surface cyclone position (origin). Each shaded area represents the area covered by each multiband event at the analysis time. Events were overlaid when occurring in a coincident area.

3. Results

3.1 Climatology

3.1.1 Application of Classification Scheme

The band classification scheme presented in Chapter 2 (Table 2.1) was applied to the 88 study cases to document mesoscale band formation frequency in the northeast US, and to provide a database of banded events to study. The results of this application are summarized in Table 3.1. It is important to note that several cases exhibited a particular band type more than once, and/or more than one band type during their evolution through the northeast US. Each of these events is accounted for in the events category.

The most common banded structure observed in the northeast US was the single (48 events), followed by the transitory (40), narrow cold-frontal (36), and multi (29) banded structures. Nine events were classified as undefined. The large number of transitory events reveals that banded structure is often observed that does not maintain its identity for more than 2 h. Additionally, the predominance of single banded events over narrow cold-frontal events reflects the relative lack of narrow cold-frontal events observed in the northeast US during the cold season as compared with the Pacific Northwest (Houze et al. 1976) and Great Britain (Browning 1985). This finding also agrees with the relative proportion of single bands compared to narrow cold-frontal bands found during CASP in adjacent Atlantic Canada (Stewart 1991).

Not all cases exhibiting significant precipitation in the northeast US exhibit mesoscale banding. A total of 13 study cases were classified as nonbanded, representing

~15% of the study cases. This subset of cases serves as an important dataset to be utilized to discriminate between banded and nonbanded cases.

3.1.2 Single Band Characteristics

Strictly speaking the single-banded structure may be composed of several finescale bands during its lifetime. The finescale bands have widths < 20 km, intensities > 10 dBZ over the background reflectivity, and are usually maintained for a short duration (< 2 h). Radar animations of the single-banded structure show the structural evolution may locally exhibit finescale bands which reach maturity in place, dissipate, but then are readily replaced by another finescale band in the same location. This observation is consistent with the theoretical work of Xu (1992), who showed through numerical modeling that the large-scale ascent can evolve into multiple smaller-scale updrafts when the EPV is greatly reduced to large negative values. In this case the single-banded structure may be considered a dominant band axis, or a band accumulation zone, rather than one single band.

Radar animations of northwest class bands revealed that many of the bands pivoted as they translated with the system. In fact, subjective analysis revealed 24 of the 39 (62%) single-banded events in the northwest class were associated with an identifiable pivot point, with the eastward extent of the band typically swinging northwest and the westward end of the band moving southeast. Radar animations of the east class bands showed a common motion approximating the velocity of the environmental wind (often toward the northeast). In fact, subjective analysis revealed 8

of the 10 (80%) east class bands exhibited this motion [note that the addition of these two single-band classes equals 49, which conflicts with the stated number of single-band events (48). This discrepancy arises from the fact that one band could not clearly be identified as east or northwest-near, and therefore was included in both calculations]. The remaining two bands remained nearly stationary.

A graph of the single band lifetimes (Fig. 3.1) shows that the frequency of events rapidly decreases with increasing event duration. Several events just barely met the 2 h minimum, consistent with the large number of transitory bands observed. This outcome shows the 2 h time threshold was arbitrary, but does suggest that the conditions favoring single band formation occur on limited timescales. However, a number of events persisted beyond 12 h, the longest of which lasted 22.5 h (4–5 February 1998).

3.1.3 Multiband Characteristics

The multibanded structure can be conceptualized in terms of phase and group velocities. The region of multibanding moved at a group velocity that appeared similar to the velocity of the overall precipitation system. The individual finescale bands composing the multibanded region appeared to move with a phase velocity similar to the environmental wind through the multibanded region, developing on the equatorward edge, and then either dissipating or merging with a single band on the poleward edge of the region.

In contrast to the single band lifetimes, the multiband lifetimes (Fig. 3.2) exhibit a preferred mode between 4 to 10 h in duration. This preference may suggest a different kind of forcing from the single bands, although this point was not extensively studied.

The multiband distribution (Fig. 2.4) revealed that a majority of the multibanded structures occurred just ahead of the surface cyclone, suggesting a recurring favorable environment in that location. The secondary maximum of events appearing southeast of the composite centroid is believed to be an artifact of coastal redevelopment.

The multibanded structure as defined above has not been adequately represented in the modern literature (e.g., Hobbs 1978; Browning 1985; Houze 1997). Hobbs (1978) does identify “wave” bands occurring ahead of the surface low, but it is not clear from the definition if they are synonymous with the multibanded structures identified presently. Recently, Rauber et al. (2001) and Stuart (2001) have conducted preliminary investigations of similar finescale structures, but their results have not been reviewed.

3.2 Composite Results

3.2.1 *Composite members*

The geographical distribution of the 48 single-banded events comprising the single-band composite members is shown in Fig. 3.3a. Although only five cold seasons were studied, most of the study domain experienced at least one single-banded event. The surface low positions corresponding to the initial analyses of the 48 banded events are shown in Fig. 3.3b. Although the low centers represent a single time, the clustering of centers off the east coast highlights the dominant coastal storm track, with evidence of a secondary storm track apparent in the Midwest.

Subdivision of the single-banded events shows that the northwest class events (Fig. 3.4) were primarily associated with surface low positions located off the east coast (note the centroid position in Fig. 3.4b) with the mean band location approximately 400 km to the northwest of the cyclone center. Further subdivision into the northwest-near (Fig. 3.5) and northwest-far (Fig. 3.6) class events shows the northwest-near class surface lows were generally farther north than the northwest-far class surface lows (consistent with the definitions), but the mean band position was nearly in the same geographical region (Pennsylvania). This similarity exposes the fault of forecasting precipitation structure based solely on the surface low position. The east class surface lows (Fig. 3.7b) had the greatest spatial spread, but were generally located in the western domain of the study area. Note that the east class bands have a WNW–ESE orientation (Fig. 3.7a) as opposed to the predominate NE–SW orientation of the northwest class bands. This difference is characteristic of the expected thickness gradient orientations in the east and northwest sectors of the cyclone. The multiband distribution exhibited a large concentration of events in southern New England (Fig. 3.8a), which is likely linked to the concentration of cyclone centers off the southern New England coast (Fig. 3.8b). The nonbanded cases (Fig. 3.9) were associated with identifiable surface lows scattered throughout the study domain.

3.2.2 Synoptic-Scale Composites

The NCEP/NCAR reanalysis dataset was used to develop composites for each event class. Although the resolution of this dataset is rather coarse for mesoscale study,

it is suitable for synoptic-scale flow analysis. Composites were computed at 6 h intervals from 12 h before ($T = -12$ h) to 12 h after ($T = 12$ h) the initial event analysis time ($T = 0$ h), but in the interest of brevity only the $T = -12$ h, $T = 0$ h, and $T = 12$ h composite analyses will be shown. Animations utilizing the full composite time resolution for each event class are provided at <http://www.atmos.albany.edu/student/dnovak/CSTAR.html>.

3.2.2 Northwest Composite Class

Using the composite stratification outlined in section 2, 39 events were included in the northwest composite class. The results of the composite (centered at the surface low centroid position for geographical reference) at $T = -12$ h are summarized in Fig. 3.10. A surface cyclone is found in the Carolinas (Fig. 3.10a) associated with a digging midlevel trough (Figs. 3.10c,d). There is evidence that the cyclone is deepening since the disturbance tilts west with height, and progressively exhibits a more open structure with height (Figs. 3.10b–d). Note that at this time the 700 hPa low remains open (Fig. 3.10c). At 300 hPa (Fig. 3.10e) a strong jet is rounding the base of the trough, and a weaker jet is found in the confluence region over southeast Canada. This pattern resembles the common jet configuration that Kocin and Uccellini (1990, 58–62) cited for northeast US snowstorms.

Twelve hours later at $T = 0$ h (Fig. 3.11) the surface cyclone has deepened and moved northeast (Fig. 3.11a) as the 500 hPa trough is becoming negatively tilted (Fig. 3.11d). The upper levels continue to exhibit a double jet structure, enhancing upper-level divergence and providing support for ascent over the surface low center (Figs. 3.10e,f).

Consistent with cyclogenesis, the 850 hPa low has deepened (Fig. 3.11b) and a closed low has formed at 700 hPa (Fig. 3.11c). Note that the confluence between the southerlies ahead of the 700 hPa closed low and the westerlies in southern Canada sets up a large-scale deformation zone associated with a confluent asymptote over southern Canada. This deformation acting on the ambient thermal gradient contributes to midlevel frontogenesis to the north and northwest of the surface low (Fig. 3.11c). An alternative interpretation is that the frontogenesis is maximized on the poleward side of the warm air advection (see Fig. 3.11b). Although the bulk of the frontogenesis is located well to the north and east of the mean band position, the maximum tails towards the southwest, aligning near the mean band position in central Pennsylvania (see Fig. 3.4b).

During the next 12 h the cyclone continued to deepen as it moved up the northeast US coast (Fig. 3.12a). At $T = 12$ h a closed circulation extended nearly to 500 hPa (Figs. 3.12a–d) as the cyclone became vertically stacked. However, forcing for ascent was still evident as significant midlevel frontogenesis was found in the deformation zone northeast of the cyclone (Fig. 3.12c), and the double jet structure was maintained (Figs. 3.12e,f).

3.2.2b Northwest-Near and Northwest-Far Composite Classes

Subdivision into the northwest-near (incorporates 26 events) and northwest-far (14 events) composite classes results in subtly different evolutions [note that the addition of the northwest-near and northwest-far class events equals 40, which conflicts with the stated number of northwest class events (39). This discrepancy arises from the fact that

one band could not clearly be identified as northwest-far or northwest-near, and therefore was included in both classes]. Comparison of the composite summary evolution for northwest-near class (Figs. 3.13–3.15) and northwest-far class (Figs. 3.16–3.18) shows the northwest-far composite flow is much more amplified, with a deeper negatively tilted trough (Figs. 3.16d–3.18d) and subsequent deeper surface low (Figs. 3.16a–3.18a). Despite their flow differences, both composites develop a large-scale deformation zone in southern Canada in the confluence of the westerly Canadian airstream and the southerlies ahead of the respective 700 hPa disturbance (see Figs. 3.14c and 3.17c). Subsequently, both composites exhibit a comma shaped frontogenesis maximum to the north and northwest of the surface cyclone (Figs. 3.14c and 3.17c), although the northwest-far composite frontogenesis maximum exhibits a more pronounced comma shape, which is consistent with the greater flow amplification. In both cases the midlevel frontogenesis increases during the 12 h period preceding band development (Figs. 3.13c and 3.14c; Figs. 3.16c and 3.17c). By band initiation the southwest tail of the frontogenesis maximum in each composite roughly aligns with the respective mean band positions (Figs. 3.5b and 3.6b). Further similarities at $T = 0$ h include a westward tilt with height (Figs. 3.14a–d and 3.17a–d), progression from a closed circulation in the low levels to an open wave in the midlevels (Figs. 3.14a–d and 3.17a–d), and double jet structure (Figs. 3.14e,f and 3.17e,f). These features are consistent with the noted cyclogenesis.

3.2.2c East Composite Class

The composite of the 10 east events at $T = -12$ h is shown in Fig. 3.19 [note that the addition of the east and northwest class events equals 49, which conflicts with the stated number of single-banded events (48). This discrepancy arises from the fact that (in addition to the previously stated northwest-far/northwest-near ambiguity) one band could not clearly be identified as northwest or east, and therefore was included in both classes]. The primary difference from the northwest composite classes is the westward shift of the flow pattern (consistent with the location of the bands east of the surface cyclone). At this time a broad, weak surface low located in the lower Mississippi Valley (Fig. 3.19a) was developing in response to a weak shortwave found at the leading edge of the broad 500 hPa trough (Fig. 3.19d). Cyclone development was supported by its position in the poleward exit region of a zonally oriented jet along the Gulf Coast (Figs. 3.19e,f). Weak frontogenesis (Fig. 3.19c) was found along the poleward edge of warm air advection, associated with the developing warm front extending through the eastern Great Lakes.

At $T = 0$ h the surface low had deepened and moved into the Ohio Valley (Fig. 3.20a), placing the northeast under deep-layer warm air advection (Fig. 3.20b), while the 700 hPa cutoff cyclone was shifted west into the western Great Lakes (Fig. 3.20c). Similar to the northwest, northwest-near, and northwest-far composite classes, the 700 hPa frontogenesis had strengthened during the preceding 12 h period (Figs. 3.19c and 3.20c), but unlike the previous composite classes the maximum is now found well ahead (northeast) of the surface cyclone, associated with the highly diffluent flow ahead of the

closed midlevel low. As with the previous composites, the frontogenesis is closely correlated to the leading edge of the warm air advection (Fig. 3.20b), and the mean band position (Fig. 3.7) is near the frontogenesis maximum—in this case just equatorward from the maximum. At higher levels a strong zonal jet is found along the Gulf Coast with wind speeds exceeding 50 m s^{-1} at 200 hPa (Fig. 3.20f), which was the strongest composite jet of all five composite classes.

By $T = 12 \text{ h}$ the surface low has moved into the eastern Great Lakes (Fig. 3.21a), as the associated 500 hPa short wave is ejected out of the central US trough (Fig. 3.21d). It is hypothesized the rapid progression of the short wave was aided by the strong zonal flow ($40\text{--}50 \text{ m s}^{-1}$) in the upper levels (Figs. 3.21e,f). The 700 hPa frontogenesis maximum (Fig. 3.21c) has weakened to values less than $0.12 \text{ }^\circ\text{C (100 km)}^{-1} (3 \text{ h})^{-1}$, now located in eastern New England in accordance with the progressive eastward movement of the system.

3.2.2d Multibanded Composite Class

The multibanded composite evolution (incorporating 29 events; Figs. 3.22, 3.23, and 3.24) is quite similar to the northwest (Figs. 3.10, 3.11, and 3.12) and northwest-near composite evolutions (Figs. 3.13, 3.14, and 3.15). This result may have been expected since northwest events occurred simultaneously with multibanded events on 10 occasions. Although the multibanded composite exhibits the development of a negatively tilted trough (Figs. 3.22c, 3.23c, and 3.24c), cyclogenesis is slightly weaker than the northwest composite (compare Figs. 3.10a and 3.11a with Figs. 3.22a and

3.23a). Consistent with this observation, the 700 hPa closed low fails to form in the multibanded composite (Figs. 3.22, 3.23c, and 3.24c). The mean multiband position (see Fig. 3.8b) lies in a region of warm air advection (Fig. 3.23b) ahead of the warm or occluded front. The 700 hPa frontogenesis fields (Figs. 3.22c, 3.23c, and 3.24c) look strikingly similar to the northwest composite, although the mean multiband is not well correlated to the frontogenesis maximum at this level (Fig. 3.23c). This discrepancy suggests the multibands may be forced by frontogenesis at a lower level. The multibanded composite also exhibits a more uniform jet structure (Figs. 3.22e,f; 3.23e,f; and 3.24e,f), only hinting at the double jets that were apparent in the northwest composite.

3.2.2e Nonbanded Composite Class

Not all cyclones associated with significant precipitation in the northeast US exhibit mesoscale banding. These cases serve as a type of null case, highlighting the synoptic-scale features important in the formation of mesoscale bands. The composite of the 13 nonbanded cases at $T = -12$ h is shown in Fig. 3.25. The synoptic-scale features at all levels are the weakest of the five composite classes. The only closed cyclonic circulation is found at the surface, associated with a weak surface low in the Tennessee Valley (Fig. 3.25a). This surface low is associated with a weak 500 hPa vorticity maximum (magnitude $\sim 12 \times 10^{-5} \text{ s}^{-1}$; Fig. 3.25d) embedded in zonal flow (Figs. 3.25c–f).

Unlike the previous composite classes, little cyclogenesis occurs over the next 24 h period (Figs. 3.26a and 3.27a). This observation can be understood by noting that a

confluent entrance region of a jet is positioned over the northeast US (Figs. 3.26e,f; and 3.27e,f) as southwesterlies ahead of the short-wave disturbance merge with westerlies across southern Canada. The short-wave disturbance is sheared as it enters the jet (Figs. 3.26d and 3.27d), reducing vorticity advection and subsequent surface development. Despite this fact, the midlevel confluence contributes to substantial frontogenesis northeast of the surface cyclone (Figs. 3.25c, 3.26c, and 3.27c). The placement of the frontogenesis maximum is consistent with the expected location in the equatorward entrance region of the jet, but the magnitude was somewhat unexpected since conventional knowledge might suggest that the nonbanded cases would exhibit weaker frontogenesis than the banded cases.

3.2.2f Composite Evolution Summary

The synoptic composites show a spectrum of development, from the well-developed northwest-far composite to the weak nonbanded composite. Figure 3.28 quantifies this spectrum in terms of the evolution of the minimum 1000 hPa height. Note that all banded composite classes exhibit significant deepening before band initiation, which slows (in the case of the northwest, northwest-near, northwest-far, and multibanded composite classes) or reverses (in the case of the east composite class) after band initiation. This behavior is in contrast to the evolution of the nonbanded composite, which essentially maintains its original height through time. This comparison corroborates the assertion made by Nicosia and Grumm (1999) that banded structure is favored during cyclogenesis.

3.2.3 Model Composites and Cross Sections

Composites incorporating the operational Eta model 80 km display grids were calculated from the same cases with available data (see section 2.2.2c) as the synoptic composites to obtain higher-resolution fields conducive to cross-sectional display. Due to missing data, the northwest, northwest-near, northwest far, multibanded, and nonbanded model composite classes were calculated with a few less analyses than their respective synoptic composite counterparts. The higher-resolution composite class synoptic summaries at $T = 0$ h are briefly presented, highlighting key features. In general, the higher-resolution composites enhance the amplitude of the derived fields (frontogenesis, temperature advection, wind speeds) while retaining the same flow pattern. The composite cross sections will be discussed at length. Note that the cross-section lengths and frontal baroclinicity were nearly equal among the composite cross sections, facilitating comparisons of key features and frontal slope between composite cross sections.

3.2.3a Northwest Model Composite Class

A summary of the northwest model composite (incorporating 36 analyses) is shown in Fig. 3.29. The higher-resolution composite enhances the amplitude of the features of interest including the 850 hPa warm air advection (compare Fig. 3.29b with Fig. 3.11b), 700 hPa frontogenesis (compare Fig. 3.29c with Fig. 3.11c), 500 hPa vorticity (compare Fig. 3.29d with Fig. 3.11d), and 300 hPa wind speeds (compare Fig.

3.29e with 3.11e). Note that the 700 hPa frontogenesis is now focused in a narrow ribbon, located in the diffluent flow ahead of the 700 hPa low center (Fig. 3.29c), with the strongest gradient on the equatorward edge. Also note that the confluent asymptote northwest of the cyclone is better correlated to the frontogenesis maximum and mean band position (Fig. 3.29f).

A cross section normal to the band axis at initiation (cross-section orientation is shown in Figure 3.29f) is presented in Fig. 3.30. Figure 3.30a offers an assessment of the symmetric stability through the calculation of geostrophic equivalent potential vorticity (EPV; negative values shaded) and an assessment of conditional instability through evaluation of the θ_{es} field. Although geostrophic EPV will be shown, caution is advised when interpreting the results since the full wind may be more representative of the flow in most cases. The assessment of symmetric stability with the inclusion of the full wind changes the magnitude only slightly, but this may affect the sign of EPV in some cases. This potential problem as well as other calculation issues concerning EPV will be further discussed in detail in section 3.3.5b. As suggested by Schultz and Schumacher (1999), θ_{es} is used instead of θ_e in Figure 3.30a since saturation is a necessary condition for symmetric instability. Figure 3.30b shows frontogenesis (shaded) with θ_e overlaid. Figure 3.30c exhibits the model vertical velocity (ω) field with the -12 to -16 °C layer shaded to highlight the maximum dendritic growth region for ice crystals. Saturation is assessed via the relative humidity in panel (d). The mean band position is centered in the cross section.

Figure 3.30a shows a sloping frontal boundary equatorward of the mean band position. Examination of the θ_{es} and EPV fields reveals that this front separates a

conditionally unstable atmosphere equatorward, from a conditionally stable atmosphere poleward. However, it is important to note the midlevel small EPV overhang between 550 and 400 hPa in the center of the cross section, which is coincident with the mean band position. This feature suggests that the band may be enhanced by weak midlevel symmetric stability in the manner proposed by Emanuel (1985) and shown in Fig. 1.11. An interesting caveat to this interpretation is that the weak vertical dipole in EPV at the band position may be a result of midlevel heating associated with latent heat release from the band itself. In this case the noted weak midlevel symmetric stability may be a symptom of heating in the 600–800 hPa layer, and not a precursor condition.

Frontogenesis is readily evident (Fig. 3.30b), as the sloping maximum is collocated with the mean band position under the weak midlevel symmetric stability overhang. As shown by Emanuel (1985), the frontogenetical response in the presence of weak symmetric stability takes the form of a concentrated updraft on the equatorward flank of the frontal zone (Fig. 1.11). Examination of the composite ω field (Fig. 3.30c) reveals a narrow ascent maximum with a slight tilt into the cold air, consistent with Emanuel (1985). The band position is clearly evident in the relative humidity field (Fig. 3.30d), with a narrow maximum correlated with the ascent maximum. The tilt of these two fields into the cold air is suggestive of slantwise ascent.

3.2.3b Northwest-Near Model Composite

A synoptic summary of the northwest-near model composite (incorporating 23 analyses) is shown in Fig. 3.31. The 500 hPa trough is slightly more positively tilted

(Fig. 3.31d) than the northwest model composite (Fig. 3.29d) and the 300 hPa jet maximum is farther north (compare Figs. 3.31e and 3.29e), which is consistent with the more northern location of the surface low (compare Figs. 3.31a and 3.29a). Note the close correlation between the 700 hPa confluent asymptote, frontogenesis maximum (Fig. 3.31c), and mean band position (Fig. 3.31f).

A cross section through the northwest-near mean band position is displayed in Fig. 3.32. All of the aforementioned features in Fig. 3.30 are present in the display such as CI evident in the θ_{es} field just equatorward of the band position, the small midlevel EPV overhang and weak conditional stability in the middle of the cross section (Fig. 3.32a), and the deep layer of frontogenesis within the frontal zone (Fig. 3.32b). Similar to the northwest composite cross section, the ω and relative humidity fields (Figs. 3.32c,d) highlight the band position and suggest rapid slantwise ascent.

3.2.3c Northwest-Far Model Composite

A synoptic summary of the northwest-far model composite (incorporating 10 analyses) is shown in Fig. 3.33. The higher-resolution composite reveals the existence of a closed 500 hPa circulation (Fig. 3.33d), and sharp negatively tilted trough at 300 hPa (Fig. 3.33e). The higher-resolution composite also reveals that the 700 hPa closed circulation in the northwest-far composite (Fig. 3.33c) is much broader than the northwest-near composite circulation (Fig. 3.31c). This configuration places the confluent asymptote farther north from the surface low than in the northwest-near composite, accounting for the mean band location over 600 km north of the surface low

(Figs. 3.33a,f). Note that the mean band position in the northwest-near class was less than 400 km north of the surface low (Figs. 3.31a,f). The correlation between the deformation field and band location stresses the role deformation plays in band formation. The lack of a reliable relationship between the surface low position and band location suggests the band location within a storm cannot be accurately predicted based solely on the location of the surface low.

A cross section through the northwest-far mean band position is shown in Fig. 3.34. This cross section exhibits similar features as the northwest and northwest-near composite cross sections, including weak conditional stability (Fig. 3.34a), a deep layer of frontogenesis (Fig. 3.34b), narrow sloping updraft (Fig. 3.34c), and near saturation within the frontal zone (Fig. 3.34d).

3.2.3d East Model Composite

A summary of the east model composite (incorporating 10 analyses) is shown in Fig. 3.35. The higher-resolution composite shows the broad area of warm air advection in the northeast US (Fig. 3.35b), narrow frontogenesis maximum within the 700 hPa diffluence along the Canadian border (Fig. 3.35c), leading short wave in the lower Great Lakes (Fig. 3.35d), and strong southwesterly jet in the southeast US (Fig. 3.35e).

A cross section through the east class mean band position is shown in Fig. 3.36. The cross-section orientation slices through the warm front, revealing a strong baroclinic zone (Figs. 3.36a,b). Similar to the previous cross sections, a sloping region of intense frontogenesis is noted along the frontal zone (Fig. 3.36b) within a layer of weak

conditional stability (Fig. 3.36a), although the lowest layers appear more conditionally stable than in the northwest composite cross sections (Figs. 3.30b, 3.32b, and 3.34b). The band location is again evident in the ω (Fig. 3.36c) and relative humidity fields (Fig. 3.36d), exhibiting a tilt into the cold air. The dynamical similarities between the northwest and east composite cross sections suggest that these bands, although found in different regions of the cyclone and exhibiting different band motions (see section 3.1.2), may be similarly forced.

3.2.3e Multibanded Model Composite

A synoptic summary of the multibanded model composite (incorporating 23 analyses) is shown in Fig. 3.37. As noted in section 3.2.2d, the multibanded composite exhibited many similarities to the northwest composites; however, the higher-resolution composite reveals the warm air advection occurs over a larger area (compare Fig. 3.37b to Figs. 3.29b, 3.31b, and 3.33b). Note also that, in contrast to the northwest model composites (Figs. 3.29c, 3.31c, and 3.33c), the 700 hPa frontogenesis maximum (Fig. 3.37c) is quite removed from the composite multibanding region in the mid-Atlantic (Fig. 3.37f), as it was in the synoptic composite (Fig. 3.23).

The multibanded composite cross section (Fig. 3.38) exhibits a similar frontal structure to the northwest composite cross sections. This is consistent with several multibanded events occurring in conjunction with single band events. A region of CI is found equatorward from the frontal zone, but the θ_{es} and θ_e surfaces are vertical or slightly sloped into the cold air within the frontal zone (Fig. 3.38a,b), suggesting a

transition from upright ascent to slantwise ascent within the frontal zone. Similar to previous composites, a deep sloping region of frontogenesis is found within the frontal zone (Fig. 3.38b), although it is slightly weaker than the previous band composites [< 0.8 compared to $> 0.8 \text{ }^\circ\text{C (100 km)}^{-1} (3 \text{ h})^{-1}$]. Note that the multibanding (center of cross section) is occurring in a region of low-level frontogenesis, as opposed to a region of midlevel frontogenesis noted in the other banded composite cross sections (see Figs. 3.30b, 3.32b, and 3.34b)

The ω field is perhaps most revealing with two ascent maxima embedded within a broad region of ascent (Fig. 3.38c). An ascent maximum is found between 900 and 800 hPa on the equatorward flank of the frontal zone and is connected to an elevated ascent maximum within the frontal zone. Note that the low-level ascent maximum is found in a region of negative EPV characterized by CI, while the elevated maximum is found in a region of small EPV and weak conditional stability (Fig. 3.38). It is hypothesized the low-level ascent maximum is reflecting ascent associated with the multibanded structure, while the elevated ascent maximum is reflecting ascent associated with the deeper synoptic-scale precipitation band and/or single banded structure often found further within the frontal zone. The relative humidity field corroborates these ideas with shallow saturation equatorward of the frontal zone, sloping into a deeper band of relative humidity maximum (Fig. 3.38d).

3.2.3f Nonbanded Model Composite

A synoptic summary of the nonbanded model composite (incorporating 11 analyses) is shown in Fig. 3.39. The composite highlights the weak nature of the system, with a minimum 1000 hPa height barely below 90 m (Fig. 3.39a), and 500 hPa vorticity maximum magnitude less than $16 \times 10^{-5} \text{ s}^{-1}$ (Fig. 3.39d). However, the higher-resolution composite better defines the dominant upper-level jet (compare Fig. 3.39e with Fig. 3.26e) and structure of the frontogenesis maximum (compare Figs 3.39c with 3.26c). Note that the frontogenesis location ahead of the warm front, and east–west elongated shape is similar to that of the east composite frontogenesis field (Fig. 3.35c), supporting the contention that nonbanded cases represent east class null events.

The nonbanded composite cross-section orientation was chosen normal to the 1000–500 hPa thickness, through the 700 hPa frontogenesis and ascent (not shown) maxima as opposed to through the mean band position since cases included in the nonbanded composite, by definition, did not exhibit a band. The 700 hPa frontogenesis and ascent maxima were located along the developing warm front (Fig. 3.39c), similar to the east composite (Fig. 3.35c).

As in the east composite cross section, the developing warm frontal structure is evident in the θ_{es} and θ_e fields (Figs. 3.40a,b) although it has less baroclinicity than the east composite front (Figs. 3.36a,b). A region of CI is found equatorward and above the frontal zone (Fig. 3.40a), although the depth is shallower than observed in the east class cross section (Fig. 3.36a). Furthermore, the frontal zone appears more horizontal than for all previous cross sections, suggesting larger conditional (and implied static) stability

within the frontal zone (compare Fig. 3.40a with 3.36a). A sloping region of frontogenesis is also evident along the frontal boundary (Fig. 3.40b), but the maximum frontogenesis magnitude [$0.4\text{--}0.8\text{ }^{\circ}\text{C (100 km)}^{-1} (3\text{ h})^{-1}$] and depth (lowest 100 hPa) is the smallest of all previous model composite frontogenesis maxima. Consistent with apparent larger conditional stability and weaker frontogenesis, the ascent accompanying this frontogenesis is the weakest of all composites, barely reaching $-2 \times 10^{-3}\text{ hPa s}^{-1}$ and occurring over a broad region (Fig. 3.40c). Also note that this composite is much drier than the previous composites (Fig. 3.40d).

3.2.3g Northwest Model Dissipation Composite

Although the anticipation of the onset of a banded event is challenging, predicting its demise can be equally difficult. The northwest model dissipation composite (incorporating 30 analyses) is provided to compare band initiation environments to band dissipation environments in the comma-head portion of cyclones.

Although the synoptic summary at band dissipation (Fig. 3.41) appears similar to band initiation (Fig. 3.29), close inspection of the thermal advection pattern (Fig. 3.41b) shows that the greatest warm air advection has shifted farther northeast from the cyclone center (Fig. 3.41b). Also note that the warm air advection gradient has weakened on the poleward edge of the system. It is hypothesized this thermal advection signature is in response to the occlusion process, whereby the cyclone becomes progressively removed from the main baroclinic zone. Also note that the frontogenesis strength has diminished from nearly $3.5\text{ to }2.5\text{ }^{\circ}\text{C (100 km)}^{-1} (3\text{ h})^{-1}$ (compare Fig. 3.29c with Fig. 3.41c). It is

hypothesized that this behavior is also in response to the occlusion process since the deformation is acting on a weaker temperature gradient; however, more study is required to establish this contention.

Two cross sections were chosen to evaluate the band environment. The first (1) is taken from a Eulerian framework, with the exact same orientation as the cross section at band initiation. The second (2) is taken from a quasi-Lagrangian perspective, moving with the cyclone and composite band structure.

Cross section 1 (Fig. 3.42) shows considerable change from the initiation cross section (Fig. 3.30). The frontal zone has become more horizontal, suggesting greater conditional stability (compare Fig. 3.30a with Fig. 3.42a) and, more importantly, the frontogenesis maximum has weakened from values above $0.8 \text{ }^{\circ}\text{C (100 km)}^{-1} (3 \text{ h})^{-1}$ to values below $0.4 \text{ }^{\circ}\text{C (100 km)}^{-1} (3 \text{ h})^{-1}$ (compare Figs. 3.29b with Fig. 3.42b). Consequently, only weak ascent is noted in the ω field (Fig. 3.42c), with a shallow and broad “band” of moisture evident in the relative humidity field (Fig. 3.42d).

Cross section 2 (Fig. 3.43) has a more vertical frontal structure and exhibits greater frontogenesis than cross section 1 [nearly $0.8 \text{ }^{\circ}\text{C (100 km)}^{-1} (3 \text{ h})^{-1}$ compared with less than $0.4 \text{ }^{\circ}\text{C (100 km)}^{-1} (3 \text{ h})^{-1}$; compare Fig. 3.43b with Fig. 3.42b], but exhibits a more horizontal frontal structure and weaker frontogenesis than the band initiation cross section [$\sim 0.8 \text{ }^{\circ}\text{C (100 km)}^{-1} (3 \text{ h})^{-1}$ compared with $> 0.8 \text{ }^{\circ}\text{C (100 km)}^{-1} (3 \text{ h})^{-1}$; compare Fig. 3.42b with Fig. 3.30b]. Consistent with weaker frontogenesis a band of vertical motion is noted in cross section 2, but its maximum is elevated and is a third of the magnitude of the composite initiation maximum (compare Fig. 3.43c with Fig. 3.30c).

3.3 Case Studies

Since the northwest class events were the most common event type challenging forecasters in the region, case study analysis focused on discriminating between cases exhibiting northwest class events and cases which do not. In order to illustrate discriminating features, three representative study cases of banded, nonbanded, and null case (banded structure expected but not observed) evolutions are presented. This spectrum of cases will be used to demonstrate how the synoptic flow influences mesoscale substructure within cyclones. In addition, cross-section analysis will document the environmental differences between each case. Lastly, the performance of model diagnostics will be assessed.

3.3.1 Analysis of the 5–6 February 2001 Snowstorm

3.3.1a Case Description

On 5–6 February 2001, a major winter storm produced widespread snow accumulations greater than 30 cm through most of New England, with over 75 cm locally in New Hampshire (Fig. 3.44). The large snowfall accumulations were primarily attributed to an intense snowband that developed during the event. Snowfall rates in excess of 10 cm h^{-1} were observed in the extensive band, producing near “white out” conditions.

Figure 3.45 shows composite radar images every 6 h during the event. At 1200 UTC 5 February 2001 (hereafter times will be abbreviated as day/time UTC) a shield of

nonbanded, heavy precipitation was expanding over the mid-Atlantic (Fig. 3.45a). By 5/18 the precipitation shield had expanded and moved into southern New England (Fig. 3.45b). A faint band of heavier precipitation is evident, arcing from eastern Pennsylvania towards eastern Massachusetts. During the next 6 h this band narrowed and intensified as it pivoted into central New England by 6/00 (Fig. 3.45c), exhibiting 35–40 dBZ reflectivities along its length and observed snowfall rates of 10 cm h^{-1} . By 6/06 (Fig. 3.45d) the band had diminished in intensity ($\sim 30 \text{ dBZ}$ along its length), but was still evident—arcing from central Maine into eastern Massachusetts. By 6/12 (Fig. 3.45e) the band had dissipated, with only the southern tail of the precipitation shield evident in eastern Maine.

Figure 3.45f shows the time evolution of the single band axis. Note that the band pivoted as it translated with the system, consistent with the climatological motion of the northwest class events (see section 3.1.2). This motion placed central New Hampshire at the effective pivot point, prolonging the heavy snowfall and resulting in a snowfall accumulation maximum (Fig. 3.44).

3.3.1b Synoptic Summary

Figure 3.46 provides a synoptic summary of the formative stages of the event. At 5/12 cyclogenesis was occurring along a strong baroclinic zone off the North Carolina coast (Fig. 3.46a). This cyclogenesis was in response to a strong short wave (Fig. 3.46d) embedded in the base of a deep trough (Figs. 3.47d,e) progressing eastward from the Ohio Valley. Precipitation over the mid-Atlantic region (Fig. 3.45a) is supported by the

ascent maximum shown in Fig. 3.46f, and the maximum in warm air advection at 850 hPa shown in Fig. 3.46b. Thermal advection is also contributing to midlevel frontogenesis (Fig. 3.46c), which is coincident with the region of precipitation.

At 5/18 cyclogenesis continued as the surface cyclone moved north off the mid-Atlantic coast (Fig. 3.47a). By this time a closed circulation extended from the surface nearly to 700 hPa (Figs. 3.47b,c). Cyclogenesis is occurring as the 500 hPa eastern US trough amplifies in conjunction with ridge development over Atlantic Canada (Fig. 3.47d). Warm air advection has increased off the New Jersey coast from $2^{\circ}\text{C day}^{-1}$ (Fig. 3.46b) to $6^{\circ}\text{C day}^{-1}$ (Fig. 3.47b), which contributes to a larger area of midlevel frontogenesis exceeding $1.6^{\circ}\text{C (100 km)}^{-1} (3 \text{ h})^{-1}$ northwest of the cyclone center (Fig. 3.47c). This frontogenesis is associated with a focused ascent maximum just north and northwest of the cyclone center (Fig. 3.47f). Note that this ascent maximum also corresponds to the entrance region of an anticyclonically curved jet at 300 hPa (Fig. 3.47e).

Strong development occurred during the next 6 h (Fig. 3.48a) as the 500 hPa trough became negatively tilted (Fig. 3.48d). A closed circulation was noted from the surface to nearly 500 hPa (Figs. 3.48a–d), which resulted in a well-developed deformation zone associated with a confluent asymptote north and northwest of the surface cyclone, just as in the $T = 0$ h northwest composite (Fig. 3.29). This deformation acting on the thermal gradients results in significant midlevel frontogenesis with maxima greater than $2^{\circ}\text{C (100 km)}^{-1} (3 \text{ h})^{-1}$ (Fig. 3.48c) that arcs around the surface center. The combination of the digging trough and downstream ridge amplification led to the development of a double jet structure (Fig. 3.48e) similar to that cited by Kocin and

Uccellini (1990, 58–62) as a common feature of northeast storms, and also noted in the northwest class composite (Fig. 3.11e). The combination of forcing resulted in an elongated ascent maximum over a large portion of New England (Fig. 3.48f), but the observed band location (Fig. 3.45c) most closely corresponds to the axis of maximum midlevel frontogenesis (Fig. 3.48c).

The cyclone continued to develop during the next 6 h, moving to the Gulf of Maine by 6/06 (Fig. 3.49a). However, by this time the cyclone was occluded, with the strongest warm air advection shifted from just north of the cyclone center (Fig. 3.48b) to northeast of the cyclone center (Fig. 3.49b). The previously mentioned deformation zone still contributes to frontogenesis (Fig. 3.49c), but the frontogenesis has weakened slightly, now exhibiting a magnitude less than $2^{\circ}\text{C} (100 \text{ km})^{-1} (3 \text{ h})^{-1}$. Note also that the band intensity has decreased slightly (Fig. 3.45d). The combined effects of frontogenesis (Fig. 3.49c), vorticity advection (Fig. 3.49d), and implied upper-level divergence in the poleward exit region of a 300 hPa jet off the eastern US coast (Fig. 3.49e) is sufficient forcing for significant precipitation over New England (Fig. 3.45d), but again the band location is most closely correlated to the axis of maximum midlevel frontogenesis.

By 6/12 the cyclone had reached full maturity with a near vertically stacked circulation (Figs. 3.50a–e). The most significant change was the disappearance of the midlevel frontogenesis (Fig. 3.50c), coincident with the demise of the band (Fig. 3.45e). Note that at this time the most significant warm air advection has shifted well east of New England, now located east of Nova Scotia. This shift in maximum warm air advection supports the contention that the weakening frontogenesis is tied to the

occlusion process, whereby the primary baroclinic zone becomes removed from the deformation zone.

3.3.1c Cross-Section Analysis

Several cross sections are presented to further investigate the environmental stability and forcing of the case. As shown above, at 5/18 (Fig. 3.45b) the mesoscale band was developing in southeast New York state. A cross section normal to the developing band (orientation shown in Fig. 3.47f) is presented in Fig. 3.51. The sloping frontal structure is evident in both the θ_{es} and θ_e fields (Figs. 3.51a,b). Of particular interest is the region of negative geostrophic EPV found equatorward and within this frontal structure (Fig. 3.51a). Most of this region is characterized by CI, but a small region within the frontal zone appears stable to upright convection and is nearly saturated, suggesting the possibility of symmetric instability (SI). However, the use of geostrophic EPV in this situation may not be valid, since the flow is highly curved (see Fig. 3.47), suggesting the geostrophic wind may be a poor approximation of the flow. This point will be further discussed in section 3.3.5b.

As with the northwest class composite cross section (Fig. 3.30), the most striking aspect of this cross section is the sloping region of intense frontogenesis along the frontal zone (Fig. 3.51b). The direct circulation induced by this frontogenesis in the presence of the noted weak symmetric stability contributes to a narrow, sloping ribbon of upward vertical motion ($< -20 \times 10^{-3} \text{ hPa s}^{-1}$) on the equatorward flank of the frontal zone. Furthermore, the ascent maximum lies within the maximum dendritic growth

region (Fig. 3.51c), suggesting enhanced ice-crystal growth (Wetzel and Martin 2001; Waldstreicher 2002). This factor may have played a role in the large snowfall accumulations. Also note that the relative humidity “band” slopes into the cold air, suggesting slantwise ascent (Fig. 3.51d).

A similar cross section (orientation shown in Fig. 3.48f) is taken through the band at the height of the event at 6/00 (Fig. 3.52). Similar to the 5/18 cross section (Fig. 3.51), a sloping region of intense frontogenesis is noted along the frontal zone (Fig. 3.52b), with a narrow, sloping ascent maximum on the equatorward flank of the frontal zone (Fig. 3.52c). The most significant change from the 5/18 cross section is the expansion of the region of negative EPV within the frontal zone (compare Fig. 3.52a with Fig. 3.51a).

Cross-section analysis reveals the demise of the band at 6/06 (Fig. 3.53; cross-section orientation shown in Fig. 3.49f). Note that the region of negative EPV has nearly disappeared within the frontal zone (Fig. 3.53a). Although significant frontogenesis and ascent are still evident (Figs. 3.53b,c), they are not as robust as in previous times, consistent with the composite dissipation cross sections (Figs. 3.42b,c and Figs. 3.43bc).

3.3.2 Analysis of the 14–15 February 2000 Storm

3.3.2a Case Description

On 14–15 February 2000 a weak cyclone strengthened as it moved from the Ohio Valley to the Gulf of St. Lawrence. Although not an intense cyclone, the system was still responsible for a large swath of over 25 mm of precipitation that fell as a mix of rain,

sleet, and freezing rain over coastal locations, with over 20 cm of snowfall accumulation in interior New England. In contrast to the 5–6 February 2001 storm, no mesoscale banding was evident during the evolution of the 14–15 February 2000 storm.

Figure 3.54 shows the composite radar images every 6 h during the event. At 14/06 (Fig. 3.54a; days 14 and 15 refer to the 14–15 February 2000 case) heavy rain was found in the central Appalachians with scattered precipitation across the northeast US. Note the sharp northern edge to the precipitation along the Canadian border. By 14/12 (Fig. 3.54b) a broad shield of heavy precipitation covered the northeast US, although it was not organized in any banded fashion. By 14/18 (Fig. 3.54c) the heavy precipitation had moved into New England with no hint of banding. Only scattered showers remained by 15/00 (Fig. 3.54d) as the cyclone moved into the Gulf of St. Lawrence.

3.3.2b Synoptic Summary

Many of the same synoptic features noted in the nonbanded composite (recall Fig. 3.39) are present in the 14–15 February 2000 case. At 14/06 (Fig. 3.55) an elongated cyclone was centered over the Ohio Valley (Fig. 3.55a) in association with a broad confluent 500 hPa trough over the central U.S. (Fig. 3.55d). The entire northeast US was under warm air advection (Fig. 3.55b) in the broad southwest flow ahead of the cyclone. Despite the rather innocuous pattern, significant 700 hPa frontogenesis was found straddling the Canadian border (Fig. 3.55c). This frontogenesis maximum was located along the poleward edge of the warm air advection in the confluent entrance

region of the 300 hPa jet (Fig. 3.55e), which also corresponds to the knife-edge poleward boundary of radar reflectivity (see Fig 3.54a).

By 14/12 the cyclone had strengthened and moved northeast into Pennsylvania (Fig. 3.56a). This evolution occurred in response to an identifiable short-wave disturbance over the Maryland panhandle embedded within the larger-scale trough (Fig. 3.56d). Warm air advection continued over a large portion of the northeast US (Fig. 3.56b) and once again significant frontogenesis was found on the poleward edge of this warm air advection (Fig. 3.56c) in the entrance region of the 300 hPa jet (Fig. 3.56e), coincident with the poleward edge of the radar reflectivity(Fig. 3.56b). The combined forcing led to ascent over much of the northeast US (Fig. 3.56f).

The cyclone continued to develop as it entered southern New England at 14/18 (Fig. 3.57a) in response to the tightening 500 hPa vorticity gradient (Fig. 3.57d). A closed circulation was found from the surface to nearly 700 hPa (Fig. 3.57c), similar to the 5/18 analysis (Fig. 3.47). Strong frontogenesis was noted over northern Maine and New Brunswick with a faint arc of frontogenesis stretching back into eastern New York (Fig. 3.57c). It appears that the frontogenesis maximum over Maine and New Brunswick was associated with the warm air advection gradient, now in the diffluent flow ahead of the 700 hPa trough. Although there is significant deformation in the diffluent flow, it is *not* associated with a confluent asymptote since there is no identifiable col point (Fig. 3.57c). The 700 hPa flow fans out over northern Maine, but instead of a portion of the flow turning cyclonically as in the 5–6 February 2001 storm, the absence of a closed circulation allows the flow to continue northeast, eventually merging again in the

confluent entrance region of the jet (Fig. 3.57e). This flow pattern precludes the development of a confluent asymptote.

By 15/00 the cyclone (now located over eastern Maine; Fig. 3.58a) had reached maturity, as the associated 500 hPa short-wave disturbance (Fig. 3.58d) was becoming stretched in the confluent entrance region of the 300 hPa jet (Fig. 3.58e). A closed circulation has now formed at 700 hPa (Figs. 3.58c), but unlike the 5–6 February storm (Fig. 3.49c), the frontogenesis maximum does not arc around the closed low. Rather, the midlevel frontogenesis maximum was found farther east, on the poleward edge of the warm air advection (Fig. 3.58b) in the diffluent flow ahead of the 700 hPa low (Fig. 3.58c).

3.3.2c Cross-Section Analysis

As in section 3.3.1c, several cross sections are presented to further investigate the environmental stability and forcing of the case. Since the 14–15 February 2000 storm did not have an identifiable band, the cross section orientations were chosen normal to the 1000–500 hPa thickness contours, through the 700 hPa frontogenesis and ascent maxima. At 14/12 (Fig. 3.59; cross-section orientation shown in Fig. 3.56f) the developing warm frontal structure is evident in the θ_{es} and θ_e fields (Figs. 3.59a,b), with a region of CI equatorward and above the frontal zone. A sloping region of frontogenesis is also evident along the frontal boundary, although it is divided into two disconnected maxima at 1000 hPa and 700 hPa (Fig. 3.59b). The thermally direct circulation induced by this frontogenesis is evident in Fig. 3.59b, but the ascent is less than half the ascent at

the corresponding time in the 5–6 February storm (Fig. 3.51c) and occurs over a broader region.

By 14/18 (Fig. 3.60) the front had strengthened. At this time the frontogenesis magnitude of $\sim 5\text{--}6\text{ }^{\circ}\text{C (100 km)}^{-1} (3\text{ h})^{-1}$ (Fig. 3.60b) rivals that at the height of the 5–6 February 2001 storm (Fig. 3.52b). The thermally direct circulation induced by this frontogenesis contributes to a narrow, sloping ribbon of upward vertical motion on the equatorward flank of the frontal zone, just as in the 5–6 February 2001 case. However, note that the frontal structure is less upright than in the 5–6 February 2001 case, suggesting greater conditional stability within the frontal zone. The composite radar imagery at this time (Fig. 3.54c) shows an area of heavy precipitation in eastern Maine correlated with the ascent maximum, but there is no evidence of organized mesoscale banding.

By 15/00 (Fig. 3.61) the front maintained its strength, and a region of weak conditional stability was still found above the frontal zone. The frontal zone continued to be marked by robust frontogenetical forcing, with a narrow ascent maximum again found on the equatorward flank of the frontal zone. However, the noted low-level conditional stability (Fig. 3.61a) limited band development.

3.3.3 Analysis of the 21–22 March 1998 Storm

3.3.3a Case Description

On 21–22 March 1998 a strong short wave rotating around a cutoff cyclone induced cyclogenesis off the mid-Atlantic coast. The surface cyclone strengthened

modestly as it moved off the eastern US coast into Atlantic Canada. Although not an intense cyclone, the system was responsible for a prolonged period of precipitation, initially falling as rain, but changing over to heavy snow, with accumulations exceeding 30 cm in parts of the interior northeast US. Although transitory and narrow cold-frontal banded structures were observed, no single banded structure was observed during the storm.

Figure 3.62 shows the composite radar images every 6 h during the event. At 21/12 (Fig. 3.62a; days 21 and 22 refer to the 21–22 March 1998 storm) heavy precipitation was found in a synoptic-scale band arcing from southern New England into the eastern Great Lakes. This precipitation was associated with a weak disturbance ejected out of the cutoff circulation. By 21/18 (Fig. 3.62b) the synoptic band weakened as it swung into southern Canada and New England. At 22/00 (Fig. 3.62c) the first sign of the stronger short-wave disturbance is an expanding precipitation shield in eastern Virginia, although a full precipitation shield is slow to form (Fig. 3.62d). Precipitation intensity begins to increase in New England at 22/00 (Fig. 3.62d) and by 22/12 (Fig. 3.62e) heavy precipitation is found through much of the northeast, although it is clearly nonbanded. Only light precipitation remained by 22/18 (Fig. 3.62f).

3.3.3b Synoptic Summary

At 21/12 (Fig. 3.63) the well-established cutoff cyclone was clearly evident, with a closed cyclonic circulation even observed at 300 hPa (Fig. 3.63e). The initial short wave responsible for the first batch of precipitation in the northeast US is manifested as

an inverted trough at 700 hPa (Fig. 3.63c) and as a 500 hPa vorticity lobe in Pennsylvania (Fig. 3.63d). A larger vorticity maximum is noted at the base of the cutoff circulation (Figs. 3.63c,d) with an attendant jet streak along the Gulf Coast states (Fig. 3.63e). The associated broad surface cyclone is found in North Carolina, with a long warm front extending northeast from the cyclone center (Fig. 3.63a).

Six hours later at 21/18 (Fig. 3.64) the 500 hPa cutoff has become asymmetric, as the short wave emerges on the eastern flank (Fig. 3.64d). Vorticity advection associated with the short wave at the base of the 500 hPa cutoff (Fig. 3.64d) is contributing to surface cyclogenesis off the Carolina coast (Fig. 3.64a). Also note that short-wave ridging occurs ahead of the upstream short-wave disturbance in the northern Plains (Fig. 3.64d) as the entire cutoff cyclone shifts eastward, the latter evident by the disruption of the 300 hPa closed circulation (Fig. 3.64e).

By 22/00 the broad surface low is beginning to move up the coast, with a strong warm front extending northeast from the cyclone center (Fig. 3.65a). Modest 850 hPa warm air advection (generally $2\text{--}4^{\circ}\text{C day}^{-1}$) is found ahead of the warm front (Fig. 3.65b). Despite the warm air advection, little vertical motion was observed (Fig. 3.65f) with negligible midlevel frontogenesis (Fig. 3.65c).

During the next 6 h the cyclone became better organized as the 500 hPa cutoff opened up, resulting in a negatively tilted trough (Fig. 3.66d). Despite the presence of this negatively tilted trough (Fig. 3.66d) and associated warm air advection (Fig. 3.66b), the northeast US continues to be marked by weak vertical motion (Fig. 3.66f) and negligible midlevel frontogenesis (Fig. 3.66c).

The cyclone reaches maturity by 22/12 and is centered off the New England coast (Fig. 3.67a). A strong warm front associated with warm air advection on the order of $6\text{--}8\text{ }^{\circ}\text{C day}^{-1}$ is located off the New England coast (Fig. 3.67b). The 700 hPa low has deepened (Fig. 3.67c), in addition to the re-formation of the 500 hPa cutoff (Fig. 3.67d). A narrow band of ascent is noted ahead of the warm front (Fig. 3.67f), although there is the continued absence of midlevel frontogenesis (Fig. 3.67c). In some respects this time resembles the 6/12 analysis (Fig. 3.50) with the deep cutoff, weak ascent, and absence of frontogenesis.

At 22/18 (Fig. 3.68) the surface cyclone continues to move northeast, as the associated cutoff is ejected out of the broad 500 hPa trough (Fig. 3.68b). Consequently, the ascent has weakened and moved into Atlantic Canada (Fig. 3.68f).

3.3.3c Cross-Section Analysis

Like the 14–15 February 2000 storm, cross-section orientations were chosen normal to the 1000–500 hPa thickness contours, through the 700 hPa frontogenesis and ascent maxima. At 22/06 (Fig. 3.69; cross-section orientation shown in Fig. 3.66f) the established warm front is evident in the θ_{es} and θ_e fields (Figs. 3.69a,b), with a region of CI equatorward and above the frontal zone. In marked contrast to the previous cross sections (Figs. 3.51–3.53, 3.59–3.61), the frontal zone is nearly horizontal, consistent with significant low-level conditional stability (Fig. 3.69a), with negligible frontogenesis, even in low levels (Fig. 3.69b). Ascent is still present as large-scale

overrunning is occurring (Figs. 3.69b,c), but it is relatively weak ($> -6 \times 10^{-3} \text{ hPa s}^{-1}$), elevated (above 700 hPa), and not coherently organized.

Little change occurs during the next 12 h, despite the upper-level development. The 22/12 cross section exhibits many of the same innocuous features, such as the near horizontal orientation of the frontal zone (Fig. 3.70a) and marked absence of frontogenesis (Fig. 3.70b). Stronger ascent ($-8 \times 10^{-3} \text{ hPa s}^{-1}$ versus $-6 \times 10^{-3} \text{ hPa s}^{-1}$) is noted at this time, although it is above 600 hPa (Fig. 3.70c). The 22/18 cross section similarly exhibits a nearly horizontal frontal zone (Figs. 3.71a,b), with minimal frontogenesis (Fig. 3.71b) and a weak elevated ascent maximum. (Fig. 3.71c).

3.3.4 Synoptic Synthesis

Cases are placed in the context of cyclogenesis, deformation and frontogenesis, and frontal structure. Although these case elements are considered separately, it is recognized that they are closely related. For instance, strong cyclogenesis facilitates stronger deformation than weak cyclogenesis. Consequently, frontogenesis is likely to be stronger in cases of intense cyclogenesis than in cases of weak cyclogenesis. The frontogenetical response is further augmented by the stability, taking the form of a concentrated updraft on the equatorward flank of the frontal zone in the presence of weak static stability, while the ascent will remain broad in the presence of large static stability.

3.3.4a Cyclone Development

Figure 3.72 quantifies the development of each cyclone in terms of the minimum 1000 hPa height. Although the three cyclones presented all underwent cyclogenesis, the 5–6 February 2001 cyclone clearly developed the most (1000 hPa height change of 234 m in 24 h or $\sim 16 \text{ hPa } 12 \text{ h}^{-1}$), qualifying as a “bomb” as defined by Sanders and Gyakum (1980; deepening rate of $12 \text{ hPa } 12 \text{ h}^{-1}$ at 45°N). Consistent with the northwest and nonbanded composite minimum 1000 hPa height evolutions (Fig. 3.28), the banded cyclone developed most rapidly in the period just before band initiation, while the nonbanded cyclones only exhibited modest development.

It is clear that the synoptic flow regimes differed in each case, and that these differences dictated the amount of cyclogenesis that each cyclone experienced. The 5–6 February 2001 storm began with downstream ridging, allowing the system to take on a negative tilt, which maximized vorticity advection and subsequent surface development. The 14–15 February 2000 storm developed in the confluent entrance region of the Atlantic jet, which limited the vorticity advection and subsequent surface development as the disturbance was stretched along the jet axis, consistent with the nonbanded composite evolution. The 21–22 March 1998 storm began with a well-developed cutoff cyclone, and developed in response to the rotation of a strong short wave in the cutoff circulation. Although the observed closed midlevel circulation and negatively tilted trough are consistent with the northwest composite $T = 0 \text{ h}$ analysis (Fig. 3.29), the observed storm evolution lacks the substantial cyclogenesis that is evident in the

northwest composite evolution (Figs. 3.10–3.12). It is hypothesized that the equivalent barotropic nature of the disturbance and large static stability limited development.

3.3.4b Deformation and Frontogenesis

The development of each cyclone affected the magnitude, shape, and placement of the deformation field. The 5–6 February 2001 storm quickly developed a closed midlevel circulation, which resulted in a well-developed deformation zone associated with a col point and confluent asymptote northwest of the surface cyclone. In this situation deformation acting on the temperature gradient contributed to a deep layer of frontogenesis, which aided band development in the northwest sector of the cyclone.

Since the 14–15 February 2000 storm did not establish a closed midlevel circulation until late in its evolution, significant deformation was limited in the northwest sector of the storm. Consequently, the northwest quadrant was marked by an absence of frontogenesis, which precluded band development in this region. Although diffluent flow ahead of the low-level circulation contributed to significant deformation, this flow was not associated with a col point and an associated confluent asymptote. Regardless of the flow configuration, the deformation still contributed to frontogenesis, which was now found *ahead* of the cyclone along the warm front.

The 21–22 March 1998 storm was characterized by an absence of midlevel frontogenesis. Although the cyclone exhibited a closed midlevel circulation from the onset, which deepened with time, the broad nature of the cutoff circulation forced the main deformation zone into southeastern Quebec and Newfoundland (Figs. 3.63–3.68),

which was well north of the cyclone center and baroclinic zone. Consequently, weak midlevel frontogenesis [$< 1.6 \text{ }^\circ\text{C (100 km)}^{-1} (3 \text{ h})^{-1}$] was limited to this region. Over the northeast US, low-level temperature advection ahead of the warm front supported limited frontogenesis, but it was confined to below 900 hPa (Figs. 3.70 and 3.71).

3.3.4c Frontal Structure

Cross-section analysis revealed that the frontal slopes in each case varied considerably. The 5–6 February 2001 frontal zone was the most upright, while the 14–15 February 2000 frontal zone was more horizontally sloped, and the 21–22 March 1998 frontal zone was nearly horizontal. Although many factors affect both the environmental stability and frontal slope, the slope of the frontal zone is inversely proportional to the stability for a given cross-front thermal gradient. This relationship is important since the environmental stability affects the frontogenetical response, as predicted by the Sawyer–Eliassen equation and shown by Emanuel (1985). Since the frontal zones in the 14–15 February 2000 case and 21–22 March 1998 case were less upright than in the 5–6 February 2001 case, they exhibited greater conditional stability, which limited the frontogenetical response and subsequent band development.

3.3.5 Model Diagnostics

The variety of cases presented provides the opportunity to examine the performance of model diagnostics using the operational Eta model. Attention will focus

on the 5–6 February 2001 storm since it exhibited a well-defined single band, but comparisons will also be made with the 14–15 February 2000 and 21–22 March 1998 cases.

3.3.5a Conventional diagnostics

The most obvious signature of a mesoscale band in model forecast fields would be a narrow maximum of forecast accumulated precipitation. The 80 km display grid Eta model forecast 6-h accumulated precipitation at 6-h intervals during the 5–6 February 2001 snowstorm from the 0000 UTC and 1200 UTC initialized model runs are shown in Fig. 3.73. Although the precipitation fields are elongated in the same direction as the observed band, the coarse spatial and temporal resolution make it difficult to discern whether the model creates a band. In response to this limitation, forecast accumulated precipitation fields on 3-h and 40 km temporal and spatial scales were acquired (shown in Fig. 3.74). This dataset includes model runs initialized just 6 h apart, at 0000 UTC, 0600 UTC, 1200 UTC, and 1800 UTC. The increased temporal and spatial scale elicits an elongated precipitation structure similar to the observed band, but this structure is consistently found equatorward from the observed band location. It is acknowledged that the pivoting band motion would favor an equatorward offset to the maximum on the eastern extent since the forecast precipitation field incorporates 3-h precipitation accumulation, during which time the eastern extent of the band moves poleward. Similarly the pivoting motion would also favor a poleward offset to the maximum on the western extent of the band as this portion of the band swings southeast during the 3-h

forecast period. However, the forecast maximum precipitation axis should fall between the band positions at the beginning and end of the forecast period. The fact that it does not highlights that mesoscale bands may not be resolved or simulated in current operational model forecasts. Ideally comparison would be made between high temporal (~1) observed precipitation and model forecast precipitation, but the present comparison between radar reflectivity and 3-h model forecast accumulated precipitation highlights the problem of using model-accumulated precipitation to identify band location.

Another obvious signature of a mesoscale band would be a narrow ribbon of strong ascent. Cross sections from the 5–6 February 2001 case (Figs. 3.51–3.53) exhibit a narrow ascent maximum, coincident with the banded structure; however, the relatively coarse model display resolution and sloping nature of the ascent maximum prohibit clear identification of the band location relative to geography. This shortcoming is made evident by the 800–600 hPa layer-averaged ω (Figs. 3.46f–3.50f), which smears the narrow sloping ascent maximum into a rounder shape. Note that the layer averaged ascent maximum consistently is found equatorward from the band location through time, consistent with the forecast accumulated precipitation field. Although the layer-averaged ascent maximum is elongated in a similar direction as the observed band, the observed band location is consistently located poleward from the axis of the ascent maximum, as it was in the precipitation fields.

3.3.5b Derived diagnostics

Geostrophic EPV is a critical component of the winter season ingredients maps proposed by Wetzel and Martin (2001) and the VRS band diagnostic proposed by Dixon et al. (2002). However, the calculation of EPV is sensitive to the choice of representative wind. The decision to use the geostrophic instead of the full wind in the EPV calculation rests on the theoretical tenets of SI. However, the flow surrounding the frontal zones of interest is often highly curved, suggesting that the geostrophic wind is not an accurate approximation to the actual flow.

This effect was evident upon further examination of the 6/00 cross section (Fig. 3.75). The geostrophic EPV field calculated on the 80 km display grid (Fig. 3.75a), exhibits a deep layer of small to negative EPV near the middle of the cross section, suggesting the possibility of SI. However, use of the full wind instead of the geostrophic wind (Fig. 3.75b) eliminates a large portion of the negative area, replacing it with weak symmetric stability. Note that this environment would not suggest SI.

The calculation of EPV is further influenced by the model resolution. Barnes et al. (1996) have shown that derived quasigeostrophic quantities can become unrepresentative in mesoscale models, such as the Eta model, as a consequence of the fine resolution and associated model-generated noise. In addition, the magnitude of the EPV may be enhanced with decreasing resolution, since the constituent fields have greater magnitude (Schultz and Doswell 2001). Since EPV is a derived field dependent on absolute vorticity and stability, its calculation is highly sensitive to the model resolution.

Use of the 40 km display grid in the calculation of geostrophic EPV along the central segment of the 06/00 cross section corroborates the effect of model resolution (Fig. 3.75c). Note that the EPV field appears noisy, with regions of negative EPV enhanced in magnitude. Use of the full wind instead of geostrophic wind with the same fields nearly eliminates the negative region (Fig. 3.75d), just as with the 80 km display grid, but the EPV field does outline a narrow sloping region where SI might occur.

Such behavior spurred further investigation of the absolute vorticity fields, since this field is directly involved in the calculation of EPV. Figure 3.76 illustrates how absolute vorticity and the subsequent calculation of EPV is affected by use of the geostrophic and full winds. The cross sections of the geostrophic and full wind cross section vorticity fields (Figs. 3.76a,b) exhibit minima near the respective EPV minima; however use of the geostrophic wind brings the absolute vorticity to zero, if not slightly below (Fig.3.75a). This result suggests inertial instability, which eliminates the possibility of SI in this region. The location of the absolute vorticity minimum correlates with the axis of a midlevel short-wave ridge (Fig. 3.76c) found ahead of the main disturbance.

Reduction of the model display resolution to 40 km dramatically affects the absolute vorticity field. Now the geostrophic absolute vorticity clearly exhibits a region of inertial instability (Fig. 3.77a) coincident with the region of large negative EPV (Fig. 3.75c), while the corresponding full wind counterpart (Fig. 3.77b) remains inertially stable. This difference suggests that the large negative values of geostrophic EPV found in the 40 km display cross section are due to inertial instability (possibly also a symptom of model noise), and not SI.

Beyond the choice of representative wind and model resolution, EPV may be influenced by diabatic effects. A weak vertical dipole in the geostrophic EPV field at the band position was noted in the composite cross sections (Figs. 3.30a, 3.32a, 3.34a, 3.36a, 3.38a, 3.40a), as well as in the 06/00 cross section (Fig. 3.52a). This dipole may be a result of heating in the 600–800 hPa layer associated with latent heat release from the precipitation band. In this situation the noted weak midlevel symmetric stability may be a symptom of diabatic effects, rather than a precursor of the band.

These results complicate utilization of current band diagnostic procedures such as the Wetzell and Martin (2002) PVQ and Dixon et al. (2002) VRS diagnostics, since the sign and magnitude of EPV based on the geostrophic wind directly affect both diagnostics. However, the VRS diagnostic explicitly eliminates areas exhibiting inertial instability, providing potential utility regardless of model resolution.

Application of the VRS diagnostic to the 80 km (all subsequent plots are derived from the 80 km grids) 6/00 analysis provides an opportunity to test its utility. Although the VRS diagnostic is intended as a plot of the number of model levels meeting the defined criteria, GEMPAK version 5.6 does not have a vertical counting utility. As a compromise, four levels (900, 800, 700, and 600 hPa) were chosen for assessment. Figure 3.78 shows the VRS diagnostic at individual levels, using the geostrophic wind in the calculation of EPV, with areas meeting the criteria for SI shaded. Note that only the 700 and 600 hPa levels (Figs. 3.78c,d) show any correlation with the observed band, and that this correlation is minimal. In fact large portions of the band length were not identified at any level. Use of the full wind in the calculation of EPV even further reduces the coincidence (Fig. 3.79).

Application of the VRS diagnostic to the nonbanded case at 14/18 analysis time (80 km resolution) is shown in Fig. 3.80. Although overlapping of the identified regions is minimal, large portions of Maine meet the criteria at 700 and 600 hPa (Figs. 3.80c,d). The full wind counterpart (Fig. 3.81) eliminates these regions, although coincidence exists near Halifax, Nova Scotia, at 800, 700, and 600 hPa.

Application of the VRS diagnostic to the null case at 22/12 analysis time is shown in Fig. 3.82. Only small areas are identified, with no coincidence noted, consistent with no banding. Use of the full wind (Fig. 3.83) once again reduces the identified area.

The VRS application results suggest that there was minimal potential for SI in all cases, even the banded case. Additionally it was shown the VRS diagnostic is sensitive to the choice of representative wind. Whether using the geostrophic or full wind in the case of the 5–6 February 2001 snowstorm the VRS diagnostic would not alert forecasters to the potential of banded structure, especially since it appears the banded structure was not a symptom of SI. The results of this climatological and composite study suggest that band formation occurs within a deep layer of frontogenesis in the presence of weak conditional stability, regardless of the presence of instability, whatever its mode. Building on the results of this study, in an attempt to better discriminate between banded and nonbanded situations, we present the Frontogenesis in the presence of Weak Stability (FWS) diagnostic. This diagnostic represents a more general application of the VRS diagnostic, focusing on regions of significant frontogenesis rather than negative EPV. Thus, it is not as sensitive to the choice of wind, and the effect of fine resolution is minimized. The FWS only highlights midlevel regions exhibiting frontogenesis

exceeding $1\text{ }^{\circ}\text{C (100 km)}^{-1} (3\text{ h})^{-1}$, weak conditional stability ($-0.1^{\circ}\text{C hPa}^{-1} < \frac{\partial\theta_{es}}{\partial p} < 0$), near saturation ($> 80\%$ relative humidity), and ascent exceeding $-5 \times 10^{-3}\text{ hPa s}^{-1}$. The choice of threshold values was guided by observed parameters in marginal banded events.

Application of the FWS to the 06/00 banded analysis time is shown in Fig. 3.84. The shaded region overlaps at four levels (note southwest New Hampshire), coincident with the observed band location. Additionally, the shaded region exhibits a coherent structure that closely mimics the shape of the observed banded structure. Admittedly the shaded region encompasses a much greater area than the observed band, but this diagnostic used in the context of the synoptic features (cyclone development deformation and frontogenesis, frontal structure) could alert forecasters to the likelihood of banding.

Application of the FWS to the 14/18 nonbanded analysis time is shown in Fig. 3.85. Although regions are shaded at each level, only two levels coincide over northern Maine. This behavior is somewhat similar to the geostrophic VRS diagnostic (Fig. 3.80). Ideally a smaller region would be shaded, but this discrepancy may be related to the near appearance of banded structure in this case.

Application of the FWS to the 22/12 analysis time is shown in Fig. 3.86. Consistent with the absence of banded structures, no susceptible areas were identified, clearly qualifying this analysis time as nonbanded. Note that the VRS diagnostic highlighted a few small areas at 22/12 (Fig. 3.82), making distinction between the 06/00 banded analysis and 22/12 nonbanded analysis ambiguous. In contrast the distinction is obvious with the FWS.

The forecasting utility of the FWS diagnostic will need to be proven with more extensive application to various situations; however, the results of its limited application to these three case studies is encouraging.

Table 3.1: Band climatology

Band Type	Single	Transitory	Narrow Cold-frontal	Multi	Undefined	Total
Events	48	40	36	29	9	162

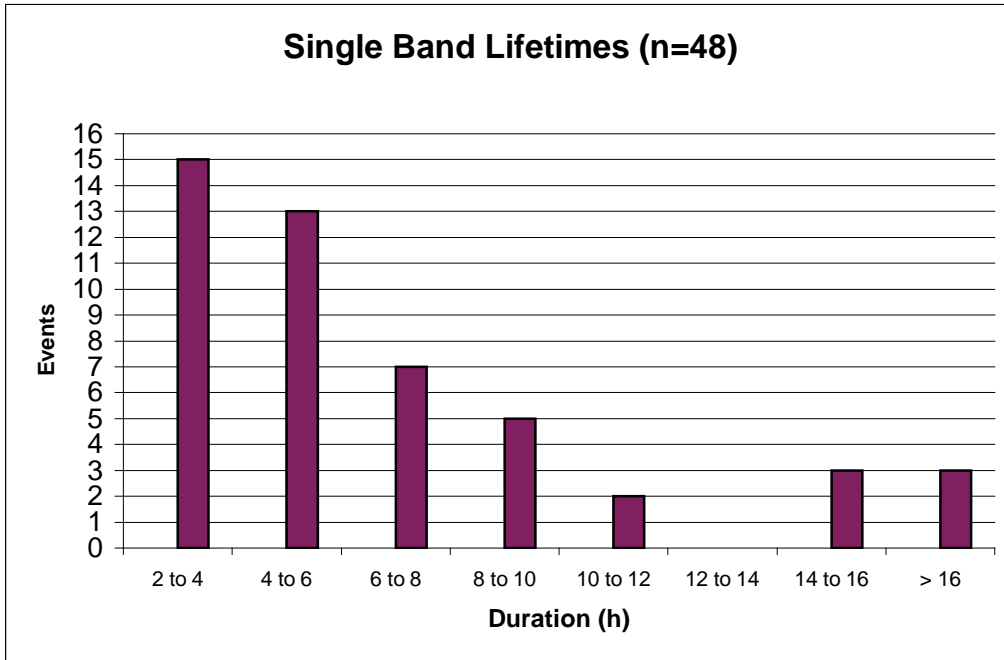


Fig. 3.1. Single band lifetimes.

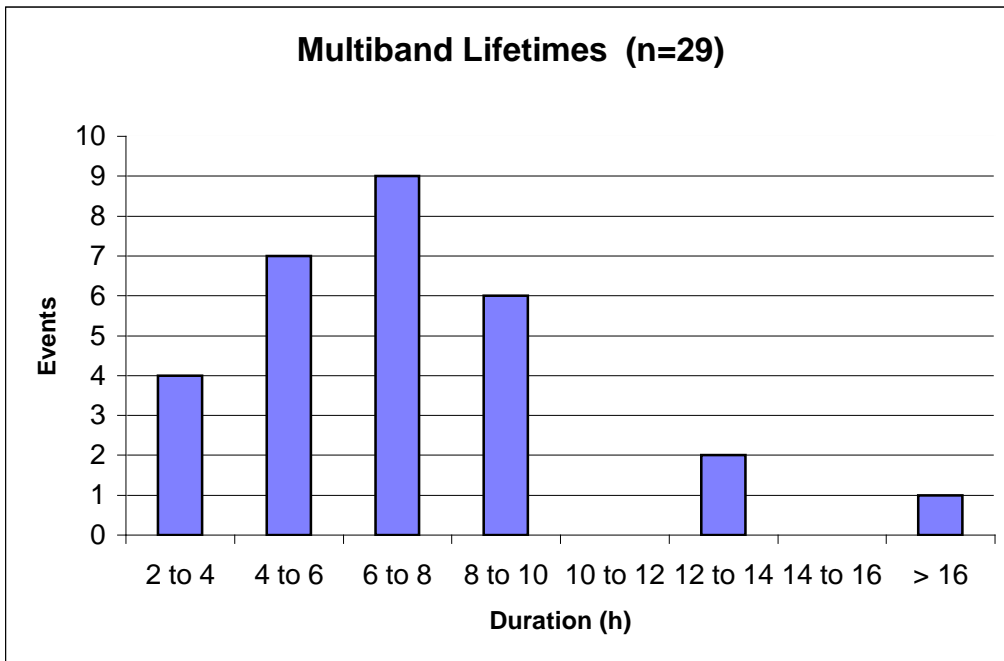
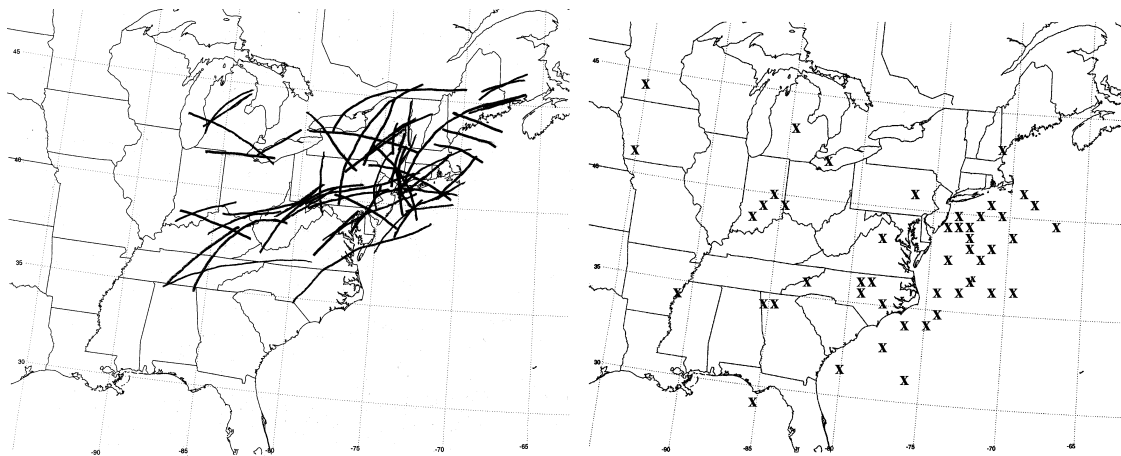
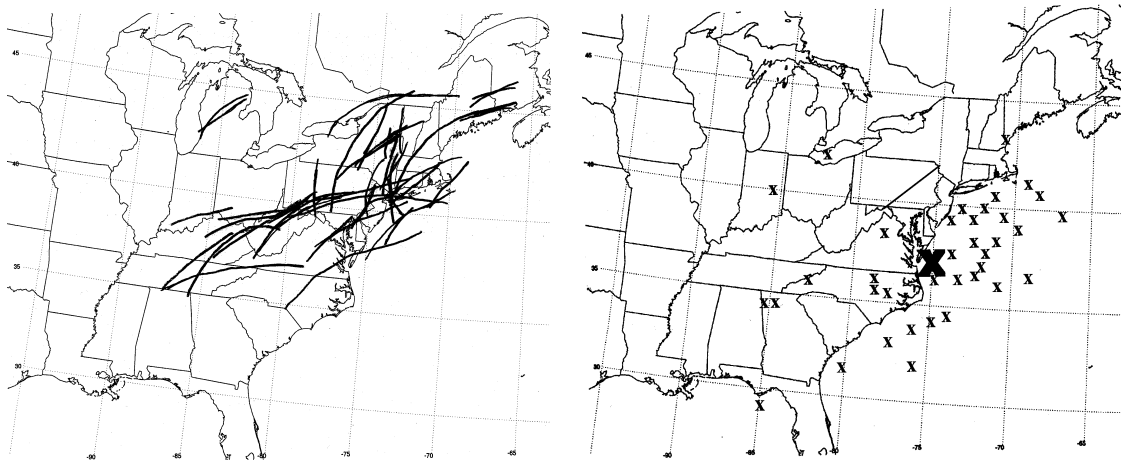


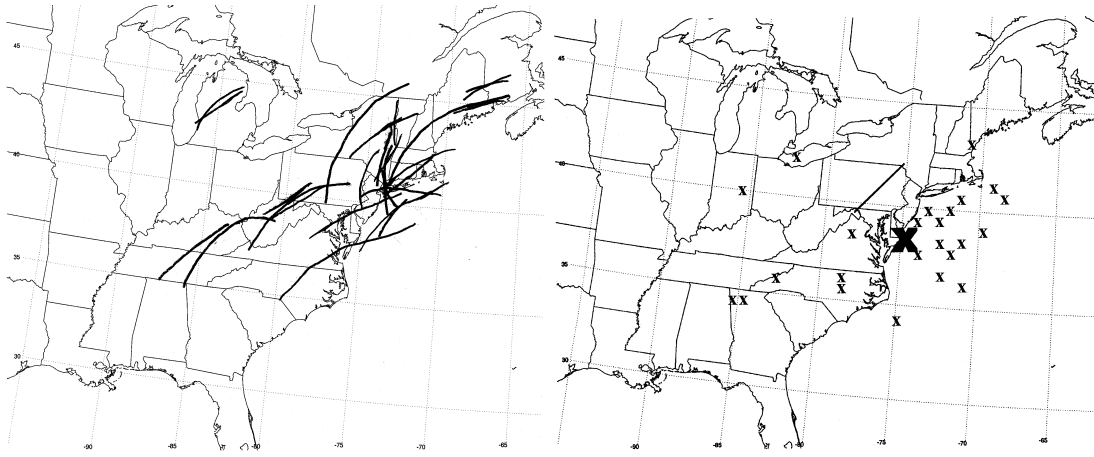
Fig. 3.2. Multiband lifetimes.



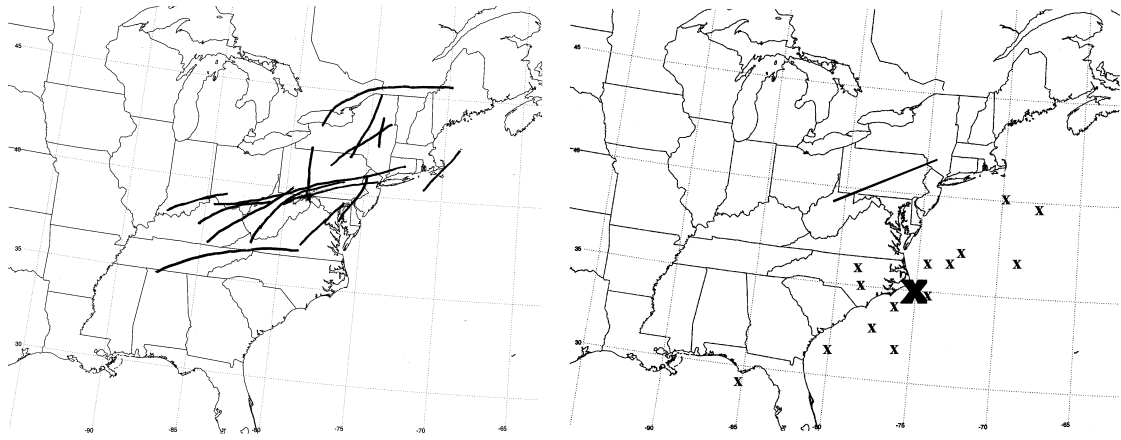
a. b.
 Fig. 3.3. (a) Geographical distribution of all 48 single bands studied. The axis of each band at the representative time is identified by a solid black line. (b) Geographical distribution of surface lows responsible for the observed single bands at the analysis time (defined in text). Each surface low position is identified as a “x”.



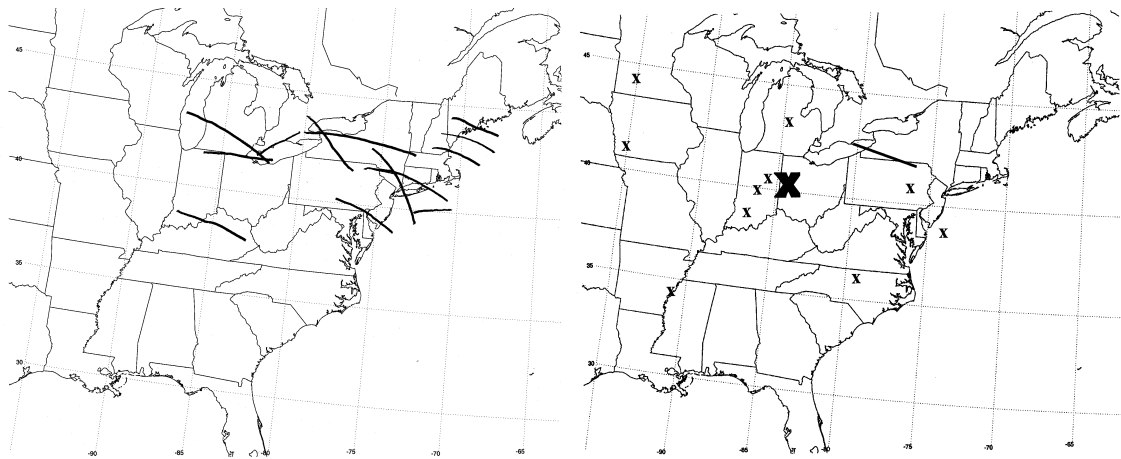
a. b.
 Fig. 3.4. (a) As in Fig. 3.3a, except with all northwest class bands. (b) As in Fig. 3.3b, except the centroid position of the surface lows is identified by the large bold **X**, and the mean position of the northwest bands is identified by the single solid line.



a. b.
 Fig. 3.5. As in Fig. 3.4, except for the northwest-near class.



a. b.
 Fig. 3.6. As in Fig. 3.4, except for the northwest-far class.



a. b.
 Fig. 3.7. As in Fig. 3.4, except for east class.

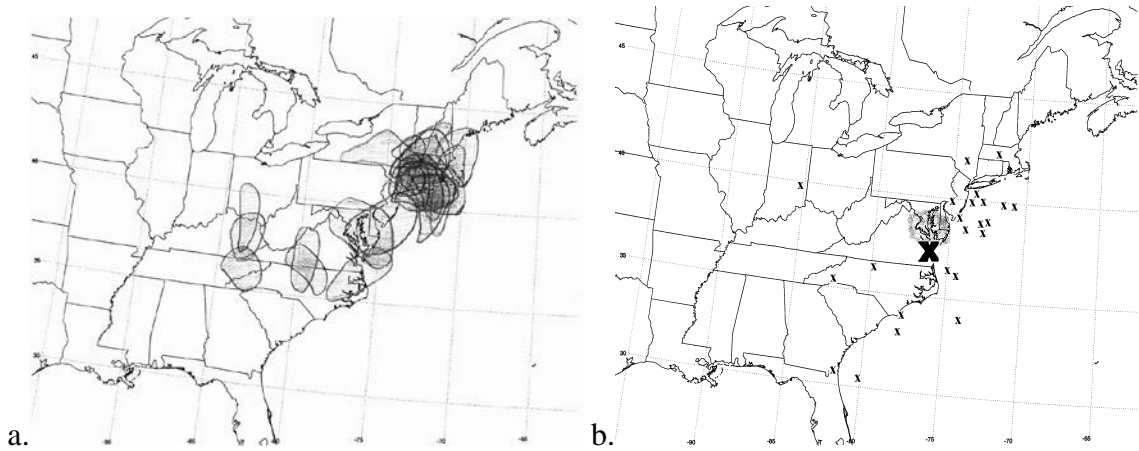


Fig. 3.8. As in Fig. 3.4, except for multiband class with multiband occurrences shaded in (a) and mean multiband region stippled in (b).

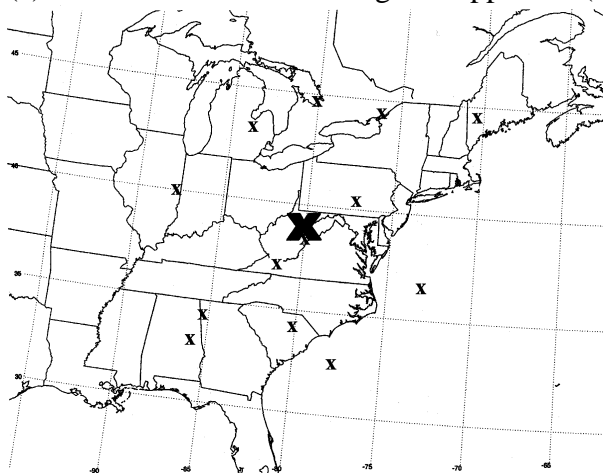


Fig. 3.9. Surface low center positions of nonbanded composite members (x) and nonbanded composite centroid position (X).

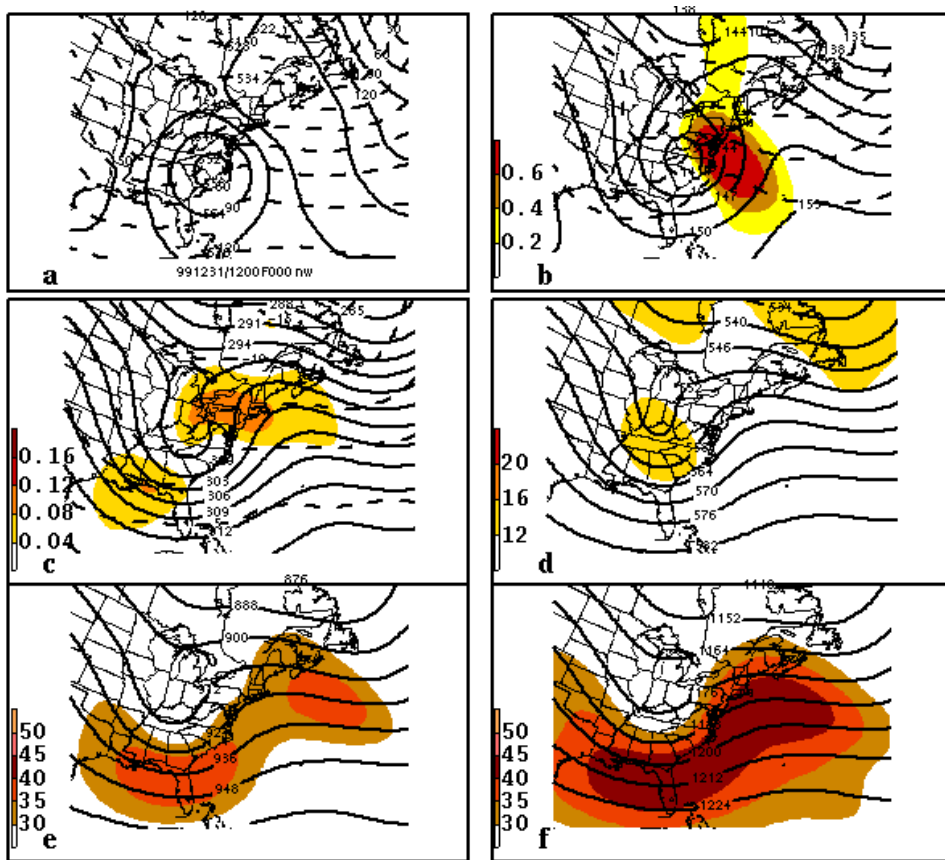


Fig. 3.10. Six-panel summary for the northwest class composite at $T = -12$ h. (a) 1000 hPa heights (black solid) contoured every 30 m (~ 4 hPa) and 1000–500 hPa thickness (black dashed) contoured every 6 dam. (b) 850 hPa heights (black solid) contoured every 3 dam, temperature (black dashed) contoured every 5°C , and temperature advection (shaded according to scale) in $^\circ\text{C} (\text{day})^{-1}$. (c) 700 hPa heights (black solid) contoured every 3 dam, temperature (black dashed) contoured every 5°C , and Miller 2-D frontogenesis (shaded according to scale) in $^\circ\text{C} (100 \text{ km})^{-1} (3 \text{ h})^{-1}$. (d) 500 hPa heights (black solid) contoured every 6 dam, and absolute vorticity, shaded according to scale above $12 \times 10^{-5} \text{ s}^{-1}$. (e) 300 hPa height (black solid) contoured every 12 dam, and windspeeds, shaded according to scale above 30 m s^{-1} . (f) 200 hPa heights and windspeeds as in (e).

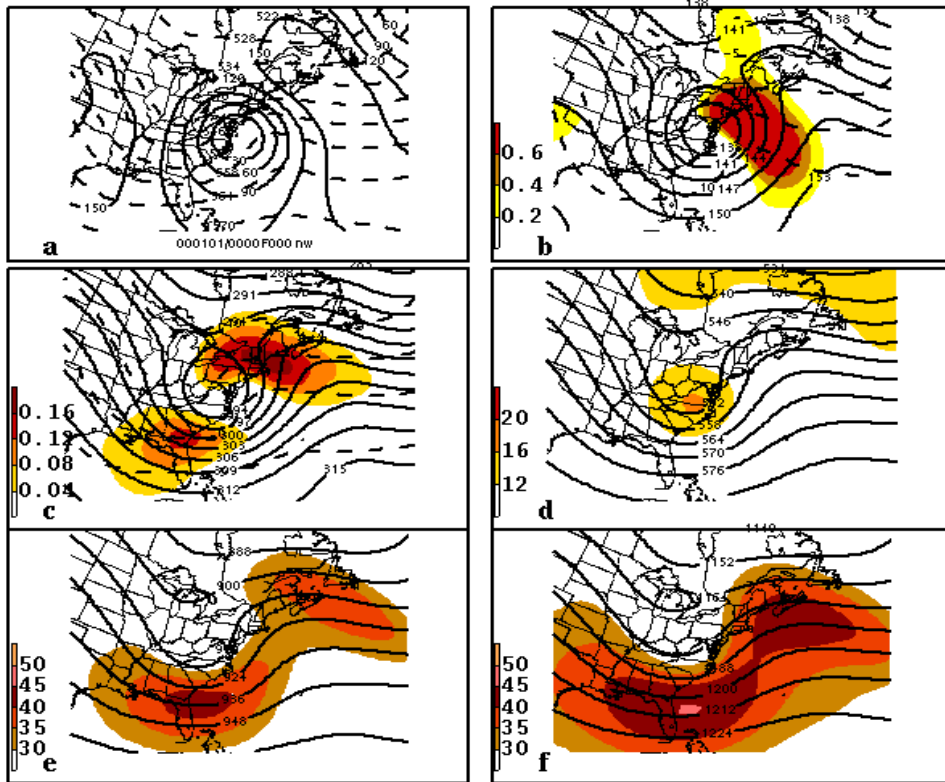


Fig. 3.11. As in Fig. 3.10, except at $T = 0$ h.

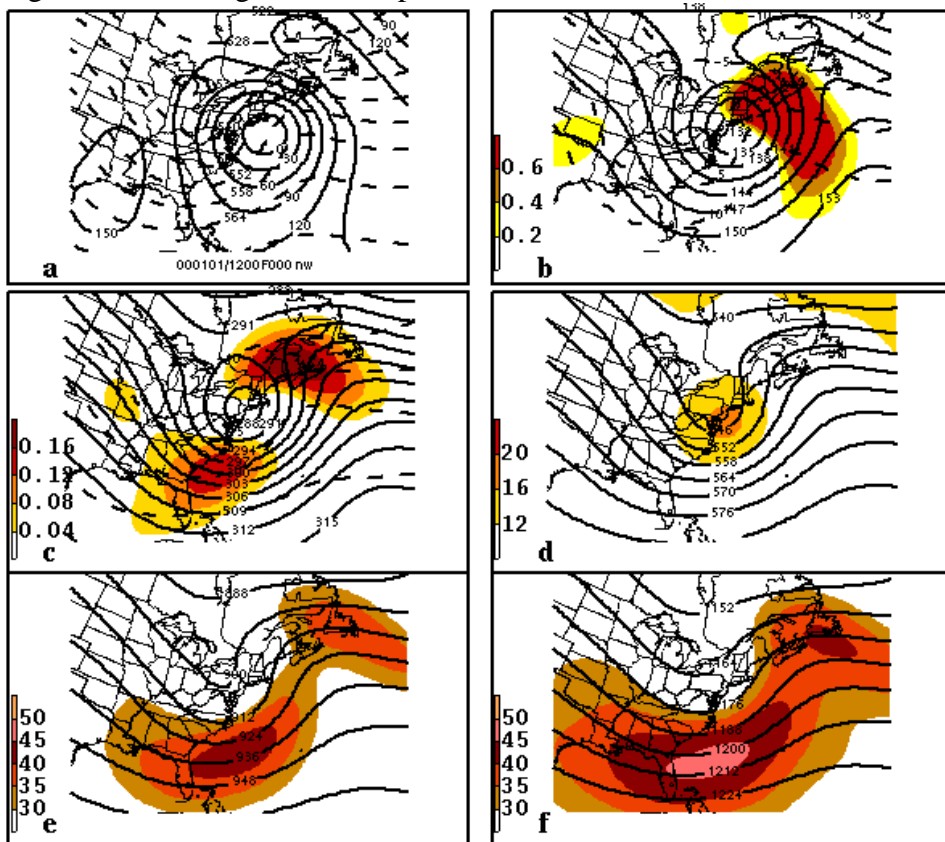


Fig. 3.12. As in Fig. 3.10, except at $T = 12$ h.

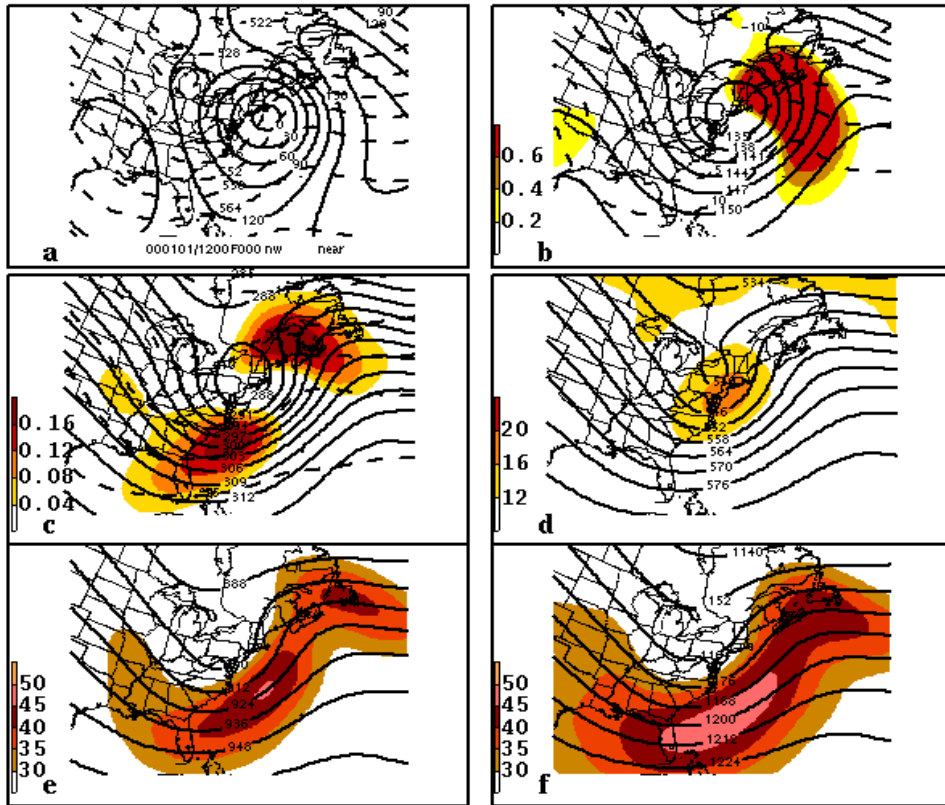


Fig. 3.15. As in Fig. 3.13, except at $T = 12$ h.

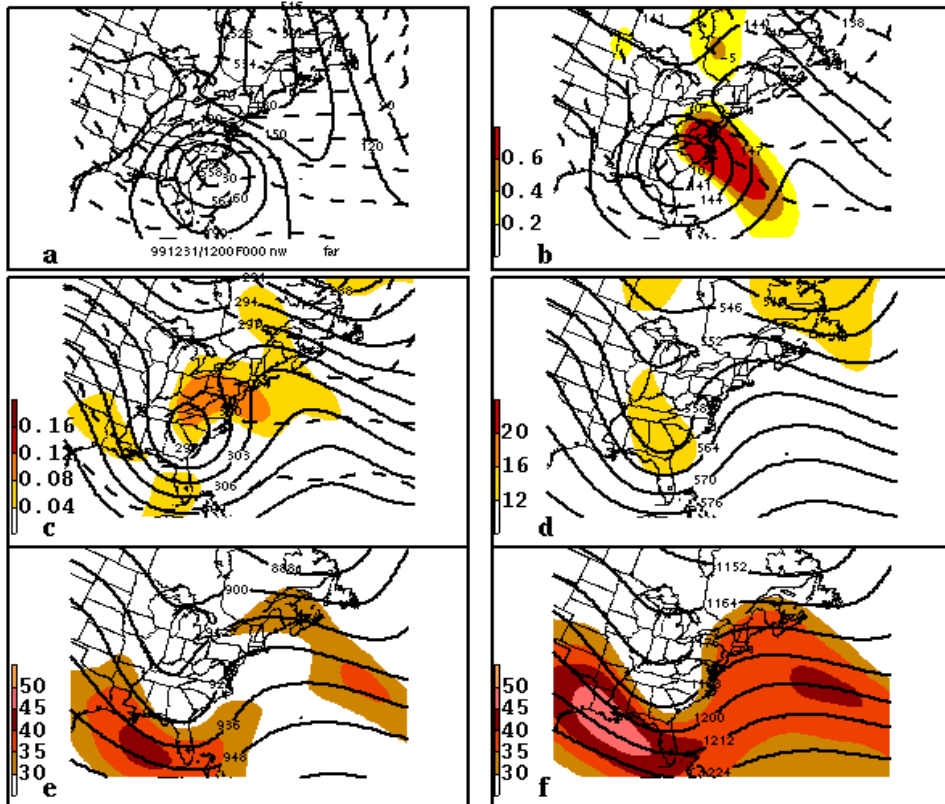


Fig. 3.16. As in Fig. 3.10, except for northwest-far class.

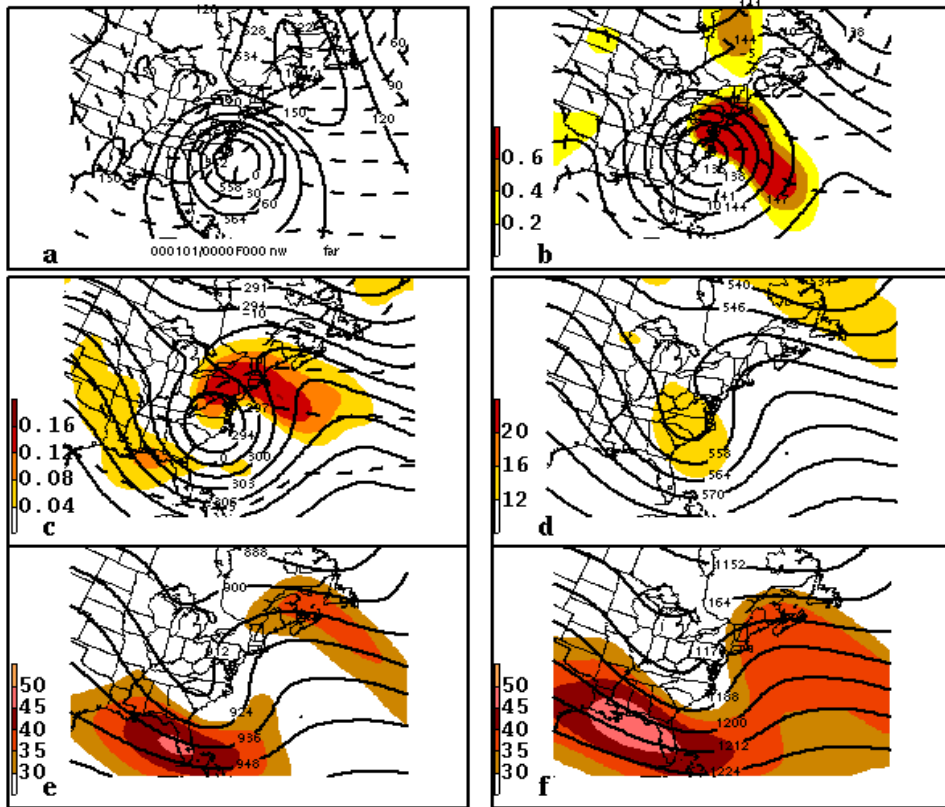


Fig. 3.17. As in Fig. 3.16, except at $T = 0$ h.

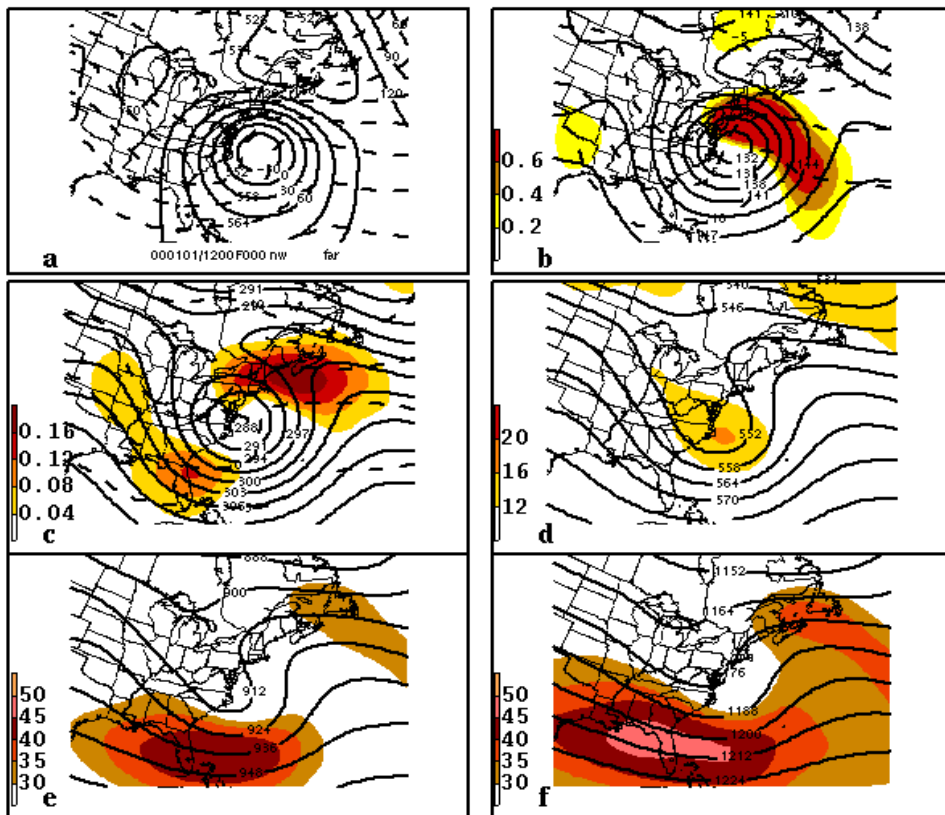


Fig. 3.18. As in Fig. 3.16, except at $T = 12$ h

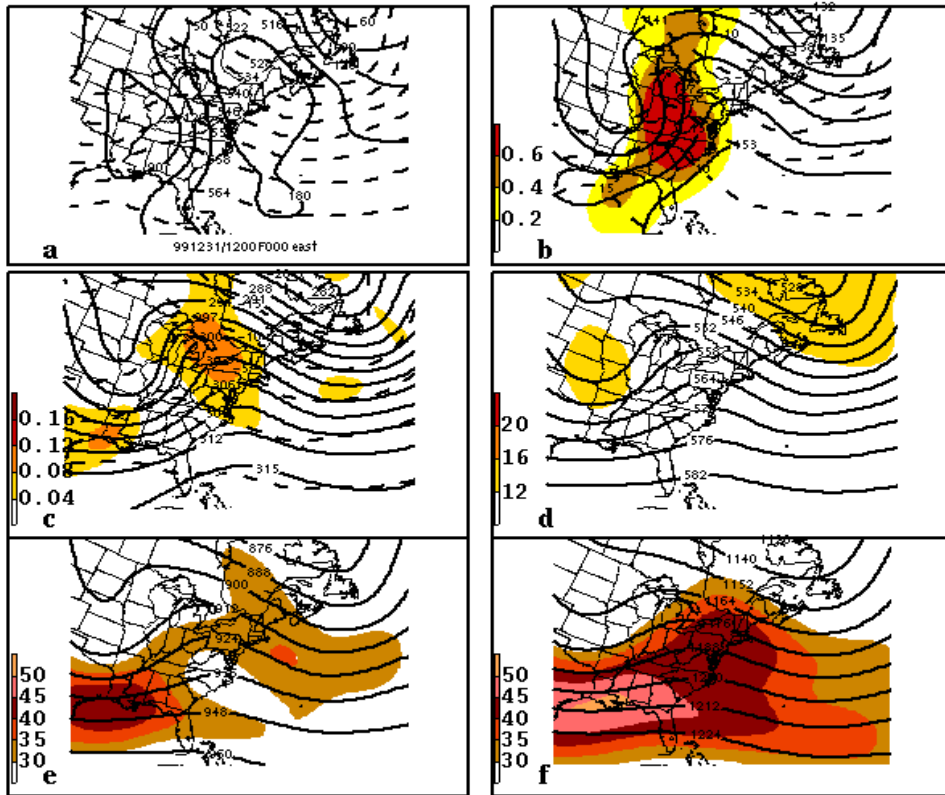


Fig. 3.19. As in Fig. 3.10, except for east class.

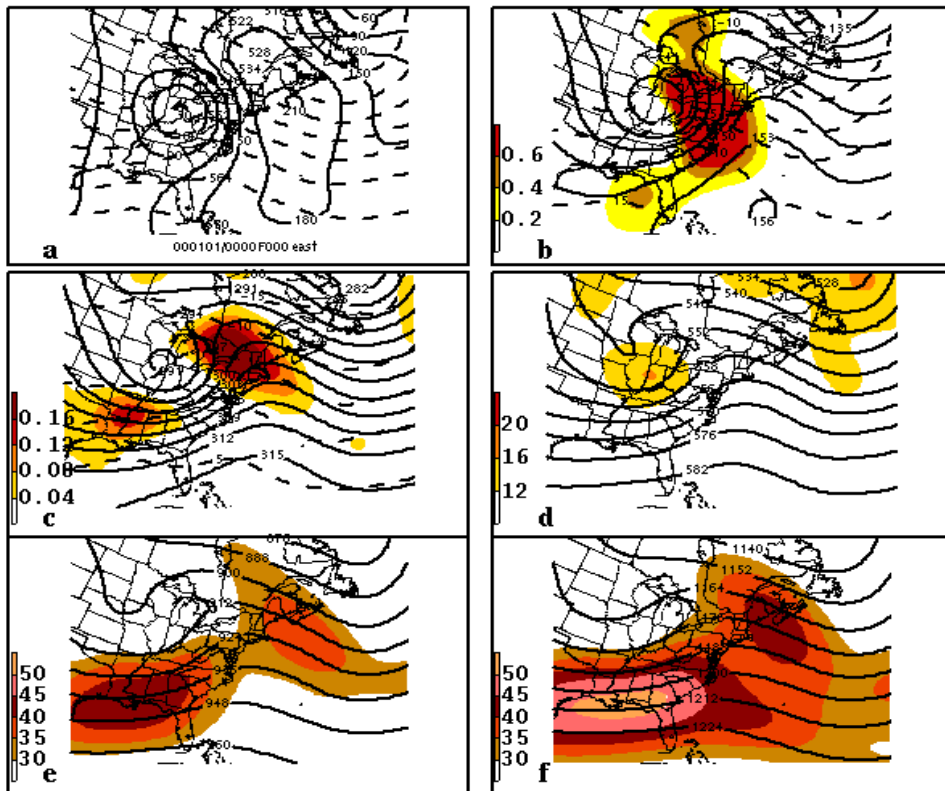


Fig. 3.20. As in Fig. 3.19, except at $T = 0$ h.

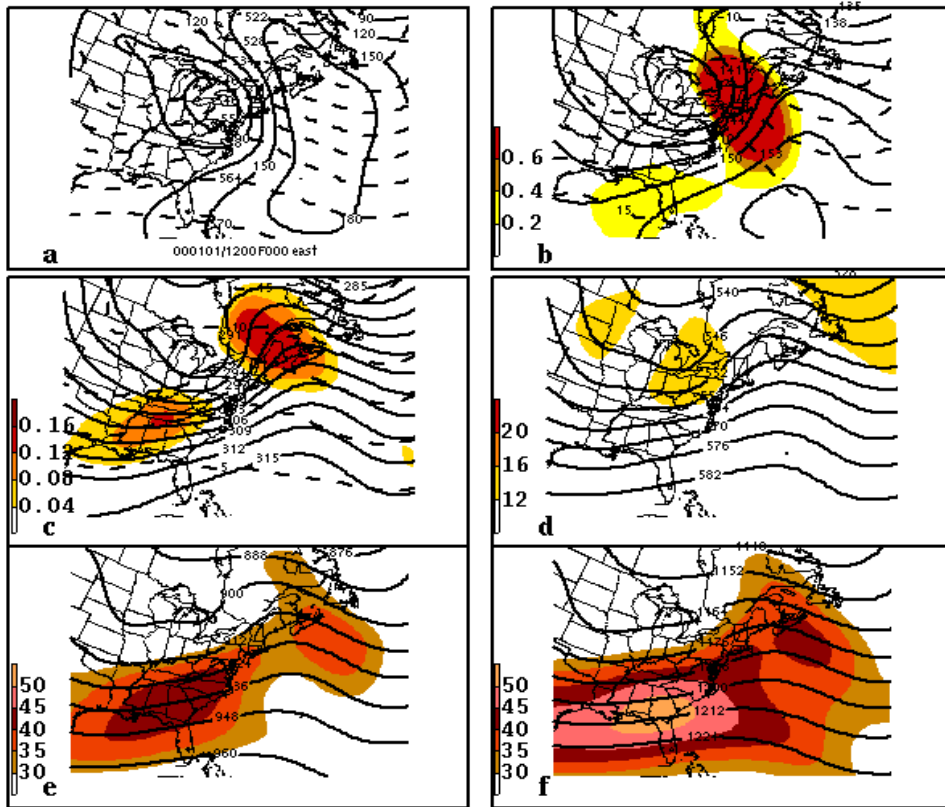


Fig. 3.21. As in Fig. 3.19, except at $T = 12$ h.

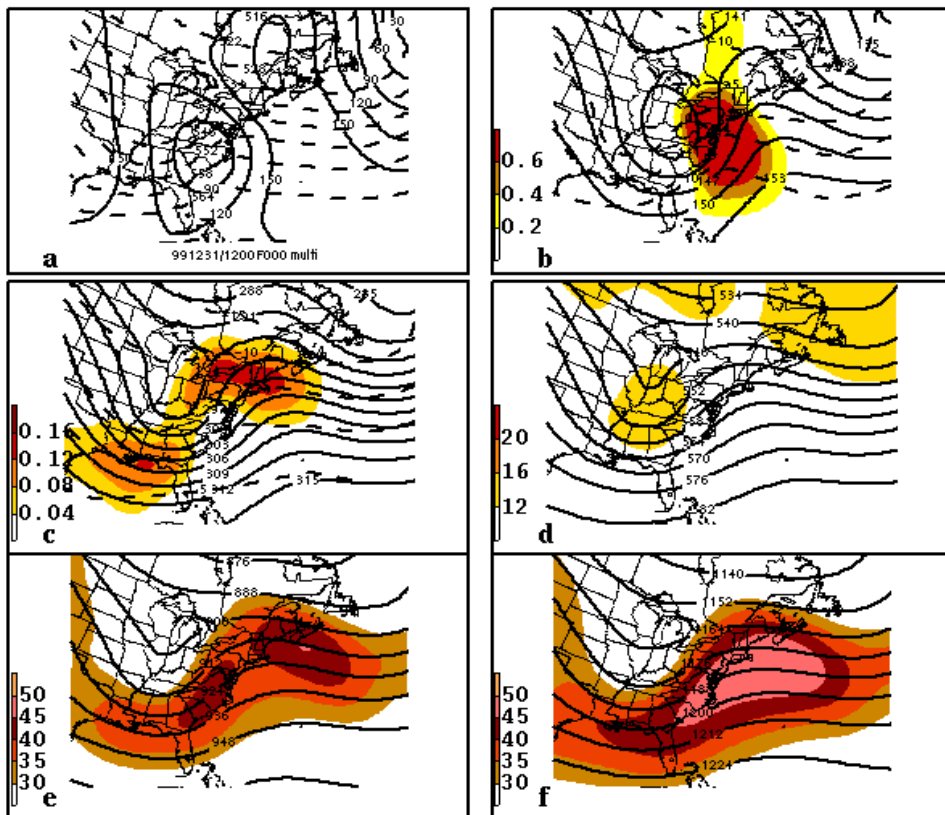


Fig. 3.22. As in Fig. 3.10, except for multibanded class.

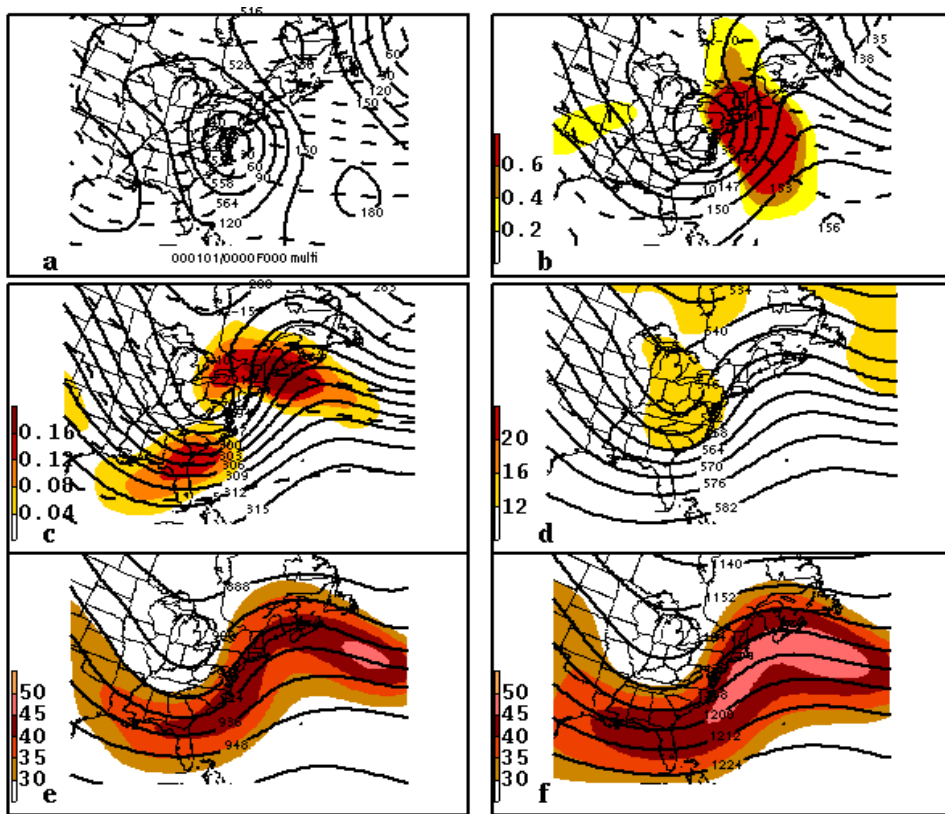


Fig. 3.23. As in Fig. 3.22, except at T = 0 h

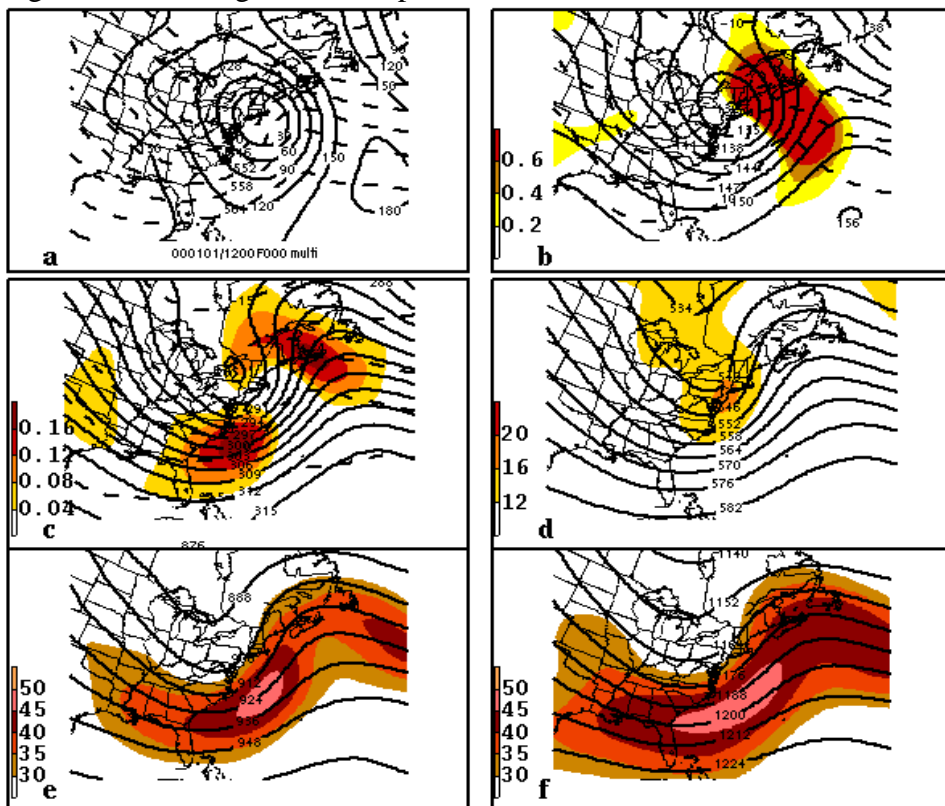


Fig. 3.24. As in Fig. 3.22, except at T = 12 h.

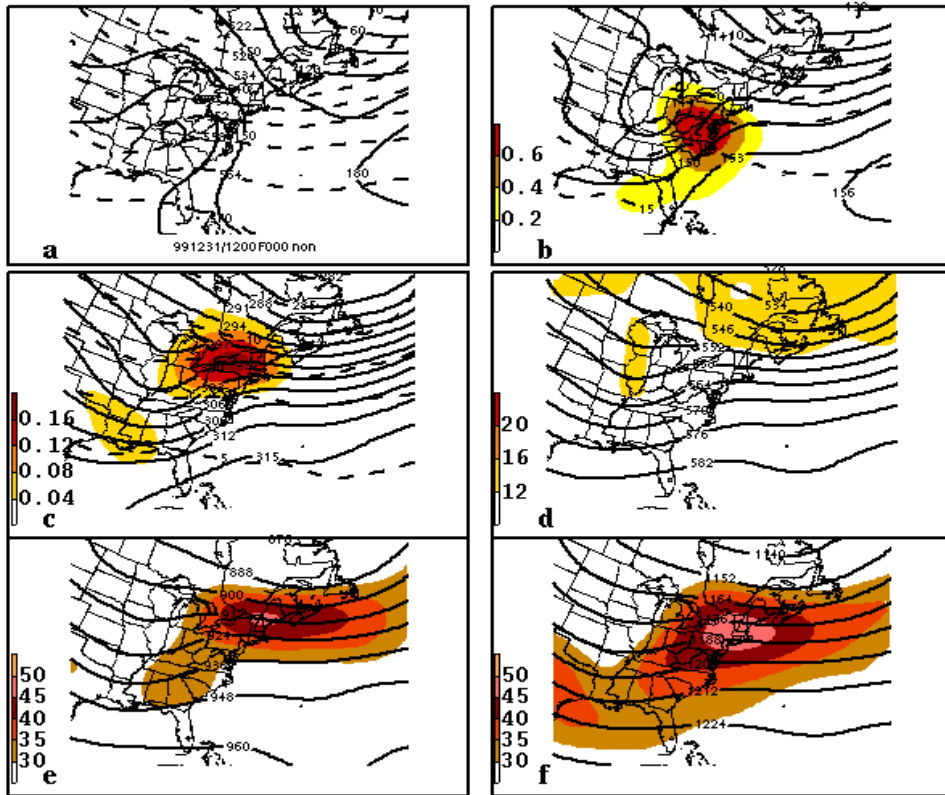


Fig. 3.25. As in Fig. 3.10, except for nonbanded class.

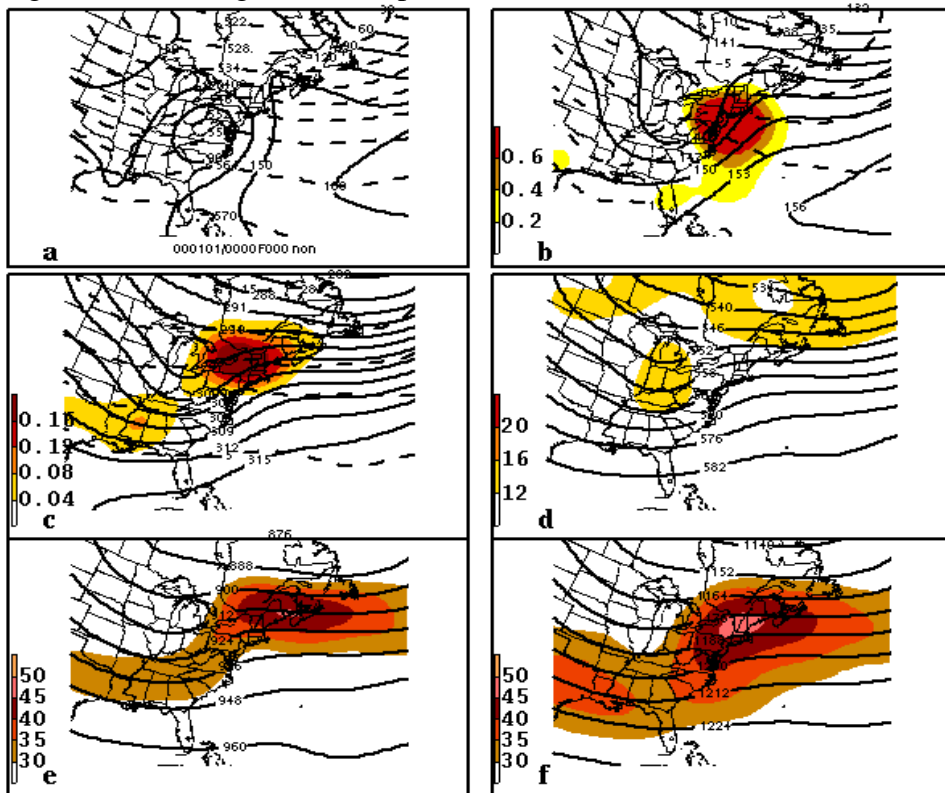


Fig. 3.26. As in Fig. 3.25, except at $T = 0$ h.

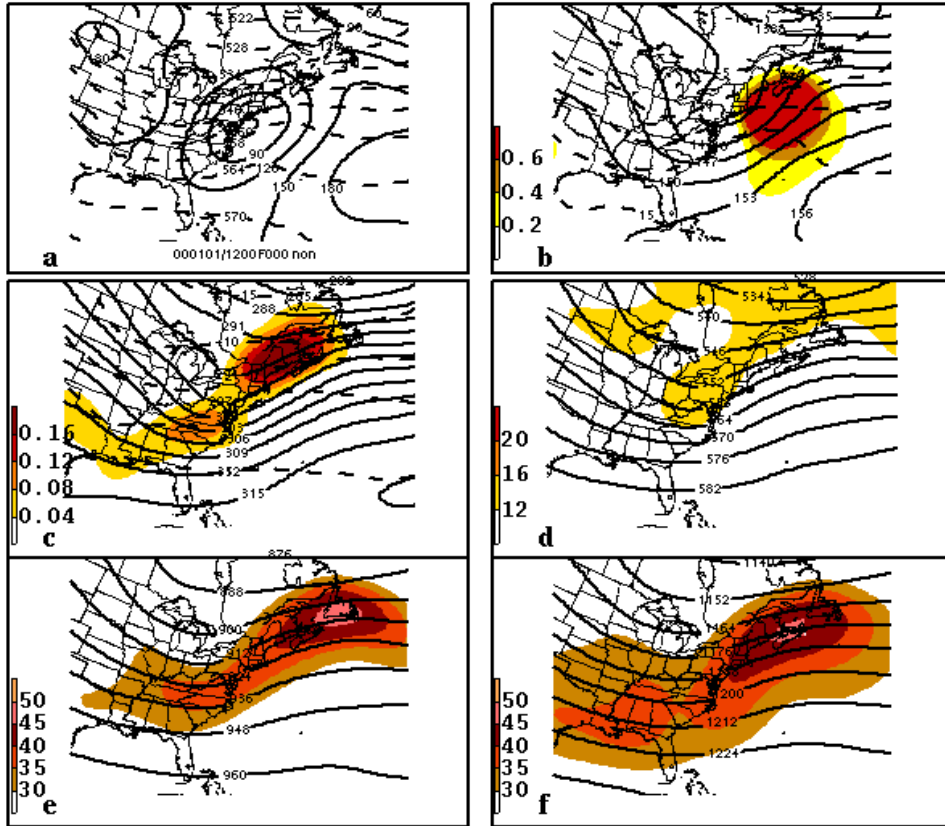


Fig. 3.27. As in Fig. 3.25, except at T =12 h.

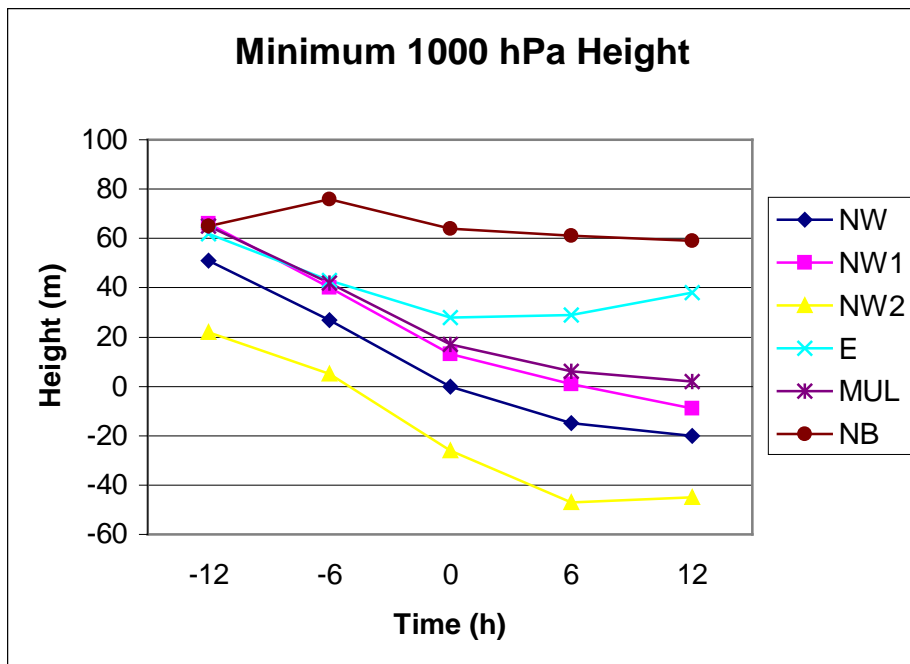


Fig. 3.28. Time series of the evolution of the minimum 1000 hPa height for each composite class (NW = northwest, NW1 = northwest-near, NW2 = northwest-far, E = east, MUL = multi, NB = nonbanded) from 12 h before to 12 h after band initiation.

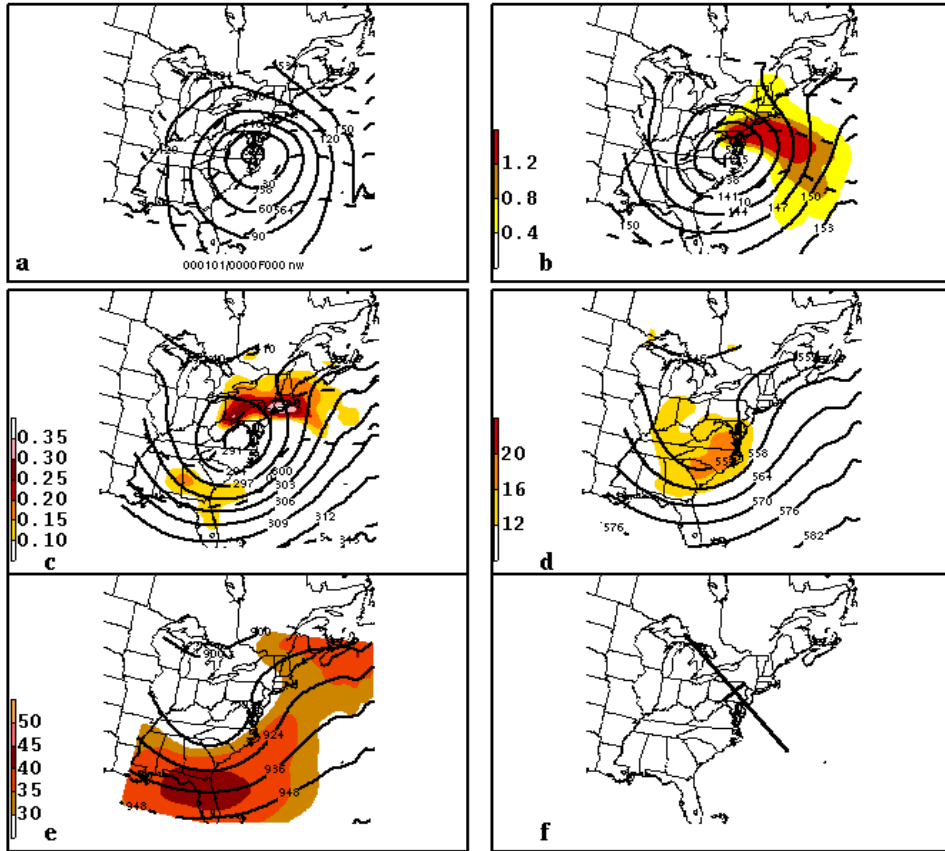


Fig. 3.29. Synoptic summary of the northwest class model composite at the initial analysis time. Fields as in Fig. 3.10, except shading values have changed in (b) and (c), and (f) shows the mean band position and cross section orientation.

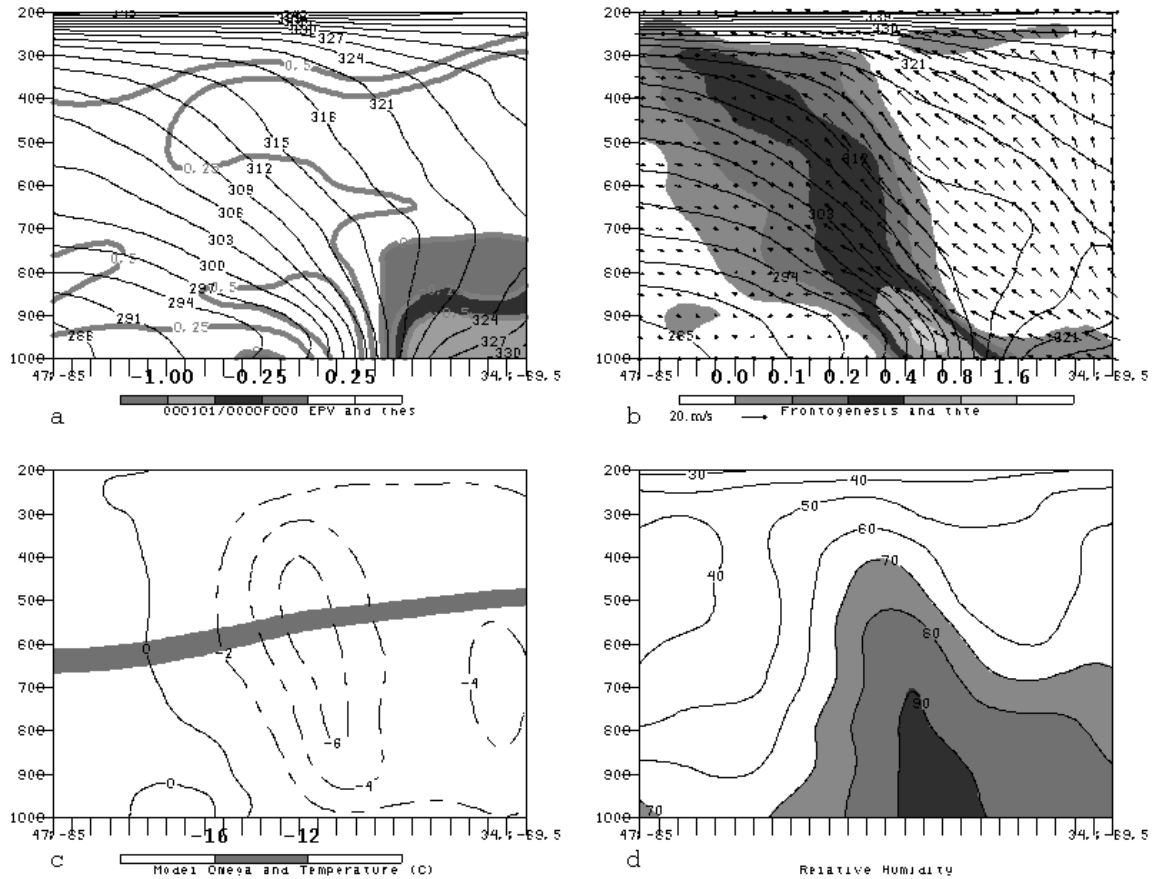


Fig. 3.30. Cross section through the composite band position in the northwest class (cross-section orientation shown in Fig. 3.29f). (a) Geostrophic saturated equivalent potential vorticity [contoured every 0.25 PVU ($1 \text{ PVU} = 10^{-6} \text{ m}^2 \text{ K s}^{-1} \text{ kg}^{-1}$)] as labeled, negative regions shaded according to scale, and equivalent potential temperature contoured every 3 K. (b) Frontogenesis [positive areas shaded according to scale in $^{\circ}\text{C} (100 \text{ km})^{-1} (3 \text{ h})^{-1}$], equivalent potential temperature (contoured every 3 K), and tangential full wind and vertical velocity (ω) (black arrows, reference vector shown near title). (c) Model ω contoured every $2 \times 10^{-3} \text{ hPa s}^{-1}$ (dashed where negative), and the -12 to $-16 \text{ }^{\circ}\text{C}$ layer (shaded). (d) Relative humidity contoured every 10%, and shaded $> 70\%$.

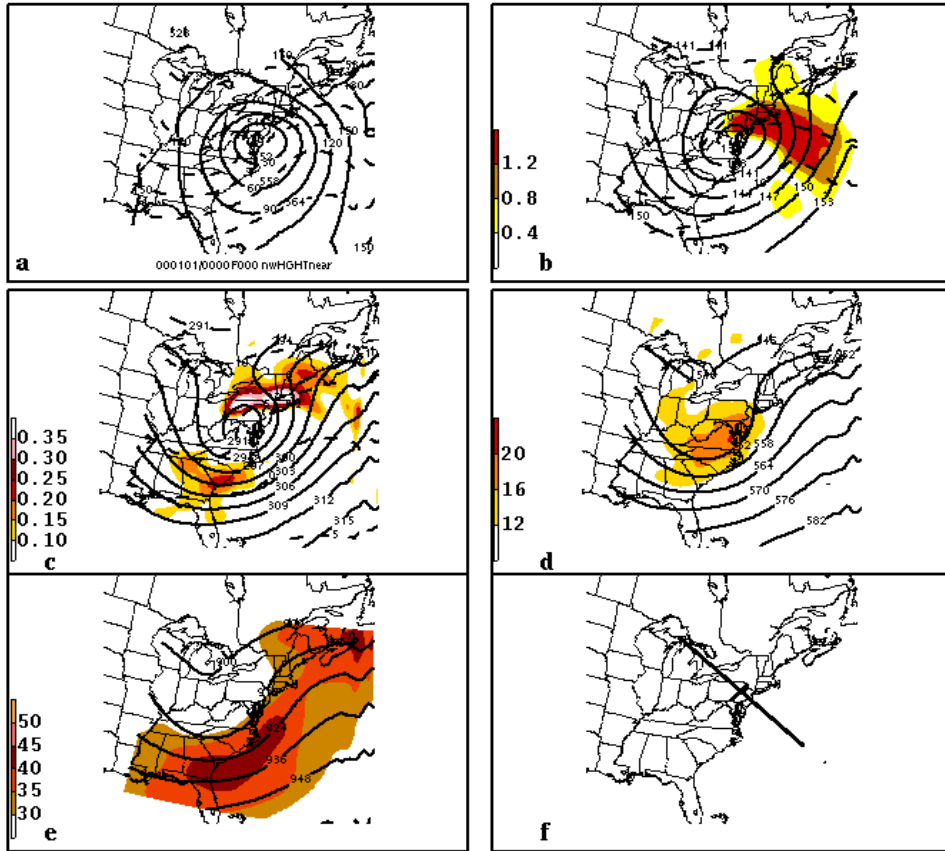


Fig. 3.31. As in Fig. 3.29, except for northwest-near class.

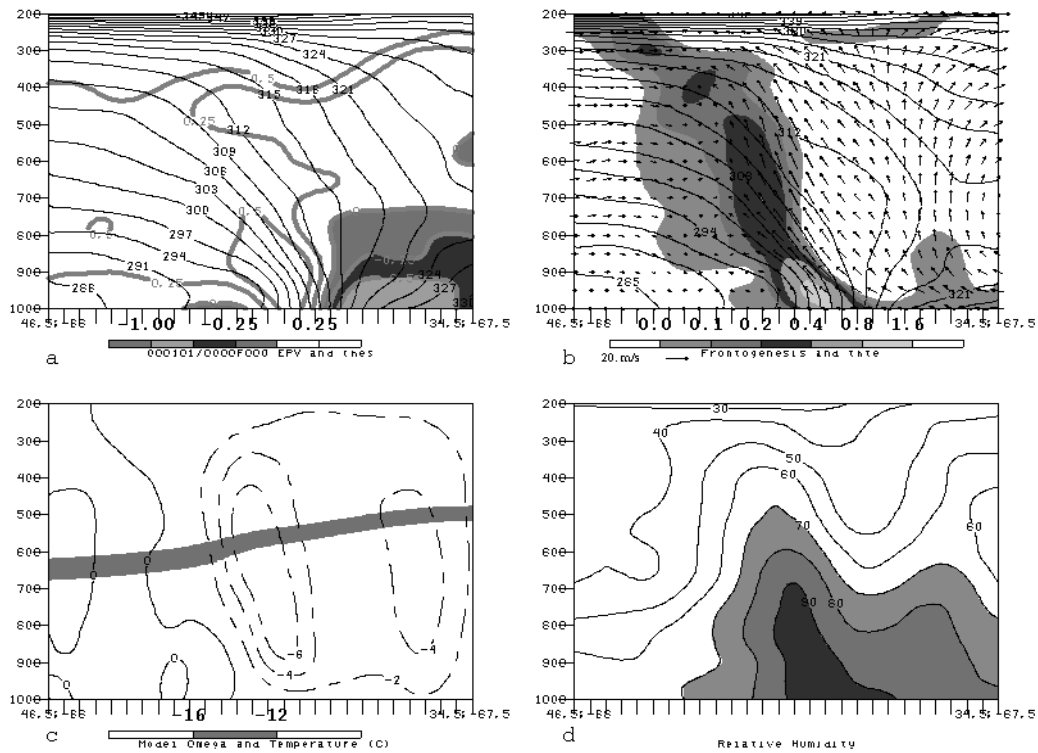


Fig. 3.32. As in Fig. 3.30, except for northwest-near class.

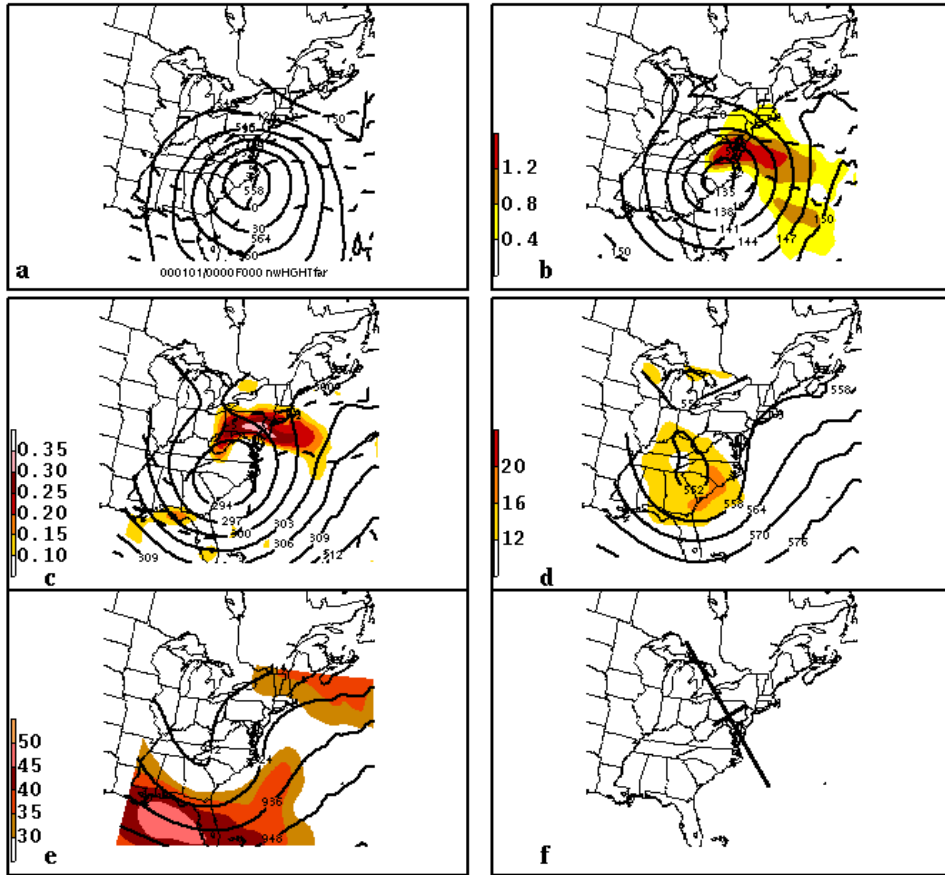


Fig. 3.33. As in Fig. 3.29, except for northwest-far class.

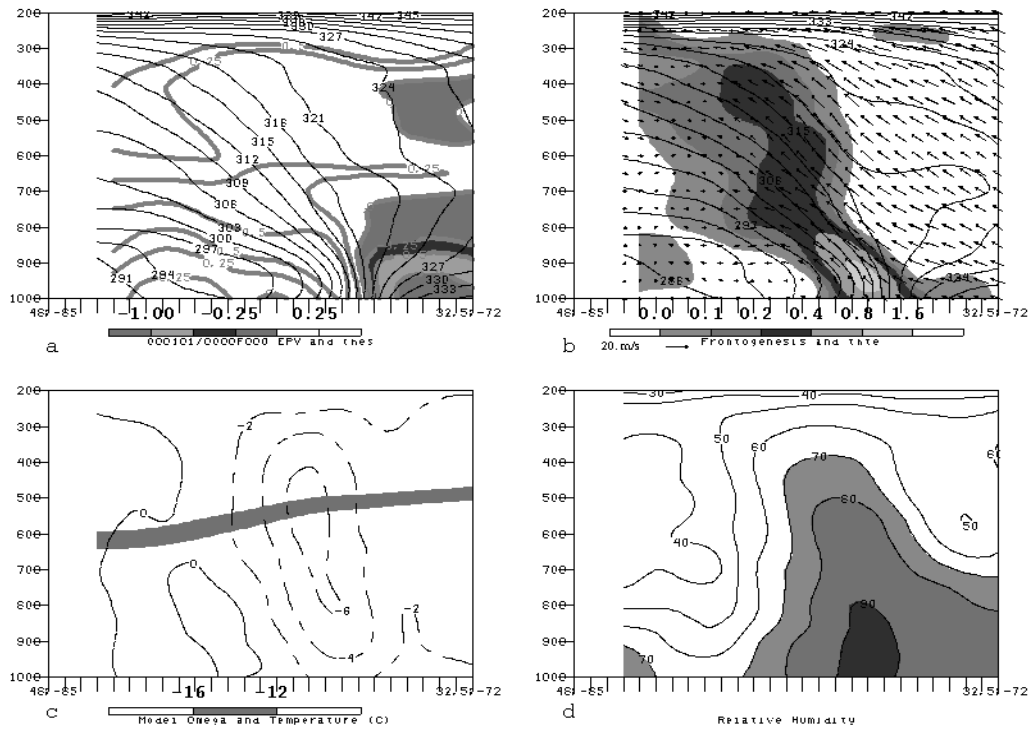


Fig. 3.34. As in Fig. 3.30, except for northwest-far class.

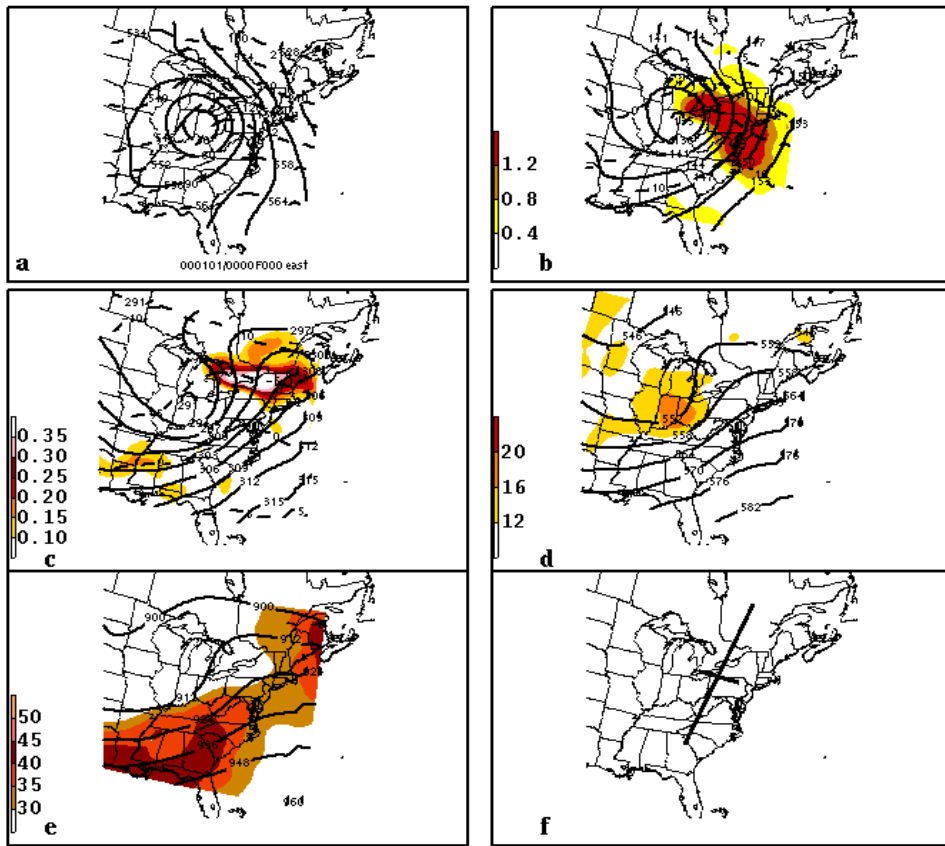


Fig. 3.35. As in Fig. 3.29, except for east class

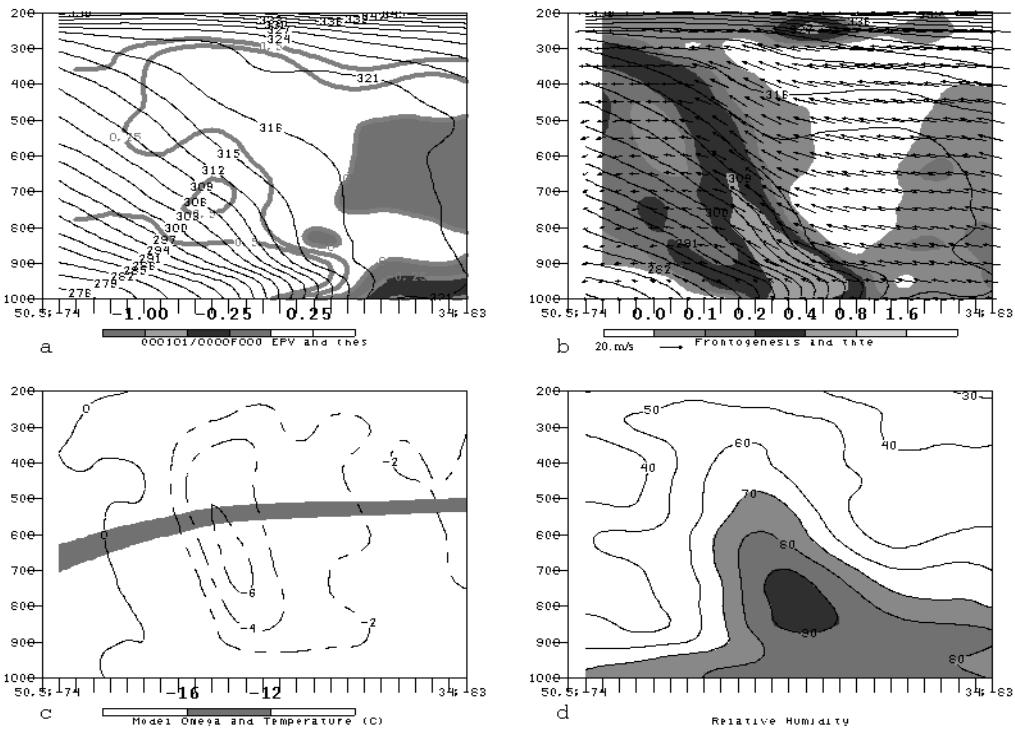


Fig. 3.36. As in Fig. 3.30, except for east class.

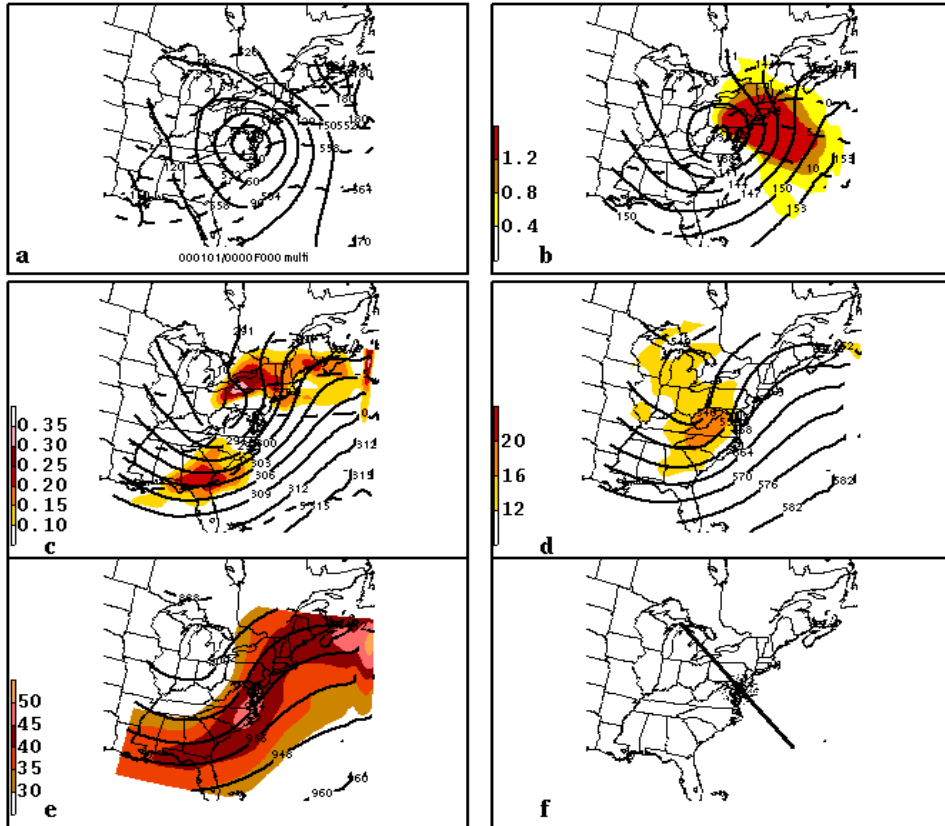


Fig. 3.37. As in Fig. 3.29, except for multiband class with mean multibanding represented by stippling.

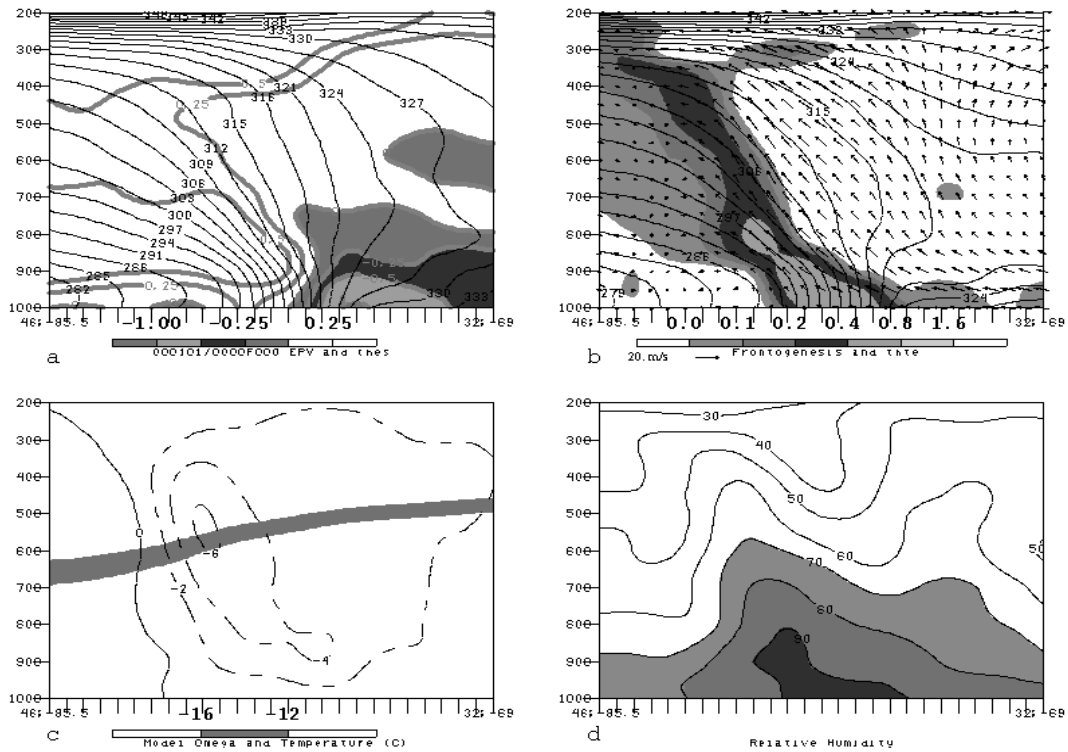


Fig. 3.38. As in Fig. 3.30, except for multiband class

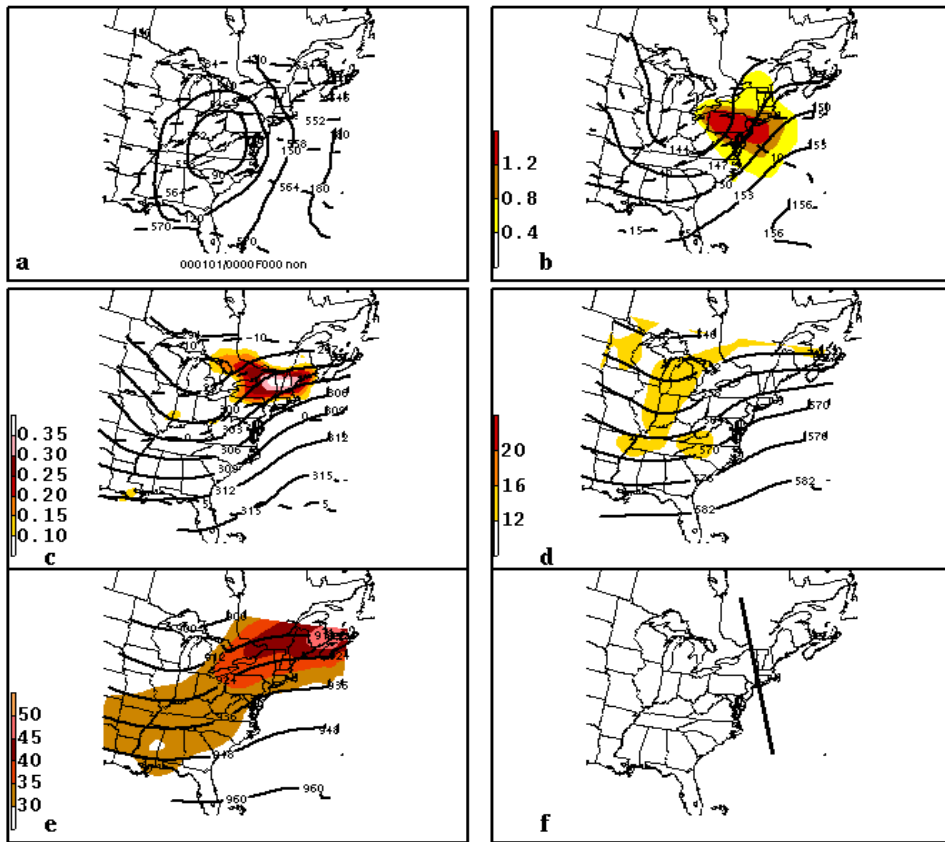


Fig. 3.39. As in Fig. 3.29, except for nonbanded class

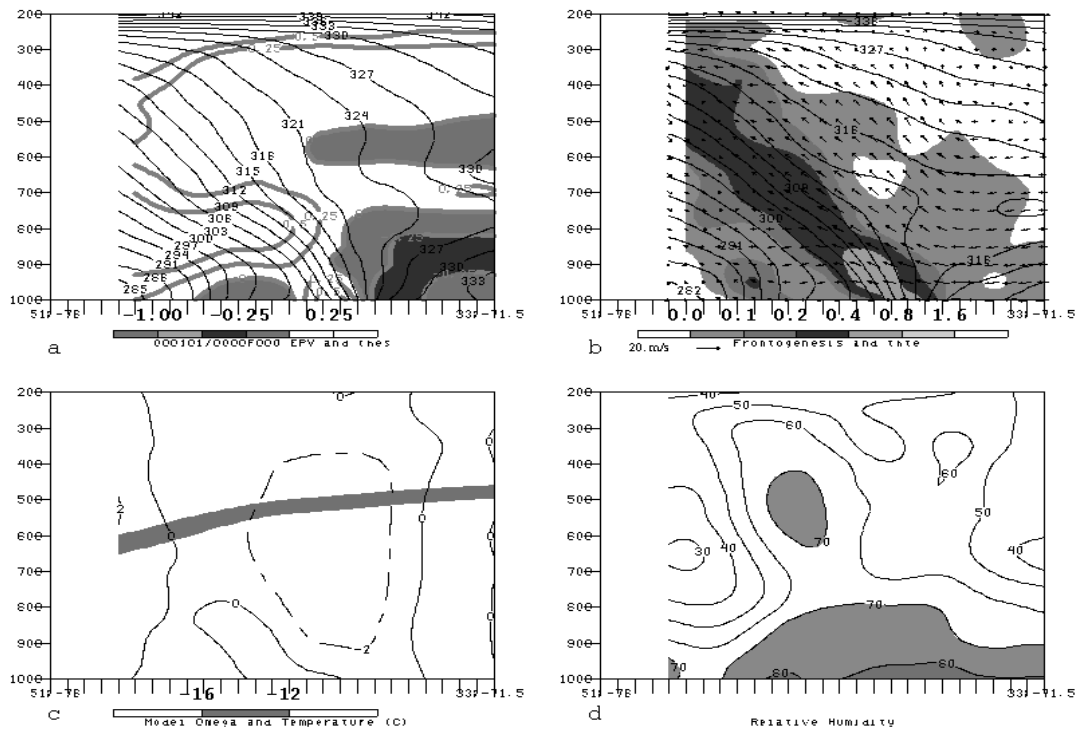


Fig. 3.40. As in Fig. 3.30, except for nonbanded class.

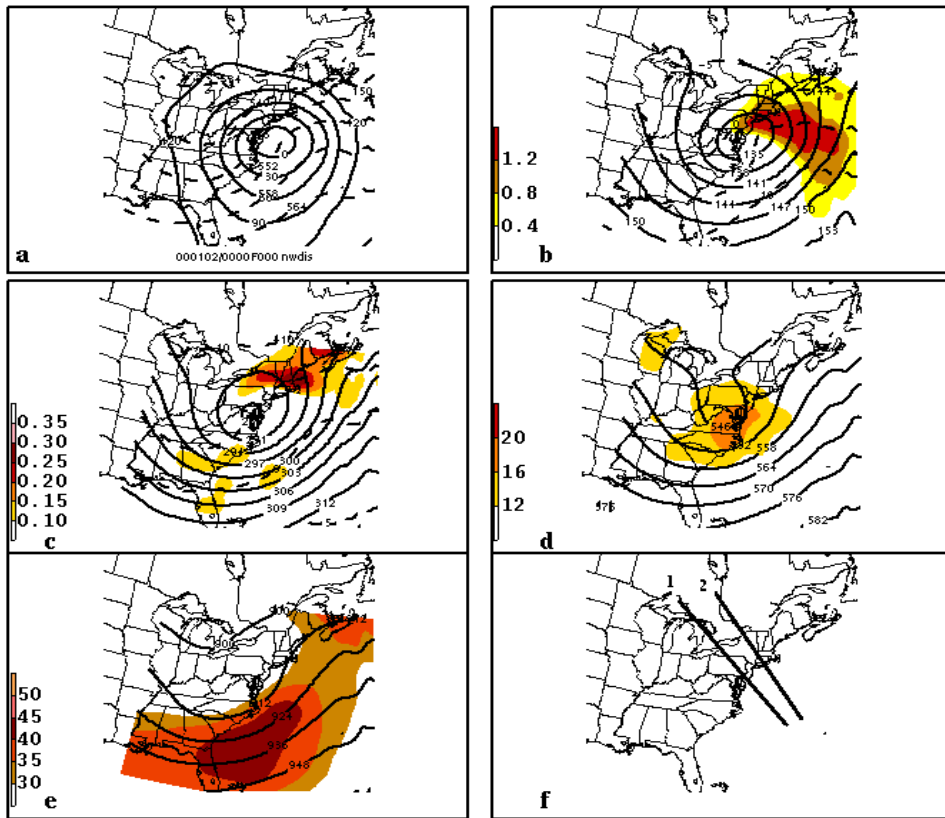


Fig. 3.41. As in Fig. 3.29, except at band dissipation.

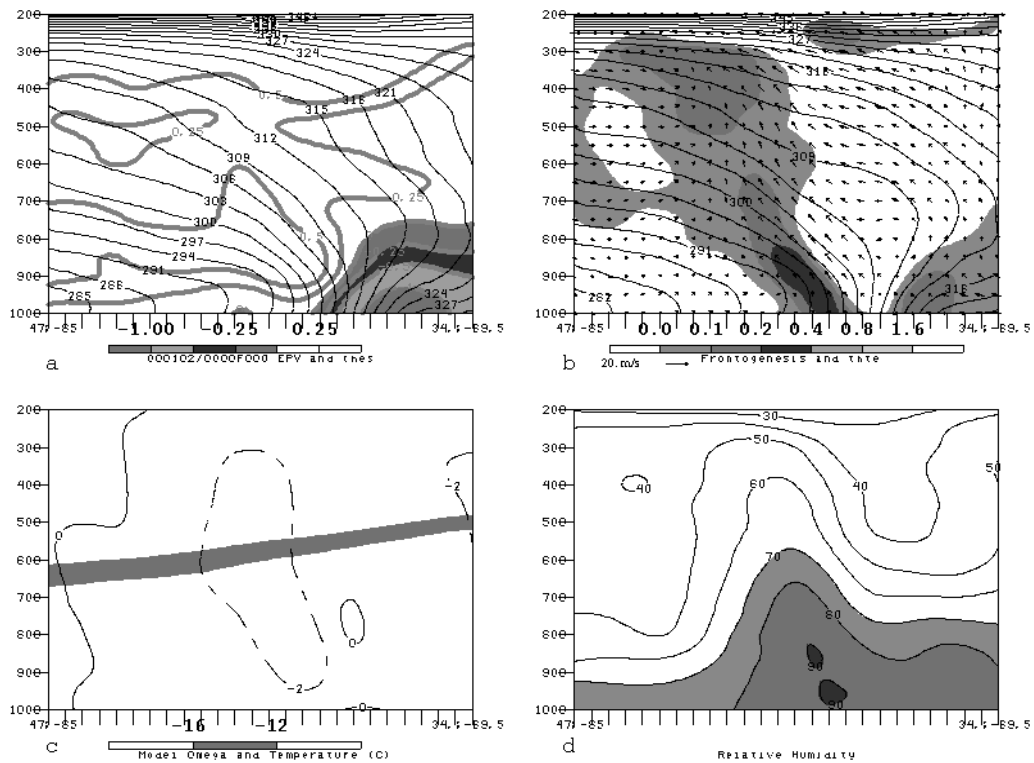


Fig. 3.42. As in Fig. 3.29, except for northwest band dissipation along cross section 1.

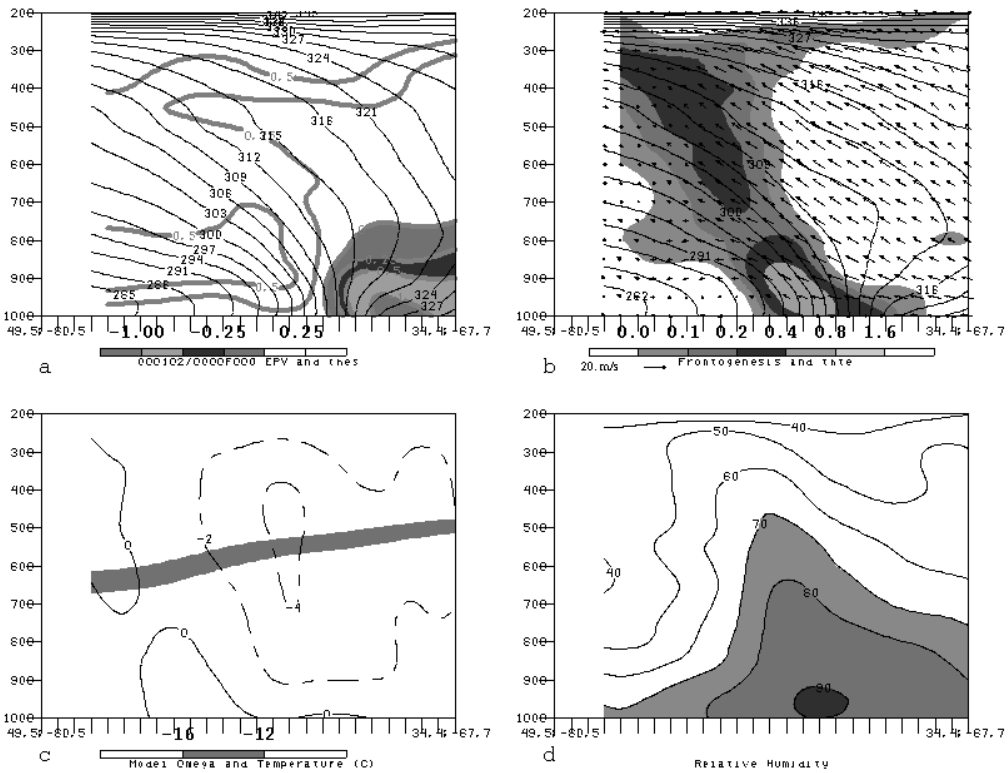


Fig. 3.43. As in Fig. 3.42, except along cross section 2.

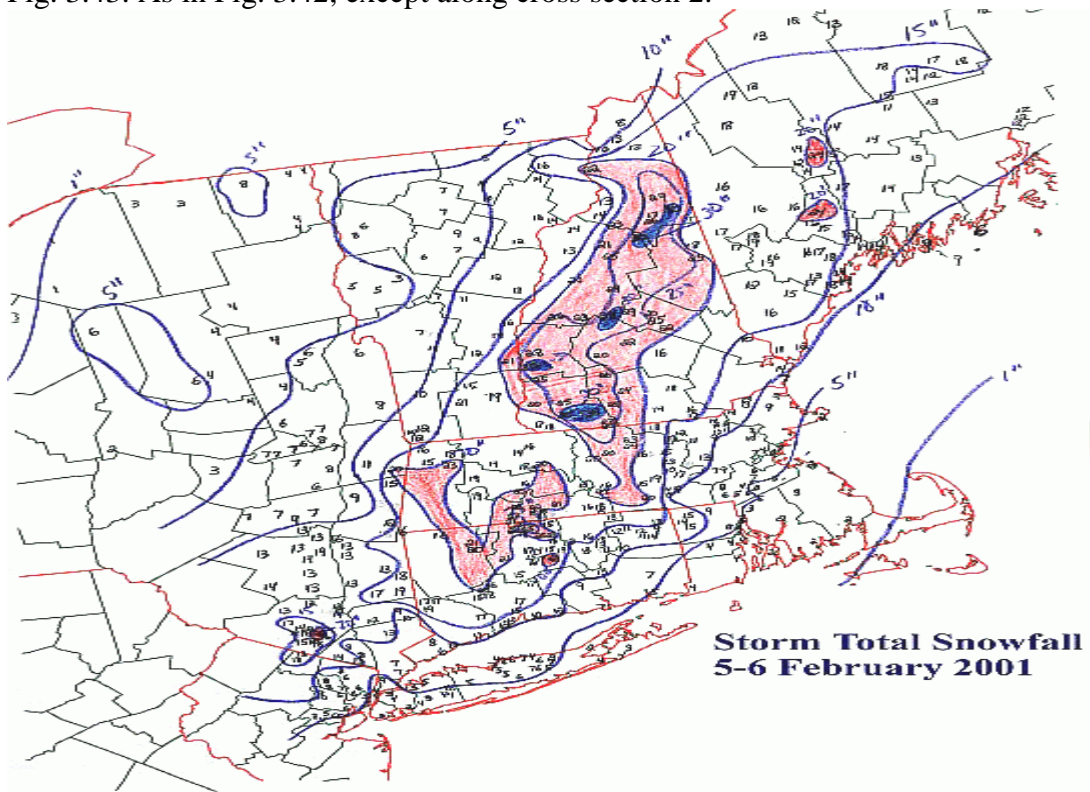


Fig. 3.44. Observed total snowfall (in) from the 5–6 February 2001 snowstorm with overlaid hand analysis.

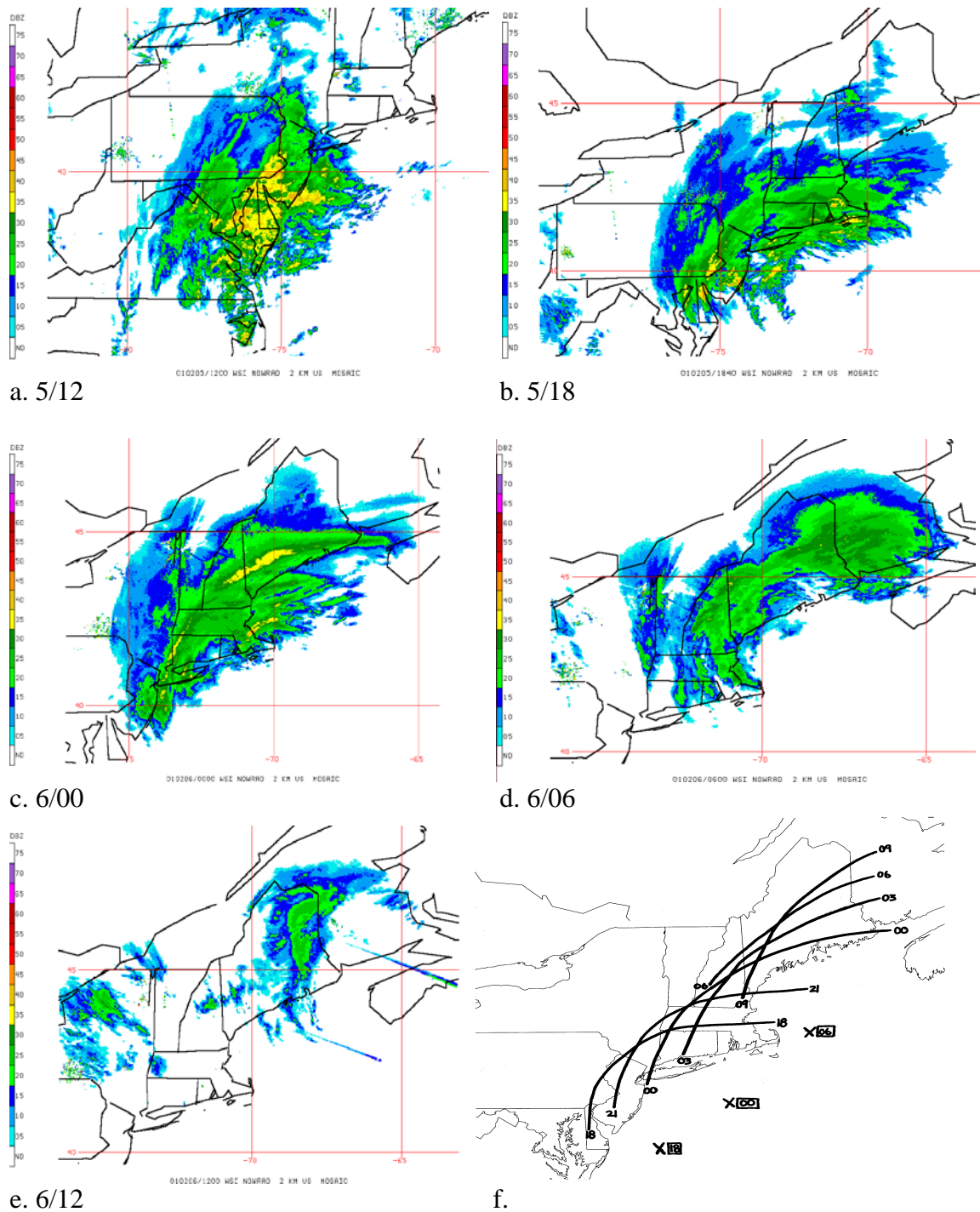


Fig. 3.45. WSR-88D radar composite images for the 5–6 February 2001 snowstorm at (a) 5/12, (b) 5/18, (c) 6/00, (d) 6/06, (e) 6/12, with the band axis evolution depicted in (f) by solid line, and surface low position marked by an “x” at respective times from 5/18 to 6/06. Note the development of the intense band by 6/00 (c), and that it pivots as it translates with the system.

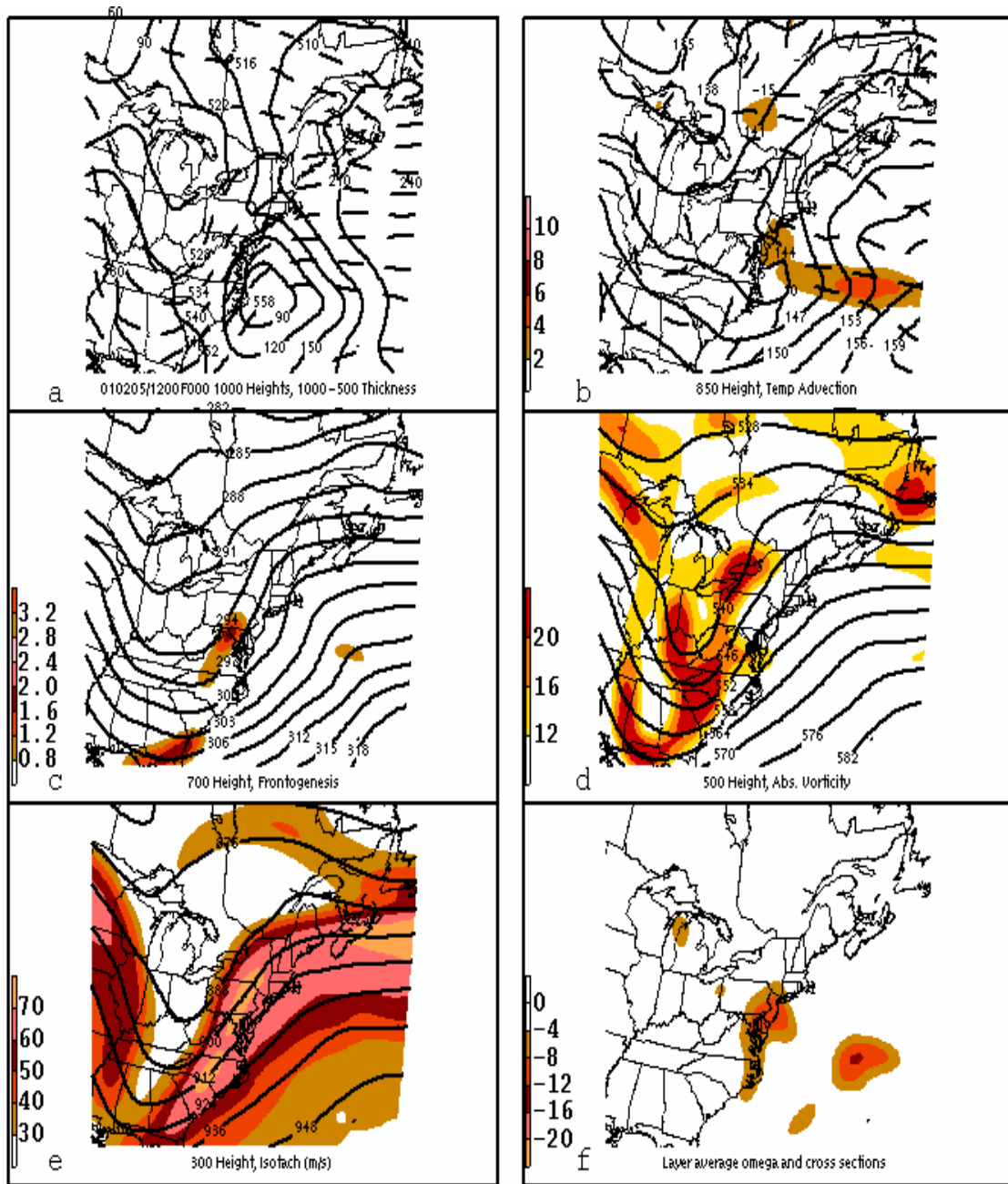


Fig. 3.46. Six-panel synoptic summary for the 5–6 February 2001 snowstorm at 5/12. (a) 1000 hPa heights (black solid) contoured every 30 m (~ 4 hPa) and 1000–500 hPa thickness (black dashed) contoured every 6 dam. (b) 850 hPa heights (black solid) contoured every 3 dam, temperature (black dashed) contoured every 5°C , and temperature advection, shaded according to scale in $^{\circ}\text{C day}^{-1}$. (c) 700 hPa heights (black solid) contoured every 3 dam, and Miller 2-D frontogenesis (shaded) in $^{\circ}\text{C (100 km)}^{-1}$ (3 h^{-1}). (d) 500 hPa heights (black solid) contoured every 6 dam, and absolute vorticity, shaded according to scale above $12 \times 10^{-5} \text{ s}^{-1}$. (e) 300 hPa height (black solid) contoured every 12 dam, and windspeeds contoured every 5 m s^{-1} , shaded above 30 m s^{-1} . (f) 800–600 hPa layer-averaged ω , shaded every $-4 \times 10^{-3} \text{ hPa s}^{-1}$.

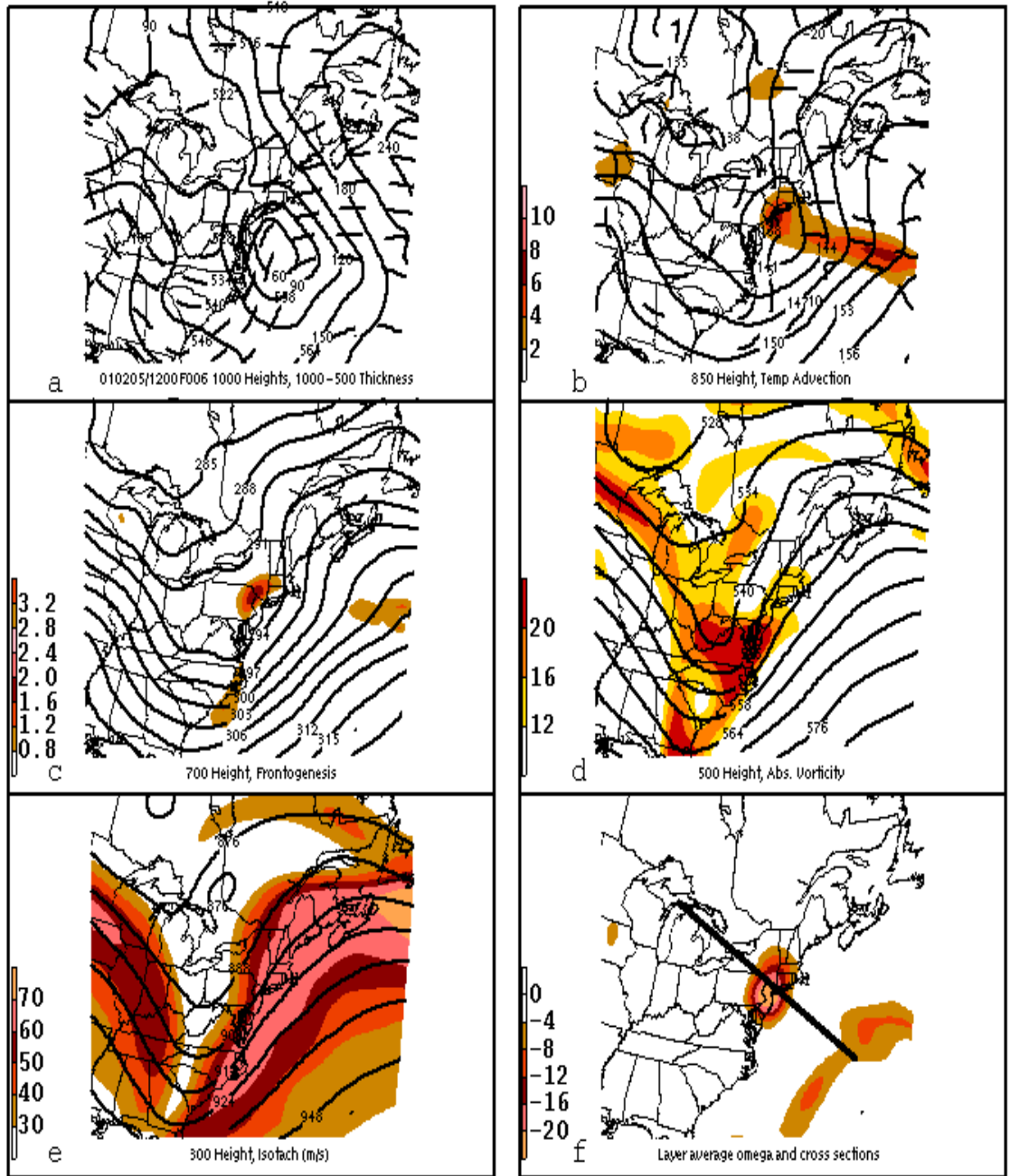


Fig. 3.47 As in Fig. 3.46, except at 5/18, and (f) shows cross-section orientation.

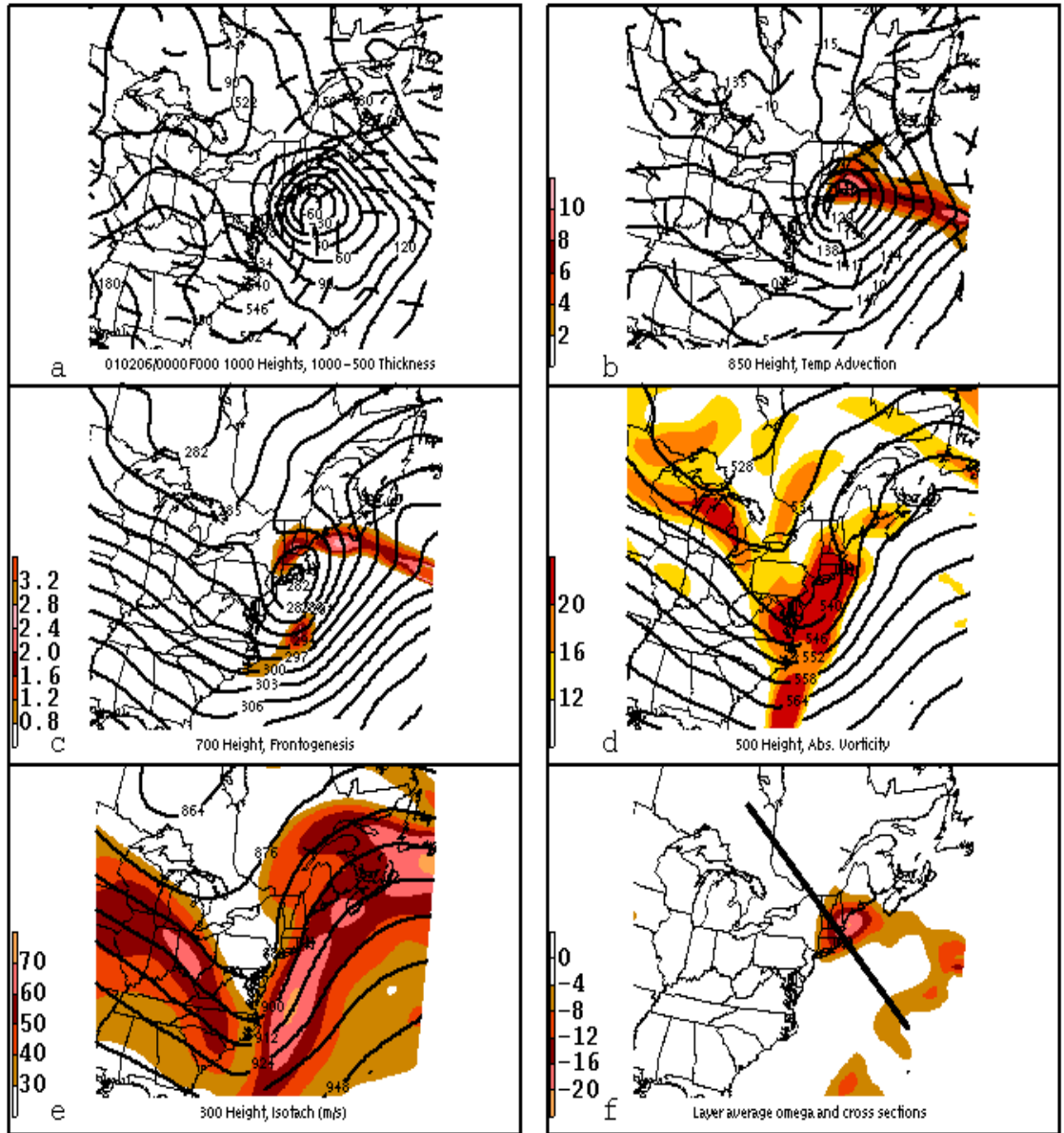


Fig. 3.48. As in Fig. 3.47, except at 6/00.

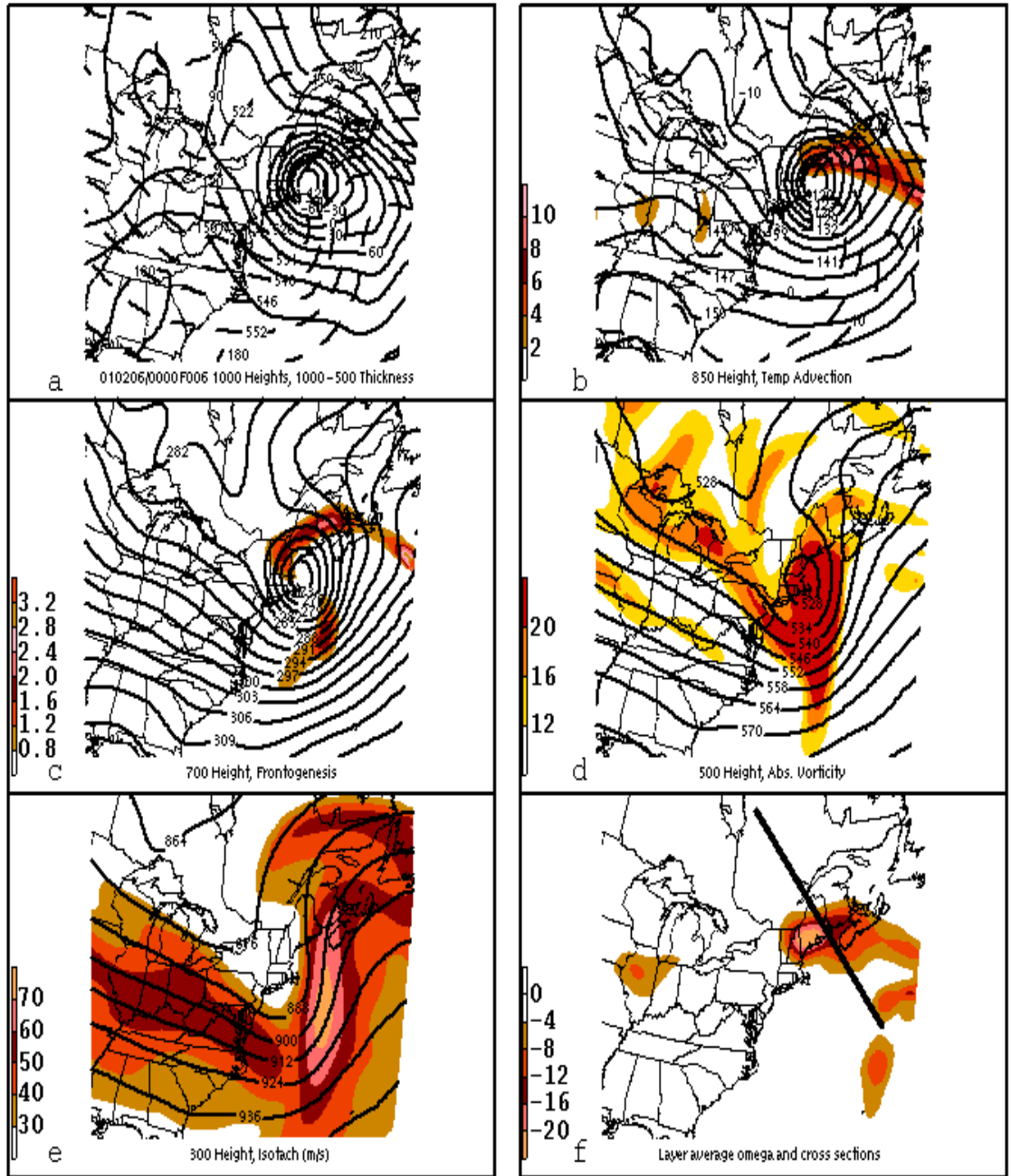


Fig. 3.49. As in Fig. 3.47, except at 6/06

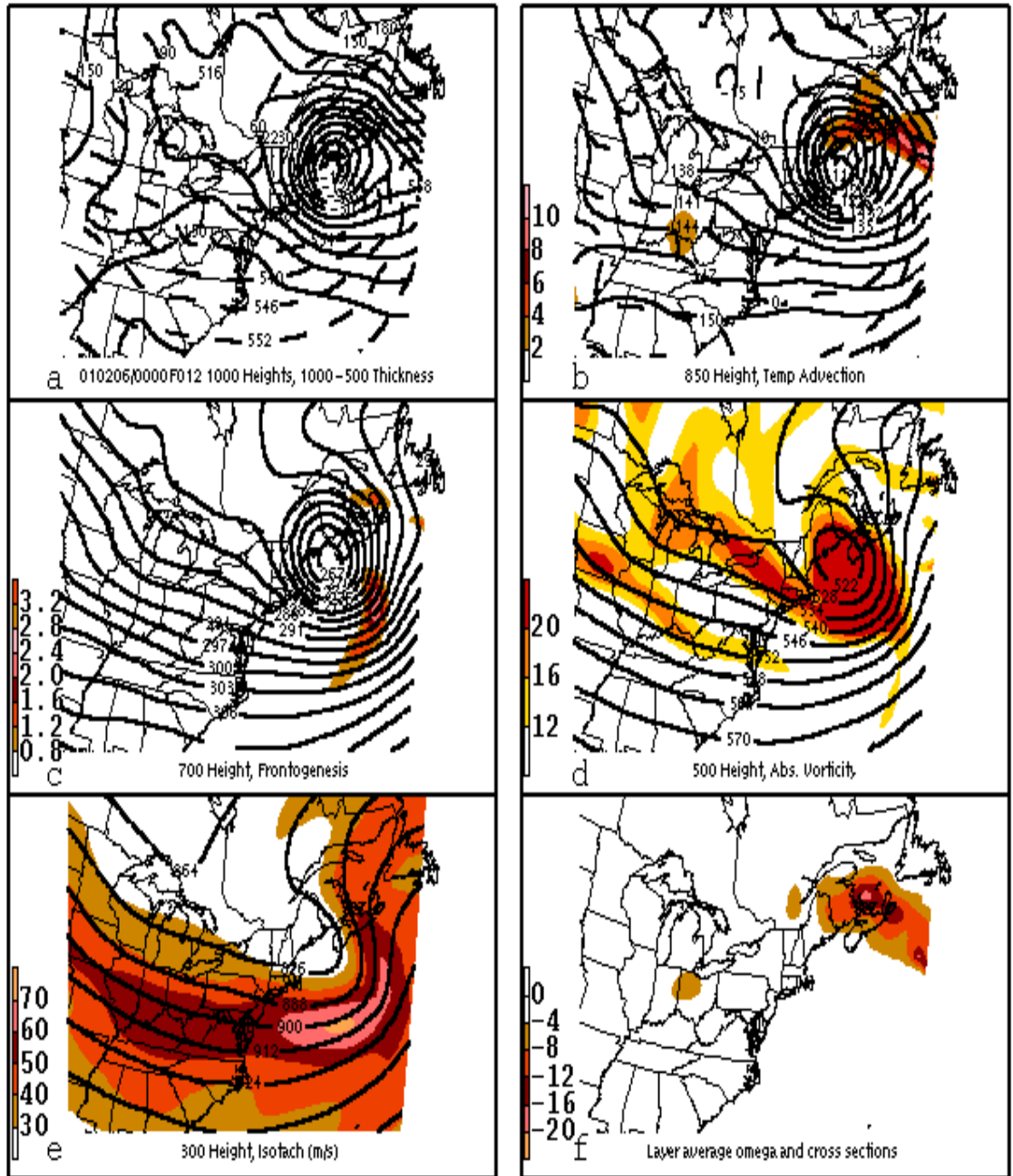


Fig. 3.50. As in Fig. 3.47, except at 6/12 and without cross section in (f).

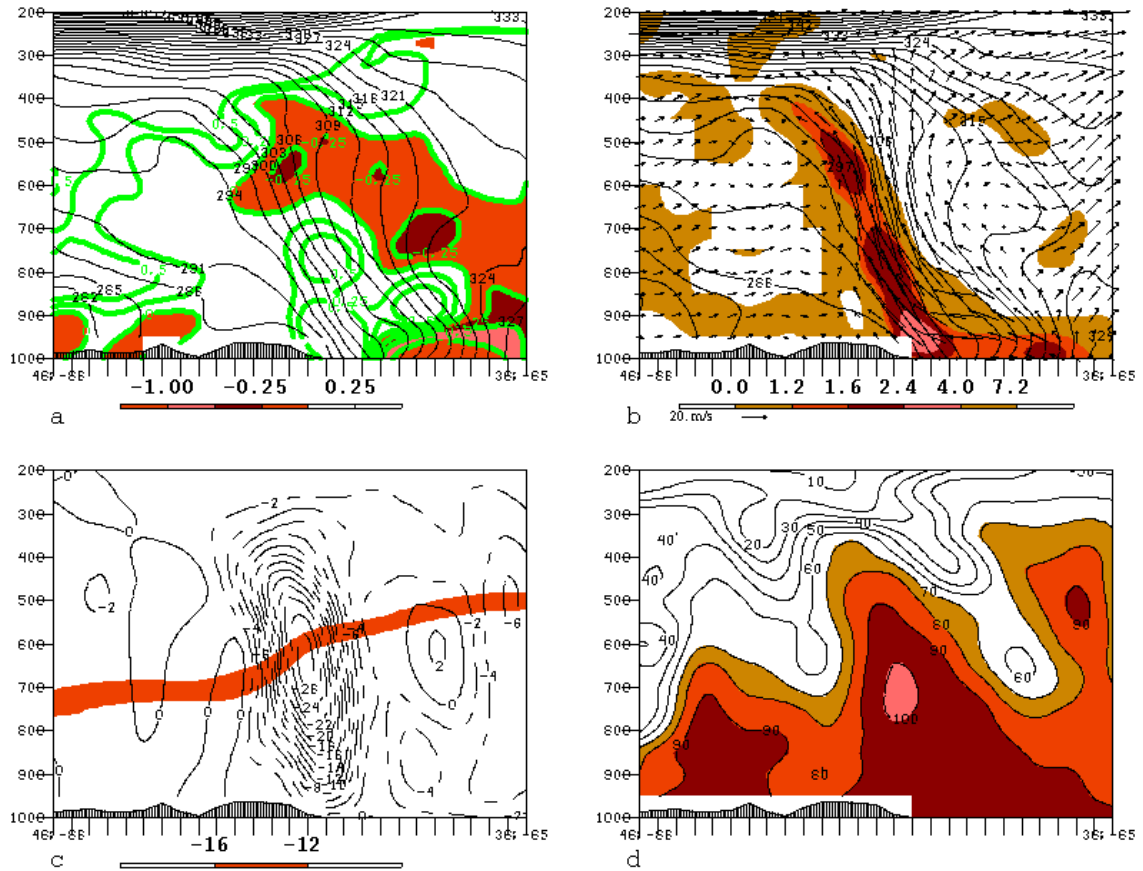


Fig. 3.51. Cross section through band at 5/18 (cross-section orientation shown in Fig. 3.47f). (a) Geostrophic saturated equivalent potential vorticity [contoured every 0.25 PVU ($1 \text{ PVU} = 10^{-6} \text{ m}^2 \text{ K s}^{-1} \text{ kg}^{-1}$) as labeled, negative regions shaded according to scale], and equivalent potential temperature contoured every 3 K. (b) Frontogenesis [positive areas shaded according to scale in $^{\circ}\text{C} (100 \text{ km})^{-1} (3 \text{ h})^{-1}$], equivalent potential temperature (contoured every 3 K), and tangential full wind and vertical velocity (black arrows, reference vector shown near title). (c) Model vertical velocity contoured every $2 \times 10^{-3} \text{ hPa s}^{-1}$ (dashed where negative), and the -12 to $-16 \text{ }^{\circ}\text{C}$ layer (shaded). (d) Relative humidity contoured every 10%, and shaded $> 70\%$.

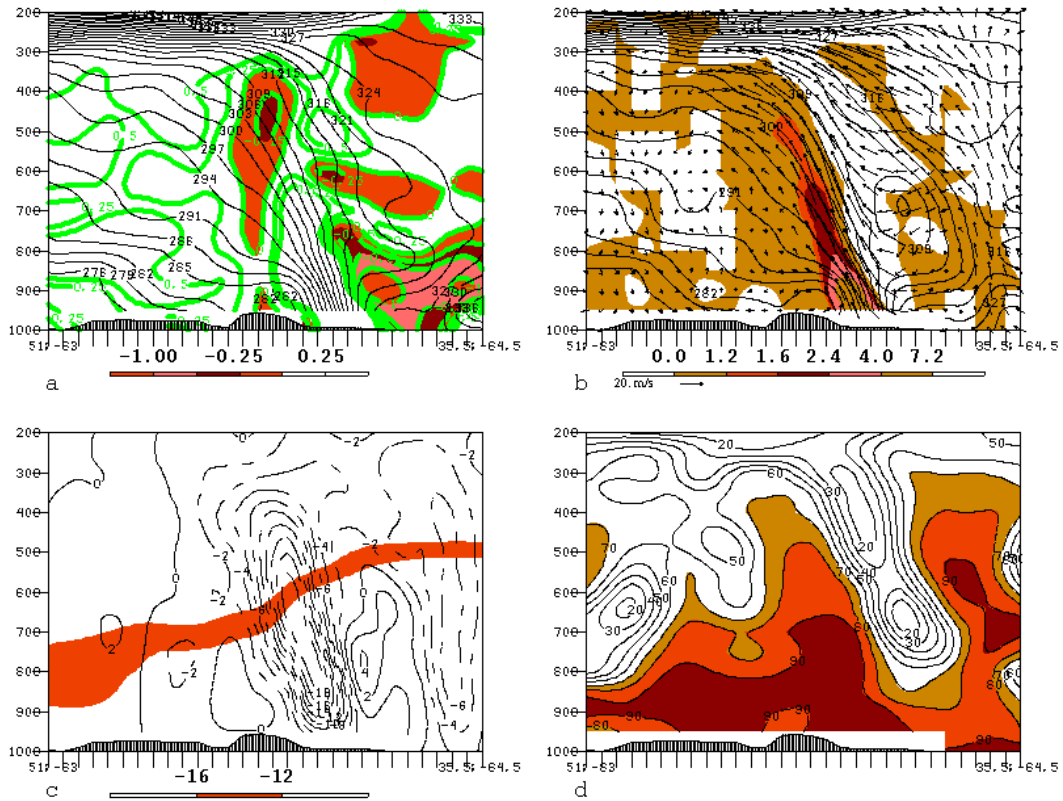


Fig. 3.52. As in Fig. 3.51, except at 6/00 (cross-section orientation shown in Fig. 3.48f).

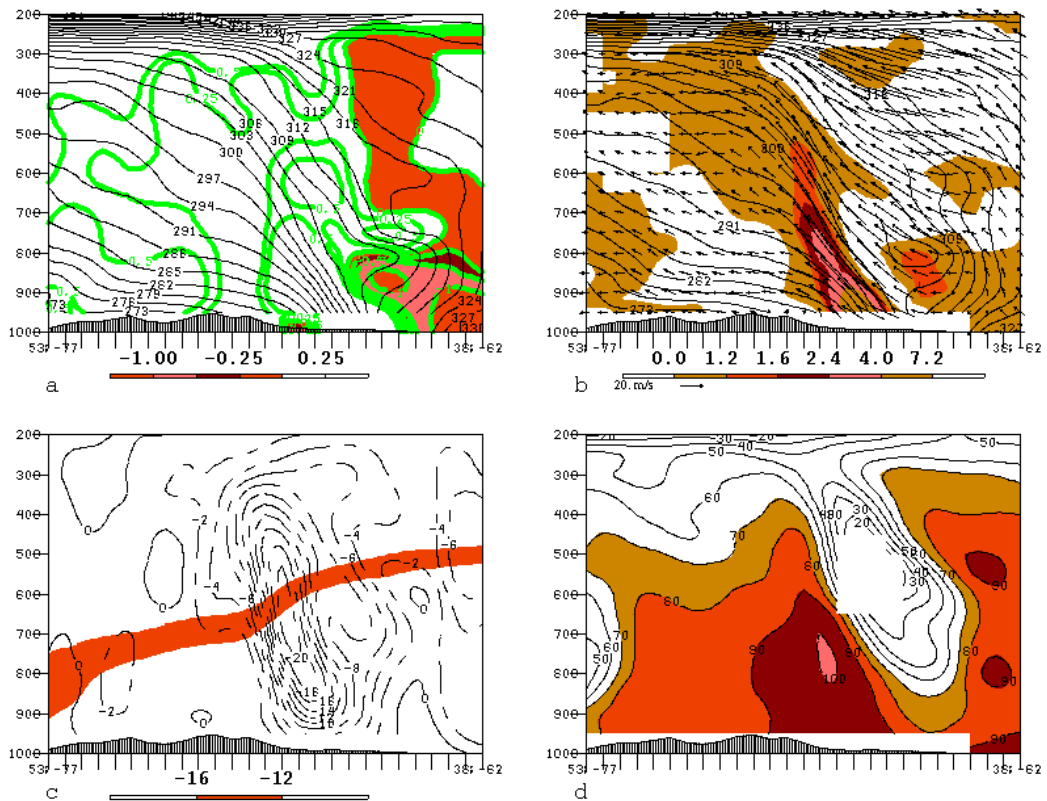


Fig. 3.53. As in Fig. 3.51, except for 6/06 (cross-section orientation shown in Fig. 3.49f).

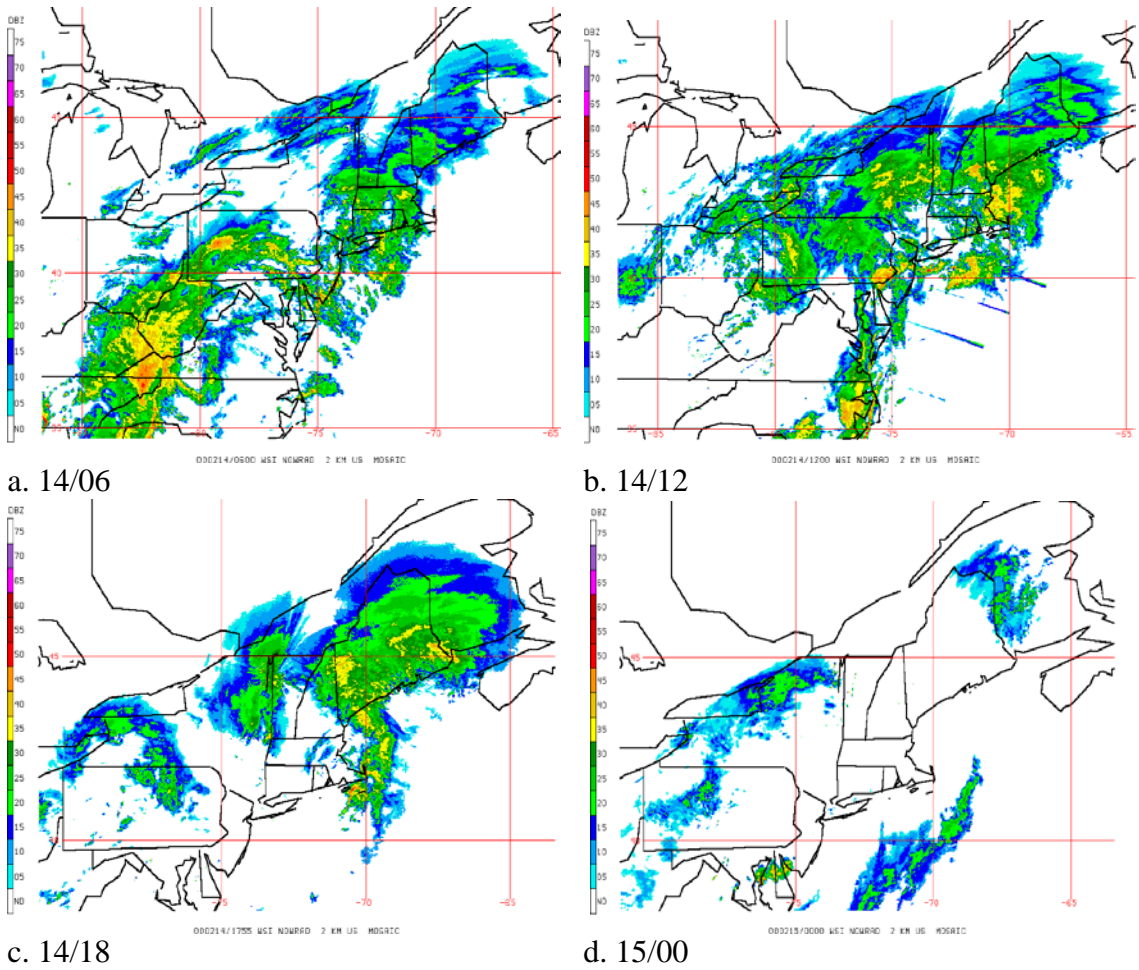


Fig. 3.54. WSR-88D composite radar images for (a) 1406, (b) 1412, (c) 1418, and (d) 1500.

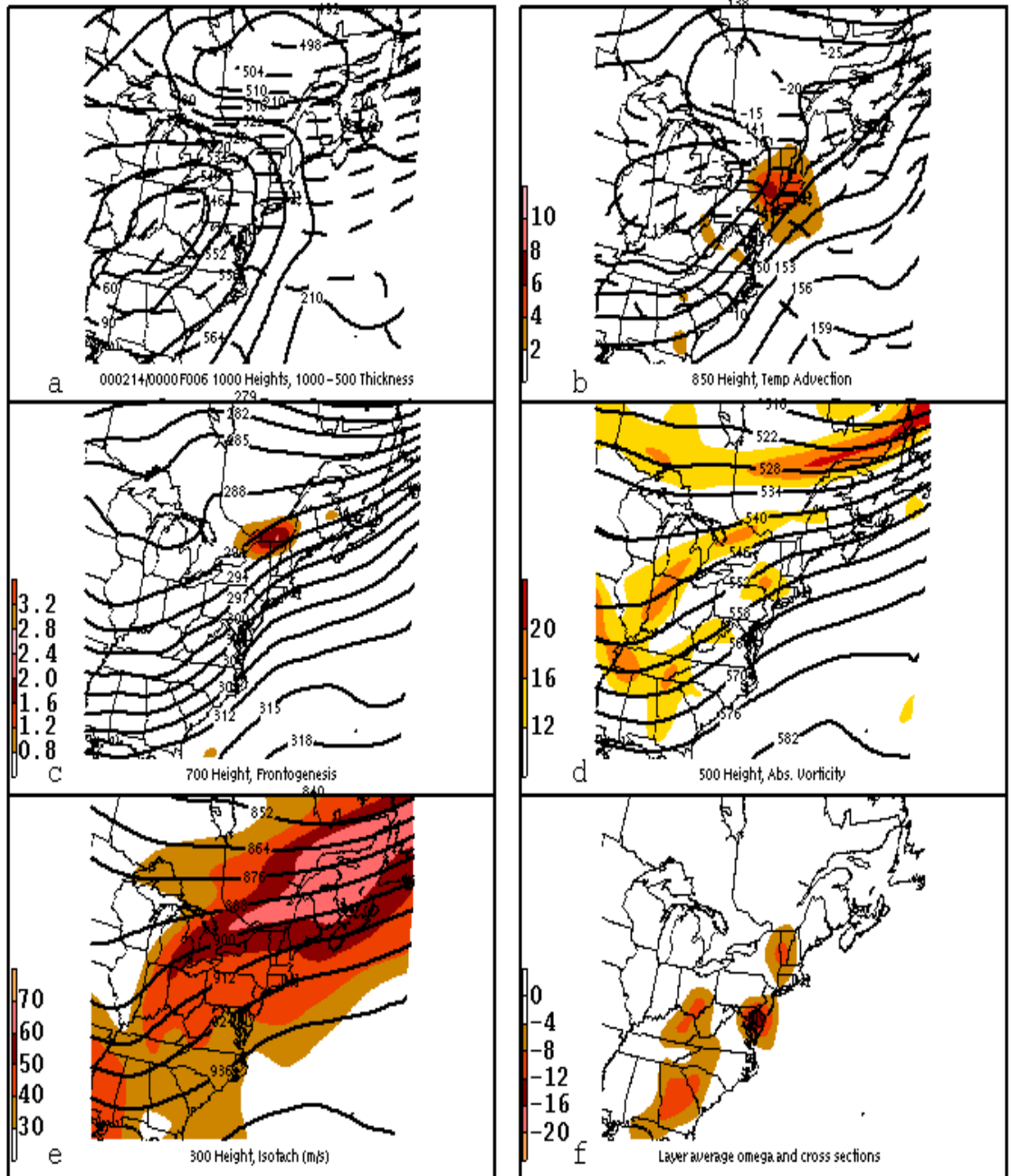


Fig. 3.55. As in Fig. 3.46, except for the 14–15 February 2000 snowstorm at 14/06.

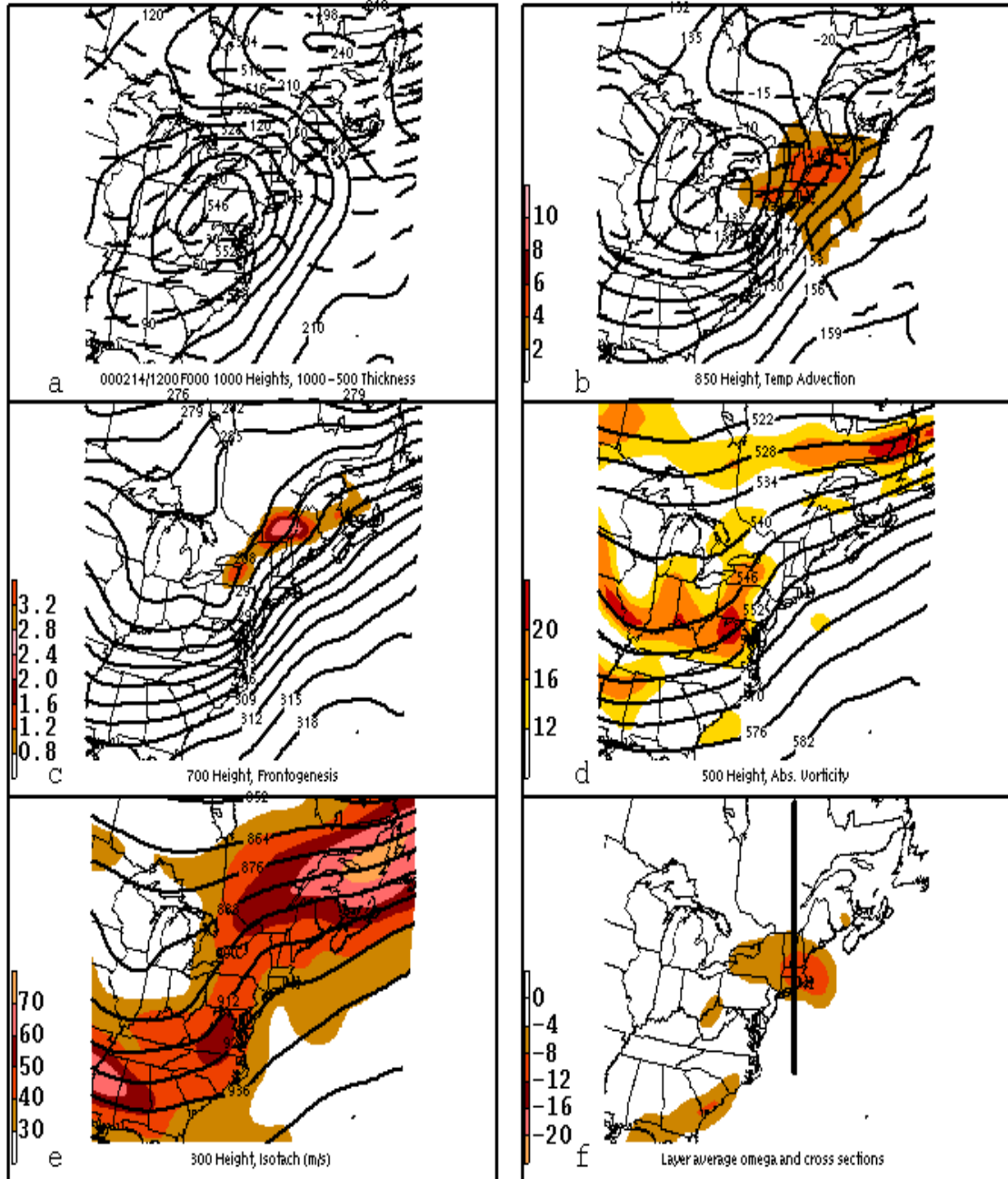


Fig. 3.56. As in Fig. 3.55, except at 14/12 and lower right panel shows cross-section orientation.

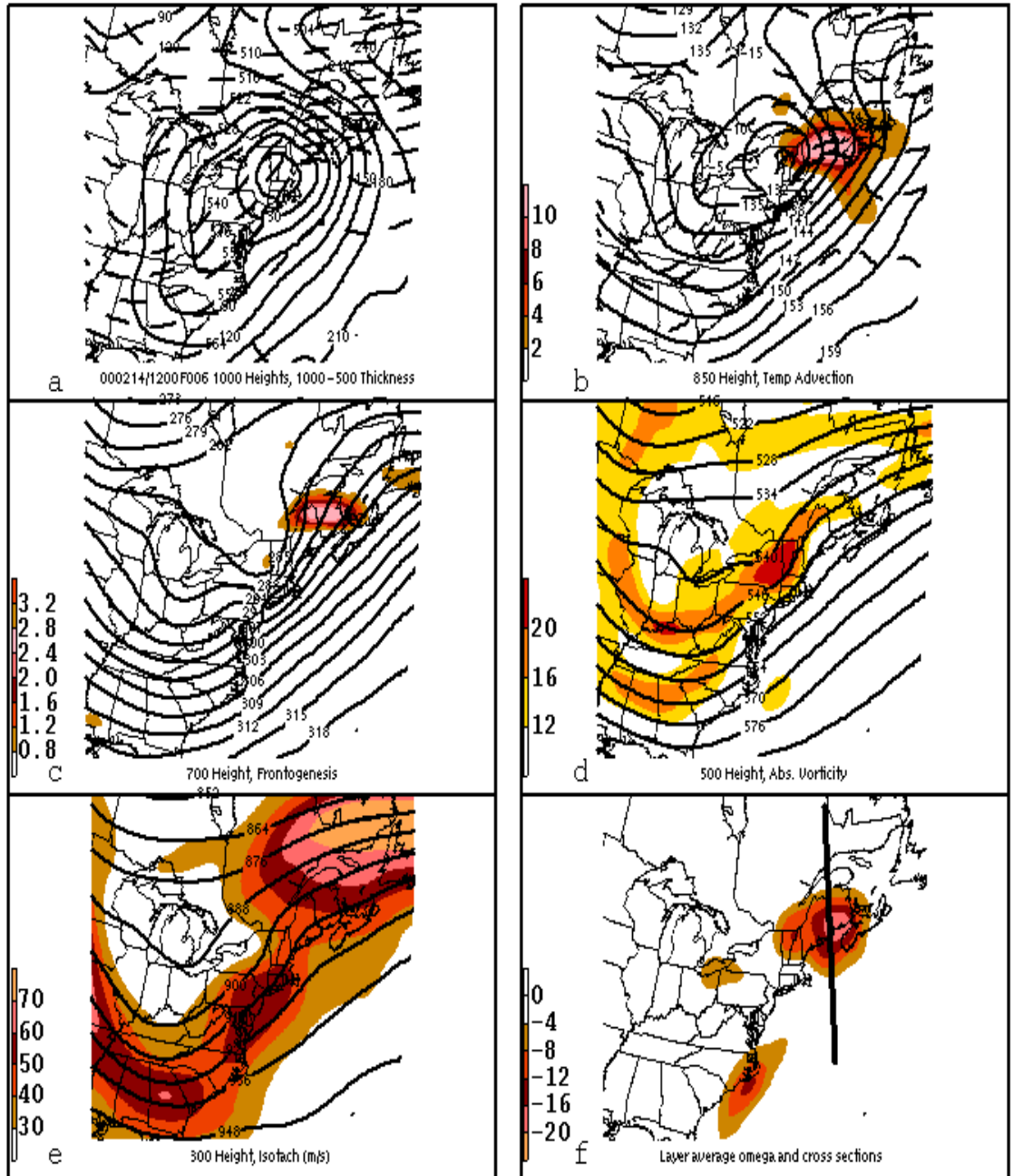


Fig. 3.57. As in Fig. 3.56, except at 14/18.

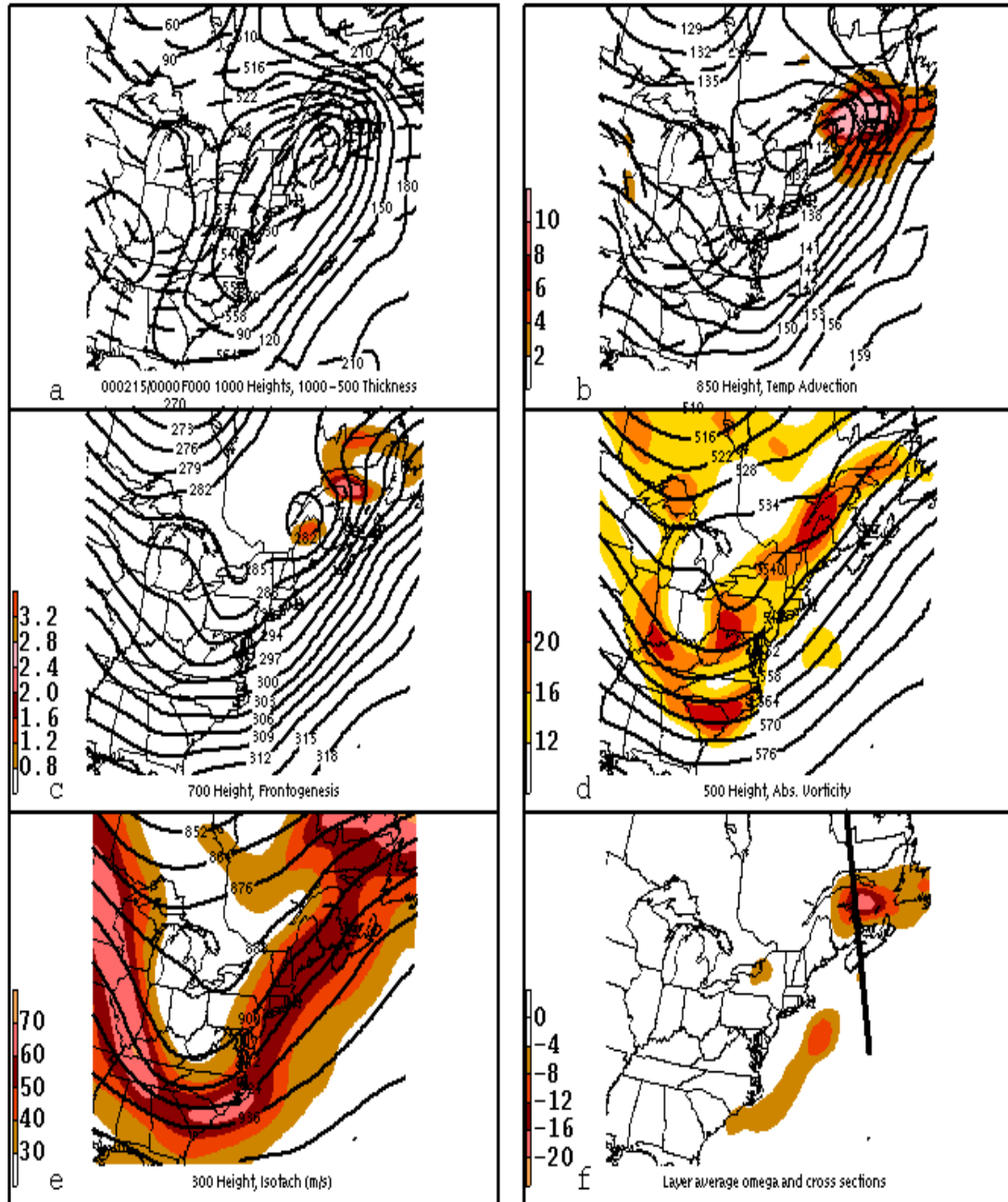


Fig. 3.58. As in Fig. 3.56, except at 15/00.

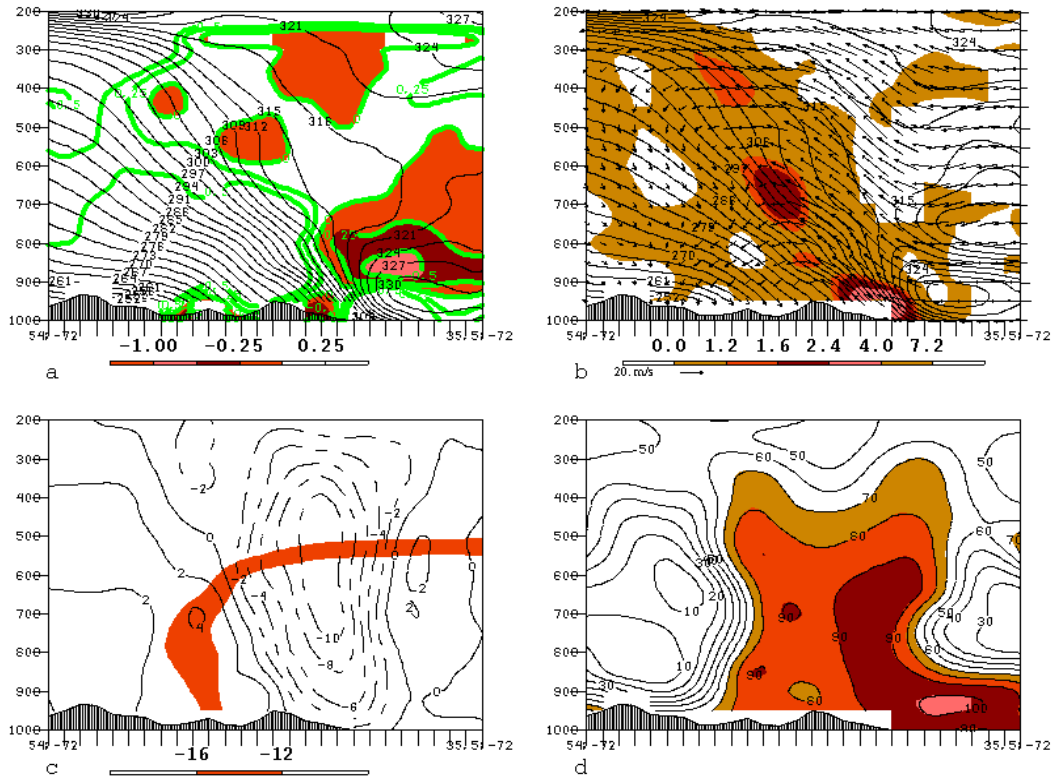


Fig. 3.59. As in Fig. 3.51, except through frontogenesis maximum at 14/12 (cross-section orientation shown in Fig. 3.56f).

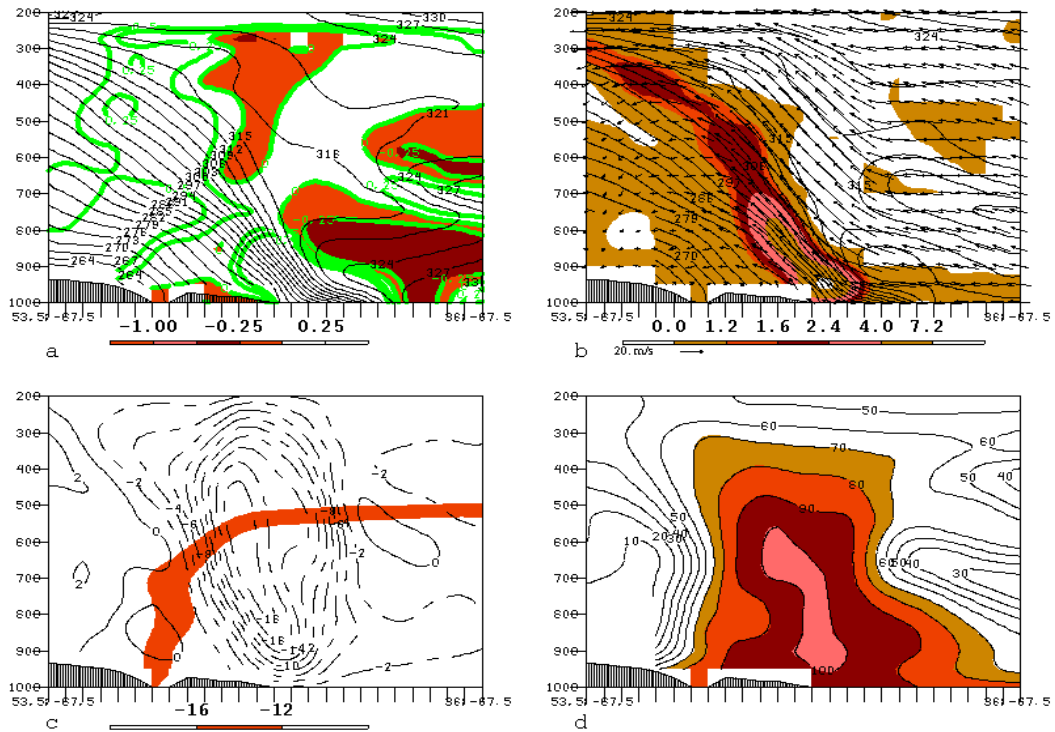


Fig. 3.60. As in Fig. 3.59, except for 14/18 (cross-section orientation shown in Fig. 3.57f).

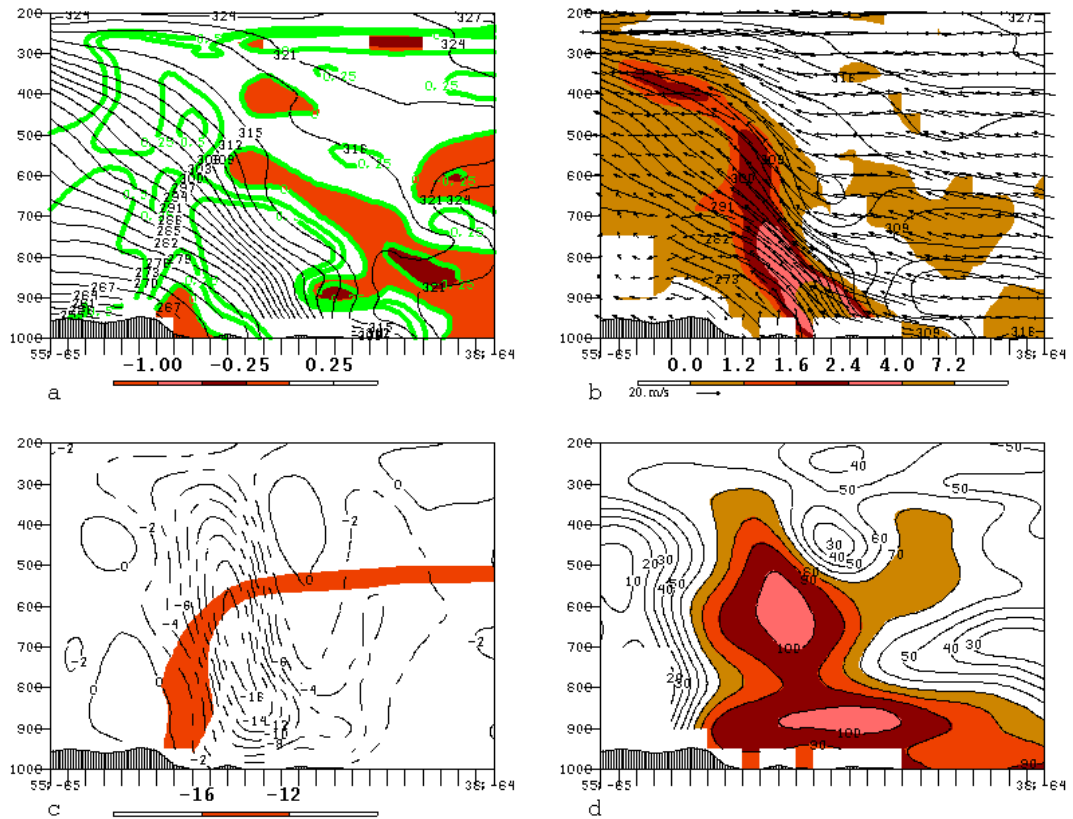


Fig. 3.61. As in Fig. 3.59, except at 15/00 (cross-section orientation shown in Fig. 3.58f).

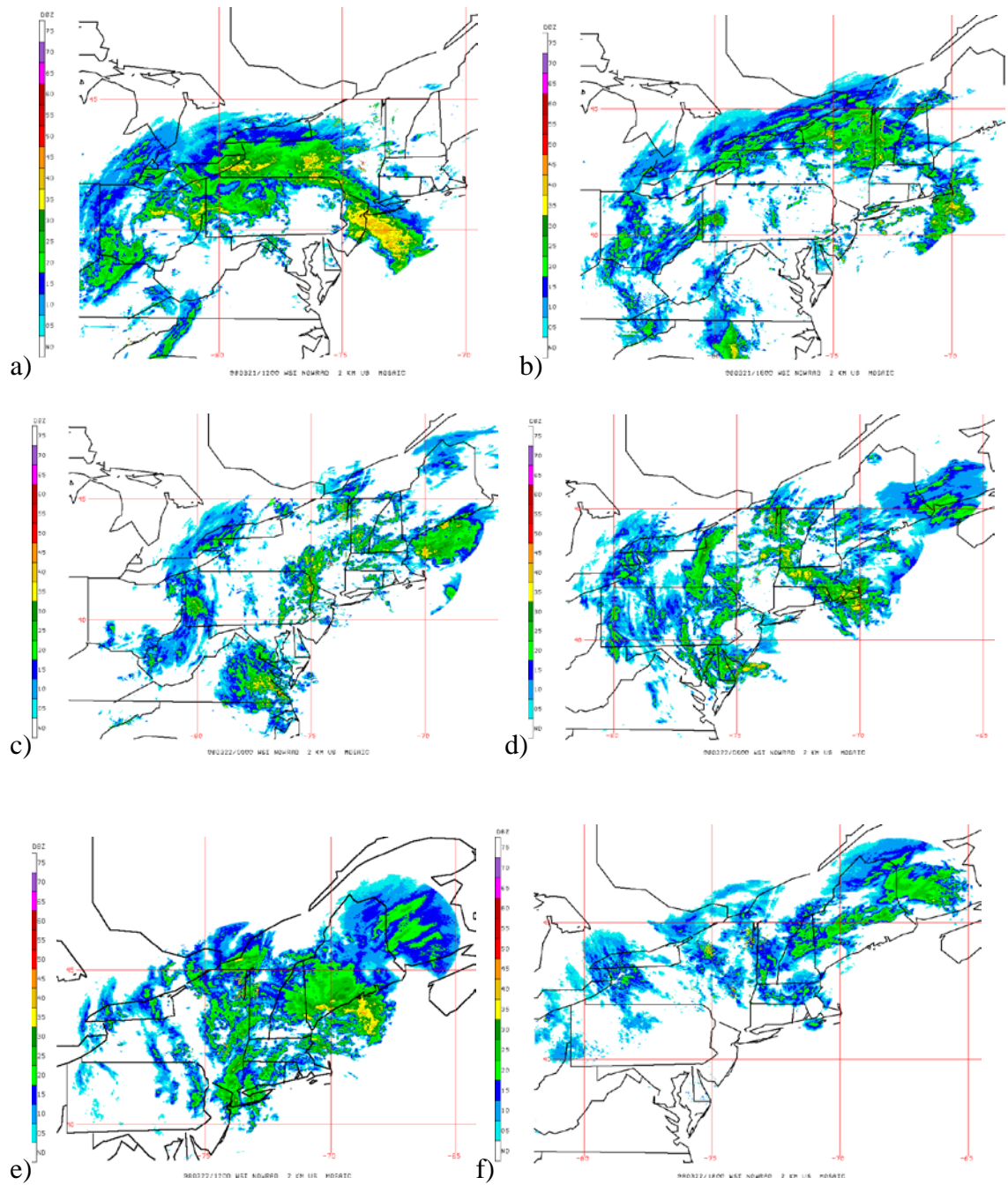


Fig. 3.62. WSR-88D radar composite images for the 21–22 March 1998 snowstorm at (a) 21/12, (b) 21/18, (c) 22/00, (d) 22/06, (e) 22/12, and (f) 22/18.

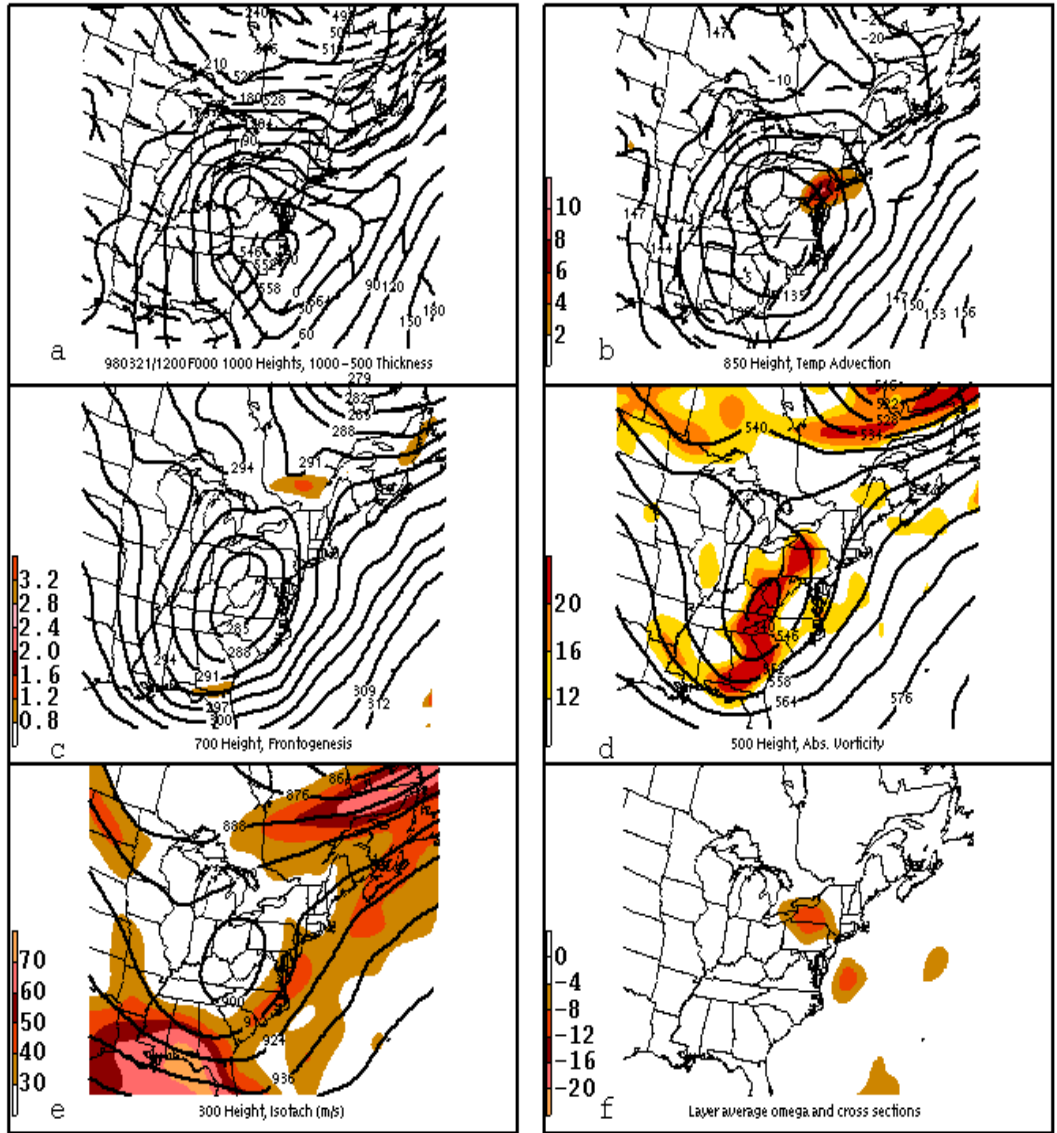


Fig. 3.63. As in Fig. 3.46 except for the 21–22 March 1998 storm at 21/12.

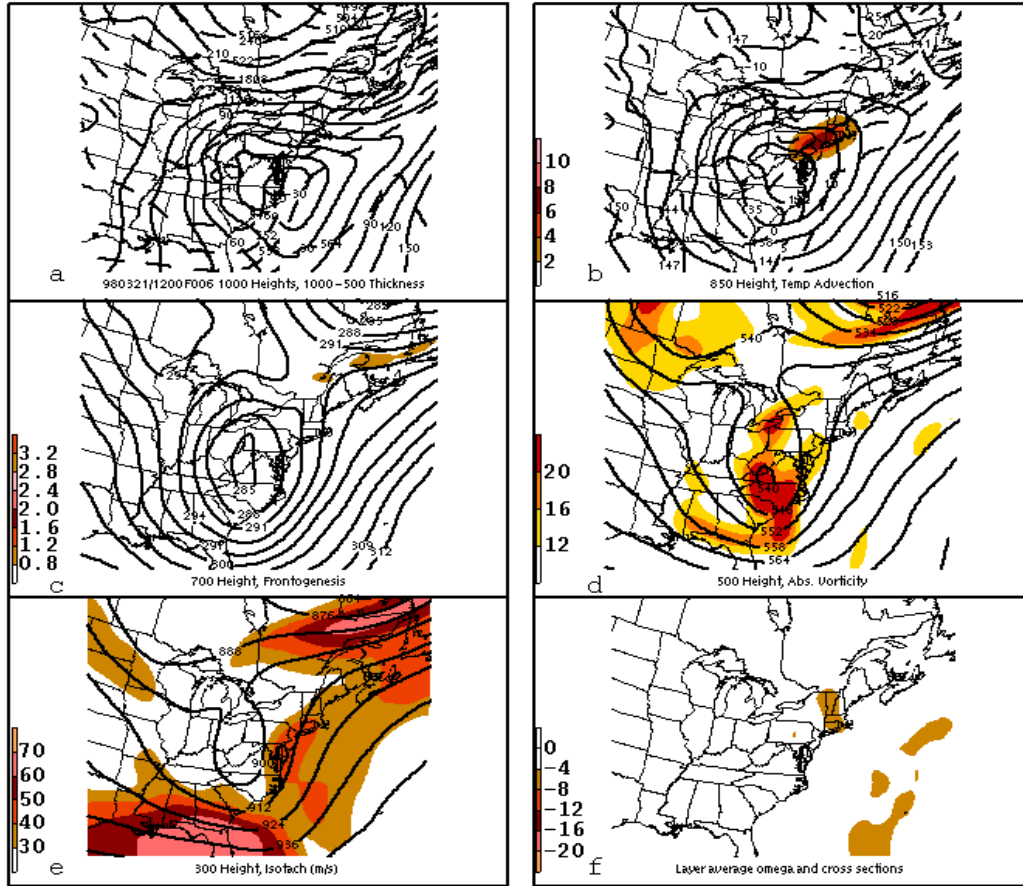


Fig. 3.64. As in Fig. 3.46, except at 21/18.

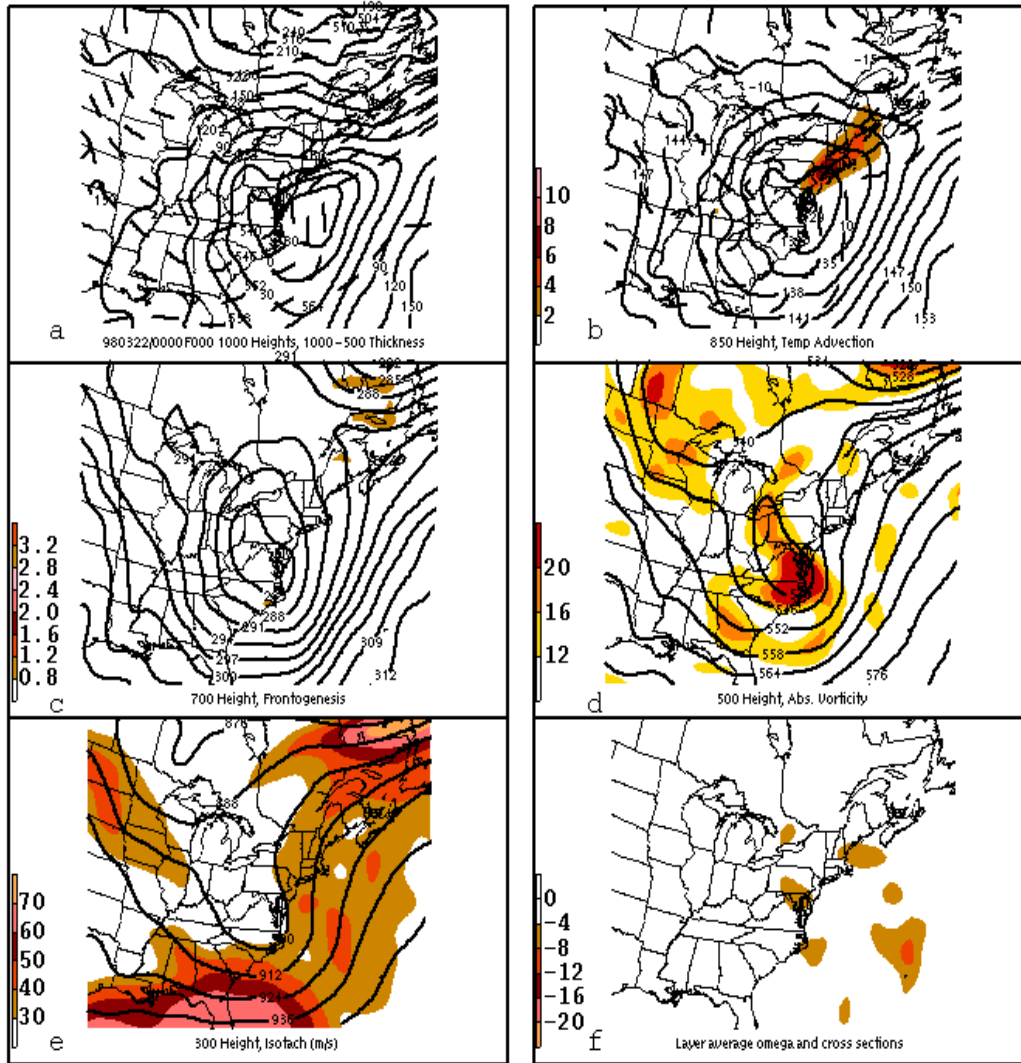


Fig. 3.65. As in Fig. 3.46, except at 22/00.

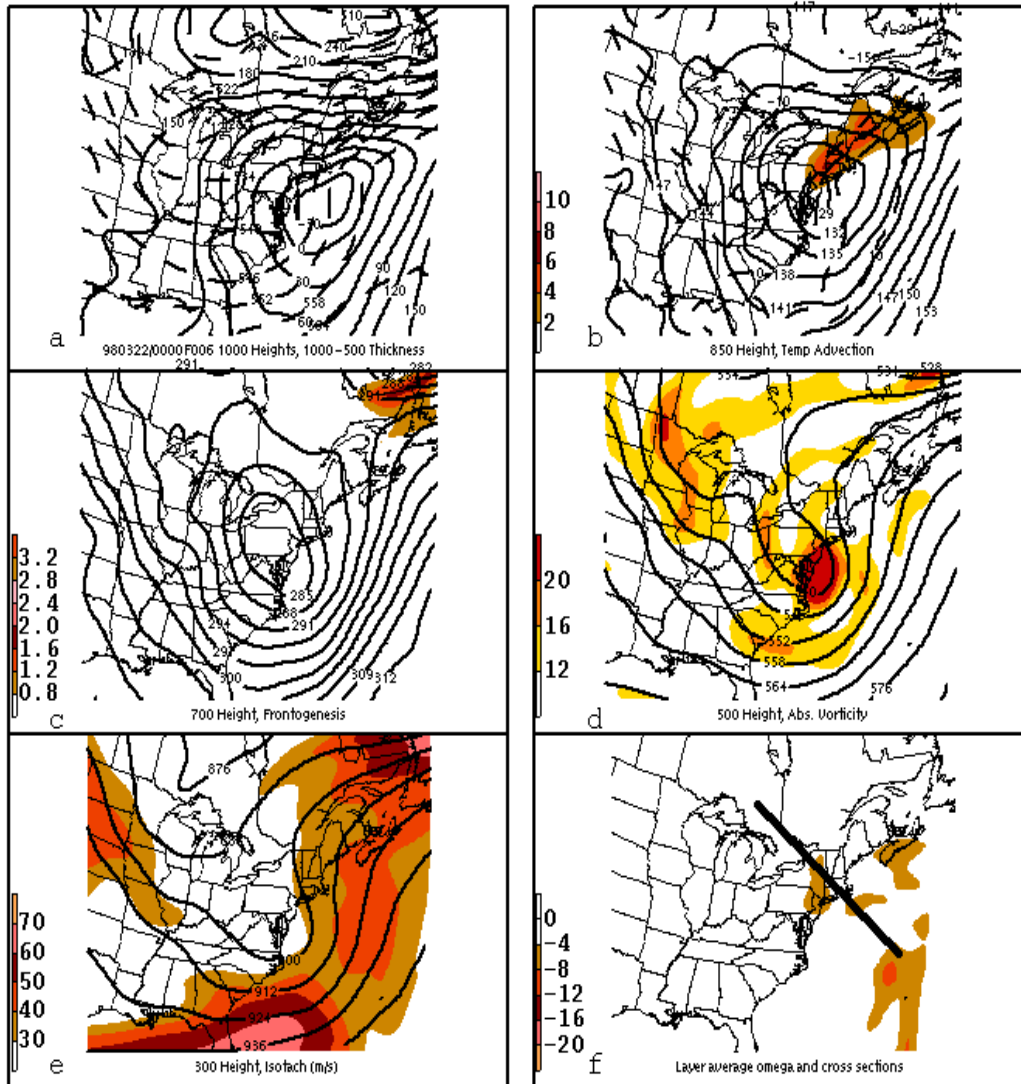


Fig. 3.66. As in Fig. 3.47, except at 22/06.

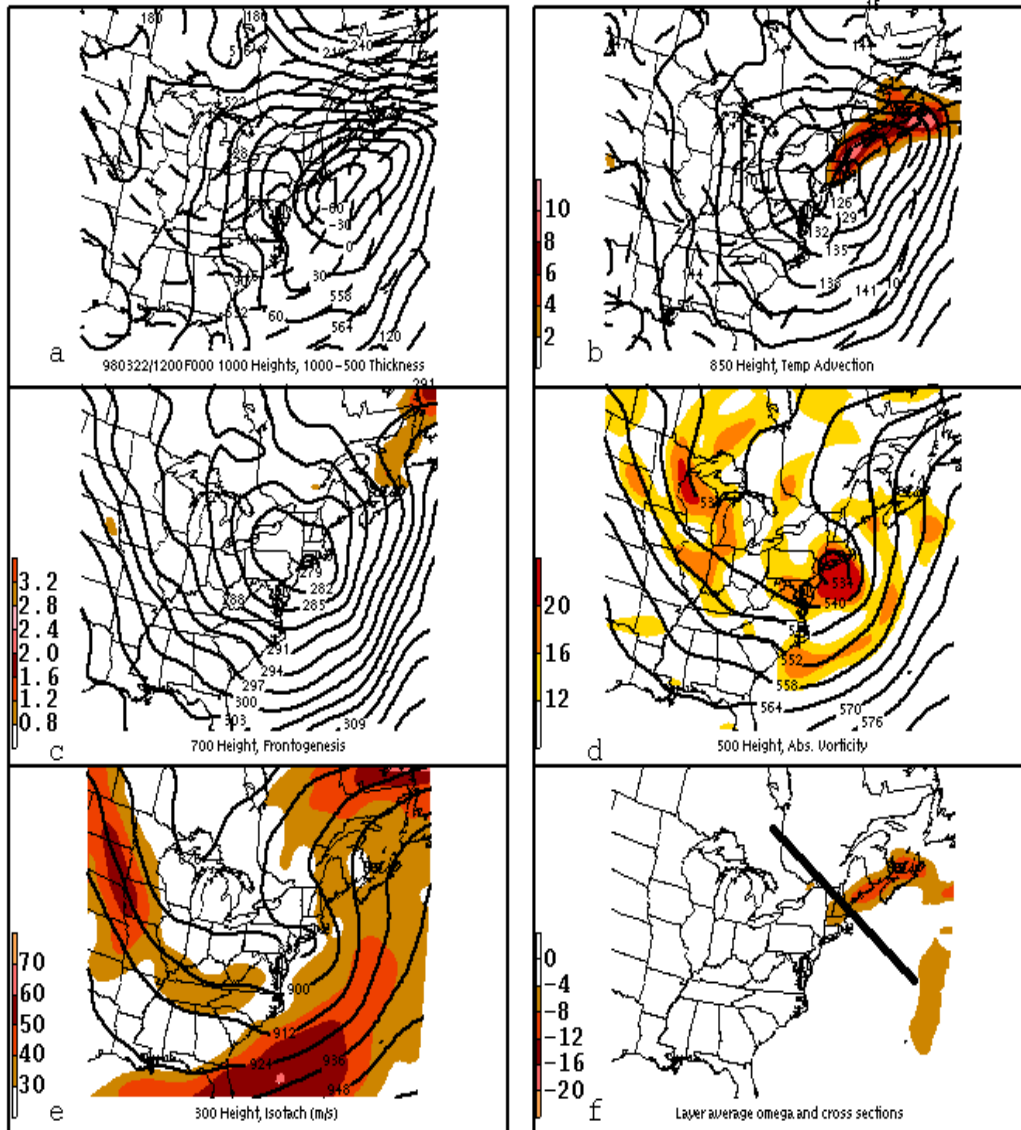


Fig. 3.67. As in Fig. 3.47, except at 22/12.

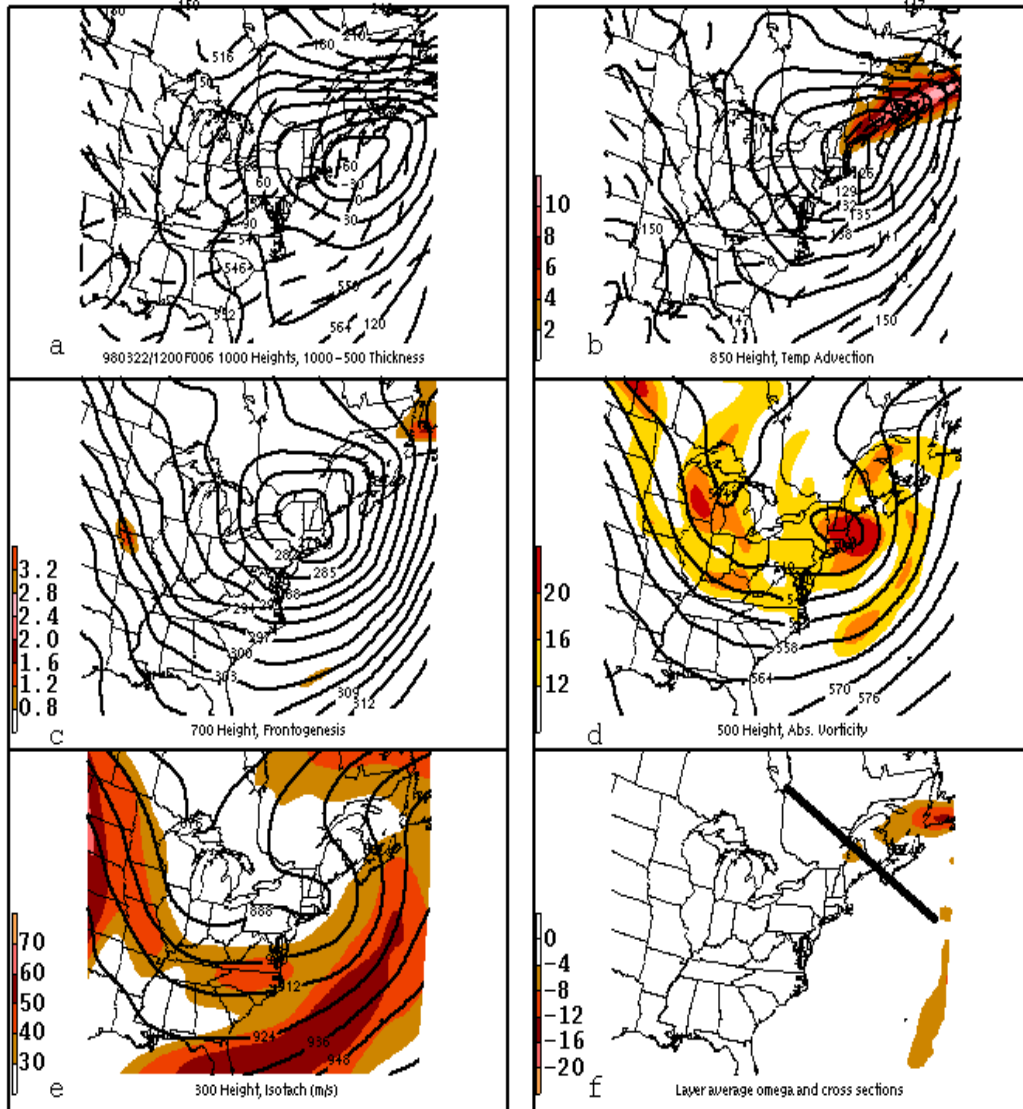


Fig. 3.68. As in Fig. 3.47, except at 22/18.

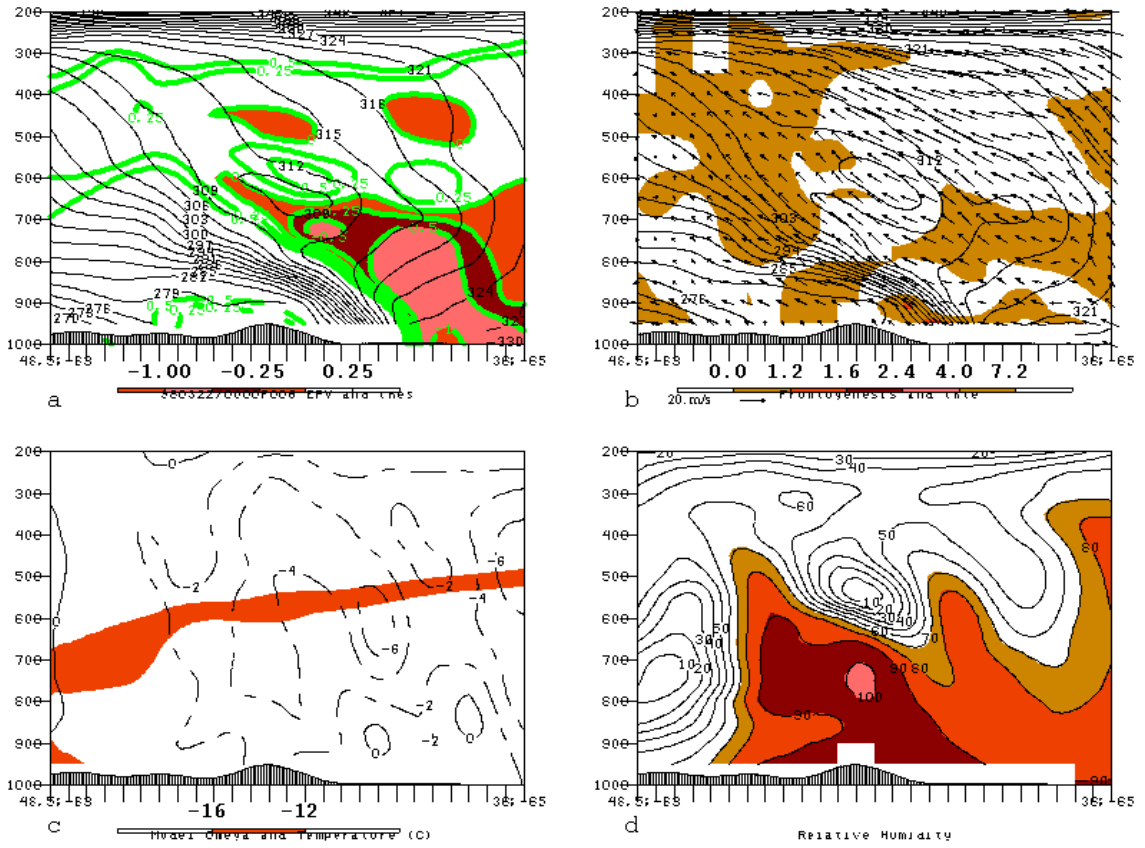


Fig. 3.69. As in Fig. 3.51, except at 22/06 (cross-section orientation shown in Fig. 3.66f).

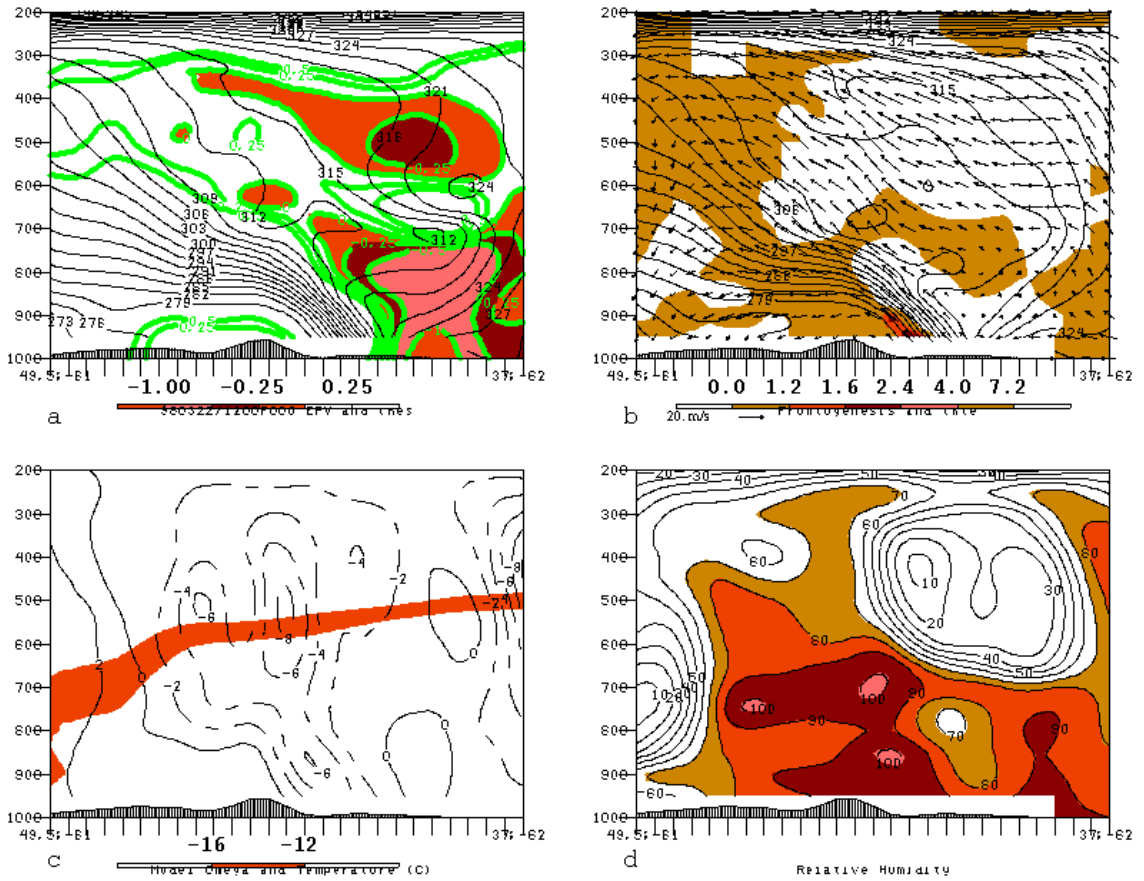


Fig. 3.70. As in Fig. 3.51, except at 22/12 (cross-section orientation shown in Fig. 3.67f).

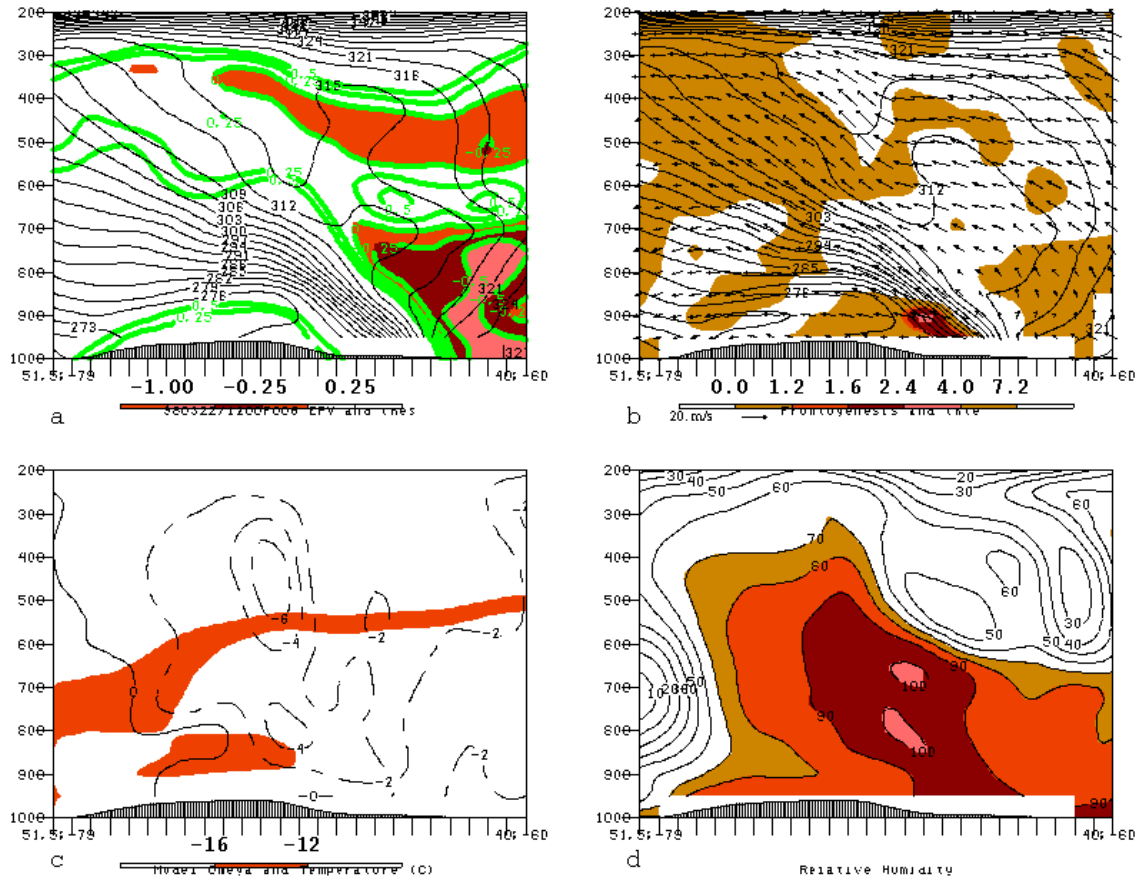


Fig. 3.71. As in Fig. 3.51, except at 22/18 (cross-section orientation shown in Fig. 3.68f).

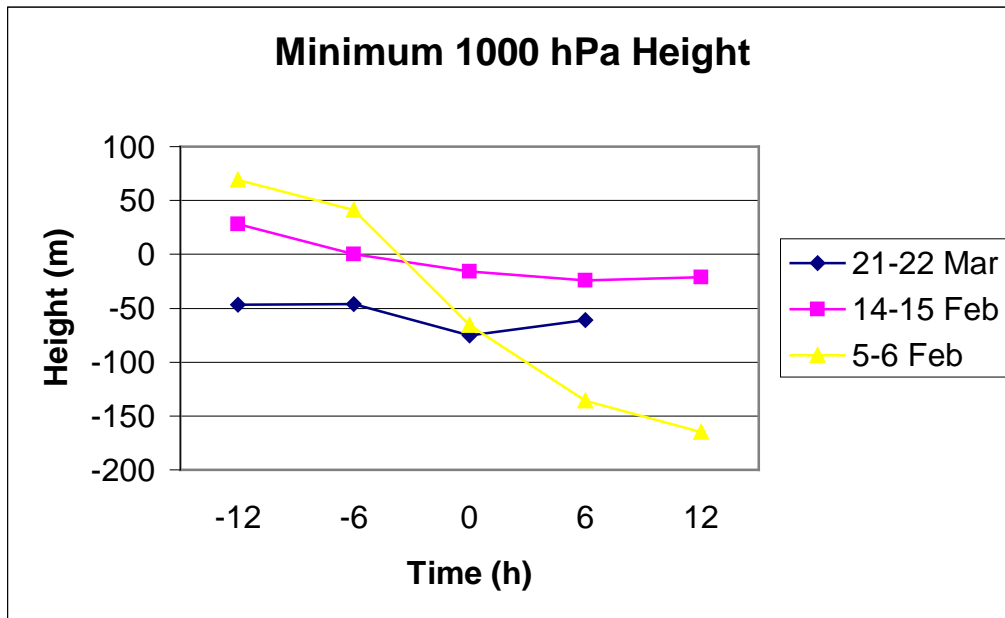


Fig. 3.72. Time series of the evolution of the minimum 1000 hPa height observed for each storm during its evolution. The 0 h time for each storm was defined as 22/12, 14/18, and 6/00, respectively.

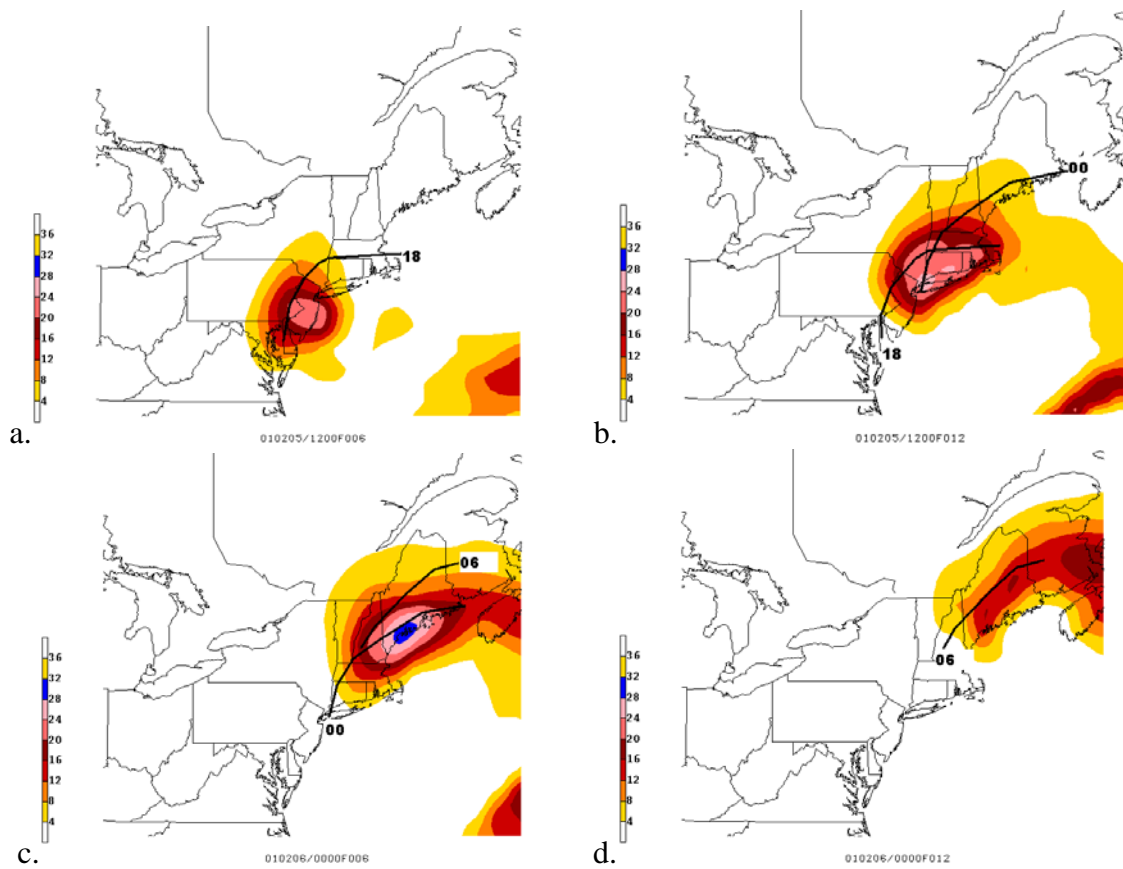


Fig. 3.73. Eta model 80 km display grid 6-h accumulated forecast precipitation (mm) shaded according to scale: (a) 6-h forecast valid at 05/18, (b) 12-h forecast valid at 6/00, (c) 6-h forecast valid at 6/06, (d) 12-h forecast valid at 6/12. Solid lines represent band axis at the start and end of each precipitation accumulation period (6 h), with times labeled.

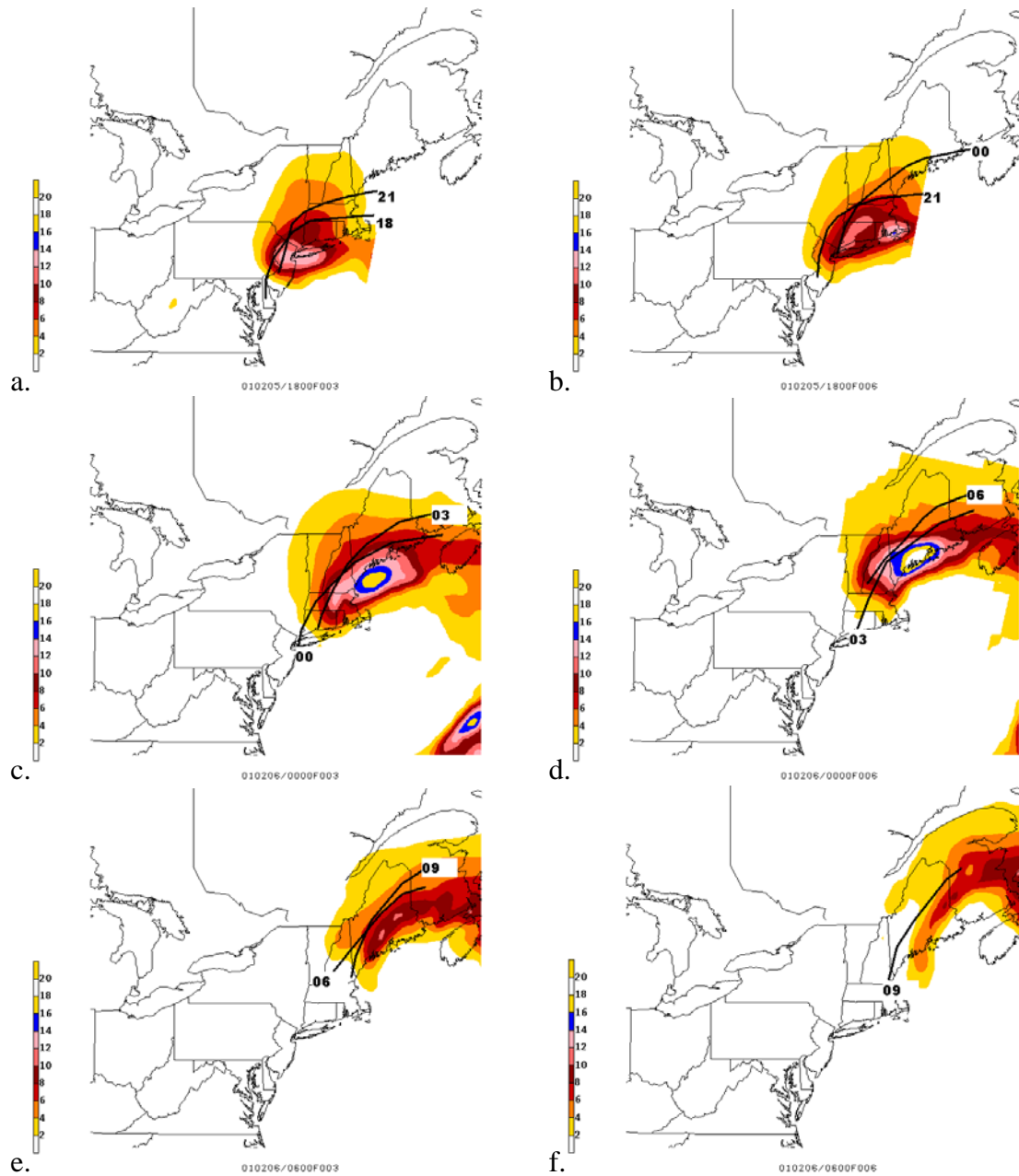


Fig. 3.74. Eta model 40 km display grid 3-h accumulated forecast precipitation (mm) shaded according to scale: (a) 3-h forecast valid at 05/21, (b) 6-h forecast valid at 6/00, (c) 3-h forecast valid at 6/03, (d) 6-h forecast valid at 6/06, (e) 3-h forecast valid at 6/09, (f) 6-h forecast valid at 6/12. Solid lines represent the band axis at the start and end of each precipitation accumulation period (3 h), with times labeled.

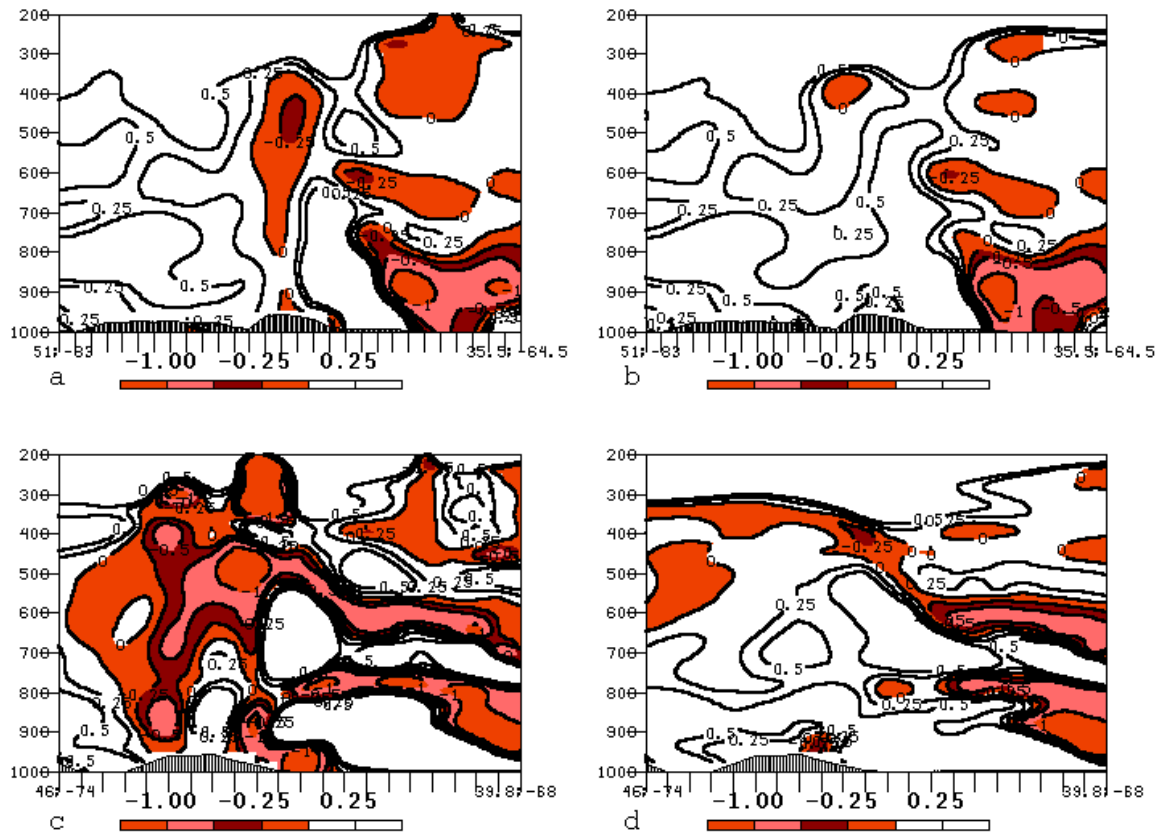


Fig. 3.75. Comparison of EPV calculations along 6/00 cross section: (a) Eta analysis 80 km display grid geostrophic EPV contoured below 0.5 PVU, shaded where negative according to scale, (b) as in (a) except full wind EPV, (c) Eta analysis 40 km display grid geostrophic EPV along central segment of original cross section, (d) as in (c) except full wind EPV.

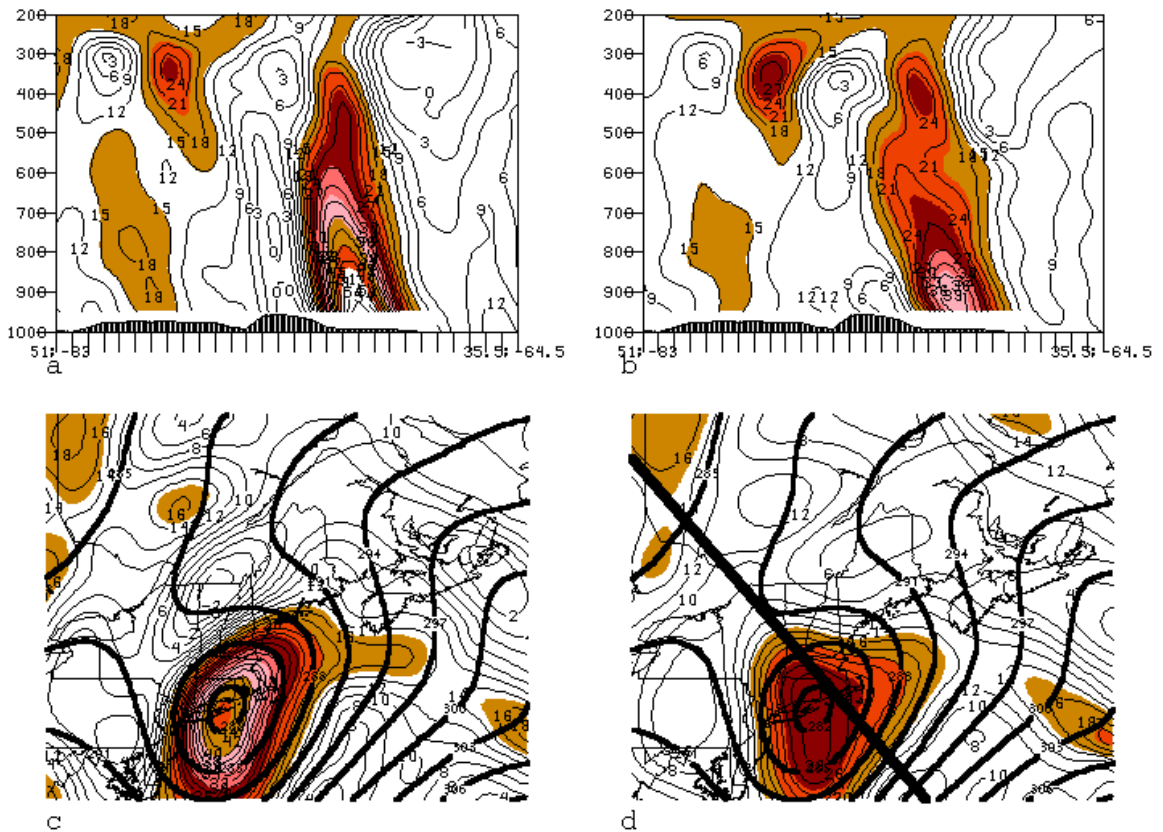


Fig. 3.76. Model analysis at 6/00 illustrating how absolute vorticity and subsequent calculation of EPV is affected by use of the geostrophic and full winds: (a) Cross section (as in Fig. 3.52; orientation shown in Fig.3.76d) of geostrophic absolute vorticity (shaded above $15 \times 10^{-5} \text{ s}^{-1}$). (b) As in (a), except absolute vorticity calculated with the full wind. (c) 700 hPa geostrophic absolute vorticity (thin solid contours every $2 \times 10^{-5} \text{ s}^{-1}$, dashed when negative, shaded above $15 \times 10^{-5} \text{ s}^{-1}$), and heights (thick solid, contoured every 3 dam). (d) As in (c), except absolute vorticity calculated with full wind, and cross section orientation shown.

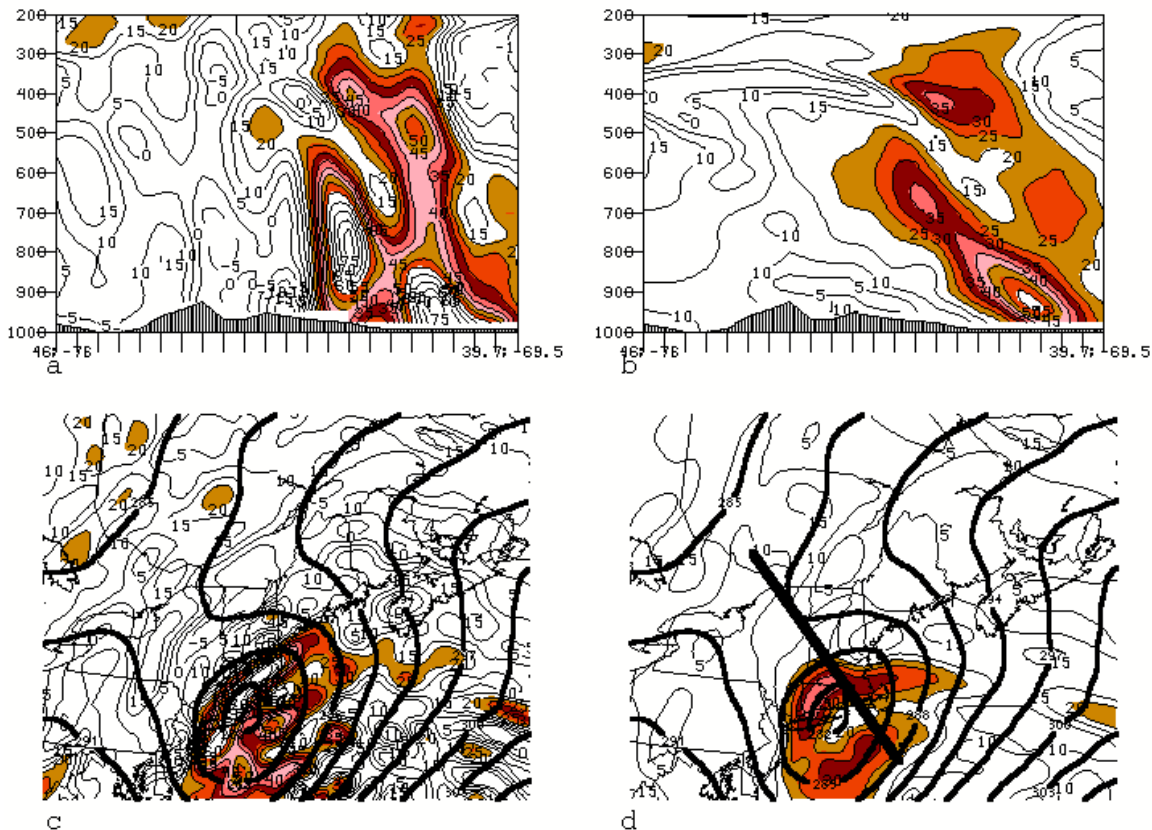


Fig. 3.77. As in Fig. 3.76, except with 40 km display grid, thin solid contours every $5 \times 10^{-5} \text{ s}^{-1}$, and shorter portion of original cross section (orientation shown in Fig. 3.77d).

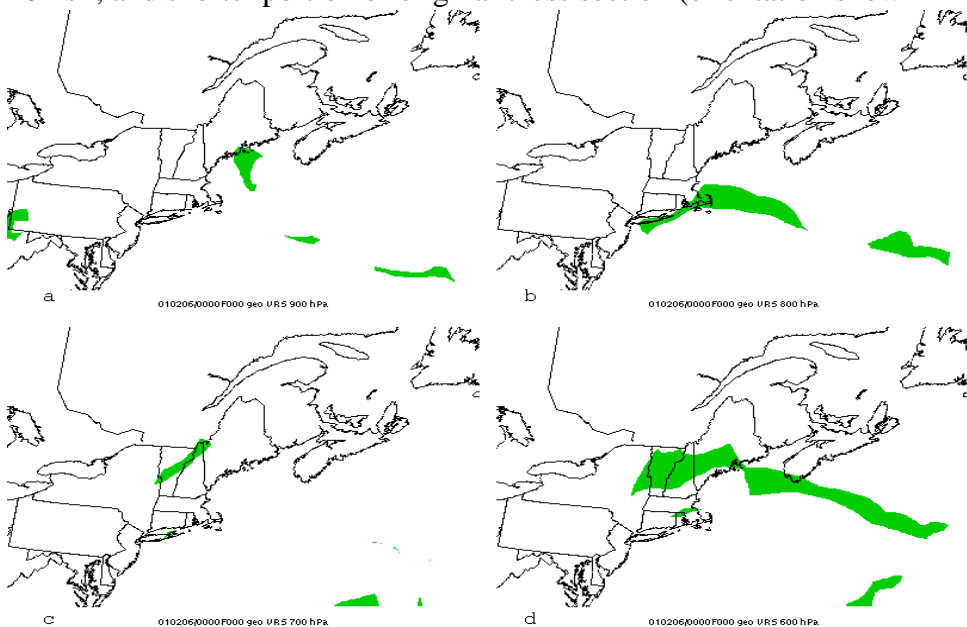


Fig. 3.78. VRS diagnostic results valid at 06/00 for (a) 900 hPa, (b) 800 hPa, (c) 700 hPa, and (d) 600 hPa. Shaded regions represent areas that exhibit negative geostrophic EPV (calculated over 50 hPa layer), conditional stability, inertial stability, near saturation ($> 80\%$ relative humidity), and ω exceeding $-5 \times 10^{-3} \text{ hPa s}^{-1}$.

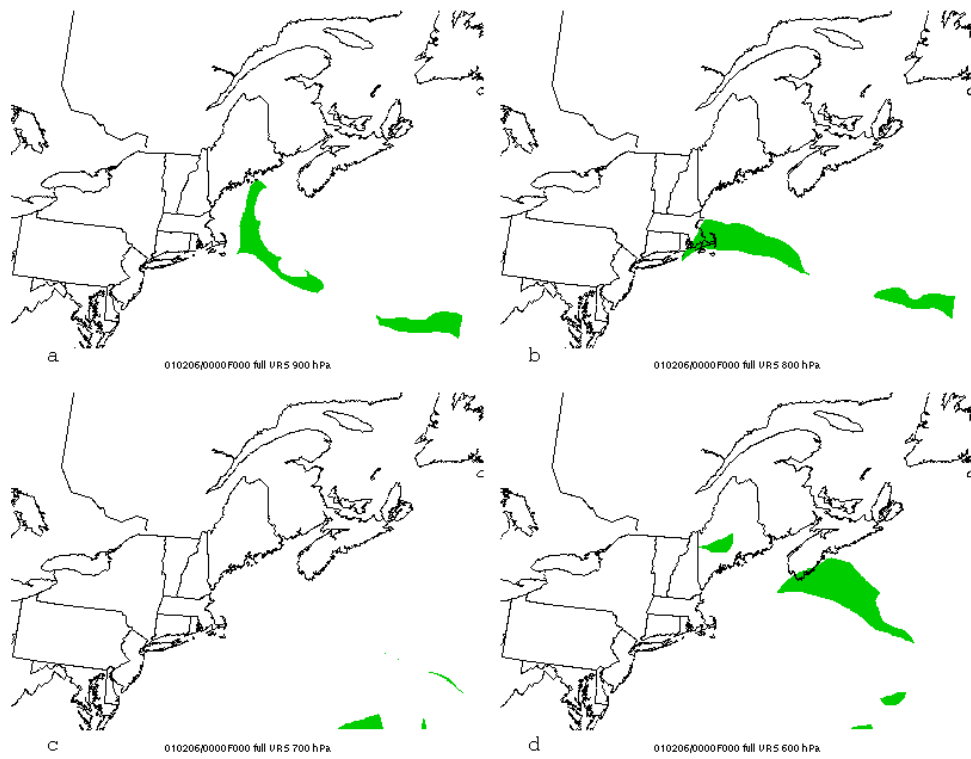


Fig. 3.79. As in 3.78, except EPV calculated with full wind.

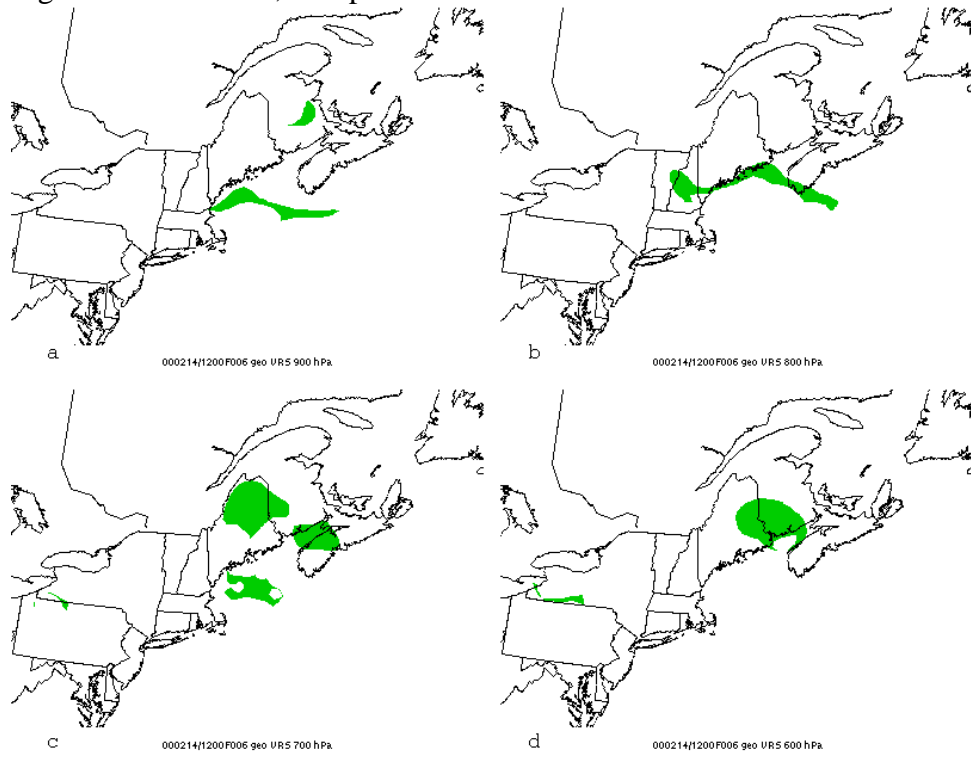


Fig. 3.80. As in Fig. 3.78, except valid at 14/18.

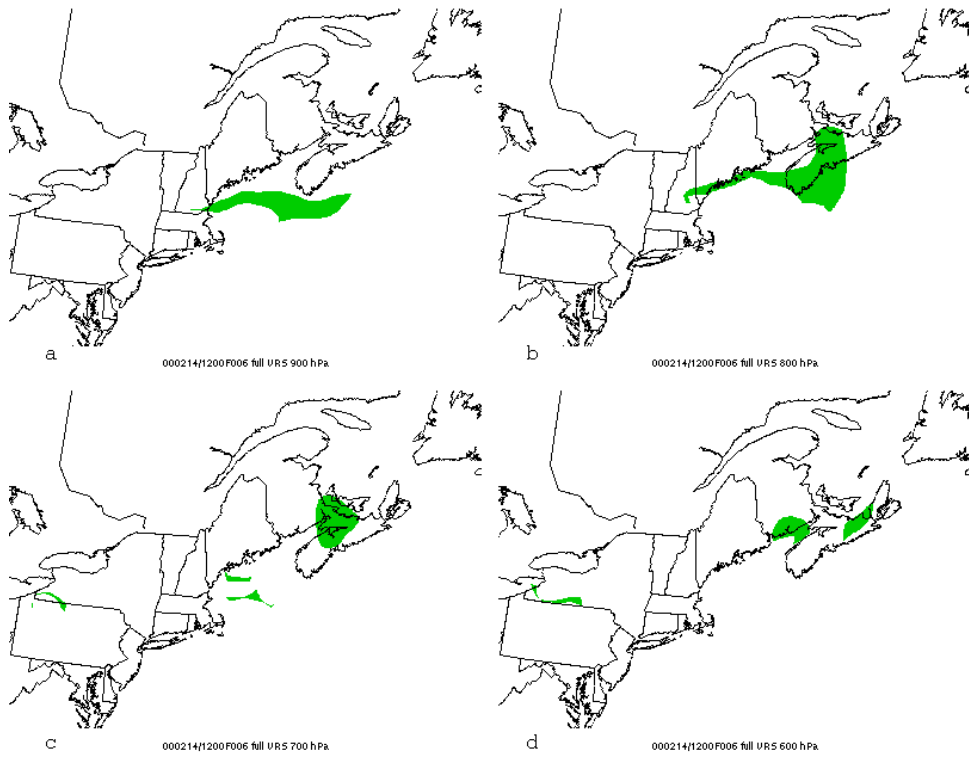


Fig. 3.81. As in Fig. 3.79, except valid at 14/18.

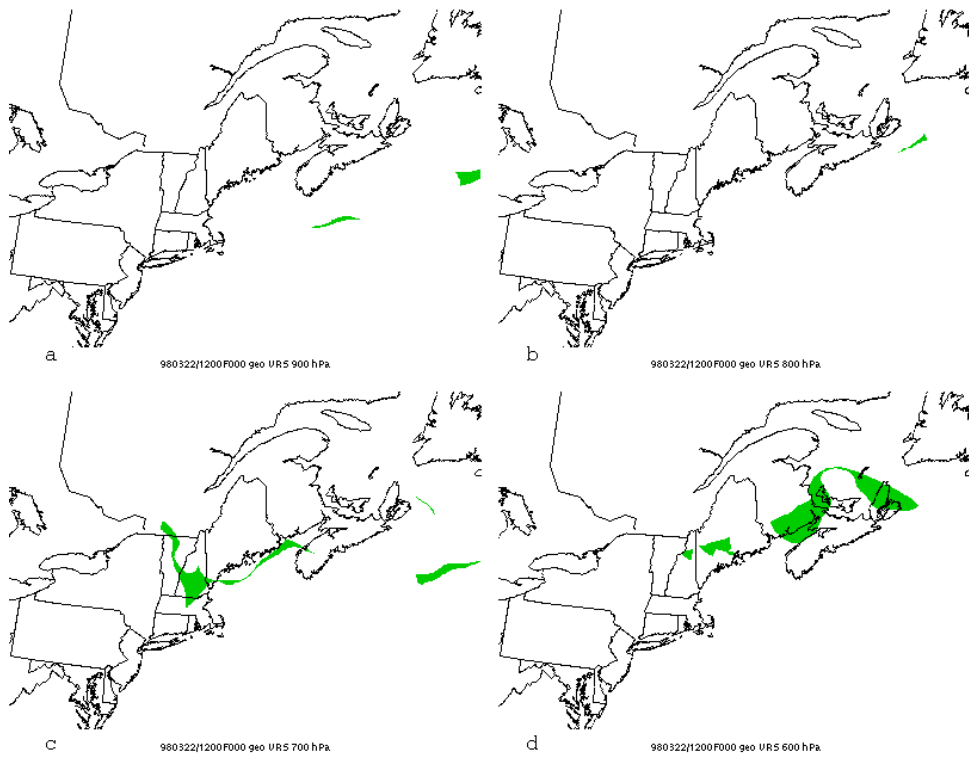


Fig. 3.82. As in Fig. 3.78, except valid at 22/12.

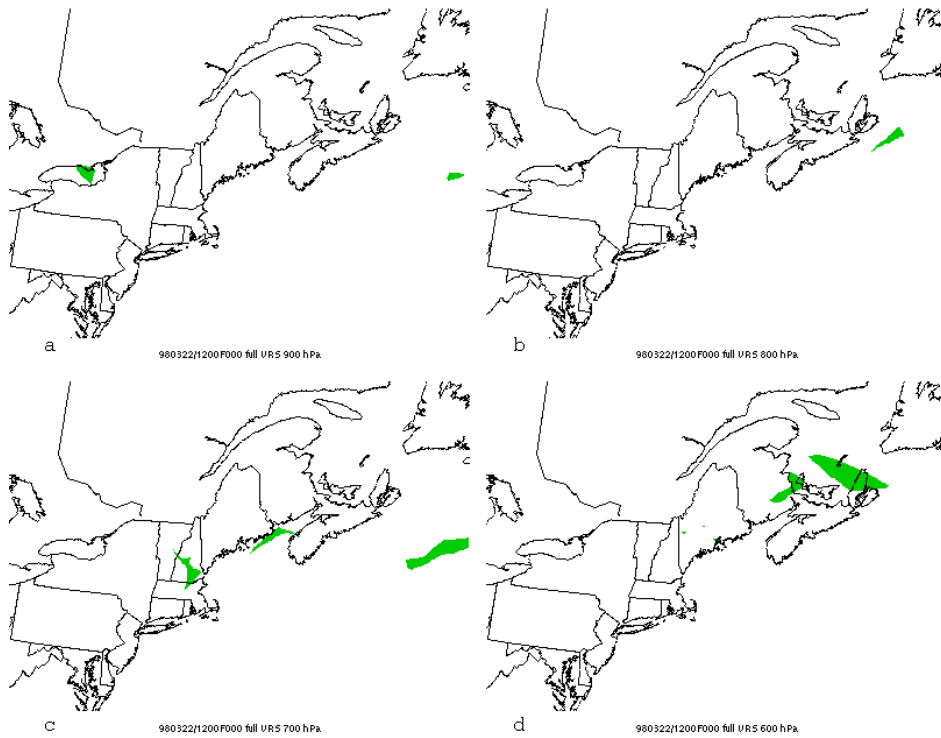


Fig. 3.83. As in Fig. 3.79, except valid 22/12.

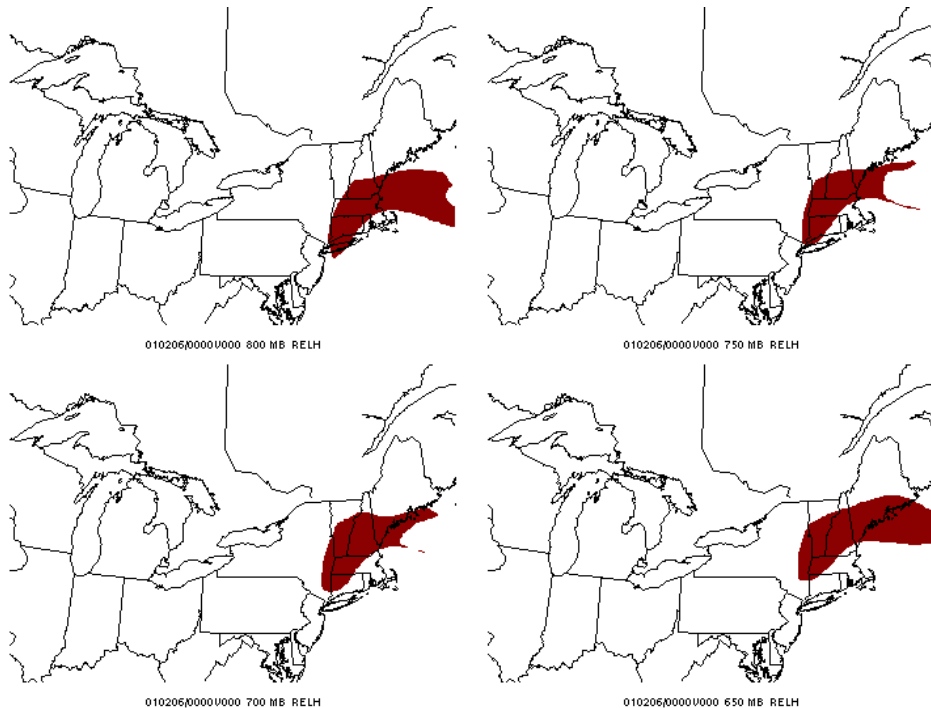


Fig. 3.84. FWS diagnostic valid at 06/00 for (a) 800 hPa, (b) 750 hPa, (c) 700 hPa, (d) 650 hPa. Shaded region represents area exhibiting 2-D Miller frontogenesis exceeding $1^{\circ}\text{C} (100 \text{ km})^{-1} (3 \text{ h})^{-1}$, weak stability ($-0.1^{\circ}\text{C hPa}^{-1} < \frac{\partial\theta_{es}}{\partial p} < 0$), near saturation ($> 80\%$ relative humidity), and ω exceeding $-5 \times 10^{-3} \text{ hPa s}^{-1}$.

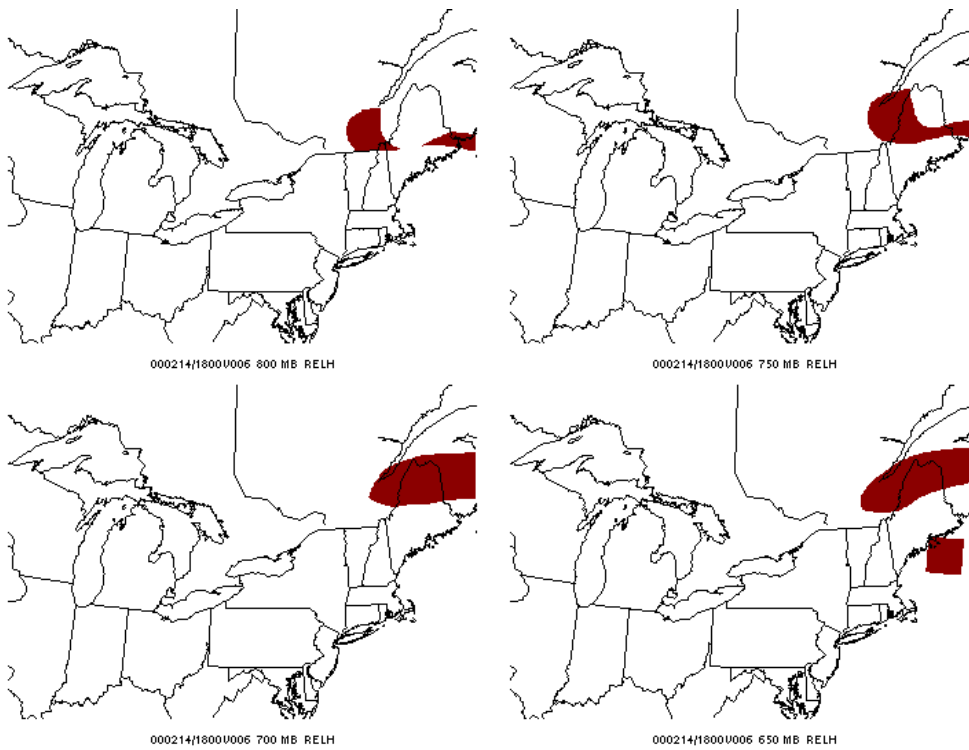


Fig. 3.85. As in Fig. 3.74, except valid at 14/18.



Fig. 3.86. As in Fig. 3.84, except valid at 22/12.

4. Discussion

4.1 Climatology

Despite the rather strict criteria used to define mesoscale banded events, 113 events (excluding transitory and undefined) were documented in the northeastern US study region during five cold seasons. This number testifies to the frequency with which operational forecasters are challenged by mesoscale bands. The predominance of single- and multi-banded structures in the northeast US is intriguing since previous band climatology studies (e.g., Houze et al. 1976; Browning 1985) found a majority of bands associated with the cold frontal zone. The location of these studies (Pacific Northwest, Great Britain) in the exit region of the Pacific and Atlantic storm tracks may influence the type of mesoscale banding experienced, especially considering results from this study and Nicosia and Grumm (1999) have suggested that single- and mutibanded events tend to be associated with cyclogenesis, which is more frequent in the western ocean basins (Whittaker and Horn 1984).

Of further interest is the predominance of single bands found in the northwest quadrant relative to the surface cyclone. Thirty-nine of the 48 single-banded events were found in this quadrant. Although band occurrences northwest of the surface cyclone have been well documented in case studies in the eastern half of the US (e.g., Sanders and Bosart 1985; Nicosia and Grumm 1999; Martin 1998a,b), they differ from the predominate single-band occurrences ahead of the warm front documented in the CYCLES project (Houze et al. 1976; Hobbs 1978) and in the work of Browning (Browning 1985; Browning 1990). It is believed the absence of single bands in the

comma-head portion of the Hobbs (1978) cyclone schematic (Fig. 1.10) is a consequence of the small number of storms studied (11), limited radar network (just western Washington state), and region of study (Pacific Northwest).

Although the behavior of narrow-cold frontal bands has been well documented, the behavior of single- and multibanded structures has not. In fact, the multibanded structure has only loosely been identified as wave bands in the CYCLES study. The concentration of the multibanded events just ahead of the surface cyclone roughly corresponds to the location of wave bands proposed by Houze et al. (1976), but it is not clear if wave bands are synonymous with the presently defined multibanded structure since the motion of the wave bands was not documented in Houze et al. (1976). In many cases the multibanded structure was found to interact with a single-banded structure, with finescale bands elongating and merging into the primary single band. This behavior has also been noted by Stuart (2001) and demands further investigation.

The occurrence of 13 nonbanded cases during the study stresses that not all cases associated with significant precipitation exhibit mesoscale banding. These cases also help clarify the discriminating features of banded and nonbanded cases, as was shown through composite study.

4.2 Composites

4.2.1 *Synoptic Flow*

The synoptic composite evolutions and higher-resolution model composites document how the synoptic flow configuration influences cyclone substructure. The

process of cyclogenesis (Fig. 3.28) guides the development of deformation zones, dictating their location relative to the cyclone center. In the case of northwest bands, the midlevel deformation zone is formed northwest of the surface cyclone when a closed circulation develops in the midlevels. In the east composite, the midlevel deformation zone forms in the diffluent flow ahead of the cyclone as the disturbance amplifies. In each composite class deformation acting on the temperature gradient contributes to frontogenesis, which provides forcing for the single-banded structures. Midlevel deformation associated with confluence in the nonbanded composite contributes to frontogenesis, but cross-section analysis showed the frontal zone was marked by greater conditional stability than the banded composite frontal zones (see sections 3.3.2 and 4.2.2).

A conceptual model of the single-banded event initial time analysis is shown in Fig. 4.1. The double jet structure (Fig. 4.1; see also Fig. 3.11e) places the surface cyclone under upper-level divergence, which promotes cyclogenesis. The existence of a closed midlevel low creates a deformation zone associated with a confluent asymptote northwest of the surface cyclone. This deformation zone supports frontogenesis, which provides forcing for subsequent band development northwest of the surface cyclone. Diffluent flow ahead of the midlevel disturbance also contributes to deformation and subsequent frontogenesis, supporting band development ahead of the warm front. Note that this conceptual model is consistent with the findings of Nicosia and Grumm (1999; see Fig. 1.12).

The nonbanded conceptual model (Fig. 4.2) highlights the dominance of the upper-level jet. A weak surface low associated with a weak midlevel trough is found in

the equatorward entrance region of the jet. Confluent flow ahead of this midlevel trough contributes to deformation and subsequent frontogenesis; however, the deformation zone is not associated with a confluent asymptote.

These synoptic differences among composite classes and respective conceptual models are large enough to be recognized in one-to-two day model forecasts, affording forecasters a heightened awareness of potential mesoscale banding.

4.2.2 Model Cross Sections

The composite model cross sections provide an illustration of the characteristic single-band environments. A schematic of the banded and nonbanded cross sections is shown in Fig. 4.3. The banded composite frontal zone (Fig. 4.3a) is marked by a sloping region of frontogenesis extending through the middle troposphere, coincident with weak conditional stability. Application of the semi-geostrophic form of the Sawyer–Eliassen equation would predict that the direct circulation induced by the frontogenesis in the presence of weak static stability would lead to a narrow sloping updraft on the equatorward flank of the frontal zone. The composite vertical velocity fields exhibited this very feature (shown schematically in Fig. 4.3a), corroborating both established theory and observations. It is important to note that all single-banded composites (northwest-near, northwest-far, and east) exhibited the above features, suggesting frontogenesis in the presence of weak conditional stability is the primary forcing mechanism for single bands in both the northwest and east quadrants.

Although the single-banded composites were marked by weak conditional stability, the preferred mode of instability associated with the single-banded structures in

the individual cases comprising the composites, whether it be CI, CSI, or just weak conditional stability, could not be discerned since the process of compositing and the use of a relatively coarse resolution gridded dataset smeared such signatures. It is believed that both CI and CSI were present in the region of banding in a number of the study cases, but determining the proportions of each is left to future study.

The nonbanded frontal zone (Fig. 4.3b) exhibits many of the same features as the banded cross section; however the ascent is weaker and broader than the banded frontal zone (Fig. 4.3a). This difference can be understood by noting that the slope of the frontal zone is more horizontal than in the banded cross section. As a first-order assessment of conditional stability for a given baroclinicity the more horizontally sloped frontal zone would imply greater atmospheric stability. In this situation the Sawyer–Eliassen equation would predict that the ascent forced by the frontogenesis would be weaker and broader, as is evident in the vertical velocity field (Fig. 4.3b).

The primary difference between the single-banded and multibanded cross sections is the abundance of CI in the multibanded cross section (see Fig. 3.38a). This mode of instability may counter conventional wisdom, which would assert multibanding is more indicative of CSI, with horizontal rolls providing periodic forcing. Whatever the mode, it is evident that some type of instability is present. The remaining question is what dictates the periodic nature of the convection. Future investigation is needed to establish a forcing mechanism consistent with observations.

4.3 Case Studies

The case studies highlight the key dynamical features evident in the composites and conceptual models, and afford the opportunity to test various band diagnostics. In order to compare case characteristics with the conceptual models, synoptic summaries at the key analysis times for each case study are provided.

4.3.1 5–6 February 2001

Consistent with the northwest composite (Fig. 4.1), the 5–6 February 2001 case (Fig. 4.4) exhibited the development of a closed midlevel circulation, deformation zone and attendant confluent asymptote, and subsequent frontogenesis maximum northwest of the surface cyclone, which was coincident with band onset. Cross sections revealed a relatively upright frontal structure and deep layer of frontogenesis in this same region through the life of the band (Figs. 3.59–3.61). It appears that frontogenetical forcing in the presence of small conditional stability supported a strong, narrow updraft on the equatorward flank of the frontal zone, consistent with Emanuel (1985). Although it is possible that a portion of the frontal zone exhibited SI, the first order forcing mechanism for the band was frontogenesis in the presence of weak conditional stability.

The pivoting nature of the band in the 5–6 February 2001 case highlighted the impact of this motion in subsequent snowfall accumulation. Obviously, anticipating this motion is key to a successful forecast. During the 5–6 February 2001 case the pivoting

band motion mimicked the evolution of the midlevel frontogenesis field (compare Fig. 3.45f with Figs. 3.47–3.50), which again is tied to the evolution of the deformation field. Such correlation between the midlevel frontogenesis evolution and band motion suggests that once a favorable banding environment is anticipated, a forecaster may further anticipate band motion by assessing the forecast midlevel frontogenesis evolution.

Band dissipation occurred with the simultaneous weakening of the midlevel frontogenesis and the increasing horizontal slope of the frontal zone. It appears that these processes are related to the occlusion process, whereby the deformation zone becomes removed from the primary baroclinic zone as the midlevel circulation broadens (forcing the deformation zone farther north). The weakening frontogenesis and decreasing slope of the frontal zone are consistent with decreasing baroclinicity, whereby weakening deformation acts on weakening temperature gradients leading to weakening frontogenesis, and decreasing baroclinicity decreases the frontal slope if $\frac{d\theta}{dz}$ stays relatively constant. Furthermore, the semigeostrophic form of the Sawyer–Eliassen equation predicts a weaker frontogenetical response in the presence of stronger static stability. Consequently, the band diminishes in response to these processes. In the 5–6 February 2001 case band dissipation occurred over a longer period than band initiation, consistent with subjective single band observations made by the author, but this behavior will need to be quantified.

The forecast accumulated precipitation and vertical velocity fields from the 6/00 analysis time were elongated in the same orientation as the observed band, but were consistently found by 50–100 km equatorward from the observed band location. This result suggests that the model was able to define an axis of maximum ascent and

subsequent precipitation, but erred in its location. This distance is relatively accurate from a synoptic-scale perspective, but obviously too large for precision forecasts. The fact that the precipitation and vertical velocity fields hinted at banded structure is encouraging, and such signals call for further investigation by operational forecasters; however, it is clear that relying on the location of forecast precipitation and ascent maxima for precision forecasts is premature using present-generation operational models.

4.3.2 14–15 February 2000

The 14–15 February 2000 case was dominated by its position in the confluent entrance region of the Atlantic jet (Fig. 4.5). A modest surface cyclone associated with a midlevel trough was found in the equatorward entrance region of the jet, consistent with the nonbanded class conceptual model (Fig. 4.2). Since a closed midlevel circulation did not form, deformation associated with a confluent asymptote and subsequent frontogenesis were absent northwest of the surface cyclone (Fig. 4.5). Although frontogenesis was found ahead of the warm front in diffluent flow ahead of the midlevel disturbance, cross-section analysis revealed the frontal structure was rather horizontal (see Fig. 3.60a), suggesting greater conditional stability. It is hypothesized this greater stability limited band development.

4.3.3 21–22 March 1998

The 21–22 March 1998 case afforded an opportunity to examine a null case (Fig. 4.6). Although the surface cyclone exhibited a central pressure of ~ 980 hPa, a closed midlevel circulation (Fig. 4.6), and a negatively tilted trough (see Fig. 3.67d), the vertically stacked nature of the disturbance and large conditional stability limited further development (see Fig. 3.72). This limited development was especially made evident by the lack of deformation and frontogenesis associated with the cyclone (Fig. 4.6). Cross-section analysis affirmed the absence of frontogenesis and large conditional stability within the frontal zone. These results highlight the importance of deformation, frontogenesis, and weak conditional stability in mesoscale band formation.

4.3.4 Diagnostic Methods

CSI and the implied region of negative EPV has become synonymous with mesoscale banding based on the theory of CSI (Bennetts and Hoskins 1979). As such, the existence of negative EPV has become an integral component of modern band diagnostics such as the PVQ (Wetzel and Martin 2001) and VRS (Dixion et al. 2002) diagnostics. However, a limited investigation of the calculation of EPV in this study has shown that it is quite sensitive to the choice of representative wind and model resolution. A limited comparison of the VRS diagnostic using the geostrophic wind versus the full wind shows that this sensitivity can dramatically affect the diagnostic, even with the exclusion of inertial instability (compare Figs. 3.78 and 3.79; Figs. 3.80 and 3.81; Figs.

3.82 and 3.83). Even without taking this sensitivity into consideration, application of the VRS diagnostic to the three case studies had limited success in discriminating banded versus nonbanded events.

The results of this study highlight the utility of using frontogenesis in the presence of weak conditional stability to identify regions susceptible to banding, regardless of the presence of instability, whether upright or slantwise. This result is in agreement with the Sawyer–Eliassen equation, diagnostic studies by Emanuel (1985) and Hakim and Keyser (2001), and observational studies by Sanders and Bosart (1985). The FWS diagnostic represents an attempt to quantify the existence of frontogenesis in the presence of weak conditional stability, extending the VRS diagnostic to more general circumstances. The FWS diagnostic shifts the focus from the existence of negative EPV to the existence of significant frontogenesis, with an advantage being that it is not as sensitive to the choice of representative wind and the detrimental effects of using fine resolution are minimized. The most difficult aspect of defining the FWS diagnostic is what qualifies as “significant” frontogenesis and “weak” conditional stability. For the purposes of this study a frontogenesis threshold of $1 \text{ }^\circ\text{C (100 km)}^{-1} (3 \text{ h})^{-1}$ and a conditional stability threshold of $-0.1^\circ\text{C hPa}^{-1} < \frac{\partial\theta_{es}}{\partial p} < 0$ was used, but such criteria could be modified after additional operational experience.

4.4 Proposed Forecast Process

The aim of this study was to provide forecasters with a physical understanding of how the multiscale dynamics of a cyclone affect band formation and evolution. The

identified “smoking gun” of single band formation is frontogenesis in the presence of weak conditional stability. Although previous studies have reached this conclusion, this study places band formation in the context of the larger synoptic picture.

The key parameter relationships identified in this study are summarized in Fig. 4.7. The first three parameters (cyclogenesis, deformation, and frontogenesis) influence the location and strength of forcing. For instance, rapid cyclogenesis will lead to the formation of a closed midlevel circulation or diffluent flow ahead of the cyclone, maximizing deformation. This deformation, acting on the horizontal temperature gradient, contributes to significant frontogenesis (see Fig. 4.1). The frontogenetical response is dependent on the environmental stability, as dictated by the Sawyer–Eliassen equation. As illustrated by the 5–6 February 2001 case study, frontogenesis in the presence of weak conditional stability will lead to an intense narrow updraft and subsequent band formation. As illustrated by the 14–15 February 2000 case study, frontogenesis in the presence of large conditional stability will still result in ascent, but it will not be focused into a narrow updraft. Assessment of these parameters in a “top-down” approach provides forecasters a flow chart for addressing band development, and may alert forecasters to the possibility of a banded event as much as a few days before the event.

In response to these study results, the following forecast process is envisioned:

(a) Two to three days before the event:

Assess for potential banded precipitation event from the forecast synoptic flow. Key parameters include:

-strength of cyclogenesis

- formation of closed midlevel circulation or diffluent flow

- nature of deformation zone

- coincidence of deformation with strong baroclinicity

(b) From 24 to 12 h before the event:

Assess approximate band location by examining the cross-sectional environment through the above identified deformation zones. Key parameters include:

- intensity and depth of frontogenesis

- frontal slope (conditional stability)

- frontal saturation

- shape and magnitude of vertical velocity maximum (e.g., narrow band/broad maximum)

- coincidence of vertical motion maximum with the -12 to -16°C maximum dendritic growth layer

(c) From 6 to 0 h before the event:

Assess the forecast location and timing of band formation by evaluating short-range guidance, with focus turning to the anticipated band evolution. Key parameters include:

- forecast frontogenesis evolution

- possible pivoting motion

(d) During the event:

Monitor radar for band location, movement, and intensity. During prolonged events, short-range model guidance can be analyzed to anticipate band evolution.

While the lack of explicit representation of the mesoscale slantwise ascent associated with banded events limits model forecast precision, the larger-scale precursor environment, which is well represented in model forecasts, allows forecasters to anticipate tight snowfall gradients and significant accumulation rates at least 24 h prior to the event occurrence. For example, the short-range guidance from the 5–6 February 2001 case was relatively accurate in the location, timing, and shape of the frontogenetical forcing and subsequent vertical velocity maxima, suggesting county-by-county accuracy is possible at the onset of the event. The ever-increasing resolution of operational models may further enhance such accuracy in the future.

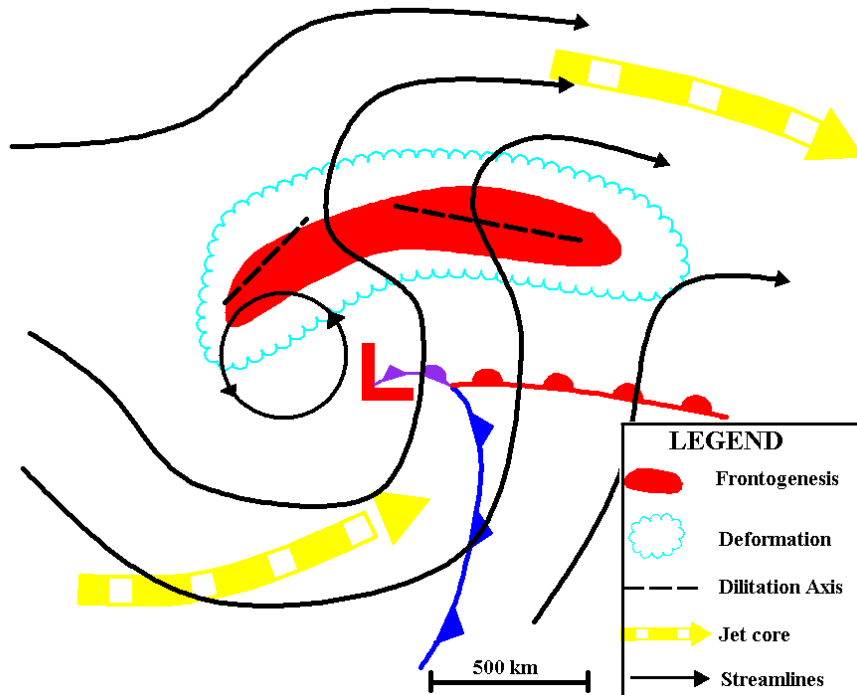


Fig. 4.1. Conceptual model of a single-banded system highlighting the key parameters. Features drawn include 700 hPa frontogenesis (shaded), 700 hPa deformation zone (encompassed by scalloped line) and associated primary dilatation axes (dashed line), 700 hPa streamlines (black lines), and 300 hPa jet cores (wide dashed arrows).

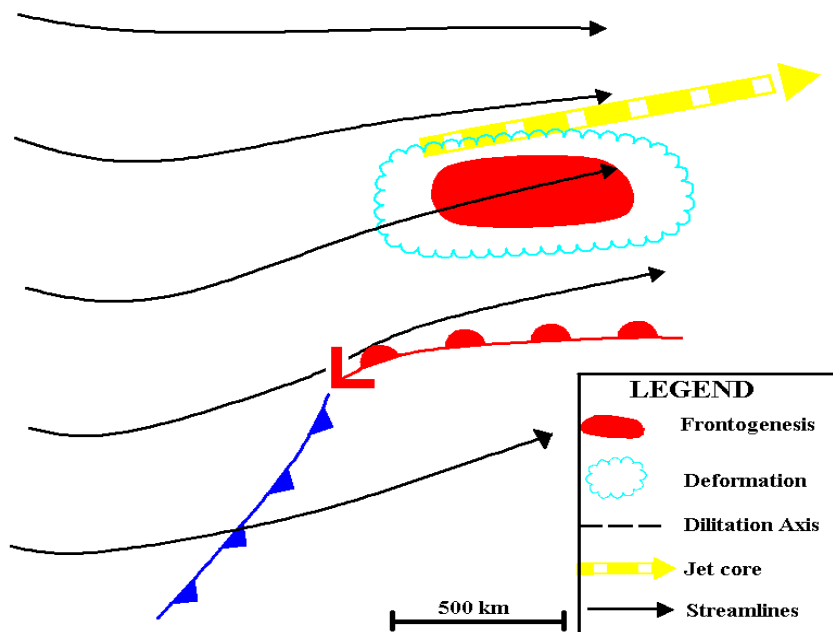
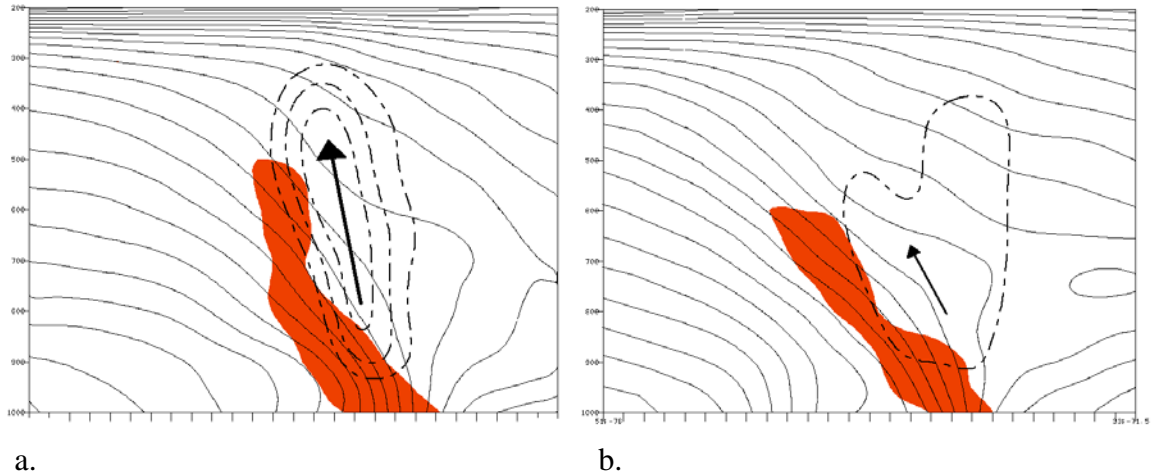


Fig. 4.2. As in Fig. 4.1, except for nonbanded system.



a. b.
 Fig. 4.3. Schematic cross sections through a (a) typical mesoscale band environment and (b) a typical nonbanded environment. Fields shown are frontogenesis (shaded), saturated equivalent potential temperature (thin solid), and ascent (dashed) with length of arrow proportional to the magnitude of ascent. Cross-section length is approximately 1000 km.

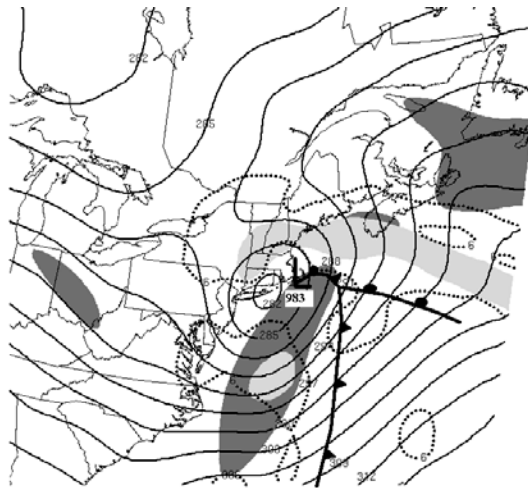


Fig. 4.4. Summary of the 5–6 February 2001 storm from the 6/00 Eta model analysis. Fields plotted include 700 hPa heights (black solid) contoured every 3 dam, 700 hPa frontogenesis (values exceeding $1^{\circ}\text{C} (100 \text{ km})^{-1} (3 \text{ h})^{-1}$ in light shading), deformation (contoured in dotted line at $6 \times 10^{-5} \text{ s}^{-1}$), and 300 hPa wind speed (values exceeding 60 m s^{-1} in dark shading), with conventional surface features overlaid and surface low pressure labeled in hPa (bold type).

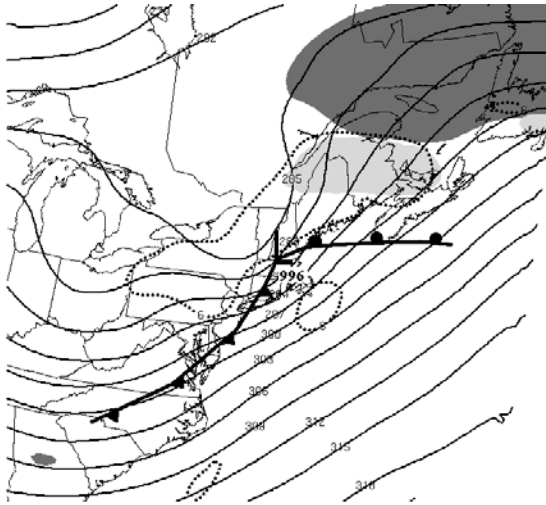


Fig. 4.5. As in Fig. 4.4, except for 14/18 analysis.

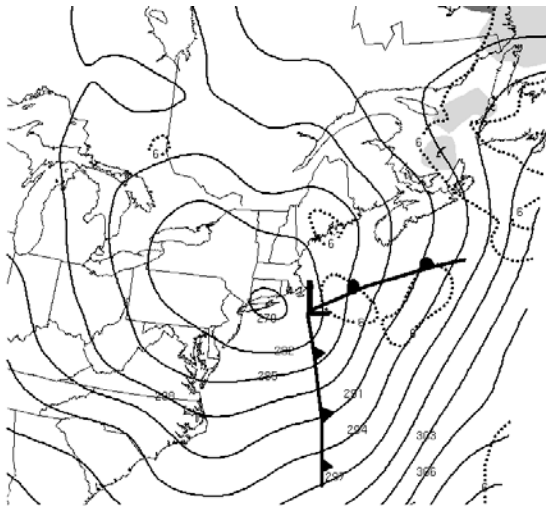


Fig. 4.6. As in Fig. 4.4, except for 22/12 analysis.

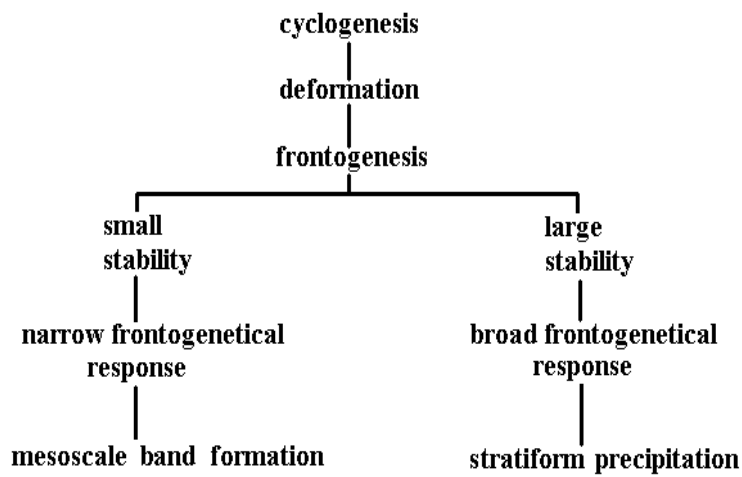


Fig. 4.7. Flow chart of the key components and interactions involved in band formation.

5. Conclusions

5.1 Summary and Conclusions

A climatology of banded precipitation events, composites of banded and nonbanded events, and selected case studies in the northeast U.S. during the cold season (October through April) are presented. Precipitation systems in the northeast U.S. that exhibited greater than 25 mm of rainfall or 12.5 mm liquid equivalent during a 24 h period were identified as cases for study using the Unified Precipitation Dataset (UPD). Composite radar data from these cases were viewed to develop a band classification scheme. The resultant band classification scheme represents a refinement of previous classification schemes, incorporating intensity thresholds from the national WSR-88D radar network. This scheme was then applied to cases in April 1995 and from October 1996 through April 2001. Out of the 111 cases identified during this period, 88 cases had complete radar coverage (termed study cases).

Application of the band classification scheme to these study cases established that mesoscale banding is a fairly frequent phenomenon in the northeast US, with over 85% of the 88 study cases over the 1996 – 2001 period exhibiting some form of significant mesoscale banding. In contrast to other parts of the continental US, single-banded events were found to be the most common with 48 events documented, followed by 40 transitory events, 36 narrow cold-frontal events, 29 multibanded events, and 9 undefined events. Thirteen cases exhibited no defined banding, while a number of cases exhibited more than one type of banded event during their duration. Further investigation of the single-banded events identified banded structure in the comma-head portion of

storms, with nearly 80% of the bands exhibiting some portion of their length in the northwest quadrant of the surface cyclone.

The tendency for single bands to be short-lived, and the large number of transitory events, suggest the conditions favoring single band development occur on limited time-scales, although a number of single bands persisted beyond 12 h. The tendency for multibands to occur just ahead of the surface cyclone and the preferred lifetime mode of 4–10 h is intriguing, and may point to favorable dynamics in this location and on these time scales, but such conjectures require more study.

Composites were calculated from the NCEP/NCAR reanalysis dataset and Eta model analysis and 6-h forecast fields for the single, multi, and nonbanded events to distinguish characteristic flow regimes. The composites document how cyclogenesis and the attendant synoptic flow evolution influence cyclone substructure via the location, strength, and character of deformation, and associated location and magnitude of frontogenesis. The northwest composite class revealed the formation of a deformation zone associated with a confluent asymptote northwest of the surface cyclone as a midlevel closed circulation developed during cyclogenesis. This flow configuration helped to focus frontogenesis along the confluent asymptote through a deep layer. This deep-layer frontogenesis provided a focused forcing mechanism for the single-banded events. The east composite class revealed the formation of diffluent midlevel flow ahead of the disturbance, which contributed to midlevel deformation and associated frontogenesis ahead of the warm front. This frontogenesis provided forcing for the east single-banded events. The nonbanded composite, similar to the east composite, exhibited a midlevel deformation zone ahead of the disturbance; however, this deformation was

associated with midlevel confluence rather than midlevel diffluence as observed in the east composite.

Composite cross sections highlighted the importance of a deep layer of frontogenesis coincident with weak conditional stability. The northwest, northwest-near, northwest-far, and east composite class cross sections revealed a deep layer of significant frontogenesis within a relatively upright frontal zone. Although the nonbanded composite cross section exhibited significant frontogenesis, the frontal structure was much more horizontal, suggesting greater conditional stability. This result is in direct agreement with the Sawyer–Eliassen equation, which suggests that the frontogenetical response will be enhanced in the presence of weak conditional stability. Further investigation of the northwest class bands revealed dissipation occurred in response to the simultaneous weakening of frontogenesis and increasing conditional stability during cyclone occlusion.

The three case studies illustrated the association between cyclogenesis, deformation, and conditional stability, and the location and magnitude of the resulting frontogenetical response. Consistent with the northwest composite, the rapid deepening of the 5–6 February 2001 case facilitated the development of a closed midlevel circulation, attendant confluent asymptote, and subsequent frontogenesis maximum northwest of the surface cyclone, with the development of these features coincident with band onset. Cross sections revealed a nearly upright vertical frontal structure and deep layer of frontogenesis in this same region through the life of the band, enhancing the frontogenetical response. The 14–15 February 2000 case evolution was dominated by its position in the confluent entrance region of the Atlantic jet, consistent with the

nonbanded composite evolution. Since a closed midlevel circulation did not form until late in its development, deformation associated with a confluent asymptote and significant frontogenesis were absent northwest of the surface cyclone. Although frontogenesis was found ahead of the warm front in diffluent flow ahead of the midlevel disturbance, cross-section analysis revealed the frontal structure in this region of the cyclone was rather horizontal, suggesting greater conditional stability and a more limited frontogenetical response. Although a closed midlevel circulation and negatively tilted trough were present in the 21–22 March 1998 case, the vertically stacked nature of the disturbance and large conditional stability limited development. This vertical structure was especially evident in cross-section analysis, which showed a marked absence of frontogenesis, and large conditional stability.

Evaluation of the 5–6 February 2001 case Eta model forecast precipitation and vertical velocity fields revealed that these respective precipitation and ascent maxima exhibited an elongated orientation similar to the observed band, but were consistently 50–100 km equatorward from the observed band location. The fact that the precipitation fields and vertical velocity fields hinted at banded structure is encouraging, and such a signal may encourage further investigation by operational forecasters, but it is clear that relying on the location of forecast precipitation and vertical velocity maxima for precision forecasts is premature using present-generation operational models.

Investigation of the calculation of saturated equivalent potential vorticity in this study has shown that it is quite sensitive to the choice of representative wind and model resolution. A limited comparison of the vertically integrated realizable symmetric instability diagnostic using the geostrophic wind versus the full wind shows this

sensitivity can dramatically affect the diagnostic. Even without taking this sensitivity into consideration, application of the vertically integrated realizable symmetric instability diagnostic to the three case studies had limited success in discriminating banded versus nonbanded events.

The results of this study highlight the utility of frontogenesis in the presence of weak conditional stability in identifying regions susceptible to mesoscale banding, regardless of the presence of instability, whether upright or slantwise. The frontogenesis in the presence of weak stability diagnostic quantifies this fact by identifying deep layers of significant frontogenesis coincident with weak conditional stability, near saturation, and ascent. Regardless of the choice of operational diagnostic, this study provides the context in which to apply the diagnostic. Additionally, the dynamical link to the process of cyclogenesis and attendant deformation zones affords a longer forecast lead-time, alerting forecasters to the possibility of a banded event one to two days in advance.

5.2 Future Work

This study focused on the single-banded structure, most specifically the northwest class single-banded events. Future work should investigate east class events, establishing similarities and differences from nonbanded cases. The advent of sub-10 km operational model “data” will facilitate detailed examination of the individual finescale bands within the multiband structure, an elaboration not afforded in the current study.

Although composite evolutions were provided by the NCEP/NCAR reanalysis dataset, future work could extend the Eta model composites back and forward in time.

Limited composites incorporating higher resolution model data from recent cases could also be envisioned. Although higher resolution data is noisier and may not conform to quasigeostrophic diagnostics, it facilitates detailed cross-sectional information that may prove useful.

Finally, since the one-to-two day forecast model fields are vital to the success of a band forecast, investigation should establish model forecast biases and consistency with respect to cyclogenesis, deformation, frontogenesis, and conditional stability. Such investigation may strengthen forecaster confidence in anticipating band development one to two days in advance.

REFERENCES

- Austin, P. M., and R. A. Houze Jr., 1972: Analysis of the structure of precipitation patterns in new england. *J. Applied Met.*, **11**, 926-935.
- Barnes, S. L., F. Caracena, and A. Marroquin, 1996: Extracting synoptic-scale diagnostic information from mesoscale models: The Eta model, gravity waves, and quasigeostrophic diagnostics. *Bull. Amer. Meteor. Soc.*, **77**, 519–528.
- Bennetts, D. A., and B. J. Hoskins, 1979: Conditional symmetric instability – A possible explanation for frontal rainbands. *Quart. J. Roy. Meteor. Soc.*, **105**, 945-962.
- Bjerknes, J., 1919: On the structure of moving cyclones. *Geofys. Soc.*, **1**, 1-8.
———, and H. Solberg, 1922: Life cyclone of cyclones and the polar front theory of atmospheric circulation. *Geofys. Publ.*, **12**, 1-61.
- Black, T. L., 1994: The new NMC mesoscale eta model: Description and forecast examples. *Wea. Forecasting*, **9**, 265–278.
- Boucher, R. J., and R. Wexler, 1961: The motion and predictability of precipitation lines. *J. Meteor.*, **18**, 160-171.
- Browning, K. A., 1985: Conceptual models of precipitation systems. *Meteorological Magazine*, 114, 293-318.
- , and T. W. Harrold, 1969: Air motion and precipitation growth in a wave depression. *Quart. J. Roy. Meteor. Soc.*, **95**, 288-309.
- , and T. W. Harrold, 1970: Air motion and precipitation growth at a cold front. *Quart. J. Roy. Meteor. Soc.*, **96**, 369-389.
- , 1990: Organization of clouds and precipitation in extratropical cyclones. *Extratropical Cyclones*, Erik Palmén Memorial Volume, C. W. Newton and E. O. Holopainen, Eds., Amer. Meteor. Soc., 129-153.
- , and N. M. Roberts, 1994: Structure of a frontal cyclone. *Quart. J. Roy. Meteor. Soc.*, **120**, 1535-1557.
- , and N. M. Roberts, 1999: Mesoscale analysis of arc rainbands in a dry slot. *Quart. J. Roy. Meteor. Soc.*, **123**, 3495-3511.

- , 1999: Mesoscale aspects of extratropical cyclones: An observational perspective. *The Life Cyclones of Extratropical Cyclones*, M. A. Shapiro and S. Gronas, Eds., Amer. Meteor. Soc., 265-283.
- Byrd, G. P., 1989: A composite analysis of winter season overrunning precipitation bands over the Southern Plains of the United States. *J. Atmos. Sci.*, **46**, 1119-1132.
- Carlson, T. N., 1980: Airflow through midlatitude cyclones and the comma cloud pattern. *Mon. Wea. Rev.*, **108**, 1498-1509.
- Crocker, A. M., W. L. Godson, and C. M. Penner, 1947: Frontal contour charts. *J. Meteor.*, **4**, 95-99.
- Danielsen, E. F., 1968: Stratospheric-tropospheric exchange based on radioactivity, ozone and potential vorticity. *J. Atmos. Sci.*, **25**, 502-518.
- desJardins, M. L., K. F. Brill, and S. S. Schotz, 1991: Use of GEMPAK on UNIX workstations. *Proc. Seventh Int. Conf. On Interactive Information and Processing Systems for Meteorology, Oceanography, and Hydrology*, New Orleans, LA, Amer. Meteor. Soc., 449-453.
- Dirks, R. A., J. P. Keuttner and J. A. Moore, 1988: Genesis of atlantic lows experiment (GALE): An overview. *Bull. Amer. Meteor. Soc.*, **69**, 148-160.
- Dixion, R. S., K. A. Browning, and G. J. Shutts, 2002: The relation of moist symmetric instability and upper-level potential-vorticity anomalies to the observed evolution of cloud heads. *Quart. J. Roy. Meteor. Soc.*, **128**, 839-859.
- Eliassen, A., 1962: On the vertical circulation in frontal zones. *Geophys. Publ.*, **24**, 147-160.
- Elliott, R. D., and E. L. Hovind, 1964: On convection bands within Pacific coast storms and their relation to storm structure. *J. Appl. Meteorol.*, **3**, 143-154.
- Emanuel, K.A., 1985: Frontal circulations in the presence of small moist symmetric stability. *J. Atmos. Sci.*, **42**, 1062-1071.
- , 1988: Observational evidence of slantwise convective adjustment. *Mon. Wea. Rev.*, **116**, 1805-1816.
- Galloway, J. L., 1958: The three-front model: Its philosophy, nature, construction and use. *Weather*, **13**, 3-10.
- , 1960: The three-front model, the developing depression and the occluding process. *Weather*, **15**, 293-301.

- Grumm, R. H., and G. Forbes, 1994: WSR-88D observations of conditional symmetric instability snowbands over central Pennsylvania. Eastern Region Tech. Attachment 94-12B, National Weather Service, NOAA, U.S. Department of Commerce, 21 pp. [Available from NOAA-National Weather Service, Airport Corporate Center, 630 Johnson Avenue, Bohemia, NY 11716.]
- Godson, W. L., 1951: Synoptic properties of frontal surfaces. *Quart. J. Roy. Meteor. Soc.*, **77**, 633-653.
- Hadlock, R., and C. W. Kreitzberg, 1988: The Experiment on Rapidly Intensifying Cyclones over the Atlantic (ERICA) field study: Objectives and plans. *Bull. Amer. Meteor. Soc.*, **69**, 1309-1320.
- Hakim, G. J., and D. Keyser, 2001: Canonical frontal circulation patterns in terms of Green's functions for the Sawyer–Eliassen equation. *Q. J. R. Meteorol. Soc.*, **127**, 1795-1814.
- Harper, W. G., and J. G. D. Beimers, 1958: Movement of precipitation belts. *Quart. J. T. Meteor. Soc.*, **84**, 242-249.
- Hobbs, Peter, 1978: Organization and structure of clouds and precipitation on the mesoscale and microscale in cyclonic storms. *Reviews of Geophysics and Space Physics*, **16**, 741-755.
- , J. D. Locatelli, and J. E. Martin, 1990: Cold fronts aloft and the forecasting of precipitation and severe weather east of the Rocky Mountains. *Wea. Forecasting*, **5**, 613-626.
- , J. D. Locatelli, and J. E. Martin, 1996: A new conceptual model for cyclones generated in the lee of the Rocky Mountains. *Bull. Amer. Meteor. Soc.*, **77**, 1169-1178.
- Hoskins, B. J., 1976: Baroclinic waves and frontogenesis. Part I: Introduction and Eady waves. *Quart. J. Roy. Meteor. Soc.*, **102**, 103-122.
- , and N. V. West, 1979: Baroclinic waves and frontogenesis. Part II. Uniform potential vorticity jet flows—cold and warm fronts. *J. Atmos. Sci.*, **36**, 1663-1680.
- Houze, Robert A. Jr., Peter V. Hobbs, Kumud R. Biswas, and William M. Davis, 1976: Mesoscale rainbands in extratropical cyclones. *Mon. Wea. Rev.*, **104**, 868-879.
- , 1993: *Cloud Dynamics*, Academic Press, New York, 573 pp.
- Kalnay, E., and Coauthors, 1996: The NCEP/NCAR 40-Year Reanalysis Project. *Bull. Amer. Meteor. Soc.*, **77**, 437-471.

- Keshishian, L. G., L. F. Bosart, and E. W. Bracken, 1994: Inverted troughs and cyclogenesis over interior North America: A limited regional climatology and case studies. *Mon. Wea. Rev.*, **122**, 565-607.
- Kistler, R., E. Kalnay, W. Collins, S. Saha, G. White, J. Woolen, M. Chelliah, W. Ebisuzaki, M. Kanamitsu, V. Kousky, H. Van Den Dool, R. Jenne, and M. Fiorino, 2002: The NCEP-NCAR 50-year reanalysis: Monthly means CD-ROM and documentation. *Bull. Amer. Meteor. Soc.*, **82**, 247-267.
- Klazura, G. E., and D. A. Imy, 1993: A description of the initial set of analysis products available from the NEXRAD WSR-88D system. *Bull. Amer. Meteor. Soc.*, **74**, 1293-1311.
- Kocin, P. J., and L. W. Uccellini, 1990: Snowstorms along the northeastern coast of the United States: 1955 – 1985. American Meteorological Society, 280 pp.
- Knettner, J., 1959: The band structure of the atmosphere. *Tellus*, **11**, 267-294.
- Koch, S. E., 2001: Real-time detection of split fronts using mesoscale models and WSR-88D radar products. *Wea. Forecasting*, **16**, 35-55.
- Kreitzberg, C. W., and H. A. Brown: 1970: Mesoscale weather systems within an occlusion. *J. Appl. Meteor.*, **9**, 417-432.
- Lemaitre, Y., G. Scialom, and A. Protat, 2002: Conditional symmetric instability, frontogenetical forcing and rain-band organization. *Quart. J. Roy. Meteor. Soc.*, **127**, 2599-2634.
- Locatelli, J. D., J. M. Sienkiewicz, and P. V. Hobbs, 1989: Organization and structure of clouds and precipitation on the mid-Atlantic coast of the United States. Part I: Synoptic evolution of a frontal system from the Rockies to the Atlantic Coast. *J. Atmos. Sci.*, **46**, 1327-1348.
- Martin, Jonathan E., 1998a: The structure and evolution of a continental winter cyclone. Part I: Frontal structure and the occlusion process. *Mon. Wea. Rev.*, **126**, 303-328.
- , 1998b: The structure and evolution of a continental winter cyclone. Part II: Frontal forcing of an extreme snow event. *Mon. Wea. Rev.*, **126**, 329-348.
- , 1999: Quasigeostrophic forcing of ascent in the occluded sector of cyclones and the trowl airstream. *Mon. Wea. Rev.*, **127**, 70-88.
- Mass, C. F., 1991: Synoptic frontal analysis: Time for a reassessment? *Bull. Amer. Meteor. Soc.*, **72**, 348-363.
- Miller, J. E., 1948: On the concept of frontogenesis. *J. Meteor.*, **5**, 169-171.

- Moore, J. T., and T. Lambert, 1993: The use of equivalent potential vorticity to diagnose regions of conditional symmetric instability. *Wea. Forecasting*, **8**, 301-308.
- Nicosia, D. J., and R. H. Grumm, 1999: Mesoscale band formation in three major northeastern United States snowstorms. *Wea. Forecasting*, **14**, 346-368.
- NOAA, 1996–2001: Daily weather maps weekly series. Washington D.C. GPO.
- Penner, C. M., 1955: A three-front model for synoptic analyses. *Quart. J. Roy. Meteor. Soc.*, **81**, 89-91.
- Rauber, R. M., M. K. Ramamurthy, B. F. Jewett, and M. Han, 2001: Finescale structure and dynamics of a heavy snowband. *Preprints 9th Conference on Mesoscale Processes*, 565–568.
- Reuter, G. W., and M. K. Yau, 1990: Observations of slantwise convective instability in winter cyclones. *Mon. Wea. Rev.*, **118**, 447-458.
- Sanders, F., 1986: Frontogenesis and symmetric stability in a major New England snowstorm. *Mon. Wea. Rev.*, **114**, 1847-1862.
- , and L. F. Bosart, 1985: Mesoscale structure in the megalopolitan snowstorm of 11-12 February 1983. Part I: Frontogenetical forcing and symmetric instability. *J. Atmos. Sci.*, **42**, 1050-1061.
- , and J. R. Gyakum, 1980: Synoptic-dynamic climatology of the “bomb”. *Mon. Wea. Rev.*, **108**, 1589–1606.
- Sawyer, J.S., 1956: The vertical circulation at meteorological fronts and its relation to frontogenesis. *Proc. R. Soc. London*, **A234**, 346–362.
- Schultz, D. M., and P. N. Schumacher, 1999: The use and misuse of conditional symmetric instability. *Mon. Wea. Rev.*, **127**, 2709-2732.
- , 2001: Reexamining the cold conveyor belt. *Mon. Wea. Rev.*, **129**, 2205-2225.
- , and C. A. Doswell, III, 2002: Comments on “An operational ingredients-based methodology for forecasting midlatitude winter season precipitation”. *Wea. Forecasting*, **17**, 160-167.
- Shapiro, M. A., and D. Keyser, 1990: Fronts, jet streams and the tropopause. *Extratropical Cyclones, The Erik Palmén Memorial Volume*, C. W. Newton and E. O. Holopainen, Eds., Amer. Meteor. Soc., 167-191.

- Snook, J. S., 1992: Current techniques for real-time evaluation of conditional symmetric instability. *Wea. Forecasting*, **7**, 430-439.
- Stuart, N. A., 2001: Multi-dimensional analysis of an extreme thundersnow event during the 30 December 2000 snowstorm. *Preprints 18th Conference on Weather Analysis and Forecasting and 14th Conference on Numerical Weather Prediction*, 223–226.
- Trapp, R. J., D. M. Schultz, A. V. Ryzhkov, and R. L. Holle, 2000: Multiscale structure and evolution of an Oklahoma winter precipitation event. *Mon. Wea. Rev.*, **129**, 486-501.
- Uccellini, L. W., S. F. Corfidi, N. W. Junker, P. J. Kocin, and D. A. Olson, 1992: Report on the Surface Analysis Workshop held at the National Meteorological Center 25-28 March 1991. *Bull. Amer. Meteor. Soc.*, **73**, 459-472.
- Wallace, J. M., and P. V. Hobbs, 1977: *Atmospheric science: An Introductory Survey*. Academic Press, 467 pp.
- Wang, Peng-Yun and Peter V. Hobbs, 1983: The mesoscale and microscale structure and organization of clouds and precipitation in midlatitude cyclones. X: Wavelike rainbands in an occlusion. *J. Atmos. Sci.*, **40**, 1950-1964.
- Wakimoto, R. M, and B. L. Bosart, 2001: Airborne radar observations of a warm front during FASTEX. *Mon. Wea. Rev.*, **129**, 254-294.
- Wetzel, S. W., and J. E. Martin, 2001: An operational ingredients-based methodology for forecasting midlatitude winter season precipitation. *Wea. Forecasting*, **16**, 156-167.
- , and J. E. Martin, 2002: Reply to “Comments on ‘an operational ingredients-based methodology for forecasting midlatitude winter season precipitation. *Wea. Forecasting*, **17**, 168-171.
- Wiesmueller, J. L., and S. M. Zubrick, 1998: Evaluation and application of conditional symmetric instability, equivalent potential vorticity, and frontogenetical forcing in an operational forecasting environment. *Wea. Forecasting*, **13**, 84-101.
- Xu, Q., 1992: Formation and evolution of frontal rainbands and geostrophic potential vorticity anomalies. *J. Atmos. Sci.*, **49**, 629-648.

APPENDIX

Significant Precipitation Dataset

“UPD storm date” refers to the dates of cases meeting the significant precipitation thresholds identified from the Unified Precipitation Dataset and Daily Weather Maps series. “Start” and “end” refer to the times when the case starts and ends determined by the radar data. Times are given as day/time. If radar data were not available for a case, no start/end times are given. An * at the start time means the case started before the radar data were available. Conversely, an * at the end time means the event continued beyond the available radar data.

UPD STORM DATE	START	END
APRIL 1995		
04/24	23/1200Z	24/1200Z*
NOVEMBER 1996		
11/20	19/2000Z	20/1600Z
11/22	21/0000Z	22/0600Z
11/26-27	25/1200Z	27/1600Z
DECEMBER 1996		
12/01-03	01/0400Z	02/2300Z
12/06-07	05/2200Z	07/0200Z
12/8	07/0600Z	08/1800Z
12/12-14	13/1900Z*	15/0000Z*
12/17	16/1200Z*	17/1200Z
12/20	19/1200Z	20/1200Z
JANUARY 1997		
01/10	09/1200Z*	11/0000Z
	RADAR DATA ENDS AFTER THE 18th	
01/25		
01/28		
FEBRUARY 1997		
(NO DATA)		
02/14		
02/21		
02/27		

MARCH 1997

(NO DATA)

03/02
03/6-7
03/14
03/19
03/26
03/30

APRIL 1997

04/01 31/2200Z* 01/2300Z
04/13
04/18-19
04/28-29
04/29

OCTOBER 1997

10/15 14/2000Z 15/1200Z*
10/18 17/1200Z 18/0700Z
10/19 19/0000Z 20/2100Z
10/25 24/1200Z 25/2300Z
10/27 26/0800Z 27/2200Z

NOVEMBER 1997

11/01-02 01/1600Z* 02/1400Z
11/02-03 02/0400Z 03/0600Z
11/07-10 06/1800Z 10/0800Z
11/14-15 13/1200Z 15/1200Z
11/22 22/0000Z 22/1200Z*
11/27 26/1800Z 27/1200Z

DECEMBER 1997

12/1-2 11/30/1200Z 12/02/0300Z
12/6-7 6/0100Z* 7/0600Z
12/11
12/23 22/0300Z 23/2300Z*
12/30 29/1500Z 30/1800z

JANUARY 1998

01/5-10 5/1800Z 10/0130Z
01/15-16 15/0300Z 16/2100Z
01/22-25 22/1800Z 24/2355Z*
01/28 27/1200Z 29/1155Z

FEBRUARY 1998

02/4-6 03/1200Z 06/0600Z
02/12-13 11/1500Z 13/0000Z
02/17-20 17/1200Z 19/1155Z
02/23-26 23/0000Z 25/1155Z*

MARCH 1998

03/8-10	08/0500Z	10/0600Z
03/15	14/2000Z	15/1400Z
03/18-20	18/0000Z	19/2355Z
03/20-22	20/1600Z	22/20Z

APRIL 1998

04/02	1/0600Z	2/1700Z
04/04	4/0000Z	4/2355Z
04/10	9/0000Z	10/1455Z
04/15-17	14/1200Z	15/0900Z
	16/0000Z	16/2355
04/19-20	18/1800Z	20/1700Z
04/24	23/0600Z	24/1800Z
04/27	26/0000Z	27/1200Z

OCTOBER 1998

10/1		
10/6-11	8/1530Z*	11/2355Z
10/15-16	14/0000Z	15/1200Z

NOVEMBER 1998

11/26-27	25/2000Z	27/0900Z
----------	----------	----------

DECEMBER 1998

12/08-09	7/1200Z	9/1200Z
12/13	12/0900Z	14/0000Z
12/18	17/1200Z	18/0655Z*
12/22		
12/24		

JANUARY 1999

(note: the following case dates were identified from DMW)

1/3-5	3/0000Z	4/0600Z
1/13-15	13/0400Z	15/2145Z
1/18-19	18/0400Z	19/1000Z
1/23-24	23/1600Z	25/0600Z

FEBRUARY 1999

02/24-25		
----------	--	--

MARCH 1999

03/4-5	03/1200Z*	4/2200Z
03/6-7	06/1900Z*	7/0130Z*

03/11-12
03/13-15
03/21-23 21/0600Z 22/2355Z

APRIL 1999

04/9-10 9/1200Z 10/1200Z

OCTOBER 1999

10/4-5 3/1800Z 05/1000Z
10/9-10 9/1500Z 10/2355
10/13-16 13/1500Z 14/2355Z

NOVEMBER 1999

11/2-3/99 2/600Z 2/1600Z*

DECEMBER 1999

12/13-15/99 14/2200Z* 15/1400Z

JANUARY 2000

1/4-5 03/1200Z (gap)05/1200
1/13-14
1/25-26 25/0000Z (gap)26/1200Z
1/30-31 30/1200Z 31/2355Z

FEBRUARY 2000

2/13-14 13/1800Z 15/0400Z
2/18-19 18/0000Z 18/2255Z*

MARCH 2000

03/11-12 11/0600Z 12/2355Z
03/16-17 16/0600Z 18/0100Z
03/21-22 20/0600Z 21/1800Z*
03/27-28 27/0900Z 28/2355Z

APRIL 2000

04/8-9 07/1800Z 09/2355Z
04/21-23 20/0600Z 23/2355Z

OCTOBER 2000

10/5-6

NOVEMBER 2000

11/25-27 25/1300Z (gaps) 27/1200Z

DECEMBER 2000

12/16-17 16/0400Z 18/1200Z
12/30-31 30/0500Z 31/0800Z*

JANUARY 2001

01/20-21 20/0000Z* 21/1755Z

FEBRUARY 2001

02/5-6 05/0000Z 06/1500Z

MARCH 2001

03/5-7 04/1200Z 07/0600Z
03/9-10 09/0000Z 10/1155Z*
03/12-13 12/1800Z 13/1700Z*
03/21-23 20/1200Z 23/1200Z
03/30-31 30/0000Z 31/1800Z

APRIL 2001

04/7-8 07/1200Z 08/1800Z